Transition Metals as Catalysts for Cross-Coupling and N_2 Fixation

Thesis by

Trixia M. Buscagan

In Partial Fulfillment of the Requirements for
the degree of Doctor of Philosophy in
Chemistry

CALIFORNIA INSTITUTE OF TECHNOLOGY
Pasadena, California

2018
(Defended August 28, 2017)

Trixia M. Buscagan
ORCID: 0000-0001-8242-9203

ACKNOWLEDGEMENTS

I'd like to start by thanking Jonas and his group. Jonas, you have definitely challenged me scientifically and I appreciate all of your time and advice. Thank you for letting me spend time in your lab when I was transitioning from MIT to Caltech as part of Greg Fu's research group. And, most of all, thank you for accepting me into your group 2 years later. Your kindness and generosity are deeply appreciated. Your criticisms during subgroup and group meetings have helped me develop immensely as a scientist. In general, I think more deeply and critically about science thanks to you. I will apply the same type of scientific rigor to my future projects.

I'd like to thank the current group members; in particular, Tanvi, Kumiko, Matt, Meaghan, Javier, Nik, Trevor, Nina, Marcus, and Dirk. Tanvi, I really appreciate our tea breaks. Nina and Meaghan too! Thank you for supporting me, listening to me, and sharing your experiences with me. Thank you Javier, Nik, and Matt for helpful advice during critical times of my scientific career in the group. Thank you Kumiko, Dirk, Javier, Matt, Nik, Miles, and Marcus for proofreading parts of my thesis. The group generally has been such a wonderful resource. It's been great doing science with you all. I'd like to also thank the former Peters group members, Dr. Jon Rittle, who helped me get started in the Peters' lab, Dr. Shabnam Hematian, Dr. Hill Harman, Dr. Gaël Ung, Dr. Sid Creutz, Dr. Sam MacMillan, and Dr. Dan Suess, as well as the Fu group members I overlapped with including Dr. Chris Cordier, Dr. Rylan Lungdren, Shoshana Bachman, Crystal Chu, Dr. Nathan Schley, and many others! Thank you for your wonderful chemistry insights.

I'd also like to thank Professor Gregory Fu, my first research advisor. The chemistry I did with you was super challenging for me at first. I didn't know what a glovebox was when

I started… in the end, I learned so much from the Pd and Ni chemistry I did. Thank you for letting me pursue mechanistic work, an uncommon project theme for the group at the time.

I'd also like to thank Larry Henling, Mike Takase, Dave Vander Velde, and Paul Oyala, who are also part of these groups (although not formally)! I learned a lot from you all. I'd also like to acknowledge everyone who helped me transition from MIT (where Greg originally was when I started graduate school) to Caltech, including Agnes Tong, Douglas Duquette, Zach Wickens, Shannon Stone, Sarah Reisman, and Brian Stoltz as well as their research groups! I'd also like to thank Sarah for being a great role model and for being the chair of my committee. I'd like to thank Theo (who is also on my committee) and his group for being so enthusiastic about science!

Working towards my PhD here at Caltech has been difficult. On top of the inherent difficulties of obtaining a PhD, I've been sexually harassed and experienced a number of microagressions due to my race and/or gender. I started the Diversity in Chemistry Initiative (DICI) with Javier Fajardo Jr. (a fellow graduate student and my partner), Agnes Tong (former Chemistry Graduate Studies Coordinator), and Professor Doug Rees (DICI's faculty advisor). We are a very small group of underrepresented minority (URM) students and postdocs and I mean small… currently, we have six active URM members and I'd like to thank all of them for their help, support, and efforts in getting our program started: Dr. Dana Levine, Dr. Marchello Cavitt, Stephanie Threatt, Javier Fajardo Jr., and Mary Arrastia. I'd also like to thank the former DICI members: Dr. Sonja Francis, Dr. Alejo Lifschitz, Dr. Guy Edouard, and Paul Nunez. Our goal is to provide a support network for URM's in Chemistry and at Caltech generally. One of our main modes of action is inviting exceptional faculty from universities across the United States to give research seminars. We have successfully

hosted Professor Squire Booker and Professor Anjelica Gonzalez. My experiences with these two speakers helped me so much. It was helpful to hear them talk about the hardships they went through because of their URM status and how they worked through these situations. They are both amazing scientists and it's great to see that they've made it. There is definitely a lot more we could be doing as a division and school. I don't know why it is that out of a total of 104 Chemistry PhD graduates in the past five years, not a single URM woman has graduated with a PhD in Chemistry (and likely ever has but I hope I'm wrong). (There have been five URM males to graduate with Chemistry PhD's.)

I'd like to thank the people that invented surfing and yoga. I picked up both hobbies while I was at Caltech and they helped me find some peace during very tumultuous times. In addition, two albums helped me get through graduate school: M83's "Hurry Up, We're Dreaming" and Beyonce's "Lemonade". I'd also like to thank Felicia Hunt who helped me switch research groups and resolve Title IX issues. Her support meant so much to me during tough times. I'd like to thank all of the women who came forward who were being harassed by the same men I was being harassed by. Often, more than one voice is needed for action, and I'm so glad other people spoke up. I'd also like to thank the Diversity Center; in particular, Erin-Kate and Taso, who are such warm, open people. (Everyone at the Diversity Center is kind, but I had the luck of running into Erin-Kate and Taso during my first visit.) I'd like to thank Maggie Ateia for mediating the Grad Chat lunch discussions and everyone who attended those. Thank you for your transparency and openness to share and listen. I'd also like to thank my first therapist, Dr. Jennifer Howes as well as my current therapist, Dr. Evelyn Novello. Thank you for listening!

I'd like to acknowledge Gregory Harlow, a fellow graduate student in the Fu/Peters group, who committed suicide. He was very passionate about his chemistry. I think about him every day.

I want to thank Shoshana Bachman for her friendship. Her thoughtfulness, awareness, and honesty helped me through a lot of tough situations. I'd like to thank Dr. Miles Johnson, another friend, who is now an assistant Professor at the University of Richmond (you made it!). Thank you for sharing your experiences with me. You are one of the kindest people I know.

I'd like to thank Doug for believing in me, supporting me, and for his general kindness. Thank you for giving me hope. Thank you for listening to what I've experienced here. You were so open and caring, even when I didn't know you! I'm glad you are the Graduate Studies Dean. Thank you for accepting me into your group as a postdoc. I'm so excited to work with you and your group and to learn more about nitrogenase.

I'd also like to thank my best friend and partner, Javier Fajardo Jr. I appreciate your constant support and help, especially during times when I wasn't sure about anything anymore or when I wasn't my best. Thank you for helping me be a better person in all aspects of my life.

I'd like to thank my family starting with my family dog (Zeke) and cat (Venus) who I had since middle school and passed away while I was in graduate school. My family in Riverside, Virginia, and Florida. My Dad, Erik Evans, who currently resides in Virginia and his wife Joanne. I'd like to thank Michael, my mom's partner, who is currently undergoing radiation treatment for cancer. I'm amazed by your positivity and general outlook towards

life. Thank you for your support! My sister, Katherine Evans, who is doing her PhD in math at UC Irvine. You've really blossomed while there and it's been a pleasure to watch you grow. Thank you mom for being a wonderful role model. You are a boss. You keep growing stronger and stronger, even when I didn't think it was possible. It's been awesome to see you become a commander.

Thank you to everyone who was part of my graduate school experience.

ABSTRACT

Transition metals are used as catalysts in the laboratory and by nature to facilitate difficult chemical transformations. Herein, three different metal containing catalysts are discussed: Pd and Ni catalysts towards the formation of carbon-carbon (C-C) bonds and Fe catalysts towards the reduction of N_2 to NH_3.

In Chapter 2, mechanistic studies of Pd- and Ni-catalyzed cross-coupling reactions are discussed. The mechanism of transmetalation of a Pd-catalyzed Suzuki cross-coupling reaction is studied using a stereochemical probe, revealing that transmetalation occurs with retention of configuration, consistent with transmetalation occurring through a frontside-attack mechanism. Next, to explore the viability of a transmetalation first pathway in an asymmetric Negishi cross-coupling reaction, S = 1/2 $Ni^{I}Br$ and Ni^{I}–alkyl complexes were synthesized, crystallographically characterized, and their reactivities explored. Based on these reactivity studies, evidence against a transmetalation first pathway is provided using a variety of spectroscopic methods.

In Chapter 3, new $Fe(N_2)(H)_x$ complexes are synthesized. These complexes catalyze the reduction of N_2 to NH_3 and the yields for NH_3 are improved if the reactions are performed in the presence of Hg lamp photolysis. Preliminary mechanistic studies exploring the role of light are discussed. In the final chapter, new ligand scaffolds are developed that can bind a Lewis acidic and Lewis basic metal center. These ligand frameworks support one- and two-atom bridges between the two metal sites. Finally, we discovered that some of the new complexes are catalysts for N_2 to NH_3 reduction and olefin hydrogenation.

PUBLISHED CONTENT AND CONTRIBUTIONS

Buscagan, T. M. et al. (2017). "N_2-to-NH_3 Conversion by a Triphos-Iron Catalyst and Enhanced Turnover Under Photolysis". In: *Angew. Chem. Int. Ed.* **2017**, *56*, 6921–6926. doi: 10.1042/BJ20150183.

T.M.B. conceived of the project, synthesized the described iron complexes, studied their reactivities, solved and analyzed the crystal structures, prepared the data, and wrote the manuscript.

TABLE OF CONTENTS

LIST OF FIGURES

Number *Page*

Chapter 1. Introduction

Chapter 2. Towards Understanding the Mechanism of Palladium- and Nickel-Catalyzed Cross-Coupling Reactions with Alkyl Substrates

Chapter 3. N_2-to-NH_3 Conversion by a Triphos-Iron Catalyst and Enhanced Turnover Under Photolysis

Chapter 4. Novel Ligand Frameworks for Heterobimetallic Complexes

Appendix 1: Supplementary Data for Chapter 2

Appendix 2: Supplementary Data for Chapter 3

Appendix 3: Supplementary Data for Chapter 4

LIST OF SCHEMES

Number *Page*

Chapter 1. Introduction

Chapter 2. Towards Understanding the Mechanism of Palladium- and Nickel-Catalyzed Cross-Coupling Reactions with Alkyl Substrates

Chapter 3. N_2-to-NH_3 Conversion by a Triphos-Iron Catalyst and Enhanced Turnover Under Photolysis

Chapter 4. Novel Ligand Frameworks for Heterobimetallic Complexes

LIST OF TABLES

Number *Page*

Appendix 3: Supplementary Data for Chapter 4

LIST OF ABBREVIATIONS

A	Hyperfine coupling constant
atm	Atmosphere
Avg	Average
$BAr^{F}_{4}^{-}$	$B(3,5\text{-}C_6H_3(CF_3)_2)_4^-$
cm^{-1}	Wave number
Cp	Cyclopentadienyl
Cp*	Pentamethylcyclopentadienyl
CSD	Cambridge Structural Database
CW	Continuous wave
d	Doublet or deuterium
dd	Doublet of doublets
d_x	Compound with x deuterium atoms
depe	1,2-Bis(diethylphosphino)ethane
ENDOR	Electron nuclear double resonance
EPR	Electron paramagnetic resonance
ESE	Electron spin echo
Et	Ethyl
Equiv	Equivalents
FeMoco	Iron-Molybdenum Cofactor
G	Gauss

g	Gram
g	Electron g-factor
GC	Gas chromatography
GHz	Gigahertz
Hg	Mercury
Hz	Hertz
*i*Pr	Isopropyl
*i*Pr-Pybox	2,6-Bis[isopropyl-2-oxazolin-2-yl]pyridine
IR	Infrared
J	NMR coupling constant
L	Generic n
KC_8	Potassium graphite
kcal	Kilocalorie
m	Multiplet
M	Concentration in molarity
Me	Methyl
2-MeTHF	2-Methyltetrahydrofuran
mg	Milligram
MHz	Megahertz
mL	Milliliter
mM	Millimolar
mm	Millimeter

mmol	Millimole
mT	Millatesla
mol	Mole
n	Generic number
*n*Bu	*n*-Butyl
nm	Nanometer
NMR	Nuclear magnetic resonance
N_xH_y	Generic nitrogenous ligands with x N atoms and y H atoms
OA	Oxidative addition
P_3^B	(*o*-*i*Pr$_2$P(C$_6$H$_4$)$_3$)B or generically *o*-R$_2$P(C$_6$H$_4$)$_3$)B
$P_2^{P'Ph}$	(*o*-*i*Pr$_2$P(C$_6$H$_4$)$_2$)PPh
$P_2^{P'Cp}$	(*o*-*i*Pr$_2$P(C$_6$H$_4$)$_2$)PCp
P_3^E	(*o*-*i*Pr$_2$P(C$_6$H$_4$)$_2$)E, E = B, C, Si
Ph	Phenyl
q	Quartet
R	Generic organic group or R-factor
RE	Reductive elimination
RT	Room temperature
S	Spin quantum number
s	Singlet or second
S_E2	Bimolecular electrophilic substitution
SiP_3	(*o*-PR$_2$C$_6$H$_4$)$_3$Si$^-$

t	Triplet or time
*t*Bu	*tert*-butyl
Tf	SO_2CF_3
THF	Tetrahydrofuran
TM	Transmetalation
TMS	Trimethylsilyl
TPB	(*o*-*i*$Pr_2P(C_6H_4)_3$)B or generically *o*-$R_2P(C_6H_4)_3$)B
UV	Ultraviolet
Vis	Visible
XRD	X-ray diffraction
δ	Chemical shift or Mössbauer isomer shift
Δ_{Eq}	Mössbauer quadrupole splitting
°	Degree
°C	Degrees Celcius
ε	Extinction coefficient
η^x	Hapticity of order x
γ	Gyromagnetic ratio
λ	Wavelength
λ_{max}	Wavelength of local maximum intensity
μ-X	Bridging X ligand
μ_B	Bohr magneton

μ_{eff}	Effective magnetic moment
μL	Microliter
ν_{xy}	Vibrational frequency between atoms x and y
τ_4	Index of geometry between tetrahedral and trigonal pyramidal
Å	Angstroms
9-BBN	9-Borabicyclo[3.3.1]nonane
12-c-4	12-crown-4
^{1}H	Hydrogen-1
^{2}H	Deuterium-2
^{13}C	Carbon-13
^{15}N	Nitrogen-15
^{31}P	Phosphorus-31

Chapter 1

INTRODUCTION

1.1 Motivation: Transition Metal Catalysis

Transition metal catalysis touches many fields of chemistry. As catalysts, transition metals facilitate the synthesis of structurally diverse organic molecules, ranging from ethane ($H_3C–CH_3$) to structures with complex architectures, containing multiple carbon-carbon (C-C) bonds, ring systems, and stereocenters.[1] One particularly useful transition metal-catalyzed process discussed in this thesis is cross-coupling, in which two carbon atoms can be coupled to form a new C-C bond.[2] In these reactions, the transition metal center binds to the two carbon atoms to be coupled and mediates bond formation through a process called reductive elimination (*vide infra*).[1] To date, many cross-coupling conditions have been reported and some of these methods have been used in the synthesis of commodity chemicals.[3] In the first part of this thesis, the mechanism by which Pd- and Ni-catalyzed C-C coupling occurs is probed using a variety of spectroscopic techniques.

Long before chemists used transition metals as catalysts in the laboratory, nature did. Transition metals are found in the active sites of a variety of enzymes;[4] for example, nitrogenase, which contains both Fe and Mo centers.[5] Nitrogenase catalyzes the reduction of N_2 to NH_3 under ambient conditions. To better understand this structurally complex enzyme, many groups have studied molecular complexes that bind dinitrogen and, in some cases, reduce dinitrogen to ammonia or hydrazine.[6] In the last two chapters of this thesis, new synthetic iron catalysts are shown to reduce dinitrogen to ammonia catalytically. Most interestingly, the yield for ammonia is increased when the catalytic reactions are performed in the presence of light.

1.2 Palladium- and Nickel-Catalyzed Cross-Couplings

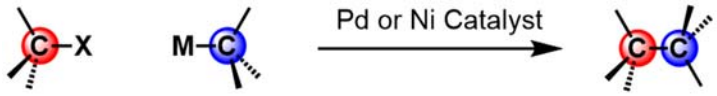

Scheme 1.1. General Pd- or Ni-catalyzed cross-coupling reaction with alkyl substrates.

One of the most important reactions in synthetic chemistry is carbon-carbon (C-C) bond formation. In fact, the scientists who pioneered the development of the transition metal-catalyzed cross-coupling reactions have been awarded Nobel prizes.[2] In a typical cross-coupling reaction, an electrophilic carbon atom (C-X) is coupled to a nucleophilic carbon atom (C-M) to form a new C-C bond (Scheme 1.1). The electrophile is typically an alkyl halide, triflate, or tosylate and the nucleophile is typically an organometallic reagent; for instance, when an alkylzinc reagent is used as the nucleophilic partner, the cross-coupling is called a Negishi reaction and when an alkylborane is used, a Suzuki-Miyaura reaction. Other varieties of cross-couplings are known and vary by the nucleophilic partner, such as the Hiyama, Stille, and Kumada reactions, which couple organosilanes, -stannanes, and Grignards, respectively.

While early cross-coupling investigations focused on the coupling of C_{sp^2} centers,[7-9] more recent studies are focused on the coupling of C_{sp^3} centers (Scheme 1.1).[10-12] Attempts to develop cross-coupling methods using C_{sp^3} centers were initially impeded due to slow oxidative addition of alkyl substrates and undesired β-hydride elimination.[13-15] Recently, the use of alkyl substrates has been made possible by the employment of bulky or polydentate

ligands with palladium, or by exchanging palladium for nickel as the transition metal catalyst.[2, 16]

By coupling two alkyl substrates, the possibility of asymmetric induction at one or both of the sp^3 carbon atoms is introduced.[17] To this end, tremendous effort has been made in the development of asymmetric cross-coupling reactions; in particular, the Fu group has specialized in the development of Pd- and Ni-catalyzed cross-coupling reactions.[18-27] Chapter 2 of this thesis focuses on understanding the mechanism of Pd- and Ni-catalyzed cross-couplings between two alkyl substrates, with an emphasis on asymmetric nickel catalysis as the details of this mechanism are not as well understood.

The mechanism of Pd-catalyzed cross-coupling reactions is thought to proceed by a polar, two-electron process, cycling between Pd(0) and Pd(II) intermediates (Figure 1.1).[1] In the first step of the catalytic cycle, oxidative addition occurs to provide a Pd^{II}-alkyl intermediate. Transmetalation between an organometallic reagent, such as an organoborane, -silane, -zinc, or –magnesium reagent, etc. provides a Pd^{II}-dialkyl intermediate, which can undergo subsequent reductive elimination to provide the cross-coupling product. The finer details of the Pd-catalyzed cross-coupling, such as the stereochemical outcome of each step, are thought to be more complicated and substrate-dependent.[28] In this thesis, a stereochemical probe is employed to gain insight into the transmetalation step of a Pd-catalyzed Suzuki cross-coupling between primary alkylborates and primary alkyl electrophiles.

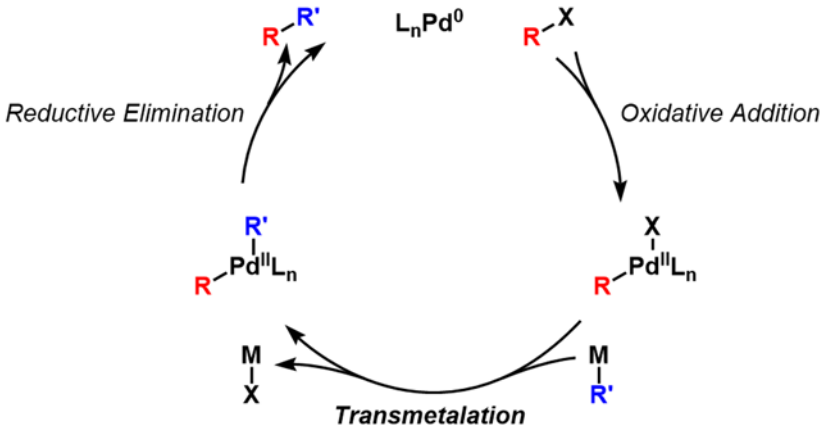

Figure 1.1 General mechanism for a Pd-catalyzed cross-coupling reaction.

While the mechanism of Pd-catalyzed cross-couplings are well understood, at the time of this work, little was known about the mechanism of Ni-catalyzed cross-coupling reactions using alkyl substrates. For the studies reported in this thesis, Vicic's proposed mechanism for a Negishi coupling between primary alkyl electrophiles (Figure 1.2) provided a starting point for thinking about the Negishi reaction discussed herein.[29-33] Unlike the Pd-catalyzed cross-coupling, this reaction was thought to proceed by odd-electron Ni species and radical intermediates. In the first step of the reaction, transmetalation between the alkylzinc cross-coupling partner and a terpyridine bound Ni^{I}-X species provides a Ni^{I}-alkyl intermediate, which can undergo subsequent oxidative addition to provide a Ni^{III}-dialkyl species that can reductively eliminate to provide the cross-coupling partner. In these particular mechanistic reports, Vicic studied primary, unactivated electrophile. In the studies reported herein, an activated electrophile is under investigation. The difference in reactivity between the two types of electrophiles may result in different reaction mechanisms.

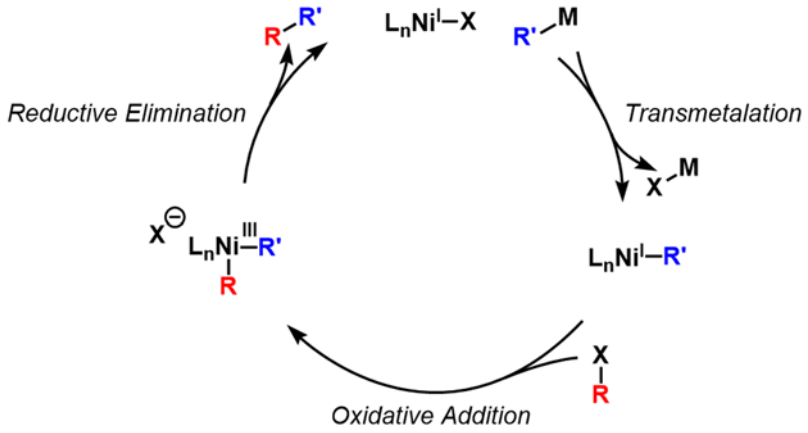

Figure 1.2. Mechanism for Negishi coupling of alkyl substrates reported by Vicic.

1.3. Iron-Catalyzed Dinitrogen Reduction to Ammonia

The main focus of Chapter 1 of this thesis is the formation of a new C-C bond. In the subsequent chapters, achieving N-N bond cleavage in dinitrogen is the primary goal. DNA, proteins, and amino acids are just a few of the nitrogen-containing biomolecules that support all life.[34] The N atoms in these molecules are ultimately derived from dinitrogen (N_2). Although N_2 makes up approximately 80% of the earth's atmosphere, it is not the direct source of N atoms for organisms because of the extremely strong nonpolar bond between the two nitrogen atoms (BDE = 225 kcal/mol) rendering it inert.[35] Instead, N_2 must first be fixed to a bioavailable source of N atoms, ammonia (NH_3).

$$N_2 + 3\,H_2 \xrightarrow[\sim 200\ atm,\ \sim 400\ ^\circ C]{\text{Fe or Ru catalyst}} 2\,NH_3 \quad \Big| \quad N_2 + 8\,H^+ + 8\,e^- + 16\,ATP \xrightarrow[rt,\ 1\ atm]{\textit{nitrogenase}} 2\,NH_3 + H_2 + 16\,ADP + 16\,P\textit{i}$$

Scheme 1.2. The methods for nitrogen reduction to ammonia include the Haber-Bosch process (left) and biological nitrogen fixation by nitrogenase (right).

The catalytic process that converts N_2 to NH_3 is called nitrogen fixation and it can be achieved industrially through the Haber-Bosch process or biologically using an enzyme, nitrogenase (N_2ase) (Scheme 1.2).[35-36] The industrial process for N_2 fixation is energy intensive and requires extreme conditions: high temperatures, pressures, an iron or ruthenium catalyst, and methane steam reforming to provide dihydrogen (H_2) (Scheme 1.2, left).[36] N_2ase, on the other hand, is capable of fixing dinitrogen at ambient temperatures and pressures (Scheme 1.2, right).[35, 37] Three nitrogenases are known and vary only in the atomic compositions of their active sites: FeMo, FeFe, and FeV nitrogenase.[38] A molecular understanding of how the active sites of these enzymes bind and reduce N_2 is unknown.

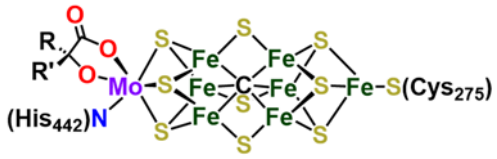

Figure 1.3. The FeMo-cofactor.

FeMo nitrogenase is a complex enzyme containing three different types of FeS clusters: a [4Fe-4S] cluster, a dicubane-like [8Fe-7S] cluster (i.e. P-cluster), and the catalytic site for N_2 reduction (shown in Figure 1.3), the FeMo-cofactor, an [Mo-7Fe-9S-C] cluster. The presence of so many metal centers hinders mechanistic and spectroscopic studies. To provide a foundation for thinking about the mechanism of biological N_2 fixation, many simplified structural and functional models of the nitrogenase cofactor have been synthesized.[39-41]

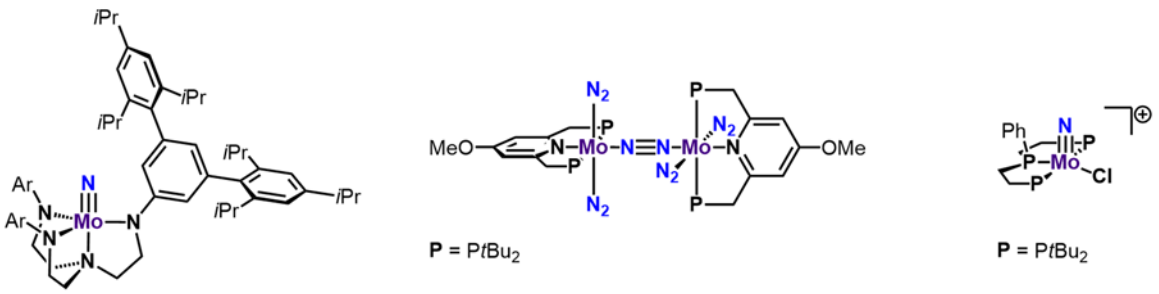

Figure 1.4. Select examples of molecular Mo catalysts for N_2 reduction.[42-44]

While the structural models exhibit the cubane nature of nitrogenase, they are generally unreactive towards dinitrogen. On the other hand, the functional models can reduce N_2 to N_2H_4 or NH_3, but differ structurally/electronically from the metal centers in the FeMo cofactor. Given that both Mo and Fe centers are present in FeMoco, functional model systems based on both Mo and Fe have been developed. Early studies focused on determining whether molecular Mo complexes could reduce N_2 to NH_3 catalytically.[45] Both Schrock and Nishibayashi showed that Mo is capable of fixing N_2 to NH_3 (Figure 1.4).[42, 46]

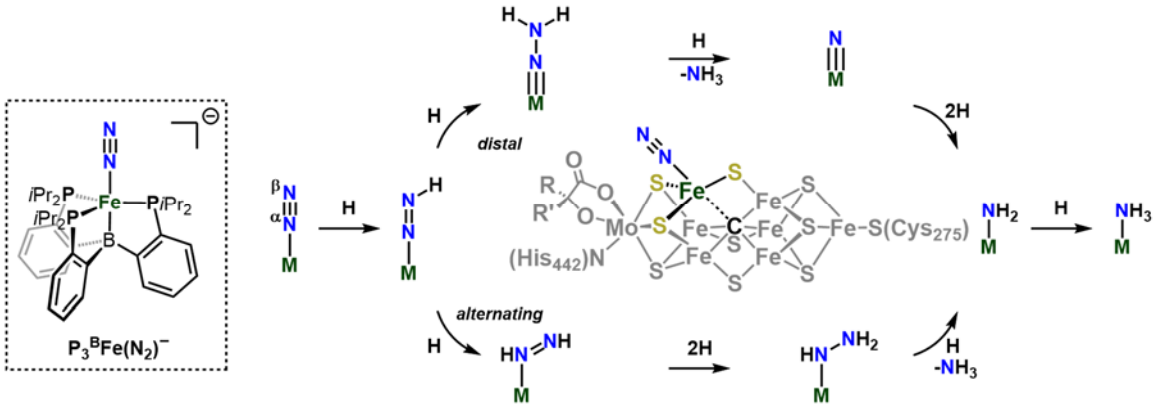

Figure 1.5. (Left) The first Fe-based molecular catalyst for dinitrogen reduction to ammonia[47] and (right) two limiting mononuclear mechanisms for N_2 reduction to NH_3.[48]

Recent studies of FeMoco have implicated Fe as the more likely substrate binding site.[49-50] In 2010, Peters et al. reported the first Fe catalyst for N_2 reduction to NH_3 (Figure

1.5, left).[47] Fe complexes with a variety of reduced N_xH_y substrates have been isolated using the trisphosphinoborane system shown above, demonstrating the possibility of forming similar intermediates during biological dinitrogen reduction (Figure 1.5).[51-52] Based on these results, Peters et al. suggested that *a single Fe center* of FeMoco could bind and activate N_2 (Figure 1.5, in color).[47, 53]

Based on reactivity studies with mononuclear metal centers, two limiting pathways for dinitrogen reduction have been proposed (Figure 1.5).[48] These pathways are called the distal, or Chatt-type, pathway while the second is called the alternating pathway. The names of the pathways reflect the manner of protonation during dinitrogen reduction. The distal pathway proceeds by protonation at the β or distal N atom (Figure 1.5, top), while the alternating pathway proceeds by sequential protonations of the α and β N atoms (Figure 1.5, bottom). Recent studies suggests that a hybrid pathway is also possible using a mononuclear Fe system.[52] All of these pathways involve one metal center, but can be applied to more than one metal center as well.

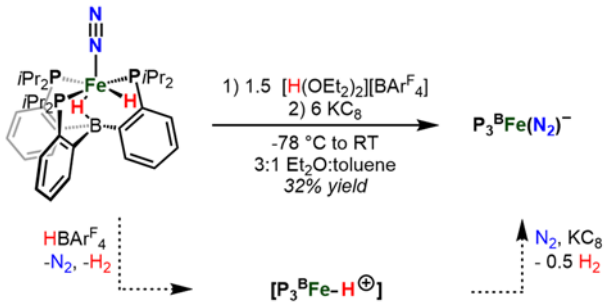

Figure 1.6. The presumed off-path iron hydride species can be converted back to an on-path intermediate with excess acid and reductant.

One interesting mechanistic feature of biological nitrogen fixation is the formation of H_2 in addition to the desired product, NH_3 (Scheme 1.2, right). Some speculate that N_2

binding is in fact coupled to H_2 loss.[54-56] The synthetic catalyst systems developed by our group,[53] including the catalyst shown in Figure 1.5, also function as hydrogen evolution catalysts. Freeze quench ^{57}Fe Mössbauer spectroscopic studies of a catalytic reaction using $P_3^BFe(N_2)^-$ have shown that a significant amount of the iron is present as an iron hydride-borohydride species (Figure 1.6, left).[53] This species is presumed to be an off-path intermediate, and can be converted back to the on-path anionic species $P_3^BFe(N_2)^-$ with excess acid and reductant. $P_3^BFe(N_2)^-$ can then undergo protonation and/or reduction to presumably provide many of the proposed intermediates shown in Figure 1.5. Chapter 3 focuses on using light to photo-eliminate H_2 from off-path hydride species as an alternative to consuming acid and reductant equivalents to transform off-path to on-path intermediates.

1.4 Chapter Summaries

In the first part of Chapter 2, the mechanism of the transmetalation step of a Suzuki cross-coupling reaction is studied using a stereochemical probe, revealing that transmetalation occurs with retention of configuration. The observed stereochemical outcome suggests that transmetalation occurs through a frontside-attack mechanism. In the second part of Chapter 2, the mechanism of an asymmetric Ni-catalyzed cross-coupling reaction between benzylic bromides and alkylzinc reagents is probed through the synthesis of Ni complexes that are proposed to be catalytically relevant. The reactivity of these Ni complexes towards each of the cross-coupling partners is assessed using EPR and UV-Vis spectroscopies. These spectroscopic studies show (1) how Ni(I) species can be generated from the Ni(II) precatalyst, (2) the presence of a Ni-centered radical during cross-coupling

reactions in progress, and (3) the formation of a Ni(I)-alkyl complex through stoichiometric transmetalation reactions of a discrete Ni(I)Br complex. Overall, we provide evidence for an oxidative addition first pathway by studying the relative rates of oxidative addition versus transmetalation of the key Ni(I)Br complex.

In Chapter 3, a new catalyst for dinitrogen reduction is described. Inspired by nitrogenase's ability to lose H_2 upon photolysis as well as literature reports of synthetic $Fe(H)_x$ losing H_2 to bind N_2 in the presence of light,[55, 57-59] we subjected our catalytic reactions to light to determine whether more ammonia would form. Excitingly, we observe enhanced ammonia yields in the presence of Hg lamp and blue LED photolysis. Preliminary mechanistic studies suggests that H_2 elimination is one role light can play in transforming an otherwise inert $Fe(N_2)(H)_2$ species to a catalytically relevant $Fe(N_2)$ species, which can undergo productive reduction and protonation to eventually yield ammonia.

In Chapter 4, FeM (M = Zr or Na) complexes are synthesized using new dinucleating ligands. These complexes are capable of bridging both hydride (when M = Zr) and N_2 ligands (when M = Na). In addition to exploring the reactivity of these complexes with N_2, we found that some of the complexes are active for catalytic dinitrogen reduction to ammonia and olefin hydrogenation to alkanes.

In summary, this thesis truly demonstrates the power of transition metals as catalysts for small molecule transformations. C-C bond formation and N-N bond cleavage are discussed specifically. Although new catalysts are developed in this thesis, we also focus on understanding how these catalysts interact with their respective substrates and mediate otherwise difficult transformations.

1.5 References

1. Hartwig, J. F., *Organotransition Metal Chemistry: From Bonding to Catalysis* University Science Books: Mill Valley, 2010.
2. Johansson Seechurn, C. C. C.; Kitching, M. O.; Colacot, T. J.; Snieckus, V. *Angew. Chem. Int. Ed.* **2012,** *51*, 5062.
3. Shen, H. C., Selected Applications of Transition Metal-Catalyzed Carbon–Carbon Cross-Coupling Reactions in the Pharmaceutical Industry. In *Applications of Transition Metal Catalysis in Drug Discovery and Development*, John Wiley & Sons, Inc.: 2012; pp 25.
4. Thomson, A. J.; Gray, H. B. *Curr. Opin. Chem. Bio.* **1998,** *2*, 155.
5. Spatzal, T.; Aksoyoglu, M.; Zhang, L.; Andrade, S. L. A.; Schleicher, E.; Weber, S.; Rees, D. C.; Einsle, O. *Science* **2011,** *334*, 940.
6. Burford, R. J.; Fryzuk, M. D. *Nat. Chem. Rev.* **2017,** *1*, 26.
7. Heck, R. F.; Nolley, J. P. *J. Org. Chem.* **1972,** *37*, 2320.
8. Negishi, E.; King, A. O.; Okukado, N. *J. Org. Chem.* **1977,** *42*, 1821.
9. Miyaura, N.; Yamada, K.; Suzuki, A. *Tetrahedron Lett.* **1979,** *20*, 3437.
10. Devasagayaraj, A.; Stüdemann, T.; Knochel, P. *Angew. Chem. Int. Ed.* **1996,** *34*, 2723.
11. Cárdenas, D. J. *Angew. Chem. Int. Ed.* **1999,** *38*, 3018.
12. Cárdenas, D. J. *Angew. Chem. Int. Ed.* **2003,** *42*, 384.
13. Pearson, R. G.; Figdore, P. E. *J. Am. Chem. Soc.* **1980,** *102*, 1541.
14. Ishiyama, T.; Abe, S.; Miyaura, N.; Suzuki, A. *Chem. Lett.* **1992,** *21*, 691.
15. Bissember, A. C.; Levina, A.; Fu, G. C. *J. Am. Chem. Soc.* **2012,** *134*, 14232.
16. Kirchhoff, J. H.; Netherton, M. R.; Hills, I. D.; Fu, G. C. *J. Am. Chem. Soc.* **2002,** *124*, 13662.
17. Choi, J.; Fu, G. C. *Science* **2017,** *356*.
18. Netherton, M. R.; Dai, C.; Neuschütz, K.; Fu, G. C. *J. Am. Chem. Soc.* **2001,** *123*, 10099.
19. Hills, I. D.; Netherton, M. R.; Fu, G. C. *Angew. Chem. Int. Ed.* **2003,** *42*, 5749.
20. Arp, F. O.; Fu, G. C. *J. Am. Chem. Soc.* **2005,** *127*, 10482.
21. Fischer, C.; Fu, G. C. *J. Am. Chem. Soc.* **2005,** *127*, 4594.
22. Powell, D. A.; Maki, T.; Fu, G. C. *J. Am. Chem. Soc.* **2005,** *127*, 510.
23. Dai, X.; Strotman, N. A.; Fu, G. C. *J. Am. Chem. Soc.* **2008,** *130*, 3302.
24. Saito, B.; Fu, G. C. *J. Am. Chem. Soc.* **2008,** *130*, 6694.
25. Lou, S.; Fu, G. C. *J. Am. Chem. Soc.* **2010,** *132*, 1264.
26. Lundin, P. M.; Fu, G. C. *J. Am. Chem. Soc.* **2010,** *132*, 11027.
27. Choi, J.; Fu, G. C. *J. Am. Chem. Soc.* **2012,** *134*, 9102.
28. Cherney, A. H.; Kadunce, N. T.; Reisman, S. E. *Chem. Rev.* **2015,** *115*, 9587.
29. Anderson, T. J.; Jones, G. D.; Vicic, D. A. *J. Am. Chem. Soc.* **2004,** *126*, 8100.
30. Jones, G. D.; McFarland, C.; Anderson, T. J.; Vicic, D. A. *Chem. Commun.* **2005**, 4211.
31. Jones, G. D.; Martin, J. L.; McFarland, C.; Allen, O. R.; Hall, R. E.; Haley, A. D.; Brandon, R. J.; Konovalova, T.; Desrochers, P. J.; Pulay, P.; Vicic, D. A. *J. Am. Chem. Soc.* **2006,** *128*, 13175.
32. Ciszewski, J. T.; Mikhaylov, D. Y.; Holin, K. V.; Kadirov, M. K.; Budnikova, Y. H.; Sinyashin, O.; Vicic, D. A. *Inorg. Chem.* **2011,** *50*, 8630.
33. Zhang, C.-P.; Wang, H.; Klein, A.; Biewer, C.; Stirnat, K.; Yamaguchi, Y.; Xu, L.; Gomez-Benitez, V.; Vicic, D. A. *J. Am. Chem. Soc.* **2013,** *135*, 8141.
34. Smil, V., *Enriching the Earth : Fritz Haber, Carl Bosch, and the Transformation of World Food Production*. The MIT Press: Cambridge, Mass, 2001.
35. Howard, J. B.; Rees, D. C. *Chem. Rev.* **1996,** *96*, 2965.

36. Ertl, G. *J. Vac. Sci. Technol.* **1983,** *1*, 1247.
37. Burgess, B. K.; Lowe, D. J. *Chem. Rev.* **1996,** *96*, 2983.
38. Eady, R. R. *Chem. Rev.* **1996,** *96*, 3013.
39. MacKay, B. A.; Fryzuk, M. D. *Chem. Rev.* **2004,** *104*, 385.
40. Lee, S. C.; Holm, R. H. *Chem. Rev.* **2004,** *104*, 1135.
41. Crossland, J. L.; Tyler, D. R. *Coord. Chem. Rev.* **2010,** *254*, 1883.
42. Yandulov, D. V.; Schrock, R. R. *Science* **2003,** *301*, 76.
43. Kuriyama, S.; Arashiba, K.; Nakajima, K.; Tanaka, H.; Kamaru, N.; Yoshizawa, K.; Nishibayashi, Y. *J. Am. Chem. Soc.* **2014,** *136*, 9719.
44. Arashiba, K.; Kinoshita, E.; Kuriyama, S.; Eizawa, A.; Nakajima, K.; Tanaka, H.; Yoshizawa, K.; Nishibayashi, Y. *J. Am. Chem. Soc.* **2015,** *137*, 5666.
45. Schrock, R. R. *Phil. Trans. R. Soc. A* **2005,** *363*, 959.
46. Arashiba, K.; Miyake, Y.; Nishibayashi, Y. *Nat. Chem.* **2011,** *3*, 120.
47. Anderson, J. S.; Rittle, J.; Peters, J. C. *Nature* **2013,** *501*, 84.
48. Seefeldt, L. C.; Hoffman, B. M.; Dean, D. R. *Annu. Rev. Biochem.* **2009,** *78*, 701.
49. Spatzal, T.; Perez, K. A.; Einsle, O.; Howard, J. B.; Rees, D. C. *Science* **2014,** *345*, 1620.
50. Spatzal, T.; Perez, K. A.; Howard, J. B.; Rees, D. C. *eLife* **2015,** *4*, 11620.
51. Anderson, J. S.; Moret, M.-E.; Peters, J. C. *J. Am. Chem. Soc.* **2013,** *135*, 534.
52. Rittle, J.; Peters, J. C. *J. Am. Chem. Soc.* **2016,** *138*, 4243.
53. Del Castillo, T. J.; Thompson, N. B.; Peters, J. C. *J. Am. Chem. Soc.* **2016,** *138*, 5341.
54. Simpson, F. B.; Burris, R. H. *Science* **1984,** *224*, 1095.
55. Whittlesey, M. K.; Mawby, R. J.; Osman, R.; Perutz, R. N.; Field, L. D.; Wilkinson, M. P.; George, M. W. *J. Am. Chem. Soc.* **1993,** *115*, 8627.
56. Lukoyanov, D.; Khadka, N.; Yang, Z.-Y.; Dean, D. R.; Seefeldt, L. C.; Hoffman, B. M. *J. Am. Chem. Soc.* **2016,** *138*, 10674.
57. Sacco, A.; Aresta, M. *Chem. Commun.* **1968**, 1223.
58. Aresta, M.; Giannoccaro, P.; Rossi, M.; Sacco, A. *Inorg. Chim. Acta* **1971,** *5*, 115.
59. Lukoyanov, D.; Khadka, N.; Yang, Z.-Y.; Dean, D. R.; Seefeldt, L. C.; Hoffman, B. M. *J. Am. Chem. Soc.* **2016,** *138*, 1320.

Chapter 2

TOWARDS UNDERSTANDING THE MECHANISM OF PALLADIUM- AND NICKEL-CATALYZED CROSS-COUPLING REACTIONS WITH ALKYL SUBSTRATES

2.1 General Introduction

Carbon-carbon (C-C) bond formation is one of the most important reactions in chemistry as a large number of molecules contain C-C bonds. Although there are many ways to form a C-C bond, transition metal-catalyzed cross-coupling reactions have truly revolutionized organic synthesis by creating new bond disconnection strategies.[1-3] Early investigations of cross-coupling reactions, including the chemistry honored by the 2011 Nobel prize in Chemistry, have focused on Pd-catalyzed bond formation with sp- or sp^2-hybridized carbon atoms.[4-6] Along with other groups,[7-9] the Fu group specializes in the development of C-C bond formation using sp^3-hybridized carbon atoms.[10-24] Relative to couplings involving C_{sp} and $C_{sp}{}^2$ carbon centers, these methods were previously unexplored, and considered challenging to develop because of the relatively slow oxidative addition of alkyl halides (when compared to $C_{sp}{}^2$-X and C_{sp}-X centers) and unproductive β-H elimination from Pd-alkyl species formed during catalysis.[25-27] In 2002, the Fu group reported the isolation of a Pd^{II}-alkyl species bearing β–hydrogen atoms which was competent for both stoichiometric and catalytic cross-coupling reactions with alkyl substrates.[28] The Pd^{II}-alkyl species was stable and only underwent β-H elimination upon heating. Of particular importance in achieving productive bond formation and suppressing β-H elimination was the choice of phosphine ligand.

In this chapter, two classes of cross-coupling reactions using alkyl substrates, the Suzuki-Miyaura and Negishi cross-coupling reactions are discussed.[10, 29] These two reaction classes differ with respect to the nucleophilic coupling partner, B vs Zn respectively. Both classes exhibit increased functional group compatibilities afforded by the milder nucleophilic

coupling partners when compared to other cross-coupling classes.[3] In the first part of Chapter 2, a stereochemical probe is employed to gain insight into a Pd-catalyzed Suzuki cross-coupling between alkylborates and alkyl electrophiles. In the second part of Chapter 2, mechanistic studies on an asymmetric Ni-catalyzed Negishi reaction between alkylzinc bromides and bromoindanes are described. Due to the different properties of Pd and Ni, these two cross-coupling reactions differ mechanistically (*vide infra*).[2, 9]

2.2 Transmetalation Study

The mechanisms of Pd-catalyzed cross-coupling reactions between two carbon atoms have been thoroughly studied.[2] The widely accepted catalytic cycle for a Suzuki cross-coupling reaction between an alkyl electrophile and alkylborate involves Pd^0 and Pd^{II} intermediates as illustrated in Figure 2.1.[2]

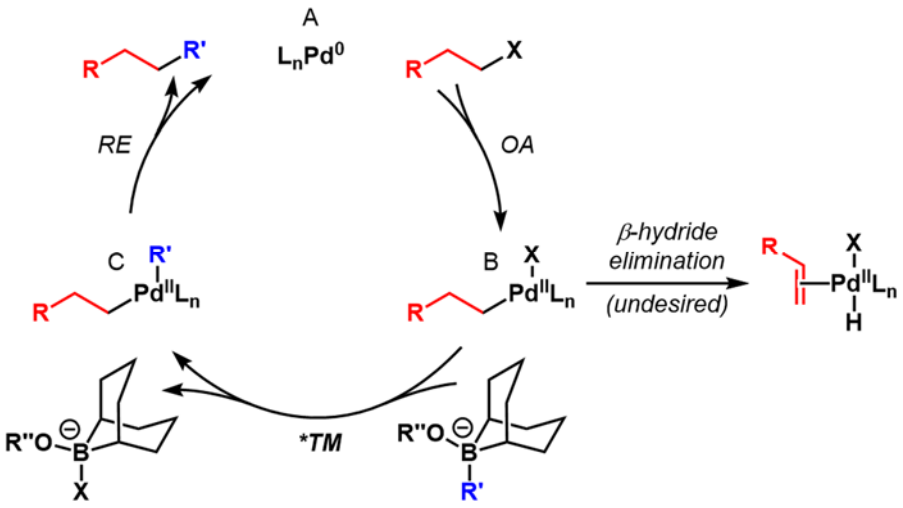

Figure 2.1. Pd-Catalyzed Suzuki Cross-Coupling Reaction Mechanism. Catalytic cycle for a Pd-catalyzed Suzuki-Miyaura cross-coupling between an alkyl halide and alkylborate. The

transmetalation step under investigation starred. *OA* = oxidative addition, *TM* = transmetalation, and *RE* = reductive elimination.

In general, a commercially available Pd^0 or Pd^{II} pre-catalyst is employed in addition to one or two equiv of an electron rich phosphine.[3] In the case of a Pd^{II} starting material, reduction to Pd^0 is required to form the catalytically active species **A**. Catalysis begins with oxidative addition (OA) of an alkyl electrophile to form Pd^{II}-alkyl intermediate **B** which undergoes subsequent transmetalation (TM) with an electron rich alkylborate to form the Pd^{II}-dialkyl species **C**. Intermediate **C** then undergoes reductive elimination (RE) to yield the cross-coupling product and the active Pd^0 catalyst. The development of cross-coupling reactions employing alkyl halide substrates has been complicated by the off-cycle β-hydride elimination of Pd^{II} alkyl intermediates such as **B** (Figure 2.1). Variations in catalyst design such as the use of sterically demanding, electron-rich phosphine ligands impede β-hydride elimination. By employing bidentate ligands, the availability of a cis open coordination site, deemed necessary for β-hydride elimination, through dissociation of a ligand becomes less likely due to the chelate effect.[28]

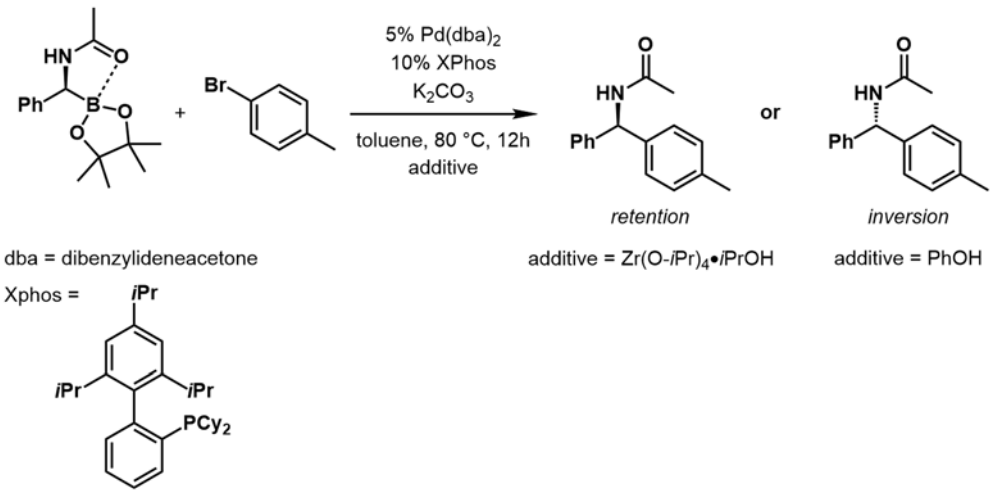

Scheme 2.1. Stereochemical outcomes of the products can be controlled by the addition of additives.[30]

Herein, we focus on the mechanism of transmetalation as this step is essential for controlling the stereochemical outcome of the cross-coupling reaction. The mechanism of transmetalation involving organotin, -silicon, -zinc, and -boron reagents have been thoroughly studied.[31-38] In many cases, the stereochemical outcome of transmetalation is substrate dependent, leading to either inversion of retention of configuration. Understanding how the substrate or reaction parameters influence the mechanism of transmetalation will allow for the rational design of stereochemically complex organic molecules. For example, Suginome et al. has reported that the stereochemical course of transmetalation with enantiomerically-enriched alkylboranes can be controlled by the employment of two different additives, allowing both enantiomers of product to be accessed through a single enantiomer of the alkylborane starting material (Scheme 2.1).[30]

2.3 Results and Discussion

2.3.1 Synthesis of Diastereomerically Enriched Deuterium-Labeled Substrates

In 2001, Fu et al. reported the first Pd-catalyzed Suzuki reaction between primary alkyl bromides and alkylboranes (Scheme 2.2).[3, 10] In this chapter, we describe a stereochemical probe using diastereomerically-enriched alkylborane reagents to study the nature of transmetalation for this reaction.[10, 39]

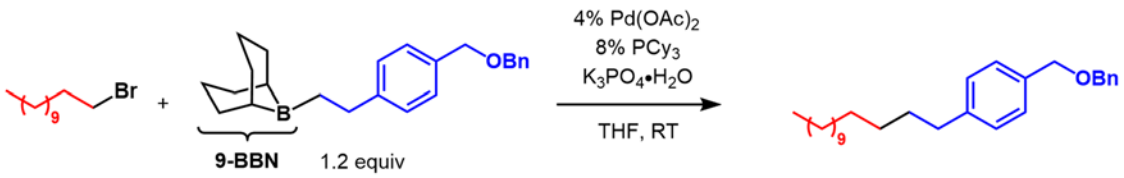

Scheme 2.2. Pd-catalyzed cross-coupling reaction under investigation.[10]

The synthesis of diastereomerically enriched deuterium-labeled substrates is shown in Scheme 2.3. Commercially available 4-bromobenzyl bromide was treated with NaH and benzyl alcohol to yield the disubstituted alkyl ether **2.1** which was then subjected to Sonagashira reaction conditions to yield TMS-protected alkyne **2.2** (TMS = trimethylsilyl).[40-41] TMS-deprotection of **2.2** followed by treatment with deuterated Schwartz's reagent and D_2O provided the *cis*-deuterium labeled alkene **2.5** required for analysis.[42-43] To obtain the *trans*-deuterium labeled alkene **2.7**, alkyne **2.3** was treated with *n*-butyllithium and quenched with D_2O to provide deuterated alkyne **2.4**. Subsequent treatment of **2.4** with deuterated Schwartz's reagent followed by a H_2O quench provided the *trans*-deuterium labeled alkene **2.7**.[42] The *cis*- and *trans*-deuterium labeled alkenes were then

hydroborated to provide the *syn* and *anti*-isomers of the alkylboranes, **2.6** and **2.8** respectively.

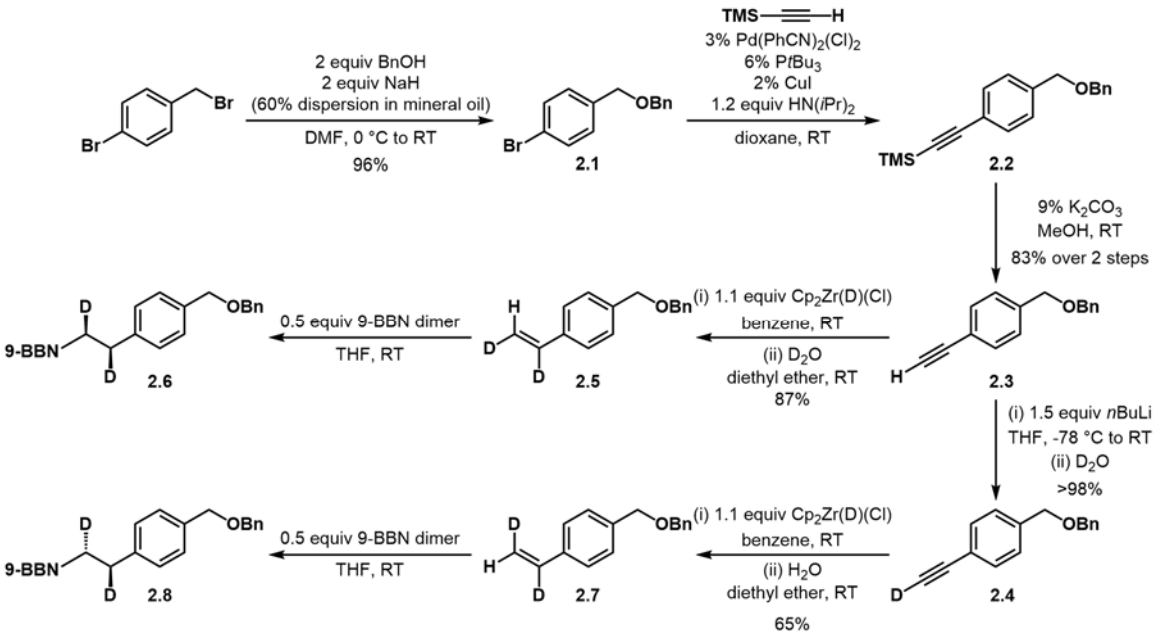

Scheme 2.3. Synthesis of deuterium-labeled substrates required for stereochemical study.

2.3.2 Stereochemical ^{1}H NMR Study

The diastereomerically-enriched substrates **2.6** and **2.8** were subjected to the previously reported cross-coupling conditions (Scheme 2.2)[10] and the stereochemical outcomes of the reactions were analyzed by ^{1}H (^{2}D decoupled) NMR spectroscopy. Based on ^{1}H NMR spectroscopy, the cross-coupled products were obtained with retention of configuration as shown in Scheme 2.4. The possible transition states for transmetalation and their resultant stereochemical outcomes are outlined in Figure 2.2.

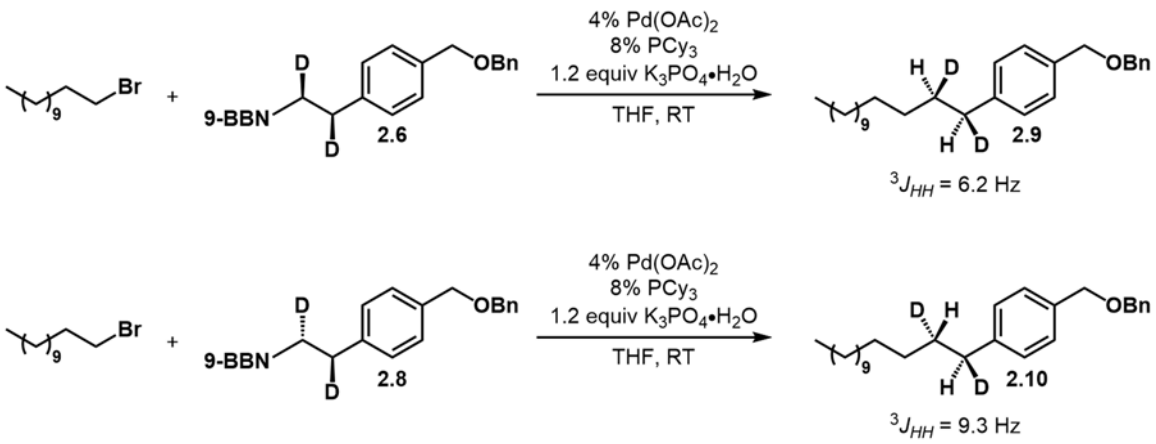

Scheme 2.4. Stereochemical probe for understanding the mechanism of transmetalation with primary alkyl cross-coupling partners.

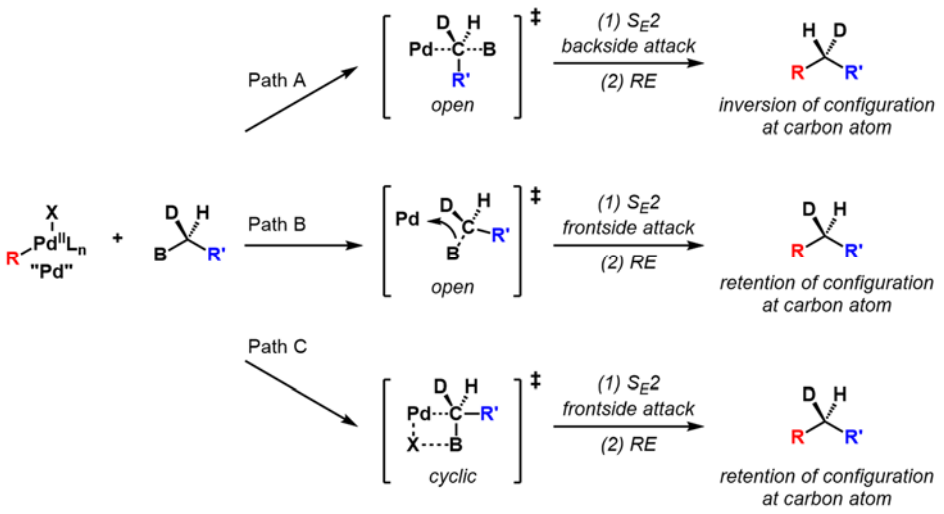

Figure 2.2. Potential transition states and stereochemical outcomes for transmetalation between an alkylborate and a palladium center. For simplicity, the borate center is designated with a "B".

Starting from an enantiomerically enriched alkylborane, transmetalation of the alkyl group may occur through one of three possible transition states.[32] In Figure 2.2 path A, transmetalation occurs through an open S_E2 backside attack, resulting in inversion of

configuration at the stereogenic carbon center. It is also possible, through an open transition state, for transmetalation to occur with an S_E2 frontside attack, leading to retention of configuration at the transferred carbon atom (Figure 2.2, path B). Finally, a cyclic transition state is also possible through intramolecular coordination of a ligand (X) to both the palladium center and the boron atom. Due to the rigidity of a cyclic transition state, S_E2 frontside attack occurs resulting in retention of configuration at the stereogenic carbon center (Figure 2.2, path C). The results reported above suggest that transmetalation between a primary alkylborane and a $Pd^{II}(X)(alkyl)$ species occurs with retention of configuration. Both pathways B and C are reasonable and cannot be distinguished experimentally.

2.4 Transmetalation Study Conclusions

Thus far, we have shown that transmetalation of a primary alkylborane to palladium occurs with retention of configuration. This stereochemical outcome is consistent with a frontside S_E2 attack during transmetalation. Because Pd-catalyzed cross-couplings are stereospecific reactions, products are often obtained with good enantioselectivity if an enantiomerically enriched starting material is used. In the next portion of Chapter 2, we will discuss an asymmetric Ni-catalyzed cross-coupling reaction between alkyl substrates. Ni-catalyzed cross-coupling reactions differ mechanistically from the previously discussed Pd-catalyzed cross-couplings and may result in the development of complementary methods. In terms of stereochemistry and mechanism, Pd-catalyzed reactions are stereospecific as oxidative addition and transmetalation occur through two-electron S_N2 and S_E2 pathways respectively.[44] Ni-catalyzed reactions, on the other hand, may proceed through achiral radical intermediates, making the development of stereoconvergent transformations possible.[45]

2.5 Well-Defined Ni(I) Complexes Provide Mechanistic Insights into an Asymmetric Cross-Coupling

The Fu group has developed a number of asymmetric Ni-catalyzed cross-coupling reactions using a variety of nitrogenous chiral ligands (Scheme 2.5).[14-16, 18, 22-23, 29] In the second portion of Chapter 2, the syntheses of the first well-defined Ni^{I}-complexes containing a chiral ligand are described.[a,46] Ni^{I} complexes are less explored relative to their Ni^{0}/Ni^{II} counterparts but they are often invoked as intermediates in a variety of catalytic reactions, including cross-couplings.[47-48] Understanding the reactivity of these species towards the electrophilic/nucleophilic cross-coupling partners will aid in the development of future catalysts for cross-coupling reactions.

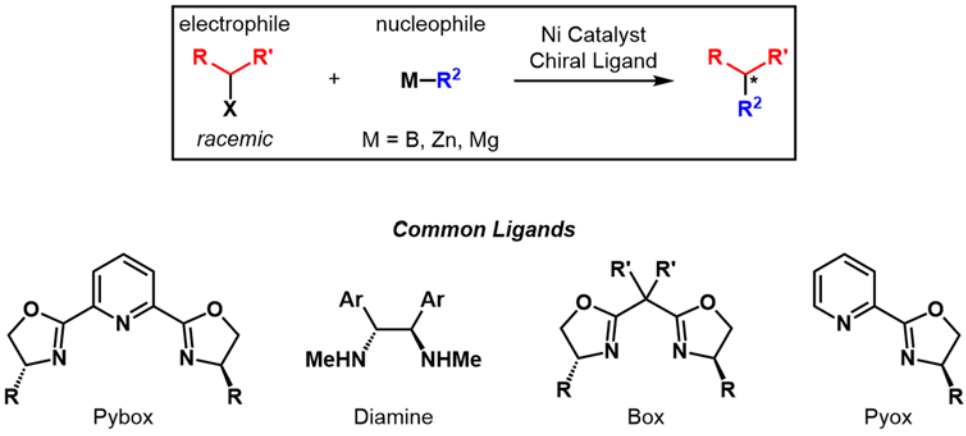

Scheme 2.5. General asymmetric Ni-catalyzed cross-coupling reaction.

[a] At the time of this work, no Ni^{I}-complexes containing a chiral ligand had been reported. **2.11** (**NiBr**) and **2.12** (**$NiBr_2$**) have since been reported. This contribution as well as the mechanistic studies discussed herein are acknowledged as preliminary results in the referenced paper.

In contrast to Pd-catalyzed cross-couplings, the mechanism of nickel-catalyzed cross-couplings has only recently been explored. Vicic reported studies on a Negishi reaction between an unactivated electrophile and alkylzinc bromide reagent.[49-51] Based on the reactivities of terpyridine-ligated Ni^{I}-Me and Ni^{II}-Me species towards the cross-coupling partners (Figure 2.3a), a *transmetalation first pathway* was proposed (*vide infra*). Hu also proposed a transmetalation first pathway with a bimetallic oxidative addition step for an alkyl-alkyl Kumada coupling using an anionic N_2N pincer ligand.[52] More recently, Wiex proposed a radical chain mechanism for a (bipyridine)Ni-catalyzed reductive cross-coupling between aryl and alkyl iodides (Figure 2.3b).[53-54]

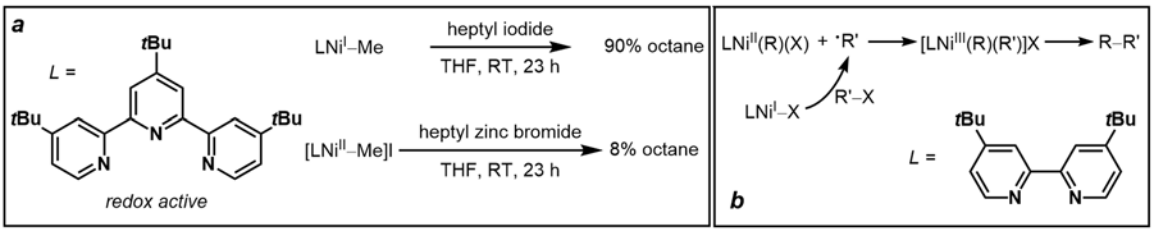

Figure 2.3. Key mechanistic insights from previous studies: (a) the stoichiometric competence of Ni^{I}-Me provides support for a transmetalation first pathway;[50] and (b) various mechanistic probes suggest a bimetallic oxidative addition step as shown.[52-53]

2.6 Results and Discussions

As a starting point for mechanistic studies, we attempted to synthesize Ni complexes bearing the pybox, diamine, and box ligands shown in Scheme 2.5. Unfortunately, attempts to synthesize four coordinate Ni complexes using bidentate ligands led to polymeric species (bridging halide structures) which were difficult to isolate and

characterize in solution. On the other hand, the tridentate *i*PrPybox ligand led to soluble, readily characterizable Ni species in high yields.

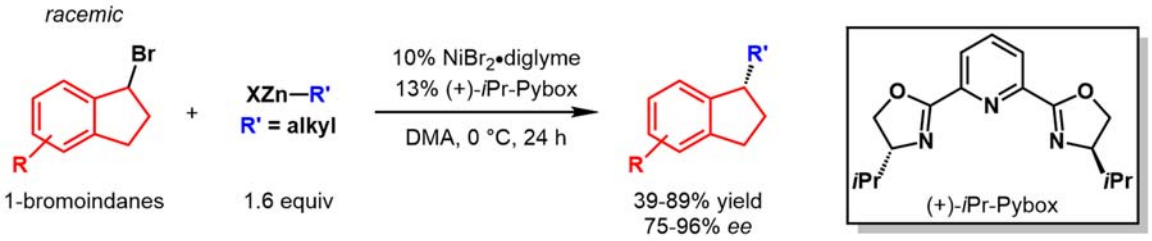

Scheme 2.6. Previously reported asymmetric coupling under investigation.[29]

Our success with *i*PrPybox led us to explore the asymmetric nickel-catalyzed Negishi cross-coupling reaction between indenyl bromides (1-bromoindanes) and alkylzinc reagents using *i*PrPybox as the chiral ligand (Scheme 2.6). Relative to the hydrocarbon electrophiles explored by Vicic, 1-bromoindanes are activated electrophiles because the bromide is in a benzylic position, making it more susceptible to homo- or heterolytic bond cleavage. The different reactivities of the activated 1-bromoindanes versus the unactivated alkyl bromides previously studied by Vicic could lead to different reaction mechanisms. Furthermore, our reaction is asymmetric and the mechanism of stereochemical induction is unknown.

2.6.1 Synthesis and Reactivity of Novel Ni^{I} Complexes

Two single-electron mechanisms were initially considered based on literature precedent (Figure 2.4).[51-53] Each pathway contains three elementary steps, oxidative addition (OA), transmetalation (TM), and reductive elimination (RE), and differ only in

the order of the TM and OA steps. Both catalytic cycles invoke a Ni^{III}(alkyl)indenyl complex which undergoes reductive elimination to yield the cross-coupling product.

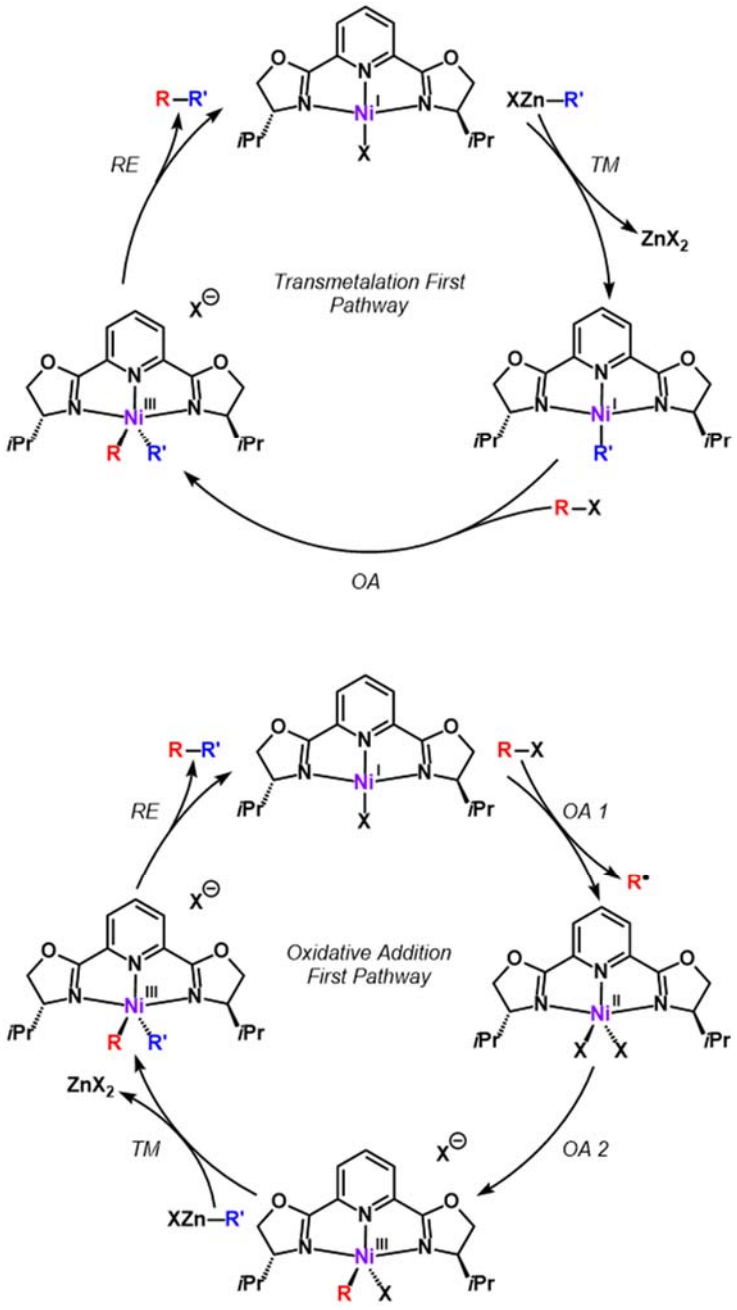

Figure 2.4. Two possible single-electron mechanisms for the asymmetric Negishi cross-coupling under investigation where X = Br, R = indenyl', and R' = alkyl.

To explore the viability of a transmetalation first pathway in an asymmetric cross-coupling reaction, relevant *S* = 1/2 2,6,-Bis[(4S/R)-(–/+)-isopropyl-2-oxazolin-2-yl]pyridine bound $Ni^{I}Br$ complex and Ni^{I}–alkyl complex (bearing β-hydrogen atoms) were synthesized and crystallographically characterized. Evidence against a transmetalation first pathway is provided by EPR, ^{19}F NMR, and UV-vis spectroscopic studies which demonstrate that the rate of oxidation of the $Ni^{I}Br$ by the electrophile is significantly faster than the rate of transmetalation of the $Ni^{I}Br$ with the alkylzinc reagent. Furthermore, attempts to prepare a Ni^{I}–alkyl complex by transmetalation with an alkylzinc reagent were not successful. Stoichiometric chemistry with a well-defined Ni^{I}-alkyl complex provides cross-coupling product in low efficiency but with comparable enantiomeric excess relative to the previously reported catalytic method. Finally, EPR spectra of catalytic cross-coupling reactions reveal the presence of a Ni^{III} species. The key novelties of this study include the crystallographic characterization of catalytically relevant (*i*PrPybox)$Ni^{I}Br$, (*i*PrPybox)$Ni^{II}Br_2$, and (*i*PrPybox)Ni^{I}-alkyl complexes (the first Ni^{I}-alkyl complex bearing β-hydrogen atoms).

The $Ni^{I}Br$ and $Ni^{II}Br_2$ complexes were synthesized, crystallographically characterized, and tested for catalytic competence. Inspired by my adoptive time in the Peters group, I attempted a comproportionation of $Ni^{II}Br_2$•glyme and $Ni(cod)_2$ in the presence of *i*PrPybox. Excitingly, this provided the midnight purple complex **2.11** in 89% yield, the first Ni^{I} complex to be isolated by the Fu group (Figure 2.5a). By EPR, **2.11** provides a rhombic EPR signal at 77K in DMA, with $g_1 = 2.26$, $g_2 = 2.17$, and $g_3 = 2.12$, consistent with a metal-centered radical (Figure 2.6). The $Ni^{II}Br_2$ complex **2.12** was readily prepared by treating $Ni^{II}Br_2$•glyme with *i*PrPybox (Figure 2.5b). The X-ray crystal structures of **2.11** and **2.12** are shown in Figure 2.5c and 2.5d respectively. Both complexes were catalytically competent

(Table 2.1, entries 2 and 3), yielding the cross-coupling product in comparable yields and enantioselectivities relative to the reported conditions (entry 1).

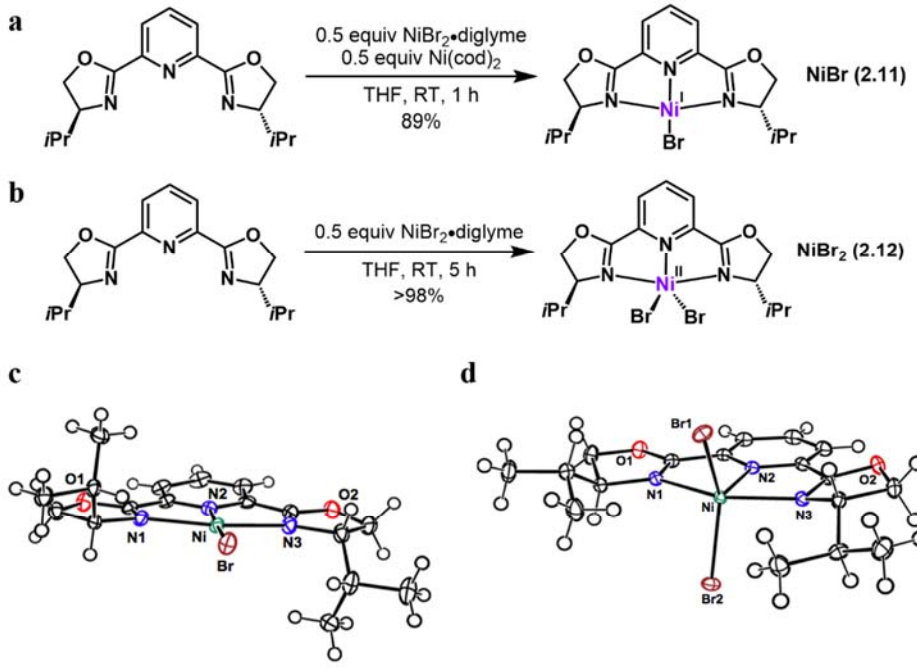

Figure 2.5. Characterization of nickel halide complexes bearing the *i*PrPybox ligand: (a) $Ni^{I}Br$ and (b) $Ni^{II}Br_2$ syntheses and (c) $Ni^{I}Br$ and (d) $Ni^{II}Br_2$ crystal structures. Ellipsoids shown at 50% probability.

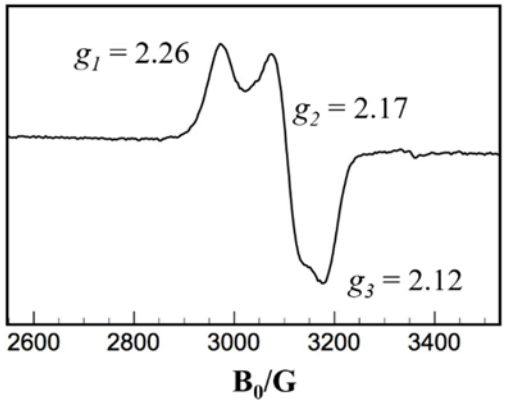

Figure 2.6. EPR spectrum of **2.11** in DMA at 77K.

Table 2.1. Catalytic competence of the nickel bromide complexes. All entries are reported as an average of two runs. *1st run with (+)-*i*PrPybox and second run with (–)-*i*PrPybox.

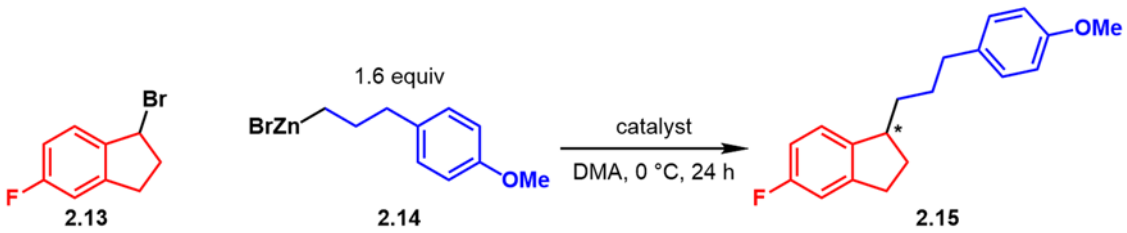

Entry	Catalyst	Yield (%)	*ee* (%)
1*	10% $NiBr_2$•diglyme and 13% *i*PrPybox	73	92
2	10% (+)-*i*PrPybox-**2.11**	65	90
3	10% (–)-*i*PrPybox-**2.12**	70	89

With complex **2.11** in hand, we sought to prepare a Ni^{I}-alkyl complex with *i*PrPybox to test for its stoichiometric reactivity. We were particularly interested in isolating a nickel(I) alkyl species bearing β-hydrogen atoms as such an intermediate is believed to participate in the cross-coupling under investigation (Figure 2.4, top pathway). Although Ni^{I}-alkyl complexes have been previously reported, no examples contain alkyl groups with β-hydrogen atoms. [49, 55-57]

When **2.11** is treated with a Grignard reagent at -78 °C, the EPR signal corresponding to the NiBr complex disappears and a new EPR signal arises with $g = 2.01$. Isolation of the putative Ni^{I}-alkyl species was not possible under these reaction conditions (presumably due to the presence of Mg salts) as the product quickly decomposed upon warming to room temperature. Alkylation reactions using softer alkylborate reagents allowed for the preparation and isolation of the σ-alkyl complex **2.17** (Figure 2.7a), which was characterized by EPR spectroscopy and X-ray crystallography (Figure 2.7b and 2.7c).

Consistent with Vicic's reported EPR spectrum of an electronically similar (terpyridine)Ni^{I}-Me complex, the EPR spectrum of (*i*PrPybox)Ni^{I}-alkyl complex shows a signal consistent with an organic-based radical, suggesting that the unpaired electron resides primarily on the *i*PrPybox ligand (Figure 2.7b).[51] The Ni^{I}-alkyl complex adopts a square planar geometry in the solid state and represents the first crystallographically characterized Ni^{I}-alkyl complex bearing β-hydrogen atoms.

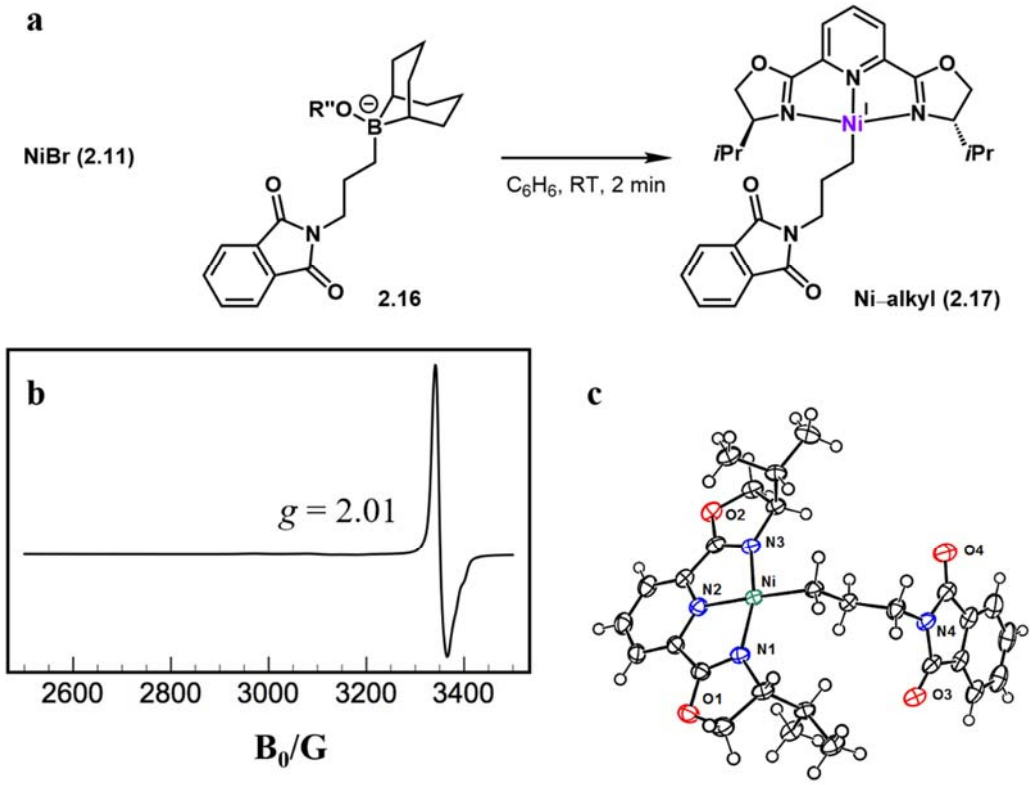

Figure 2.7. Ni^{I}-alkyl (a) synthesis, (b) EPR spectrum in DMA at 77K and (c) crystal structure. Ellipsoids are shown at 50% probability.

When **2.17** was subjected to the cross-coupling conditions, both the expected cross-coupling products **2.20** and **2.21** were formed (Scheme 2.7). Furthermore, a stoichiometric

reaction between **2.17** and the electrophile provided the cross-coupling product in low yield but with comparable enantiomeric excess to the parent catalytic system (Scheme 2.8). Although Vicic's results with discrete Ni-alkyl complexes suggests that an oxidative addition first pathway is unlikely (Figure 2.3), the competency of the Ni-alkyl species does not exclude a transmetalation or oxidative addition first pathway. **2.17** could react with the electrophile to give an on-path Ni^{III}-dialkyl intermediate; for instance, the Ni^{I}-alkyl complex could be oxidized by the bromoindane electrophile to form a $Ni^{II}Br$(alkyl) complex. Radical recombination of the benzyl radical would yield a Ni^{III}(alkyl)(indenyl) complex, which is an intermediate invoked in both pathways discussed above (Figure 2.4). Reductive elimination would provide cross-coupling product. Additional studies were performed to learn which pathway was more likely.

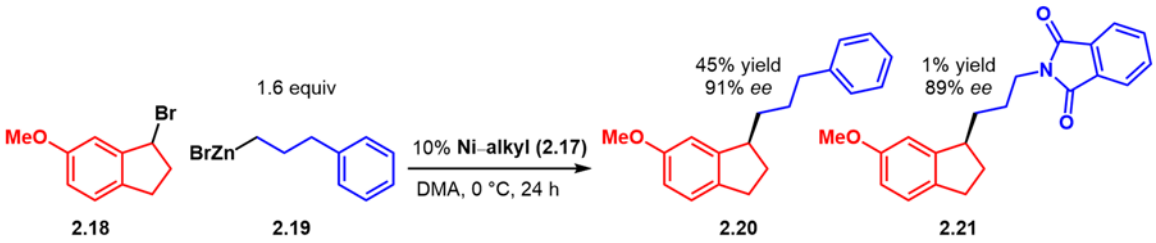

Scheme 2.7. Cross-coupling reaction using [(−)-*i*PrPybox]Ni^{I}-alkyl as a precatalyst with GC yields and enantioselectivies reported as an average of two runs.

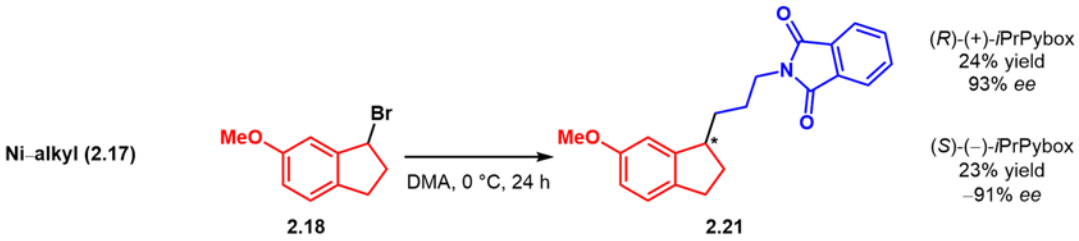

Scheme 2.8. Stoichiometric reaction between Ni^{I}-alkyl and electrophile.

In contrast to results with Grignard or alkylborate reagents, attempts to prepare **2.17** by transmetalation with alkylzinc reagents resulted in either complex EPR spectra inconsistent with the desired product or EPR spectra of unreacted NiBr. The apparent inability of alkylzinc reagents to effect alkyl transfer to provide a Ni^{I}-alkyl species raised concerns regarding the viability of a transmetalation first pathway.

The stoichiometric transmetalation reaction between alkylzinc bromide **2.22** and **2.11** was probed further using ^{19}F NMR spectroscopy, UV-Vis spectroscopy, and GC-MS. By ^{19}F NMR spectroscopy, after minutes at 0 °C, the alkylzinc reagent was intact, in line with the EPR results showing a metal-centered radical (see experimental section). UV-vis spectroscopy revealed a second order rate constant for transmetalation of 10^{-1} $M^{-1}s^{-1}$ (Figure 2.8), consistent with the slow reaction between the NiBr complex and alkylzinc reagent observed using EPR and NMR spectroscopy.

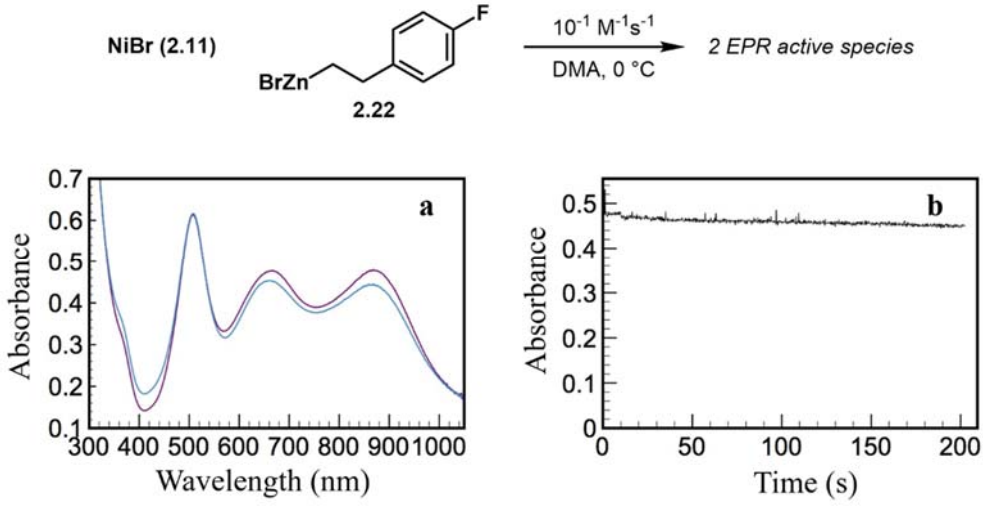

Figure 2.8. UV-vis spectra for reaction of **2.11** with alkylzinc bromide **2.22**: (a) purple trace is before addition of alkylzinc reagent and blue trace is post reaction monitoring (b) NiBr consumption monitored by following the absorbance at 870 nm over time.

To further investigate whether a transmetalation first or oxidative addition first pathway is more feasible, we next explored the reactivity of the $Ni^{I}Br$ complex with the electrophilic cross-coupling partner (Figure 2.9). When **2.11** was treated with 1-bromoindane, homocoupled electrophile was observed. In addition, the reaction mixture is EPR silent, indicating the formation of Ni^{II} products. This process is associated with an instantaneous color change from purple to orange. The formation of $Ni^{II}Br_2$ was confirmed by ^{1}H NMR spectroscopy. The second-order rate constant for this process was measured by UV-Vis spectroscopy to be approximately 10^{-4} $M^{-1}s^{-1}$.

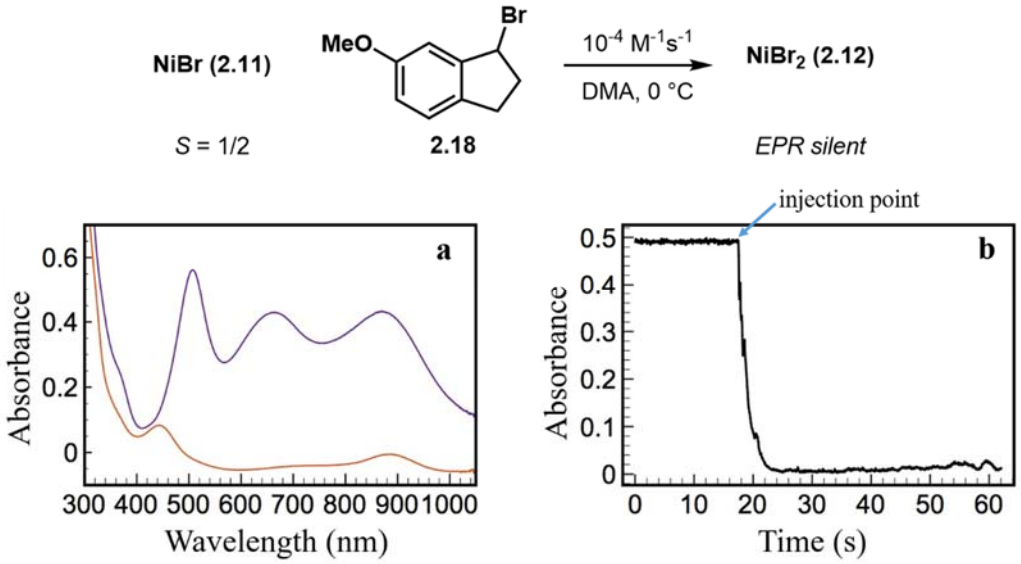

Figure 2.9. UV-vis spectra for reaction of **2.11** with a bromoindane electrophile: (a) purple trace is before addition of electrophile and orange trace is post reaction monitoring (b) NiBr consumption monitored by following the absorbance at 870 nm over time.

The relative rates of oxidation of the $Ni^{I}Br$ by the electrophile (10^{-4} $M^{-1}s^{-1}$) versus transmetalation with the nucleophile (10^{-1} $M^{-1}s^{-1}$) suggest that a mechanism involving transmetalation to **2.11** is not viable for this particular Negishi reaction. In the presence of

an activated electrophile, such as 1-bromoindane, oxidation of the NiBr complex will outcompete transmetalation. This result contrasts with Vicic's report in which a transmetalation first pathway was proposed for a coupling using unactivated alkyl bromides. The results reported herein and Vicic's studies are not inconsistent; indeed, when the reaction between **2.11** and cyclopentyl bromide was monitored by UV-vis spectroscopy, a second order rate constant for oxidation of the $Ni^{I}Br$ complex to $Ni^{II}Br_2$ was determined to be 10^{-1} $M^{-1}s^{-1}$ (Figure 2.10). This rate is comparable to the rate of transmetalation and more studies are required to determine whether unactivated electrophiles are coupled by a transmetalation first pathway under our reaction conditions.

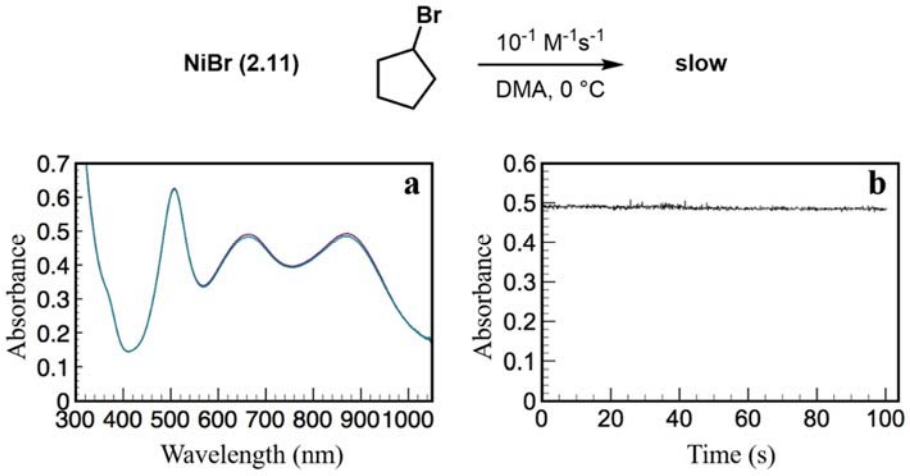

Figure 2.10 UV-Vis study of reaction between **2.11** and cyclopentyl bromide: (a) purple trace is before addition of cyclopentyl bromide and blue trace is post reaction monitoring (b) NiBr consumption monitored by following the absorbance at 870 nm over time.

2.6.2 Additional Mechanistic Insights

To investigate how EPR active species could be generated during catalysis, the EPR silent $NiBr_2$ complex was treated with nucleophile **2.14** and the reaction monitored using

EPR spectroscopy. When **2.12** is treated with one equivalent of the alkylzinc bromide reagent, a metal-centered radical is observed by EPR (Figure 2.11a). When **2.12** is treated with 16 equivalents of the nucleophile, simulating catalytic conditions, two EPR active species are observed: a ligand-based radical signal and a metal-centered radical signal (Figure 2.11b). When the $NiBr_2$ complex is treated with a bromoindane, no EPR active species are observed.

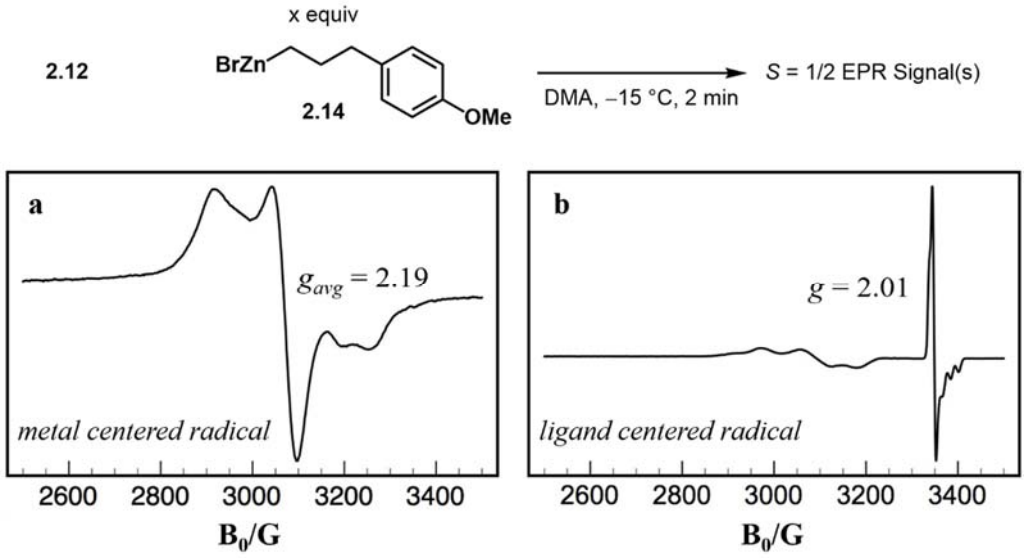

Figure 2.11. EPR spectra provide evidence for the generation of S = 1/2 species upon treatment of a DMA solution of 2.12 at –15 °C with (a) 1 equiv of **2.14** and (b) 16 equiv of **2.14**.

As previously mentioned, S = 1/2 complexes **2.11** and **2.17** were characterized by EPR spectroscopy. To determine whether these species were present under catalytic conditions, cross-coupling reactions using the various catalyst systems were monitored by

EPR spectroscopy,[b] revealing that neither of the isolated Ni^{I} species were observed; instead, unknown metal-centered radical species were encountered (Figure 2.12).

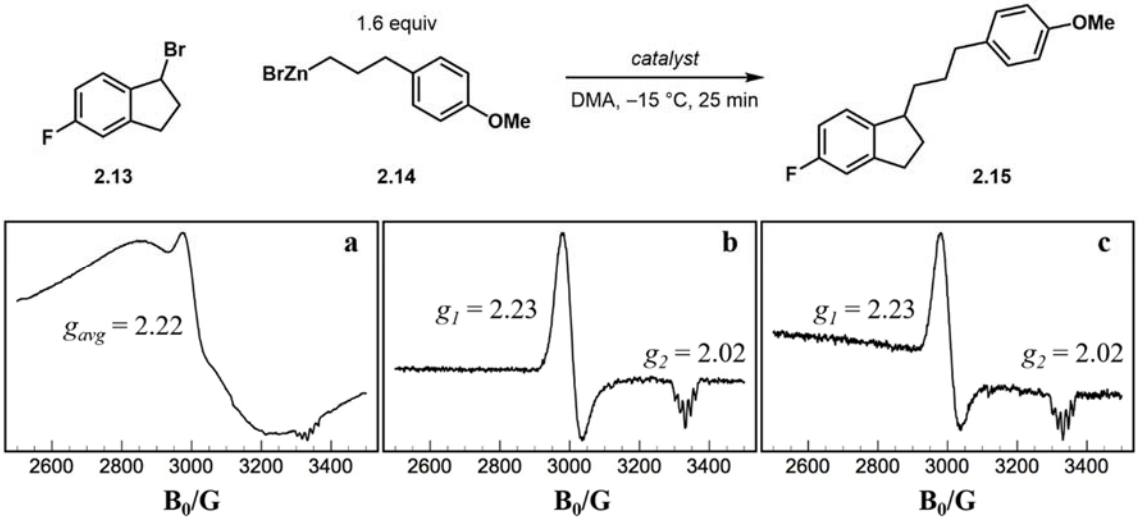

Figure 2.12. Catalytic reactions in progress monitored using EPR spectroscopy, each spectrum represents a reaction using a different catalyst: (a) the *in situ* generated catalyst system, (b) **2.11** or (c) **2.12** as the catalyst.

The EPR signal in Figures 2.12b and 2.12c is generated more cleanly when the discrete complexes **2.11** or **2.12** are employed and has been putatively assigned as a Ni^{III} complex based on comparison with reported EPR spectra of related Ni^{III} complexes.[58-60] We attempted to generate the same EPR signal by treating either the Ni^{I}-alkyl or $Ni^{I}Br$ complex with various alkyl bromide reagents, but did not observe the desired signal. Inspired by the ability of CF_3 groups to stabilize high oxidation state metal complexes,[59-60] we treated the Ni^{I}-alkyl complex with Umemoto's reagent. To our delight, the same putative Ni^{III} signal is observed (Figure 2.13). Given the EPR active species of this reaction

[b] Aliquots were taken after 25 minutes. ^{1}H NMR spectroscopy was used to monitor the depicted cross-coupling and revealed that at 25 minutes, a 10% yield of product is obtained.

mixture has not yet been isolated and the similiarities between EPR spectra of Ni^{III} with various ligands,[58-60] we cannot assign the structure based on EPR spectroscopy alone. Nonetheless, the signals observed in Figures 2.12 and 2.13 likely correspond to a Ni^{III} centered radical. More studies are needed to determine whether this species is catalytically relevant.

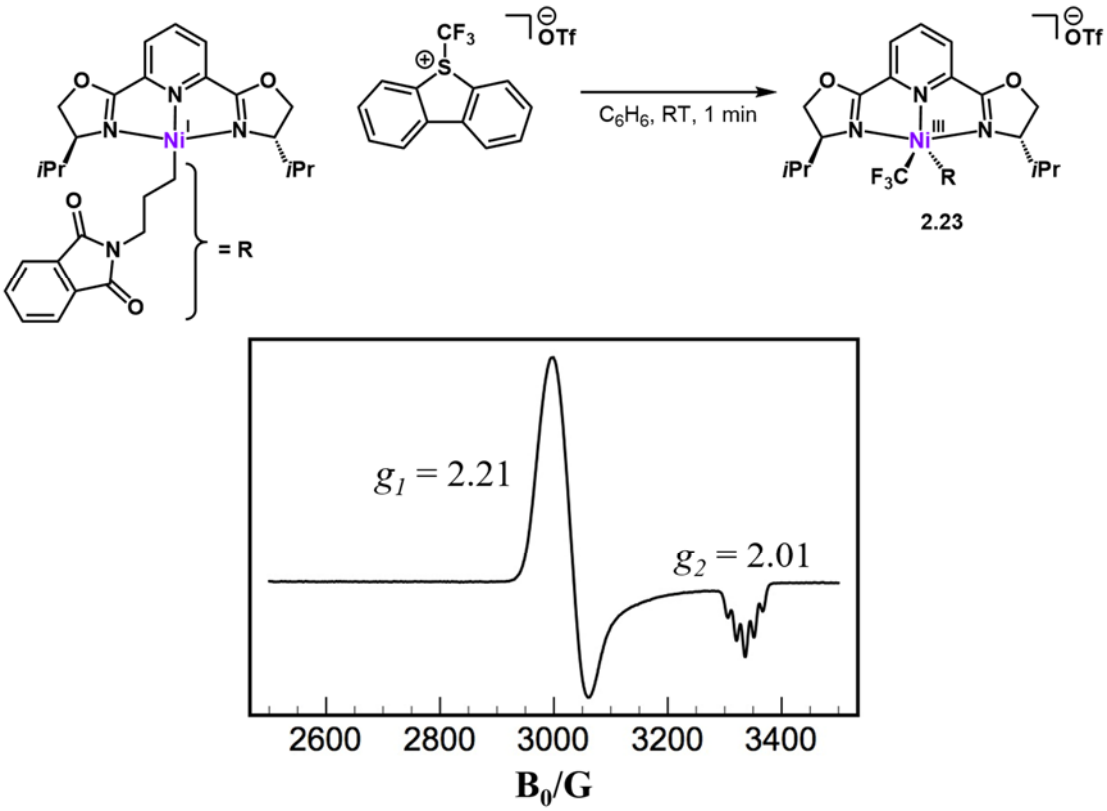

Figure 2.13. EPR spectrum of reaction between **2.17** and Umemoto's reagent.

2.7 Conclusions

Based on previously reported mechanistic studies of Negishi cross-couplings of unactivated alkyl electrophiles, we explored the viability of a transmetalation first pathway

in the context of an asymmetric Negishi reaction using an *activated* alkyl electrophile. The synthesis and crystallographic characterization of two new $S = 1/2$ Ni^{I} species are reported. Three important pieces of data, (1) the inability of an alkylzinc bromide reagent to effectively transmetalate to a well-defined NiBr complex to provide a Ni^{I}-alkyl complex stoichiometrically, (2) the high reactivity of the NiBr complex towards the electrophile under stoichiometric conditions, and (3) the poor reactivity of the Ni^{I}-alkyl complex in a stoichiometric cross-coupling reaction, suggest that a transmetalation first pathway is unlikely to be operative. Preliminary EPR spectroscopic data of catalytic reactions in progress show a signal reminiscent of previously reported Ni^{III} complexes. The same signal can be generated upon treatment of the Ni^{I}-alkyl with an electrophilic CF_3 source, presumably forming a Ni^{III}(alkyl)(CF_3) complex. Additional studies towards identifying the observed Ni^{III} complex, looking at the mechanism of oxidative addition and reductive elimination in more detail, and determining the stereochemistry-determining step of the reaction are warranted. Based on reports published after this work, one potential mechanism for oxidative addition involves two Ni centers: a Ni^{I}-X center that generates R· and a Ni^{II}-alkyl species which recombines with R· (Figure 2.14).[46, 52-53]

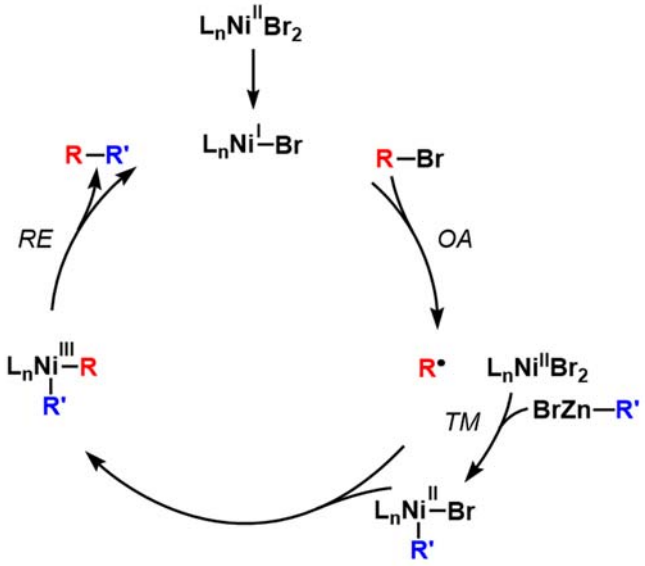

Figure 2.14. Potential mechanism based on the evidence gathered from this work and analogous studies performed with aryl zinc reagents.[46]

2.8 Experimental Section

2.8.1 General Information

The following reagents were purchased and used as received: Aldrich: benzyl alcohol, 4-bromobenzyl bromide, sodium hydride (60% dispersion in mineral oil), bis(benzonitrile)Pd(II) chloride, copper iodide, 2,6-bis[(4R)-(+)-isopropyl-2-oxazolin-2-yl]pyridine, 2,6-bis[(4S)-(−)-isopropyl-2-oxazolin-2-yl]pyridine, nickel(II) bromide ethylene glycol dimethyl ether complex, nickel(II) bromide 2-methoxyethyl ether complex, dimethylacetamide (anhydrous, 99.8%), phthalimide, 1-bromo-3-phenylpropane, 3-(4-methoxyphenyl)-1-propanol, phosphorous tribromide, allyl bromide, 9-borabicyclo[3.3.1]nonane dimer, 5-(trifluoromethyl)dibenzothiophenium trifluoromethanesulfonate. Alfa: 5-fluoro-1-indanone, 6-methoxy-1-indanone, iodine. Strem: Bis(cyclooctadiene)nickel(0). Schwartz's and deuterated Schwartz's reagents were synthesized using a known procedure.[43] THF, pentane, benzene, toluene were dried in a solvent-purification system with the aid of activated alumina. All deuterated solvents were purchased from Cambridge Isotope Laboratories. All reactions were carried out in oven-dried glassware under a nitrogen atmosphere unless otherwise specified.

^{1}H data and ^{13}C NMR data for the Ni studies were collected on Varian 600 MHz, Varian Inova 500 MHz, and Varian Mercury 300 MHz spectrometers at ambient temperature. ^{19}F NMR data and VT NMR data was collected on a Varian Inova 500 MHz spectrometer at the described temperature and ^{19}F NMR data were referenced using trifluorotoluene as an internal standard. GC analyses were carried out on an Agilent 6890 series system with DB-1 column (length 30 m, I.D. 0.25 mm), and Agilent 6850 series system with G-TA column (length 30 m, I.D. 0.25 mm). GC-MS analyses were performed on an

Agilent 6980 series system equipped with an Agilent 5973 Network Mass Selective Detector. HPLC analyses were carried out on an Agilent 1100 Series system, using Daicel CHIRALCEL® columns (internal diameter 4.6 mm, column length 250 mm, particle size – –5 μm). SFC analyses were performed on a Thar SFC system equipped with an Agilent 1315B DAD detector using Daicel CHIRALCEL® columns or Daicel CHIRALPAK® columns (I.D. 4.6 mm, column length 250 mm, particle size 5 μm) at 40 °C. X-band EPR spectra were obtained on a Bruker EMX spectrometer. Optical spectroscopy measurements were taken on a Cary 50 UV-vis spectrophotometer using a 1 cm two-window quartz cell. XRD studies were conducted at the Beckman Institute at Caltech using a Bruker SMART 1000 CCD and at the Stanford Synchrotron Radiation Lightsource (SSRL).

2.8.2 Synthesis

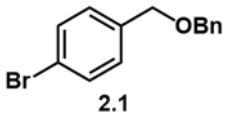

2.1

Benzyl ether 2.1. To a cooled (0 °C) solution of NaH (60% in mineral oil, 3.2 g, 80 mmol) in DMF (40 mL), benzyl alcohol (4.0 g, 25 mmol) was added. After 30 min, a solution of 4-bromobenzyl bromide (10 g, 40 mmol) in DMF was added to the stirring reaction mixture carefully. After 24h, the reaction mixture was diluted with water (100 mL). The aqueous layer was extracted with dichloromethane (2 × 160 mL) and ethyl acetate (1 × 160 mL). The combined organic layers were washed with brine, dried over Na_2SO_4, and concentrated *in vacuo*. Purification by flash chromatography (15:1 hexanes:EtOAc) gave benzyl ether 2.1 as an oil (11 g, 96%). ^{1}H NMR (500 MHz, Chloroform-*d*) δ 7.40 – 7.37 (m, 2H), 7.27 (m, 2H), 7.23 – 7.19 (m, 1H), 7.16 (s, 2H), 7.16 – 7.13 (m, 2H), 4.46 (s, 2H), 4.41 (s, 2H).

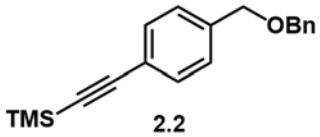

2.2

TMS-protected alkyne 2.2. Compound **2.2** was synthesized by adapting a known procedure for Sonagashira couplings.[41] To a solution of bis(benzonitrile)Pd(II) chloride (83 mg, 0.22 mmol) and copper iodide (27 mg, 0.14 mmol) in dioxane (7 mL), tri-tert-butylphosphine (1.9 mL, 0.25 M in dioxane, 0.47 mmol), diisopropylamine (1.2 mL, 8.7 mmol), benzyl ether **2.1** (2.0 g, 7.2 mmol), and ethynyltrimethylsilane (1.2 mL, 8.7 mmol) was added in a glovebox. The reaction mixture was removed from the glovebox, put under an N_2 atmosphere, and stirred at ambient temperature. After 5h, the reaction mixture was diluted with ethyl acetate (40 mL), filtered through a small silica pad with ethyl acetate (120 mL), dried over $MgSO_4$, and concentrated *in vacuo*. Purification by flash chromatography (50:1 hexanes:EtOAc) gave TMS-protected alkyne **2.2** as an oil (2.1 g, >98%). ^{1}H NMR (300 MHz, Chloroform-*d*) δ 7.47 – 7.42 (m, 2H), 7.36 – 7.35 (m, 1H), 7.34 (m, 2H), 7.30 (m, 2H), 7.27 (m, 1H), 7.25 (m, 1H), 4.53 (s, 4H), 0.24 (s, 9H).

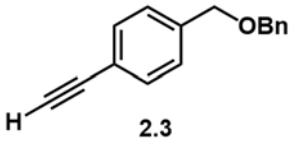

2.3

Alkyne 2.3. To a solution of TMS-protected alkyne **2.2** (2.1 g, 7.2 mmol) in MeOH (25 mL), was added potassium carbonate (90 mg, 6.5 mmol). The reaction mixture was put under an N_2 atmosphere and stirred at ambient temperature. After 3h, the reaction mixture was concentrated *in vacuo* and the resultant oil was diluted with aqueous sodium bicarbonate (25 mL). The aqueous layer was extracted with diethyl ether (3 × 100 mL) and the combined organic layers were dried over $MgSO_4$ and concentrated *in vacuo*. Purification by flash chromatography (30:1 hexanes:EtOAc to 15:1 hexanes:EtOAc

gradient) provided alkyne **2.3** as an orange oil (1.3 g, 83%). ^{1}H NMR (300 MHz, Chloroform-*d*) δ 7.52 – 7.47 (m, 2H), 7.38 (m, 2H), 7.37 (m, 2H), 7.35 (m, 1H), 7.34 – 7.31 (m, 2H), 4.57 (m, 4H), 3.08 (s, 1H).

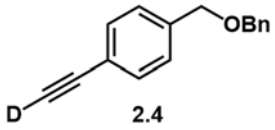

2.4

Deuterium-labeled alkyne 2.4. To a cooled (–78 °C) solution of alkyne **2.3** (250 mg, 1.1 mmol) in THF (2.25 mL), *n*BuLi (0.65 mL, 2.6 M in hexanes, 1.7 mmol) was added slowly. After 1h, D_2O (0.8 mL) was added and the reaction mixture was warmed to room temperature. Any excess base was quenched with saturated aqueous NH_4Cl (3 mL). The aqueous layer was extracted with diethyl ether (3 x 15 mL) and the combined organic layers were dried over $MgSO_4$ and concentrated *in vacuo*. Purification by flash chromatography (30:1 hexanes:EtOAc to 15:1 hexanes:EtOAc gradient) provided deuterium-labeled alkyne **2.4** as an orange oil (252 mg, >98%). ^{1}H NMR (500 MHz, Chloroform-*d*) δ 7.49 – 7.46 (m, 2H), 7.37 – 7.34 (m, 4H), 7.32 (m, 3H), 4.55 (m, 4H). ^{2}D NMR (400 MHz, Chloroform with Chloroform-*d* reference) δ 3.08 (s, 1D).

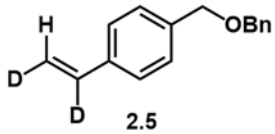

2.5

***Cis*-1,2-dideuterioalkene 2.5.** Compound **2.5** was synthesized by adapting a known procedure.[42] To a solution of bis(cyclopentadienyl)zirconium chloride deuteride (384 mg, 1.48 mmol) in toluene (2.15 mL), alkyne **2.3** (300 mg, 1.37 mmol) was added in a glovebox and stirred at room temperature. After 2h, the red reaction mixture was concentrated *in vacuo* and the resultant oil was taken up in diethyl ether (1.9 mL), removed from the glovebox, and cooled to 0 °C. To the cooled reaction mixture, degassed D_2O (1 mL) was

added. After 15 min, the crude reaction mixture was warmed to room temperature, filtered through silica with diethyl ether (50 mL), and concentrated *in vacuo*. Purification by flash chromatography (30:1 hexanes:EtOAc) gave *cis*-1,2-dideuterioalkene 5 as an oil (265 mg, 87%). ^{1}H NMR (500 MHz, Chloroform-*d*) δ 7.44 – 7.41 (m, 2H), 7.40 – 7.37 (m, 4H), 7.35 (m, 2H), 7.34 – 7.28 (m, 2H), 7.23 – 7.19 (m, 1H), 5.81 – 5.66 (m, 1H), 4.57 (m, 4H). ^{2}D NMR (400 MHz, Chloroform with Chloroform-*d* reference) δ 6,77 (s, 1D), 5.29 (s, 1D).

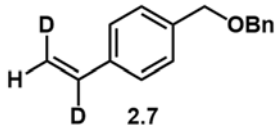

2.7

***Trans*-1,2-dideuterioalkene 2.7.** Compound **2.7** was synthesized by adapting a known procedure.[42] To a solution of bis(cyclopentadienyl)zirconium chloride deuteride (322 mg, 1.24 mmol) in toluene (1.8 mL), alkyne **2.4** (252 mg, 1.13 mmol) was added in a glovebox and stirred at room temperature. After 2h, the red reaction mixture was concentrated *in vacuo* and the resultant oil was taken up in diethyl ether (1.6 mL), removed from the glovebox, and cooled to 0 °C. To the cooled reaction mixture, degassed H_2O (1 mL) was added. After 5 min, the crude reaction mixture was warmed to room temperature, filtered through silica with diethyl ether (50 mL), and concentrated *in vacuo*. Purification by flash chromatography (30:1 hexanes:EtOAc) gave *cis*-1,2-dideuterioalkene 5 as an oil (167 mg, 65%). ^{1}H NMR (400 MHz, Chloroform-*d*) δ 7.45 – 7.41 (m, 2H), 7.40 – 7.38 (m, 4H), 7.37 – 7.30 (m, 3H), 5.25 (s, 1H), 4.60 – 4.57 (m, 4H). ^{2}D NMR (400 MHz, Chloroform with Chloroform-*d* reference) δ 6,77 (s, 1D), 5.79 (s, 1D).

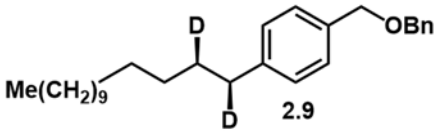

Benzyl-4-tetradecylbenzylether 2.9. To a solution of 9-BBN dimer (60 mg, 0.24 mmol) in THF (0.88 mL) was added *cis*-1,-2-dideuterioalkene **2.5** (100 mg, 0.44). The reaction mixture was stirred for 14h to provide alkylborane **2.6** as a 0.5 M solution. In a separate reaction vial equipped with a stir bar, $Pd(OAc)_2$ (3 mg, 0.015 mmol), PCy_3 (9 mg, 0.030 mmol), $K_3PO_4 \bullet H_2O$ (105 mg, 0.46 mmol) was added. To these solids, alkylborane **2.6** (0.8 mL, 0.4 mmol) and bromododecane (91 µL, 0.381 mmol) was added. The reaction was capped and stirred in the glovebox. After 24h, the crude reaction mixture was filtered through silica with diethyl ether (50 mL) and concentrated *in vacuo*. Purifation by preparative thin layer chromatography (40:1 hexanes:EtOAc) provided benzyl-4-tetradecylbenzylether **2.9** as an oil (86 mg, 57%). ^{1}H NMR (600 MHz, Chloroform-*d*) δ 7.40 – 7.33 (m, 4H), 7.29 (m, 3H), 7.17 (m, 2H), 4.56 (s, 2H), 4.53 (s, 2H), 2.58 (d, J = 6.2 Hz, 1H), 1.58 (m, 1H), 1.26 (s, 22H), 0.89 (t, J = 7.0 Hz, 3H). ^{2}D NMR (400 MHz, Chloroform with Chloroform-*d* reference) δ 2.59 (s, 1D), 1.59 (s, 1D).

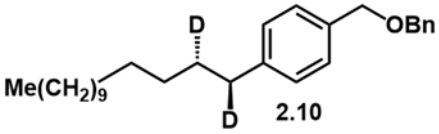

Benzyl-4-tetradecylbenzylether 2.10. To a solution of 9-BBN dimer (60 mg, 0.24 mmol) in THF (0.88 mL) was added *trans*-1,-2-dideuterioalkene **2.7** (100 mg, 0.44). The reaction mixture was stirred for 14 h to provide alkylborane **2.8** as a 0.5 M solution. In a separate reaction vial equipped with a stir bar, $Pd(OAc)_2$ (3 mg, 0.015 mmol), PCy_3 (9 mg, 0.030 mmol), $K_3PO_4 \bullet H_2O$ (105 mg, 0.46 mmol) was added. To these solids, alkylborane **2.8** (0.8 mL, 0.4 mmol) and bromododecane (91 µL, 0.381 mmol) was added. The reaction was

capped and stirred in the glovebox. After 24h, the crude reaction mixture was filtered through silica with diethyl ether (50 mL) and concentrated *in vacuo*. Purifation by preparative thin layer chromatography (40:1 hexanes:EtOAc) provided benzyl-4-tetradecylbenzylether **2.10** as an oil (56 mg, 37%). ^{1}H NMR (600 MHz, Chloroform-*d*) δ 7.32 – 7.26 (m, 3H), 7.23 – 7.16 (m, 4H), 7.09 (d, *J* = 7.7 Hz, 2H), 4.49 (s, 2H), 4.45 (s, 2H), 2.50 (d, *J* = 9.3 Hz, 1H), 1.55 – 1.46 (m, 1H), 1.18 (s, 22H), 0.81 (t, *J* = 6.9 Hz, 3H). ^{2}D NMR (400 MHz, Chloroform with Chloroform-*d* reference) δ 2.59 (s, 1D), 1.59 (s, 1D).

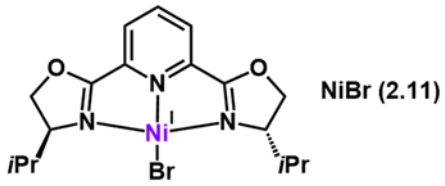

NiBr (2.11)

(2,6-Bis[((4*R*)-(+)-isopropyl-2-oxazolin-2-yl]pyridine)Ni–Br Complex 2.11. The title compound was prepared using a modified reported procedure.[61] To a solution of 2,6-Bis[((4*R*)-(+)-isopropyl-2-oxazolin-2-yl]pyridine (1.65 g, 5.47 mmol) in THF (100 mL) was added $NiBr_2$•glyme (844 mg, 2.74 mmol) and $Ni(cod)_2$ (753 mg, 2.74 mmol) sequentially as solids providing a midnight purple colored reaction mixture within minutes. After 45 min, the reaction mixture was concentrated *in vacuo* to remove any volatiles and the resultant purplish blue solid was filtered and washed with pentane (3 × 20 mL) to yield complex **2.11** as a purple, fluffy solid (73%). To a solution of a small amount of this solid in THF (2 mL), pentane was diffused to give purplish black air-sensitive crystals suitable for X-ray diffraction. Compound is paramagnetic. ^{1}H NMR (400 MHz, THF-d_8) δ 9.62 (br), 2.37 (br), 0.35 (br). Anal. Calcd for $C_{17}H_{23}BrN_3NiO_2$: C, 46.41; H, 5.27; N, 9.55. Found: C, 46.29; H, 5.17; N, 9.37.[46]

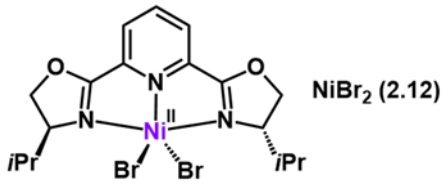

(2,6-Bis[((4*R*)-(+)-isopropyl-2-oxazolin-2-yl]pyridine)Ni(Br)$_2$ Complex 2.12. To a solution of 2,6-Bis[((4*R*)-(+)-isopropyl-2-oxazolin-2-yl]pyridine (488 mg, 1.62 mmol) in THF (30 mL) was added $NiBr_2$•glyme (500 mg, 1.2 mmol) providing a deep red orange colored reaction mixture within minutes. After 5 h, the deep red reaction mixture was filtered through celite to remove any insoluble material and concentrated *in vacuo* until a solid began to precipitate. This mixture was transferred to a 20 mL scintillation vial with a minimal amount of THF such that all the remaining solid went into solution. The 20 mL vial was placed in a large jar with pentane and capped, and yielded deep orange crystals of complex **2.12** (691 mg, 82%) overnight. These crystals were suitable for x-ray diffraction and turned green within a period of hours. Compound is paramagnetic. ^{1}H NMR (400 MHz, THF-d_8) δ 66.5 (s, 2H), 37.54 (s, 2H), 17.33 (s, 3H), 11.92 (s, 2H), 8.58 (s, 2H), 4.72 (s, 6H), 4.18 (s, 6H). Anal. Calcd for $C_{17}H_{23}Br_2N_3NiO_2$: C, 39.27; H, 4.46; N, 8.08. Found: C, 39.36; H, 4.53; N, 8.15.[46]

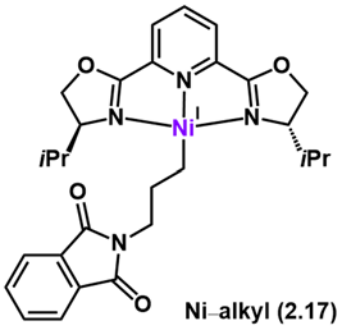

Ni–alkyl (2.17)

(2,6-Bis[((4*R*)-(+)-isopropyl-2-oxazolin-2-yl]pyridine) 2.17.

Preparation of Alkylborate. The alkylborate was prepared using a modified reported procedure. To a mixture of KO*t*-Bu (144 mg, 1.28 mmol) and *i*BuOH (195 µL, 2.11 mmol) in an 8 mL vial, the alkylborane (1.6mL, 1.0 M stock solution in iPr$_2$O) and THF (1.8 mL) was added. The reaction mixture was stirred for 30 min at ambient temperature, providing the alkylborate as a 0.45 M solution in a mixture of iPr$_2$O and THF, which was used without further purification.

Synthesis of 2.17. To a solution of (*R*)-*i*PrPybox NiBr (500 mg, 1.14 mmol) in benzene (12.5 mL), was added the alkylborate (3.28 mL, 0.45 M in THF and iPr$_2$O). The reaction was stirred vigorously for 2 min at ambient temperature. The crude mixture was filtered through celite and concentrated providing **2.17** as a brown solid (414 mg, 66% yield). *Note that a solution of complex **2.17** is not stable at ambient temperature for extended periods of time. The solid should be stored at –35 °C.

Synthesis of X-ray Quality Crystals of 2.17. To a solution of (*R*)-*i*PrPybox NiBr (80 mg, 0.182 mmol) in benzene (2 mL), was added the alkylborate (525 µL, 0.45 M in THF and iPr$_2$O). The reaction was stirred vigorously for 2 min at ambient temperature. The crude mixture was filtered through celite at –78 °C in the glovebox coldwell. Diffusion of tetramethylsilane to this toluene solution of complex **2.17** at –35 °C for 24h provided brown crystals suitable for x-ray diffraction.

Preparation of Alkylborane Precursor.

2-allylisoindoline-1,3-dione 2.16

2-allylisoindoline-1,3-dione. The title compound was prepared according to a reported procedure from allyl bromide and phthalimide.[62] The product was obtained as white needles (92% yield).

Alkylborane 2.16. The title compound was prepared according to a reported procedure using 2-allylisoindoline-1,3-dione and 9-BBN dimer.[15] The product was obtained as a 1M stock solution in *i*Pr$_2$O.

Preparation of Cross-Coupling Partners

These procedures have not been optimized.

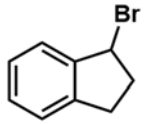

1-bromoindane

1-bromoindane. The title compound was prepared according to a reported procedure from 1-indanol.[29] The product was obtained as a clear yellow oil (95% yield).

^{1}H NMR (500 MHz, Chloroform-*d*) δ 7.48 – 7.46 (m, 1H), 7.31-7.25 (m, 3H), 5.63 (dd, *J* = 2.4, 6.1 Hz, 1H), 3.27–3.19 (m, 1H), 2.96-2.89 (m, 1H), 2.67-2.53 (m, 2H).

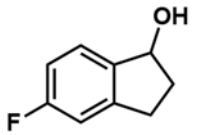

5-fluoroindan-1-ol

5-fluoroindan-1-ol. The title compound was prepared according to a reported procedure from 5-fluoro-1-indanone.[29] The product was obtained as faint yellow crystals (85% yield). ^{1}H NMR (500 MHz, Chloroform-*d*) δ 7.38 – 7.31 (m, 1H), 6.92 (m, *J* = 9.2, 6.9, 2.1, 1.2 Hz, 2H), 5.21 (q, *J* = 6.4 Hz, 1H), 3.10–3.00 (m, 1H), 2.81 (dddd, *J* = 16.2, 8.6, 6.3, 1.0 Hz, 1H), 2.51 (dddd, *J* = 13.4, 8.4, 6.8, 5.1 Hz, 1H), 1.98 (dddd, *J* = 13.4, 8.5, 6.3, 5.0 Hz, 1H), 1.73 (dt, *J* = 6.8, 1.2 Hz, 1H).

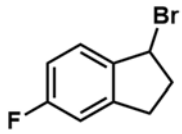

2.13

1-bromo-5-fluoroindane 2.13. 5-fluoroindan-1-ol (3.87 g, 25.5 mmol) was suspended in Et_2O (30 mL) in an oven-dried flask under nitrogen and cooled to –5 °C. A solution of PBr_3 (1.2 mL, 12.7 mmol) in Et_2O (9 mL) was added dropwise over 15 min by syringe. The reaction mixture was allowed to stir at –5 °C for 1 h. After 1 h, the reaction was quenched by the addition of icy water. The biphasic solution was transferred to a separatory funnel and the aqueous layer was extracted with Et_2O (3 × 50 mL) at low temperature. The combined organic layers were washed with icy H_2O (30 mL) and icy $NaHCO_3$ (30 mL) at low temperature, dried using $MgSO_4$, and concentrated *in vacuo* at room temperature. The resultant oil was filtered through a cotton pipette plug to provide the product as a clear faint yellow oil (78% yield) and used without further purification. ^{1}H NMR (300 MHz, Chloroform-*d*) δ 7.38 (dd, *J* = 8.1, 5.2 Hz, 1H), 6.93 (ddt, *J* = 9.5, 8.4, 1.3 Hz, 2H), 5.56 (dd,

J = 6.1, 2.3 Hz, 1H), 3.27 – 3.11 (m, 1H), 2.88 (ddd, *J* = 16.4, 7.4, 2.9 Hz, 1H), 2.72 – 2.46 (m, 2H).

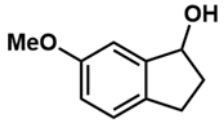

6-methoxyindan-1-ol

6-methoxyindan-1-ol. The title compound was prepared according to a reported procedure from 6-methoxy-1-indanone.[29] The product was obtained as a clear colourless oil (92% yield).

^{1}H NMR (300 MHz, Chloroform-*d*) δ 7.35 – 7.28 (m, 1H), 6.85 – 6.74 (m, 2H), 5.20 (q, *J* = 6.5 Hz, 1H), 3.80 (s, 3H), 3.15 – 2.95 (m, 1H), 2.89 – 2.69 (m, 1H), 2.48 (dddd, *J* = 13.6, 8.5, 6.7, 5.4 Hz, 1H), 1.97 (dddd, *J* = 13.2, 8.5, 5.9, 4.5 Hz, 1H), 1.69 – 1.63 (m, 1H).

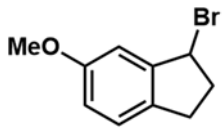

2.18

1-bromo-6-methoxyindane 2.18. 6-methoxyindan-1-ol (1.95 g, 11.9 mmol) was suspended in Et_2O (15 mL) in an oven-dried 40 mL scintillation vial under nitrogen and cooled to –5 °C. A solution of PBr_3 (0.56 mL, 5.94 mmol) in Et_2O (8 mL) was added dropwise over 15 min by syringe. The reaction mixture was allowed to stir at –5 °C for 2 h. After 2 h, the reaction was quenched by the addition of icy water. The biphasic solution was transferred to a separatory funnel and the aqueous layer was extracted with Et_2O (3 × 30 mL) at low temperature. The combined organic layers were washed with icy H_2O (15 mL) and icy $NaHCO_3$ (15 mL) at low temperature, dried using $MgSO_4$, and concentrated *in vacuo* at room temperature. The resultant oil was filtered through a cotton pipette plug to provide the

product as a clear faint yellow oil which solidified overnight after being stored at –40 °C (86% yield) and used without further purification. ^{1}H NMR (300 MHz, Chloroform-*d*) δ 7.16 (m, *J* = 8.4, 1.3, 0.6 Hz, 1H), 6.95 (dt, *J* = 2.5, 0.6 Hz, 1H), 6.83 (dd, *J* = 8.3, 2.5 Hz, 1H), 5.55 (dd, *J* = 6.1, 2.5 Hz, 1H), 3.81 (s, 3H), 3.18 – 3.03 (m, 1H), 2.88 – 2.75 (m, 1H), 2.68 – 2.46 (m, 2H).

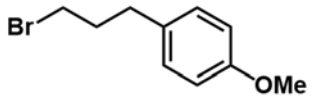

1-(3-bromopropyl)-4-methoxybenzene

1-(3-bromopropyl)-4-methoxybenzene. The title compound was prepared according to a reported procedure starting from 3-(4-methoxyphenyl)-1-propanol.[63] The product was obtained as a clear yellow oil (79%). ^{1}H NMR (300 MHz, Chloroform-*d*) δ 7.16 – 7.08 (m, 1H), 6.88 – 6.80 (m, 1H), 3.79 (s, 1H), 3.39 (t, *J* = 6.6 Hz, 1H), 2.72 (t, *J* = 7.3 Hz, 1H), 2.13 (dq, *J* = 8.2, 6.6 Hz, 1H).

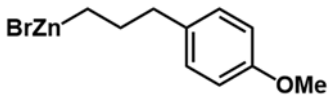

2.14

(3-(4-methoxyphenyl)propyl)zinc(II) bromide 2.14. The title compound was prepared according to a reported procedure starting from 1-(3-bromopropyl)-4-methoxybenzene with the exception that the yield was determined by titration with iodine at room temperature.[64] The product was obtained as a 1 .5 M stock solution in DMA (94% yield).

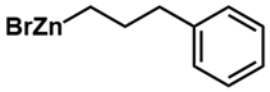

2.19

(3-phenylpropyl)zinc(II) bromide 2.19. The title compound was prepared according to a reported procedure starting from 1-bromo-3-phenylpropane[1] with the exception that the yield was determined by titration with iodine at room temperature.[3] The product was obtained as a 1.51 M stock solution in DMA (94% yield).

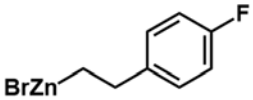

2.22

(4-fluorophenethyl)zinc(II) bromide 2.22. The title compound was prepared according to a reported procedure starting from 1-(3-bromopropyl)-4-fluorobenzene[1] with the exception that the yield was determined by titration with iodine at room temperature.[3] The product was obtained as a 1.92 M stock solution in DMA.

2.8.3 Cross-Coupling Reactions

Table 2.1. Catalytic Competence of Complexes **2.11** and **2.12**.

Entry 1. In a glovebox, $NiBr_2$•glyme (35.3 mg, 0.10 mmol) and 2,6-Bis[((4*R*)-(+)-isopropyl-2-oxazolin-2-yl]pyridine (39.2 mg, 0.13 mmol) were suspended in DMA (1.7 mL) in a 4 mL vial equipped with a stir bar. The resultant heterogenous orange mixture was capped and stirred vigorously. After 15 min, the vial was uncapped and the solution was transferred to a second 4 mL vial containing 1-bromo-5-fluoroindane and stir bar. This vial was capped and sealed with electrical tape, removed from the glovebox, and placed in a 0 °C bath. After 5 min, the alkylzinc bromide reagent (1.1 mL, 1.5M) was added via syringe and the top of the

vial greased. After 24 h of vigorous stirring at 0 °C, the reaction was quenched with EtOH (100 μL). Column chromatography (hexanes → 25%DCM) provided the product as a clear colourless oil, which slowly solidified overtime at ambient temperature. The second run was conducted with 2,6-Bis[((4*S*)-(–)-isopropyl-2-oxazolin-2-yl]pyridine.

The *ee*'s were determined via HPLC using an OJ-H column (eluent: 1% isopropanol in hexanes; flow rate: 0.5 mL/min) with t_r (major): 47.432 min, t_r (minor): 51.745 min:

1st run: 209 mg (74% yield, 92% *ee*). 2nd run: 203 mg (71% yield, 92% *ee*).

^{1}H NMR (500 MHz, Chloroform-*d*) δ 7.16 – 7.02 (m, 3H), 6.94 – 6.77 (m, 4H), 3.79 (s, 3H), 3.11 – 3.02 (m, 1H), 2.88 (ddd, *J* = 16.2, 8.6, 4.7 Hz, 1H), 2.79 (dt, *J* = 16.0, 8.0 Hz, 1H), 2.60 (qdd, *J* = 13.8, 8.4, 6.8 Hz, 2H), 2.36 – 2.24 (m, 1H), 1.83 (dddd, *J* = 12.9, 9.3, 6.6, 4.9 Hz, 1H), 1.76 – 1.61 (m, 3H), 1.49 – 1.35 (m, 1H). ^{13}C NMR (500 MHz, Chloroform-*d*) δ 157.70, 146.13, 142.92, 134.59, 129.25, 124.31, 124.24, 113.72, 113.71, 112.79, 112.61, 111.39, 111.22, 55.25, 43.95, 35.20, 34.71, 32.50, 31.48, 31.46, 29.66.

Entry 2. Entry 2 was set up in an analogous manner to entry 1, with the exception that no additional ligand was added and the (*R*)-*i*PrPybox complex **2.11** in DMA provided a homogeneous midnight purple solution.

1st run: 181 mg (64% yield, 90% *ee*). 2nd run: 188 mg (66% yield, 90% *ee*).

^{1}H NMR spectral data matched the data reported above.

Entry 3. Entry 3 was set up in an analogous manner to entry 1, with the exception that no additional ligand was added and the (*S*)-*i*PrPybox complex **2.12** in DMA provided a homogeneous deep orange/red solution.

1st run: 200 mg (70% yield, 88% *ee*). 2nd run: 200 mg (70% yield, 91% *ee*).

^{1}H NMR spectral data matched the data reported above.

Scheme 2.6. Catalytic competence of 2.17. 1-bromo-6-methoxyindane **2.18** (1.0 mmol, 1.0 M stock solution in DMA) was suspended in additional DMA (150 μL) in a 4 mL vial equipped with a stir bar, in the glovebox coldwell at –40 °C. To this frozen solution, was added (3-phenylpropyl)zinc(II) bromide (1.6 mmol, 1.49 M stock solution in DMA). The frozen solution was capped, sealed with electrical tape, and removed from the glovebox. The reaction mixture was placed in a 0 °C bath and after 1 min of vigorous stirring, (*S*)-*i*PrPybox Ni-alkyl complex **2.17** (0.5 mL, 0.2 M stock solution in DMA) was added via syringe and the vial cap greased. After 24 h at 0 °C, the reaction was quenched with EtOH (100 μL) and tetradecane (260 μL, 1 mmol) was added as an internal standard. Yield was determined by GC analysis (referenced to calibrated tetradecane). Column chromatography (1st column: hexanes → 50%Et_2O; 2nd column on product A: hexanes → 40%DCM; 2nd column on B: hexanes → 50%Et_2O) provided each product in >98% purity (determined by GC) for ee analysis. Both runs were conducted with Ni-alkyl complex bearing (*S*)-*i*PrPybox ligand.[c]

The *ee*'s for product A were determined via HPLC using an OD-H column (eluent: 1% isopropanol in hexanes; flow rate: 0.5 mL/min) with t_r (major): 13.873 min, t_r (minor): 15.852 min.

[c] As a reference, the parent cross-coupling reaction between 1-bromo-6-methoxyindane and (3-phenylpropyl)zinc(II) bromide provided the cross-coupling product in 95% *ee*.

The *ee*'s for product B were determined via SFC using an OD-H column (eluent: 5% methanol in isopropanol; flow rate: 2.5mL/min) with t_r (major): 12.743 min, t_r (minor) 13.803 min.

1st run: product A: 45% GC yield, 91% *ee*, product B: 1% GC yield, 88% *ee*. 2nd run: product A: 45% GC yield, 91% *ee*, product B: 1% GC yield, 90% *ee*.

Product A (authentic sample):

^{1}H NMR (500 MHz, Chloroform-*d*) δ 7.33 – 7.25 (m, 2H), 7.24 – 7.15 (m, 3H), 7.13 – 7.07 (m, 1H), 6.75 – 6.67 (m, 2H), 3.79 (s, 3H), 3.14 – 3.04 (m, 1H), 2.84 (ddd, *J* = 15.0, 8.5, 4.5 Hz, 1H), 2.79 – 2.60 (m, 3H), 2.28 (dtd, *J* = 12.4, 7.9, 4.5 Hz, 1H), 1.94 – 1.83 (m, 1H), 1.82 – 1.63 (m, 3H), 1.52 – 1.40 (m, 1H).

Product B (authentic sample):

^{1}H NMR (500 MHz, Chloroform-*d*) δ 7.84 (dd, *J* = 5.4, 3.1 Hz, 2H), 7.71 (dd, *J* = 5.5, 3.0 Hz, 2H), 7.12 – 7.06 (m, 1H), 6.76 – 6.66 (m, 2H), 3.78 (s, 3H), 3.78 – 3.71 (m, 2H), 3.10 (ddd, *J* = 12.3, 8.5, 6.3 Hz, 1H), 2.88 – 2.69 (m, 2H), 2.28 (dtd, *J* = 12.6, 8.0, 4.8 Hz, 1H), 1.93 – 1.79 (m, 2H), 1.83 – 1.62 (m, 2H), 1.52 – 1.39 (m, 1H).

^{13}C NMR (126 MHz, Chloroform-*d*) δ 168.42 , 148.56 , 135.89 , 133.87 , 132.14 , 124.80, 123.18 , 112.07 , 109.32 , 55.45 , 44.53 , 38.12 , 32.50 , 32.00 , 30.48 , 26.67 .

Scheme 2.7. Stoichiometric reaction between complex 2.17 and 1-bromo-6-methoxyindane 2.18. In a glovebox, (*R*)-*i*PrPybox-**2.17** (54.8 mg, 0.10 mmol) was suspended in DMA (2.65 mL) in a 4 mL vial equipped with a stir bar. The resultant homogeneous brown mixture was capped, sealed with tape, removed from the glovebox, and placed in a 0 °C bath. After 3 min, 1-bromo-6-methoxyindane (100 μL, 1.0 M stock in DMA)

was added via syringe and the cap greased. After 24 h of vigorous stirring at 0 °C, the reaction was quenched with EtOH (100 μL). Column chromatography (hexanes → 50%Et_2O) provided the product as a clear colourless oil, which slowly solidified overtime at ambient temperature. The second run was conducted with 2,6-Bis[((4*S*)-(–)-isopropyl-2-oxazolin-2-yl]pyridine bound Ni–alkyl. 1st run: 24% GC yield, 93% *ee*. 2nd run: 23% GC yield, 91% *ee*.

*2.8.4 Spectroscopic Studies of NiBr (**2.11**)*

*Transmetalation of Complex **2.11** with (4-fluorophenethyl)zinc(II) bromide*

EPR Study of Complex 2.11 with (4-fluorophenethyl)zinc(II) bromide. (+)-*i*PrPybox **2.11** (400 μL, 0.05 M stock solution in DMA) was suspended in an EPR tube equipped with a 14/20 joint, in the glovebox coldwell at 0 °C, and additional DMA (150 μL) was added. To this solution, (4-fluorophenethyl)zinc(II) bromide (10.4 μL, 1.92 M stock solution in DMA) was added, the EPR tube fitted with a stopcock, removed from the glovebox, and frozen in liquid nitrogen for an initial EPR spectrum collected at 77K (above left). The EPR tube was then carefully warmed to 0 °C. After 1 h, the EPR tube was again frozen in liquid nitrogen and a final EPR spectrum collected at 77K (above right).

^{19}F NMR Study of Complex 2.11 with (4-fluorophenethyl)zinc(II) bromide 2.22. Ni Br (2.11) (316 μL, 0.05 M stock solution in DMA) was suspended in a piercable screw cap NMR tube in the glovebox coldwell at –15 °C and additional DMA (520 μL) was added. The NMR tube was sealed, removed from the glovebox quickly, wrapped with parafilm, and placed in a –15 °C dry ice/acetone bath. An initial NMR timepoint was collected at 0 °C. To this solution at –15 °C, the alkylzinc reagent (8.2 μL, 1.92 M stock solution in DMA) was quickly added and the top of the NMR cap greased. The NMR tube was rapidly inverted 3

times followed by temperature equilibration at –15 °C in a dry ice/acetone bath. After 1 min, the NMR tube was quickly put into the NMR probe and data collected at 0 °C.

UV-vis Study of Complex 2.11 with (4-fluorophenethyl)zinc(II) bromide (Figure 2.8). (+)-*i*PrPybox-**2.11** (300 μL, 2.6 mM stock solution in DMA) was suspended in a cuvette containing DMA (2.7 mL) and a stir bar in the glovebox. The cuvette was fitted with a septum cap, removed from the glovebox, and an initial UV-vis spectrum collected at 0 °C. (4-fluorophenethyl)zinc(II) bromide (20 μL, 39 mM stock solution in DMA) was added in one shot via syringe and data collection started. Consumption of the NiBr complex was monitored by following the absorbance at 870 nm over time

*Oxidation of complex **2.1-NiBr** with electrophiles*

EPR Study of Complex 2.11 with 1-bromoindane. (+)-*i*PrPybox-**2.11** (8.8 mg, 0.02 mmol) was suspended in DMA (560 μL) in a 4 mL vial, in the glovebox coldwell at -15 °C. This resultant midnight purple/blue solution was taken up via syringe and quickly added to a vial containing 1-bromoindane (39.4 mg, 0.20 mmol) at -15 °C. The reaction mixture turned orange instantaneously. After 1 min, a portion of the reaction mixture was aliquotted to an EPR tube equipped with a 14/20 joint. The EPR tube was fitted with a stopcock, removed from the glovebox, and frozen in liquid nitrogen to provide the above EPR spectrum at 77K.

^{1}H NMR Study of Complex 2.11 with 1-bromoindane. To a midnight purple solution of (–)-*i*PrPybox-**2.11** in DMA (200 μL), 1-bromoindane (39.4 mg, 0.20 mmol) in C_6D_6 (500 μL) was added at ambient temperature. The reaction mixture turned orange instantaneously.

GC Study of Complex 2.11 with 1-bromoindane. To a 4 mL vial containing 1-bromoindane (39.4 mg, 0.20 mmol), a midnight purple solution of (–)-*i*PrPybox-**2.11** in DMA (500 μL) was added at ambient temperature. The reaction mixture turned orange instantaneously and was filtered through an acrodisc. The reaction vessel was removed from the glovebox, diluted with EtOAc, and the organic product distribution subjected to GC analysis.

UV-Vis Study of Complex 2.11 with 1-bromo-5-fluoroindane (Figure 2.9). (+)-*i*PrPybox-**2.11** (300 μL, 2.6 mM stock solution in DMA) was suspended in a cuvette containing DMA (2.7 mL) and a stir bar in the glovebox. The cuvette was fitted with a septum cap, removed from the glovebox, and an initial UV-vis spectrum collected at 0 °C. 1-bromo-5-fluoroindane **2.13** (20 μL, 39 mM stock solution in DMA) was added in one shot via syringe and data collection started. Consumption of the NiBr complex was monitored by following the absorbance at 870 nm over time

UV-Vis Study of Complex 2.11 with cyclopentyl bromide (Figure 2.10). (+)-*i*PrPybox-**2.11** (300 μL, 2.6 mM stock solution in DMA) was suspended in a cuvette containing DMA (2.7 mL) and a stir bar in the glovebox. The cuvette was fitted with a septum cap, removed from the glovebox, and an initial UV-vis spectrum collected at 0 °C. Cyclopentyl bromide (20 μL, 39 mM stock solution in DMA) was added in one shot via syringe and data collection started. Consumption of the NiBr complex was monitored by following the absorbance at 870 nm over time

2.8.5 Miscellaneous EPR Studies

Figure 2.11 (a). 77K EPR experiment of 2.12 and (3-(4-methoxyphenyl)propyl)zinc(II) bromide 2.14 in DMA (Stoichiometric reaction). 2.12 (10.4 mg, 0.02 mmol) was suspended in DMA (540 μL) in an EPR tube equipped with a 14/20 joint in the glovebox coldwell at –15 °C. **2.14** (13 μL, 1.57 M in DMA) was added. After 2 min, the EPR tube was sealed with a stopcock, removed quickly from the glovebox, carefully placed in a liquid nitrogen bath, and a 77K EPR spectrum collected. Experimental parameters; Microwave power, 2.046 mW; microwave frequency, 9.398 GHz; modulation amplitude, 2 G; gain, 5020; time constant, 40.960.

Figure 2.11 (b). 77K EPR experiment of 2.12 and (3-(4-methoxyphenyl)propyl)zinc(II) bromide 2.14 in DMA (simulating catalytic conditions). 2.12 (10.4 mg, 0.02 mmol) was suspended in DMA (345 μL) in an EPR tube equipped with a 14/20 joint in the glovebox coldwell at –15 °C. **2.14** (205 μL, 1.57 M in DMA) was added. After 2 min, the EPR tube was sealed with a stopcock, removed quickly from the glovebox, carefully placed in a liquid nitrogen bath, and a 77K EPR spectrum collected. Experimental parameters; Microwave power, 2.041 mW; microwave frequency, 9.400 GHz; modulation amplitude, 2 G; gain, 5020; time constant, 40.960.

General procedure for cross-coupling reactions monitored by EPR (Figure 2.12, a–c): Ni catalyst (0.02 mmol) [and ligand (7.8 mg, 0.026 mmol) when applicable] was suspended in DMA (345 μL) in a 4 mL vial in the glovebox coldwell at –15 °C. This solution was added

to a 4 mL vial containing **2.13** (43.0 mg, 0.20 mmol) equipped with a stirbar. The resultant mixture was removed from the coldwell and stirred at ambient temperature for 2 min. The reaction mixture was then rechilled in the glovebox coldwell at –15 °C and the alkylzinc reagent **2.14** (205 μL, 1.57 M in DMA) was added. After 25 min, a portion of the reaction was aliquoted to an EPR tube containing a 14/20 joint, sealed with a stopcock, removed quickly from the glovebox, carefully placed in a liquid nitrogen bath, and a 77K EPR spectrum collected. (a) Experimental parameters; Microwave power, 2.041 mW; microwave frequency, 9.398 GHz; modulation amplitude, 2 G; gain, 5020; time constant, 40.960. (b) Experimental parameters; Microwave power, 2.036 mW; microwave frequency, 9.399 GHz; modulation amplitude, 2 G; gain, 5020; time constant, 40.960. (c) Experimental parameters; Microwave power, 2.041 mW; microwave frequency, 9.397 GHz; modulation amplitude, 2 G; gain, 5020; time constant, 40.960.

77K EPR experiment of Ni-Alkyl (2.17) and Umemoto's Reagent (Figure 2.13). To a solution of complex **2.17** (40.0 mg, 0.073 mmol) in benzene (1.5 mL) was added Umemoto's reagent (80 μL, 1.0 M in DMA). After 1 min, the crude reaction mixture was filtered through celite, and the benzene lyophilized. The resultant red oil was taken up in toluene and aliquoted to an EPR tube equipped with a 14/20 joint, sealed with a stopcock, removed quickly from the glovebox, and carefully placed in a liquid nitrogen bath, after which a 77K EPR spectrum was collected. Experimental parameters; Microwave power, 2.051 mW; microwave frequency, 9.396 GHz; modulation amplitude, 2 G; gain, 5020; time constant, 40.960.

2.9 References

1. Diederich, F.; Stang, P. J., *Metal-Catalyzed Cross-Coupling Reactions*. Wiley-VCH: New York, 1998.
2. Hartwig, J. F., *Organotransition Metal Chemistry: From Bonding to Catalysis* University Science Books: Mill Valley, 2010.
3. Johansson Seechurn, C. C. C.; Kitching, M. O.; Colacot, T. J.; Snieckus, V. *Angew. Chem. Int. Ed.* **2012,** *51*, 5062.
4. Heck, R. F.; Nolley, J. P. *J. Org. Chem.* **1972,** *37*, 2320.
5. Negishi, E.; King, A. O.; Okukado, N. *J. Org. Chem.* **1977,** *42*, 1821.
6. Miyaura, N.; Yamada, K.; Suzuki, A. *Tetrahedron Lett.* **1979,** *20*, 3437.
7. Devasagayaraj, A.; Stüdemann, T.; Knochel, P. *Angew. Chem. Int. Ed.* **1996,** *34*, 2723.
8. Cárdenas, D. J. *Angew. Chem. Int. Ed.* **1999,** *38*, 3018.
9. Cárdenas, D. J. *Angew. Chem. Int. Ed.* **2003,** *42*, 384.
10. Netherton, M. R.; Dai, C.; Neuschütz, K.; Fu, G. C. *J. Am. Chem. Soc.* **2001,** *123*, 10099.
11. Netherton, M. R.; Fu, G. C. *Angew. Chem. Int. Ed.* **2002,** *41*, 3910.
12. Hills, I. D.; Netherton, M. R.; Fu, G. C. *Angew. Chem. Int. Ed.* **2003,** *42*, 5749.
13. Powell, D. A.; Maki, T.; Fu, G. C. *J. Am. Chem. Soc.* **2005,** *127*, 510.
14. Fischer, C.; Fu, G. C. *J. Am. Chem. Soc.* **2005,** *127*, 4594.
15. Saito, B.; Fu, G. C. *J. Am. Chem. Soc.* **2008,** *130*, 6694.
16. Dai, X.; Strotman, N. A.; Fu, G. C. *J. Am. Chem. Soc.* **2008,** *130*, 3302.
17. Lundin, P. M.; Esquivias, J.; Fu, G. C. *Angew. Chem. Int. Ed.* **2009,** *48*, 154.
18. Lou, S.; Fu, G. C. *J. Am. Chem. Soc.* **2010,** *132*, 1264.
19. Lou, S.; Fu, G. C. *J. Am. Chem. Soc.* **2010,** *132*, 5010.
20. Lundin, P. M.; Fu, G. C. *J. Am. Chem. Soc.* **2010,** *132*, 11027.
21. Kambe, N.; Iwasaki, T.; Terao, J. *Chem. Soc. Rev.* **2011,** *40*, 4937.
22. Binder, J. T.; Cordier, C. J.; Fu, G. C. *J. Am. Chem. Soc.* **2012,** *134*, 17003.
23. Choi, J.; Fu, G. C. *J. Am. Chem. Soc.* **2012,** *134*, 9102.
24. Choi, J.; Fu, G. C. *Science* **2017,** *356*.
25. Pearson, R. G.; Figdore, P. E. *J. Am. Chem. Soc.* **1980,** *102*, 1541.
26. Ishiyama, T.; Abe, S.; Miyaura, N.; Suzuki, A. *Chem. Lett.* **1992,** *21*, 691.
27. Bissember, A. C.; Levina, A.; Fu, G. C. *J. Am. Chem. Soc.* **2012,** *134*, 14232.
28. Kirchhoff, J. H.; Netherton, M. R.; Hills, I. D.; Fu, G. C. *J. Am. Chem. Soc.* **2002,** *124*, 13662.
29. Arp, F. O.; Fu, G. C. *J. Am. Chem. Soc.* **2005,** *127*, 10482.
30. Awano, T.; Ohmura, T.; Suginome, M. *J. Am. Chem. Soc.* **2011,** *133*, 20738.
31. Labadie, J. W.; Stille, J. K. *J. Am. Chem. Soc.* **1983,** *105*, 6129.
32. Hatanaka, Y.; Hiyama, T. *J. Am. Chem. Soc.* **1990,** *112*, 7793.
33. Ye, J.; Bhatt, R. K.; Falck, J. R. *J. Am. Chem. Soc.* **1994,** *116*, 1.
34. Ridgway, B. H.; Woerpel, K. A. *J. Org. Chem.* **1998,** *63*, 458.
35. Matos, K.; Soderquist, J. A. *J. Org. Chem.* **1998,** *63*, 461.
36. Boudier, A.; Darcel, C.; Flachsmann, F.; Micouin, L.; Oestreich, M.; Knochel, P. *Chem. Eur. J.* **2000,** *6*, 2748.
37. Campos, K. R.; Klapars, A.; Waldman, J. H.; Dormer, P. G.; Chen, C.-y. *J. Am. Chem. Soc.* **2006,** *128*, 3538.

38. Taylor, B. L. H.; Jarvo, E. R. *J. Org. Chem.* **2011,** *76*, 7573.
39. Bock, P. L.; Boschetto, D. J.; Rasmussen, J. R.; Demers, J. P.; Whitesides, G. M. *J. Am. Chem. Soc.* **1974,** *96*, 2814.
40. Wang, Y.; Huang, B.; Sheng, S.; Cai, M. *J. Chem. Res.* **2007,** *2007*, 728.
41. Hundertmark, T.; Littke, A. F.; Buchwald, S. L.; Fu, G. C. *Org. Lett.* **2000,** *2*, 1729.
42. Nelson, J. E.; Parkin, G.; Bercaw, J. E. *Organometallics* **1992,** *11*, 2181.
43. Buchwald, S. L.; LaMaire, S. J.; Nielsen, R. B.; Watson, B. T.; King, S. M. *Tetrahedron Lett.* **1987,** *28*, 3895.
44. Hartley, F. R.; Patai, S., *The Nature and Cleavage of Metal-Carbon Bonds*. Wiley: New York, 1985; Vol. 2.
45. Ananikov, V. P. *ACS Catalysis* **2015,** *5*, 1964.
46. Schley, N. D.; Fu, G. C. *J. Am. Chem. Soc.* **2014,** *136*, 16588.
47. Zimmermann, P.; Limberg, C. *J. Am. Chem. Soc.* **2017,** *139*, 4233.
48. Lin, C.-Y.; Power, P. P. *Chem. Soc. Rev.* **Advanced**.
49. Anderson, T. J.; Jones, G. D.; Vicic, D. A. *J. Am. Chem. Soc.* **2004,** *126*, 8100.
50. Jones, G. D.; McFarland, C.; Anderson, T. J.; Vicic, D. A. *Chem. Commun.* **2005**, 4211.
51. Jones, G. D.; Martin, J. L.; McFarland, C.; Allen, O. R.; Hall, R. E.; Haley, A. D.; Brandon, R. J.; Konovalova, T.; Desrochers, P. J.; Pulay, P.; Vicic, D. A. *J. Am. Chem. Soc.* **2006,** *128*, 13175.
52. Breitenfeld, J.; Ruiz, J.; Wodrich, M. D.; Hu, X. *J. Am. Chem. Soc.* **2013,** *135*, 12004.
53. Biswas, S.; Weix, D. J. *J. Am. Chem. Soc.* **2013,** *135*, 16192.
54. Hegedus, L. S.; Miller, L. L. *J. Am. Chem. Soc.* **1975,** *97*, 459.
55. Eaborn, C.; Hill, M. S.; Hitchcock, P. B.; Smith, J. D. *Chem. Commun.* **2000**, 691.
56. Kitiachvili, K. D.; Mindiola, D. J.; Hillhouse, G. L. *J. Am. Chem. Soc.* **2004,** *126*, 10554.
57. Laskowski, C. A.; Bungum, D. J.; Baldwin, S. M.; Del Ciello, S. A.; Iluc, V. M.; Hillhouse, G. L. *J. Am. Chem. Soc.* **2013,** *135*, 18272.
58. Baidya, N.; Olmstead, M. M.; Mascharak, P. K. *J. Am. Chem. Soc.* **1992,** *114*, 9666.
59. Tang, F.; Rath, N. P.; Mirica, L. M. *Chem. Commun.* **2015,** *51*, 3113.
60. Zhang, C.-P.; Wang, H.; Klein, A.; Biewer, C.; Stirnat, K.; Yamaguchi, Y.; Xu, L.; Gomez-Benitez, V.; Vicic, D. A. *J. Am. Chem. Soc.* **2013,** *135*, 8141.
61. Ciszewski, J. T.; Mikhaylov, D. Y.; Holin, K. V.; Kadirov, M. K.; Budnikova, Y. H.; Sinyashin, O.; Vicic, D. A. *Inorg. Chem.* **2011,** *50*, 8630.
62. Xiong, T.; Li, Y.; Mao, L.; Zhang, Q.; Zhang, Q. *Chem. Commun.* **2012,** *48*, 2246.
63. Do, H.-Q.; Bachman, S.; Bissember, A. C.; Peters, J. C.; Fu, G. C. *J. Am. Chem. Soc.* **2014,** *136*, 2162.
64. Krasovskiy, A.; Knochel, P. *Synthesis* **2006,** *2006*, 0890.

C h a p t e r 3

N_2-TO-NH_3 CONVERSION BY A TRIPHOS-IRON CATALYST AND ENHANCED TURNOVER UNDER PHOTOLYSIS

Buscagan, T. M. et al. (2017). "N_2-to-NH_3 Conversion by a Triphos-Iron Catalyst and Enhanced Turnover Under Photolysis". In: *Angew. Chem. Int. Ed.* **2017**, *56*, 6921–6926. doi: 10.1042/BJ20150183. Some additional unpublished work is included herein.

3.1 Introduction

Bridging iron hydrides are proposed to form at the active site of MoFe-nitrogenase during catalytic dinitrogen reduction to ammonia and may be key in the binding and activation of N_2 via reductive elimination of H_2. This possibility inspires the investigation of well-defined molecular iron hydrides as precursors for catalytic N_2-to-NH_3 conversion. Herein, we describe the synthesis and characterization of new $P_2^{PPh}Fe(N_2)(H)_x$ systems that are active for catalytic N_2-to-NH_3 conversion. Most interestingly, we show that the yields of ammonia can be significantly increased if the catalysis is performed in the presence of mercury lamp irradiation. Evidence is provided to suggest that photo-elimination of H_2 is one means by which the enhanced activity may arise.

Biological nitrogen reduction is catalyzed by nitrogenase enzymes and the active site of the most well-studied MoFe-nitrogenase, the FeMo-cofactor (FeMoco), contains seven iron centers and one molybdenum center (Figure 3.1, top).[1-3] Interest in understanding the mechanism/s of biological nitrogen fixation has inspired many biochemical,[4-6] spectroscopic,[7-8] theoretical,[9] and synthetic model studies.[10-20] While a wealth of insight has been gained, a detailed atomic level understanding of biological nitrogen fixation is yet to be resolved.

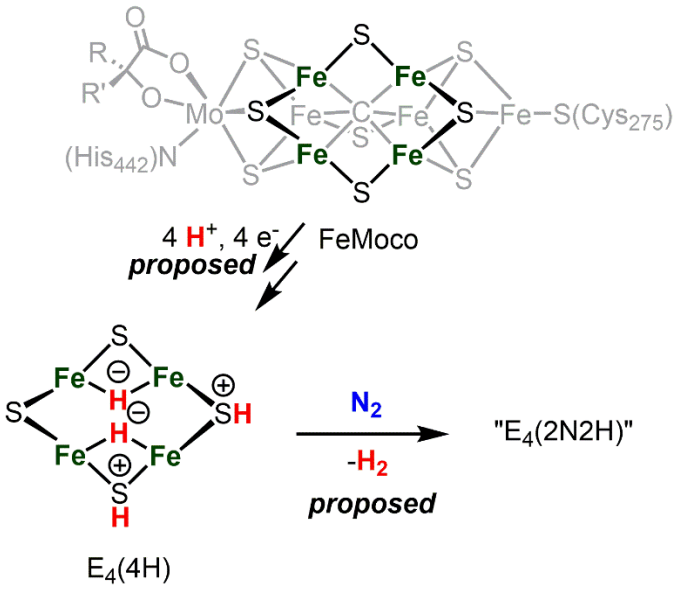

Figure 3.1. (Top) The FeMoco active site of MoFe-nitrogenase.[6] (Bottom) Conversion of a proposed $E_4(4H)$ intermediate state of FeMoco to an activated E_4 state with N_2 bound.[21]

Iron is the only metal present in all three of the known nitrogenases (MoFe-, VFe-, FeFe-nitrogenase) and heterogeneous iron catalysts are among the most common in the industrial Haber-Bosch process.[22] These facts have motivated our group and others to develop single (or multiple) site Fe complexes that can bind and activate dinitrogen.[15,17,18,23-27] To this end, we have reported the catalytic reduction of nitrogen to ammonia using Fe complexes supported by a tetradentate P_3^E ligand scaffold (E = B, C, or Si).[17, 20, 28-32] Using the P_3^BFe catalyst, significant turnover to generate NH_3 has been demonstrated.[20,32] Other Fe systems supported by carbene and phosphine ligands have also shown efficacy for catalytic N_2-to-NH_3 conversion in recent reports.[15,18] Freeze quench ^{57}Fe Mössbauer spectroscopic studies of a catalytic reaction using our P_3^BFe$(N_2)^-$ system

have shown that a significant amount of the iron is tied up as an iron hydride-borohydride complex, $(P_3^B)(\mu\text{-}H)Fe(N_2)(H)$, believed to be an off-path state of the system;[20] this species can presumably convert back to an on-path $P_3^BFe(N_2)^{\{0,1-\}}$ species via formal H_2 loss under turnover conditions.

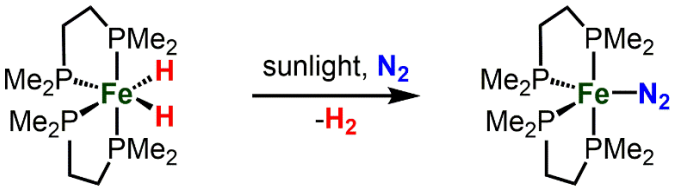

Scheme 3.1. Reductive elimination of H_2 from a polyphosphine iron complex in the presence of N_2 and sunlight leads to an activated $Fe(N_2)$ complex.[36-39]

Bridging hydride ligands have been proposed to accumulate at the FeMoco under turnover conditions ("$E_4(4H)$ state", Figure 3.1, bottom) and may be key in the binding and activation of N_2 via reductive elimination of H_2.[3,21,33-35a] Recently, photochemically induced loss of H_2 from a presumed E4 state of the FeMoco has been suggested.[35] The likelihood that M-H species may serve as common intermediates and/or side products of catalytic nitrogen fixation,[21] motivates further studies of iron hydrides using well-defined molecular systems that fix N_2. In this latter context, molecular $Fe(H)_x$ complexes bearing terminal hydride ligands have been reported to undergo photosubstitution of N_2 with concomitant release of H_2 (Scheme 3.1).[36-38] In addition, $Fe(H)_x$ (x = 2 or 3) complexes are known that readily lose H_2 upon exposure to N_2.[36, 39-40]

To expand the structural diversity of synthetic iron hydride catalysts capable of catalytic N_2-to-NH_3 conversion,[15,17,18,20] we targeted a triphosphine ligand that supports reactive $Fe(N_2)(H)_x$ fragments. Herein, we report the synthesis of a dinuclear $[Fe^{I}(H)]_2(\mu\text{-}N_2)$ complex supported by a trisphosphine ligand, P_2^{Ph} (Figure 3.2), that is a catalyst for N_2-to-NH_3 conversion in the presence of $[H(OEt_2)_2][BAr^F_4]$ ($HBAr^F_4$, BAr^F_4 = tetrakis(3,5-bis(trifluoromethyl)phenyl)borate) and potassium graphite (KC_8). Of primary interest is that significantly enhanced ammonia yields (as much as ~180% increase) are observed under Hg lamp irradiation. Based on this observation, we also examine the previously reported, $P_3^BFe(N_2)^-$ catalyst system (Figure 3.2)[17,20] and show that it too gives significantly higher catalytic turnover (by ~50%) under Hg lamp photolysis.

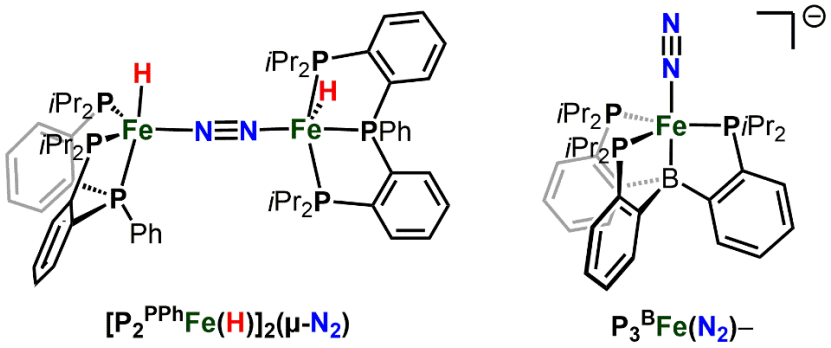

Figure 3.2. The new diiron(I)-μ-N_2 catalyst (left) and previously reported $P_3^BFe(N_2)^-$ provide higher yields of ammonia under Hg lamp photolysis.

3.2 Results and Discussion

3.2.1 Synthesis of Fe(N_2)(H)$_x$ Complexes Supported by a Novel P_2^{PPh} Ligand

Synthesis of P_2^{PPh}Fe complexes. P_2^{PPh} (**3.1**) was synthesized by the addition of phenyl Grignard to the known bis(*o*-diisopropylphosphino-phenyl)-chlorophosphine[41] and exhibits two overlapping doublets centered at δ = -2.2 ppm and two overlapping triplets at δ = -14.3 ppm by ^{31}P NMR spectroscopy, suggesting a mixture of rotamers. Complexation of **3.1** with one equivalent of $FeBr_2$ yielded paramagnetic $P_2^{PPh}FeBr_2$ **3.2** as a purple-black crystalline solid (87% yield, Scheme 3.2). The solid-state structure of **3.2-FeBr$_2$** shows a distorted trigonal bipyramidal geometry at iron with τ_5 = 0.54 (see appendix).[42] The solution magnetism of **3.2-FeBr$_2$** indicates spin equilibria, with solution magnetic moments of 3.40μ_B at 200 K and 4.29μ_B at 328 K. The $^{57}FeCl_2$ complex (**3.2-^{57}FeCl$_2$**) was analogously synthesized and exhibits similar solution magnetism. The solid-state Mössbauer spectrum of the $^{57}FeCl_2$ complex was collected (see appendix) and gives rise to two quadrupole doublets: a minor $S = 2$ species ($\delta = 0.85$ mm s^{-1} and $\Delta E_Q = 2.74$ mm s^{-1}) and a major $S = 1$ component ($\delta = 0.53$ mm s^{-1} and $\Delta E_Q = 0.62$ mm s^{-1}).

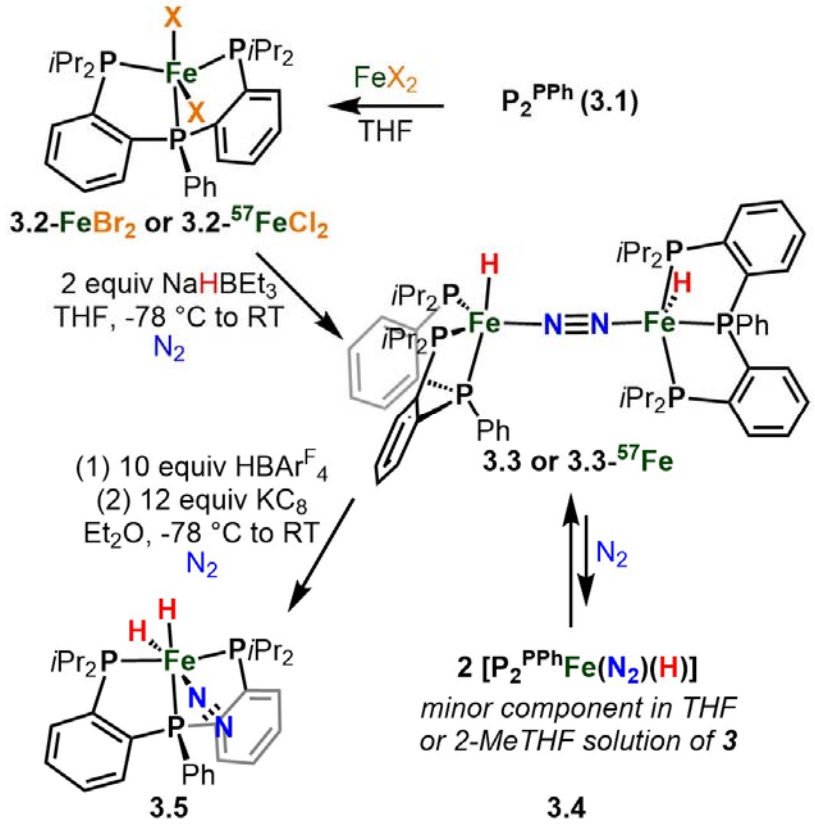

Scheme 3.2. Synthesis of Fe complexes discussed herein.

$[P_2^{PPh}Fe(H)]_2(\mu\text{-}N_2)$ synthesis and characterization. Treatment of **3.2-FeBr$_2$** with two equivalents of $NaHBEt_3$ in THF at low temperature under an N_2 atmosphere provided the diamagnetic, diiron(I) species $[P_2^{PPh}Fe(H)]_2(\mu\text{-}N_2)$ **3.3** as a green-black crystalline solid (64% yield, Scheme 3.2). The solid-state structure of **3.3** shows end-on N_2 binding between the two iron centers (N-N distance of 1.15 Å; Figure 3.3a). While the hydride ligands (one hydride ligand per Fe center) could not be located in the Fourier difference map, their presence was confirmed by IR spectroscopy. The Fe-D analogue, **3.3D**, was synthesized using $LiDBEt_3$ in toluene. Infrared spectra of solid **3.3** and **3.3D** exhibit expected peak shifts in the Fe-H(D) vibrations from 1833 and 1734 cm^{-1} for **3.3** to 1324 cm^{-1} and 1256 cm^{-1} for

3.3D (see appendix), consistent with the predicted values calculated from a simple harmonic oscillator model (1309 cm^{-1} and 1237 cm^{-1}). While **3.3** does not feature a rigorous inversion center in the solid state, its ν(NN) vibration is expected to be very weak and is not discernable in the recorded IR spectra. Additional evidence for the presence of the hydride ligands was gained by treatment of **3.3** with two equiv of methyl triflate, which led to the formation of methane in 97% yield as measured by gas chromatography (GC).

Dinuclear **3.3** populates a low spin singlet ground state, as discerned by the ^{1}H NMR spectrum (see appendix), presumably due to antiferromagnetic exchange between two S = 1/2 centers. This scenario contrasts that of a related diiron(I) linear-N_2-bridged system supported by tris(phosphine)borate ligands ([$PhBP_3$]Fe)$_2$(μ-N_2), where the ground spin state is instead S = 3 from weak ferromagnetic coupling between two S = 3/2 centers.[43] The local low spin environment of each iron center in **3.3** is derived from the presence of a strong-field hydride ligand and its 5-coordinate environment. The Fe-P distances in **3.3** are notably shorter (Fe-P_{avg} = 2.16 Å) than those in high spin ([$PhBP_3$]Fe)$_2$(μ-N_2) (ranging from 2.34 to 2.39 Å), reflecting its low spin iron centers.

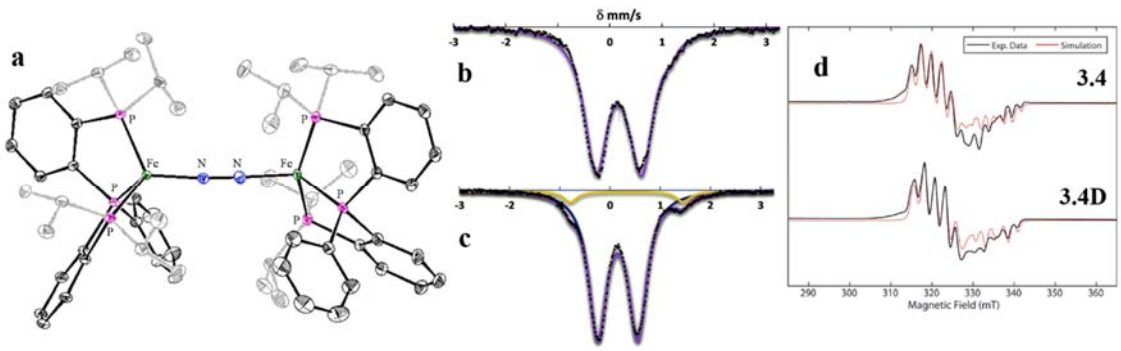

Figure 3.3. (a) X-ray structure of **3.3** with displacement ellipsoids shown at 50% probability (solvent and second dinuclear Fe molecule not shown; minor component of disordered isopropyl groups omitted for clarity). (b) The 80 K, 50 mT solid-state ^{57}Fe Mössbauer spectrum of **3.3**. Data represented by black points, simulation represented by purple line. (c) The 80 K, 50 mT ^{57}Fe Mössbauer spectrum of a 2-MeTHF solution of **3.3**. Major S = 0 component represented with a blue line, and minor S = 1/2 component represented by a yellow line. (d) X-band Continuous Wave (CW) EPR spectra (black) of **3.4** (top trace) and **3.4D** (bottom trace) in 2-MeTHF with simulations of each (red).

Whereas the 80 K solid-state Mössbauer spectrum of **3.3** in a parallel magnetic field (50 mT) shows only one quadrupole doublet (δ = 0.15 mm s^{-1} and ΔE_Q = 0.78 mm s^{-1}), consistent with a single S = 0 species (Figure 3.3b), a Mössbauer spectrum of **3.3** obtained as a 2-MeTHF glass instead shows the clear presence of two distinct quadrupole doublets in approximately a 95:5 ratio. The major component is fit satisfactorily with parameters for **3.3** (δ = 0.15 mm s^{-1} and ΔE_Q = 0.80 mm s^{-1}). The minor component is fit with the parameters δ = 0.34 mm s^{-1} and ΔE_Q = 2.25 mm s^{-1}, similar to S = 1/2 phosphine-iron compounds we have previously characterized (Figure 3.3c).[20] The 77 K X-band EPR spectrum of **3.3** in 2-MeTHF confirms the presence of a Kramer's doublet signal, consistent with the presence of a low spin S = 1/2 species [$P_2^{PPh}Fe(N_2)(H)$] (Figure 3.3d). These data suggest that, in solution under nitrogen, dinuclear **3.3** partially dissociates into two [$P_2^{PPh}Fe(N_2)(H)$] species, **3.4** (Scheme 3.2).

To confirm the identity of the minor S = 1/2 solution component **3.4**, we performed Q-band (33.7 GHz) Davies ENDOR on 2-MeTHF solutions of both **3.3** and the isotoplogue **3.3D** (see appendix). This study confirms the presence of two ^{31}P nuclei with similar hyperfine couplings ($^{31}P1$ A = [70 70 62] MHz, $^{31}P2$ A = [76 76 66] MHz) in addition to a third, more strongly coupled ^{31}P nucleus ($^{31}P3$ A = [142 144 158] MHz). A large ^{1}H coupling (^{1}H A = [18 64 52] MHz), consistent with a metal-bound hydride, is observed in the natural abundance sample and is of greatly reduced intensity in the sample containing the **3.4D** isotopologue (Figure 3.4a). Davies ENDOR was also acquired using pulse parameters optimized for detection of deuterium hyperfine couplings, and here only the **3.4D** sample shows ^{2}D ENDOR signals from a bound deuteride (Figure 3.4b), which are

well simulated by simply scaling the ^{1}H hyperfine values for the hydride by the gyromagnetic ratios of ^{2}D and ^{1}H ($\gamma = g_n(^{2}D)/g_n(^{1}H) = 0.1535$). The X-band CW EPR (Figure 3.3d) and Q-band electron spin-echo detected EPR (ESE-EPR) (see appendix) of **3.4** and **3.4D** in 2-MeTHF are well-simulated using the ^{31}P, ^{1}H and ^{2}D hyperfine values determined from the ENDOR spectra with g = [2.0980 2.0900 2.0019].

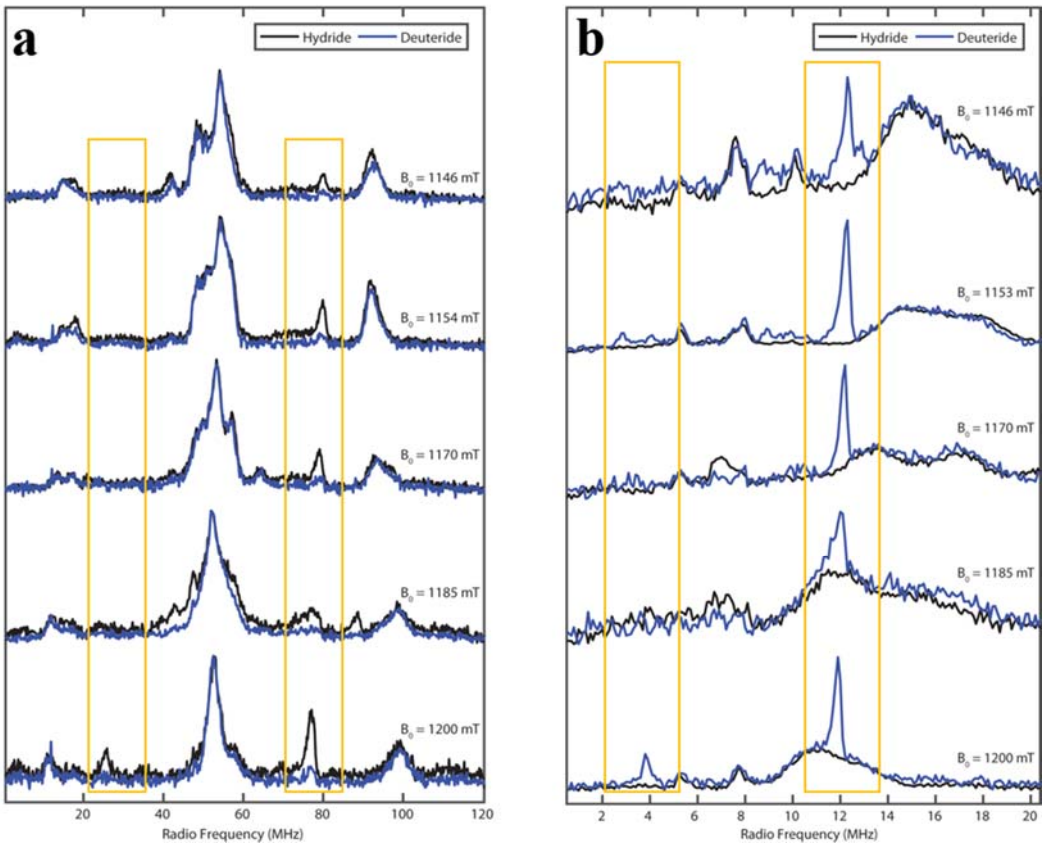

Figure 3.4. ENDOR spectra of **3.4** and **3.4D** in 2-MeTHF: (a) Comparison of field-dependent Q-band ^{1}H Davies ENDOR of **3.4** (black) and **3.4D** (blue). (b) Comparison of field-dependent Q-band ^{2}D Davies ENDOR of **3** (black) and **3-D** (blue).

3.2.2 Catalytic N_2-to-NH_3 Reduction with Light Enhancement

Table 3.1. Catalytic dinitrogen reduction to ammonia with synthetic iron complexes.[a]

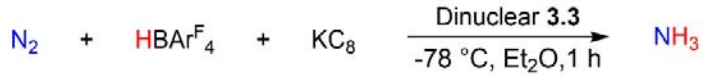

	Variation	$HBAr^F_4$ (equiv)	KC_8 (equiv)	Mean ± SD (equiv NH_3)
1	None	300	360	7.5 ± 0.8
2[b]	Overnight	300	360	8.7 ± 0.7
3	Hg Lamp	300	360	18.1 ± 0.8
4[b]	Blue LED	300	360	21.3 ± 0.4
5[b]	P_2^{PPh}, no Fe	150	180	<0.1
6[b]	P_2^{PPh}, no Fe, Hg Lamp	150	180	<0.1
7[b]	2-MeTHF instead of Et_2O	300	360	0.5 ± 0.3
8	None	3000	3600	24.5 ± 1.2
9	Hg Lamp	3000	3600	66.7 ± 4.4
10[b]	**3.5** instead of **3.3**	150	180	2.6 ± 0.1
11[b]	**3.5** instead of **3.3**, Hg Lamp	150	180	8.9 ± 0.9
12	$P_3^BFe(N_2)^-$ instead of **3.3**	1500	1800	60.0 ± 3.7
13	$P_3^BFe(N_2)^-$ instead of **3.3**, Hg Lamp	1500	1800	88.1 ± 8.0
14[b,c]	$(P_3^B)(\mu\text{-H})Fe(N_2)(H)$ instead of **3.3**	150	180	6.0 ± 0.3
15[b,c]	$(P_3^B)(\mu\text{-H})Fe(N_2)(H)$ instead of **3.3**, Hg lamp	150	180	8.5 ± 1.0

[a] All entries are an average of 3 runs unless otherwise noted.
[b] average of 2 runs
[c] Hydrazine was also detected (see main text).
Note: Ammonia yields are reported per complex.

Catalysis. Using $HBAr^F_4$ as the acid and KC_8 as the reductant, $[P_2^{PPh}Fe(H)]_2(\mu\text{-}N_2)$ catalyzed the reduction of N_2 to NH_3 at -78 °C in Et_2O and achieved turnovers of 7.5 ± 0.8 equivalents of NH_3 per complex in the presence of 300 equiv acid and 360 equiv reductant (150 and 180 equiv per Fe, respectively; Table 3.1, entry 1). Allowing the reaction to stir longer did not lead to an increase in yield (entry 2). These results establish catalytic turnover for this new iron catalyst system; its efficiency is not as high as for the $P_3^BFe(N_2)^-$ catalyst, where the

presence of substantially less acid/reductant was needed to achieve a similar amount of NH_3. We wondered whether light might improve the yield of ammonia, and employed a Hg lamp to test this possibility. We reasoned that photolysis during catalysis might enhance the break-up of $[P_2^{PPh}Fe(H)]_2(\mu\text{-}N_2)$ to a more catalytically active state, for example the $[P_2^{PPh}Fe(N_2)(H)]$ monomer discussed above, and/or might cause H_2 elimination from less active states, such as the dihydride complex $P_2^{PPh}Fe(N_2)(H)_2$ **3.5** that is discussed below. We were gratified to observe that significantly more ammonia was formed (18.1 ± 0.8 equiv NH_3; ~140% improvement in overall yield at the same loading) under Hg lamp photolysis conditions (entry 3). The catalysis was also enhanced in the presence of a Blue LED (21.3 ± 0.4 equiv NH_3, entry 4). When the reaction was performed with the P_2^{PPh} ligand and no Fe (entries 5 and 6), no NH_3 was detected regardless of mercury lamp photolysis. The effect of photolysis was more pronounced at higher loadings of $HBAr^F_4$ and KC_8; 3000 equiv acid and 3600 equiv reductant led to 66.7 ± 4.4 equiv NH_3 generated, compared to only 24.5 ± 1.2 equivalents in the absence of photolysis (entries 8 and 9). This correlates to ~180% improvement in NH_3 yield in the presence of mercury lamp irradiation.

3.2.3 Preliminary Mechanistic Investigations

To discern what types of iron species might be formed under conditions relevant to the overall catalysis, an analysis of the Fe-containing products after **3.3** was exposed to 10 equiv of acid and 12 equiv of reductant was undertaken and revealed the formation of the dihydride $P_2^{PPh}Fe(N_2)(H)_2$ **3.5** (93% yield based on ^{31}P integration) by NMR and IR spectroscopies (Scheme 3.2). The data for **3.5** show a strong N_2 vibration at 2071 cm^{-1} (IR) and two hydride

resonances in the ^{1}H NMR spectrum at δ -8.87 and -20.5 ppm in C_6D_6. The presence of two phosphine resonances in the ^{31}P NMR spectrum (δ = 119 and 110 ppm) indicate that the $^{i}Pr_2P$- donors are related by symmetry. A structure consistent with these data features a hydride ligand that bisects the two $^{i}Pr_2P$-donors, trans to the N_2 ligand, and another hydride ligand trans to the central phosphine donor of the chelated tris(phosphine) ligand. The conversion of **3.3** to **3.5** can be rationalized by the presence of proton and electron equivalents under N_2 as **3.3** and **3.5** differ by an H-atom, along with binding of an additional equiv of N_2. Although multiple pathways can be proposed to describe the conversion of dinuclear **3.3** to dihydride **3.5**, one pathway includes the reduction of **3.3** to two equiv of anionic $[P_2^{PPh}Fe(N_2)(H)]^-$ in the presence of excess KC_8 (see appendix). The X-ray structure of the sodium analogue is shown in Figure 3.5. Protonation of this anion would lead to **3.5**.

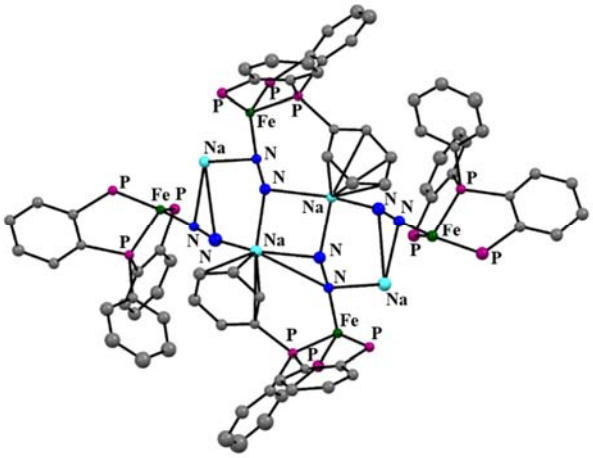

Figure 3.5. X-ray crystal structure of $[P_2^{PPh}Fe(N_2)(H)]Na$ anion.[a]

[a] Unpublished work.

Dihydride **3.5** can be independently synthesized and characterized in solution. Exposure of a degassed THF solution of **3.3** to H_2, followed by re-exposure to N_2, provides **3.5** in good yield as determined by NMR spectroscopy. The 80 K, solid-state Mössbauer spectrum of a 2-MeTHF solution of **3.5** shows one quadrupole doublet with parameters $\delta = 0.05$ mm s^{-1} and $\Delta E_Q = 0.45$ mm s^{-1} (see appendix). When **3.5** was subjected to the catalytic conditions (150 equiv of $HBAr^F{}_4$ and 180 equiv of KC_8), 2.6 ± 0.1 equiv of ammonia were detected (entry 10). A greater than 3-fold increase in yield (8.9 ± 0.9 equiv NH_3) was observed when the catalysis was instead performed in the presence of Hg-lamp irradiation (entry 11), suggesting that light-induced H_2 elimination may expose a more catalytically active state of the system, for example by liberating "$P_2{}^{PPh}Fe^0(N_2)$''.

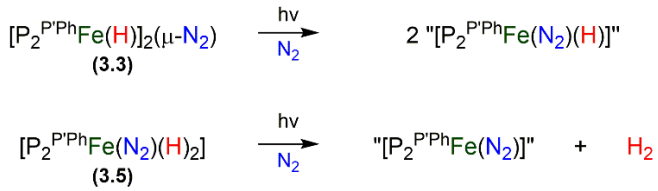

Scheme 3.3. Possible roles for light in catalysis: photodissociation of dinuclear **3.3** to a monomer (top) and/or reductive elimination of H_2 from dihydride **3.5** (bottom).

To probe whether light might facilitate the break-up of $[P_2{}^{PPh}Fe(H)]_2(\mu\text{-}N_2)$ **3.3** to monomeric $P_2{}^{PPh}Fe(N_2)(H)$ **3.4** (Scheme 3.3, top), a THF solution of **3.3** was exposed to Hg lamp photolysis at -78 °C in an EPR tube. After 10 minutes of photolysis, the tube was freeze-quenched at 77 K and its X-band EPR spectrum was acquired. The intensity of the $S = 1/2$ signal increased, but by a barely discernable amount over time (see appendix). Given that

there is appreciable break-up of **3.3** to **3.4** in solution under N_2 in the absence of photolysis (*vide supra*), a photodissociation pathway of **3.3** (Scheme 3.3) seems unlikely to be the source of the enhanced NH_3 yields under photolysis given how little the signal of **3.4** increases under irradiation.

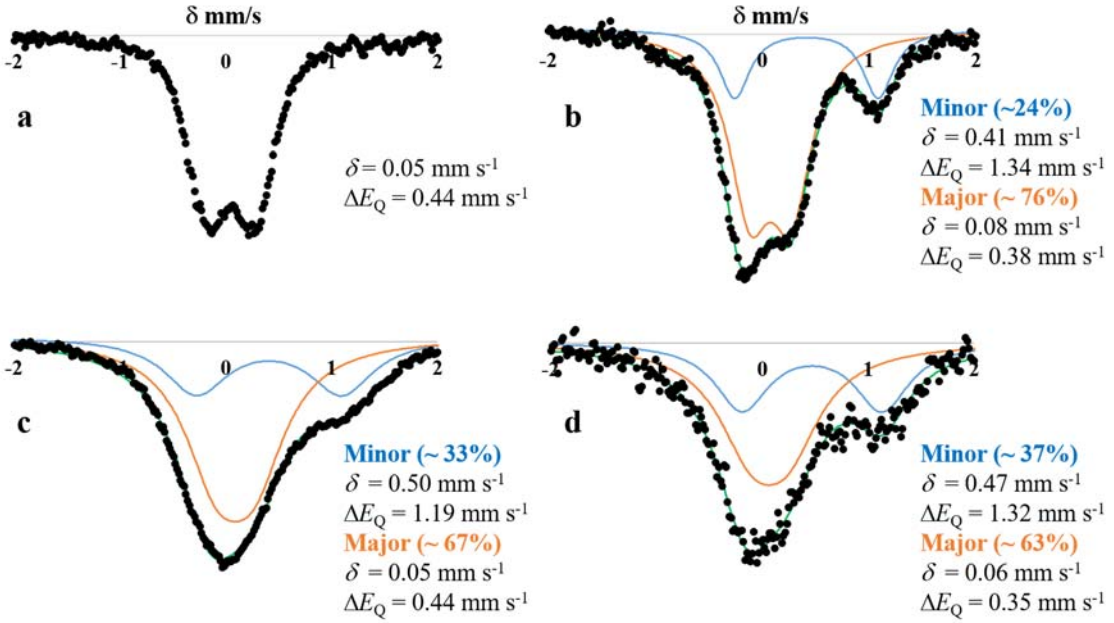

Figure 3.6. The 80 K, 0 mT, ^{57}Fe Mössbauer spectra of dihydride **3.5**; data is represented with black points, simulation in green, major component in orange, and minor component in blue (a) pre-photolysis, (b) after 10 minutes, (c) after 1 hour, and (d) after 4 hours of photolysis at 77K in 2-MeTHF.

Given the propensity of $Fe(H)_2$ species to undergo photoinduced reductive elimination of H_2 (e.g., Scheme 3.1 and Scheme 3.3, bottom) we also subjected a yellow toluene-d_8 solution of purified dihydride **3.5** in an NMR tube to Hg lamp photolysis. After 1 hour of photolysis, the yellow solution color of **3.5** had undergone a marked color change

to deep red (see appendix for a comparison), demonstrating appreciable photoinstability. To further discern the nature of this species, an EPR spectrum of a photolyzed sample of **3.5** in 2-MeTHF was acquired and no S = 1/2 signal was observed (see appendix).[b] Finally, Mössbauer data was acquired and revealed the growth of a second species with parameters most consistent with an S = 1 species (Figure 3.6).[b] While we do not know the photo-generated product/s, we speculate "$P_2^{PPh}Fe^0(N_2)$'' is one plausible candidate (Scheme 3.3).

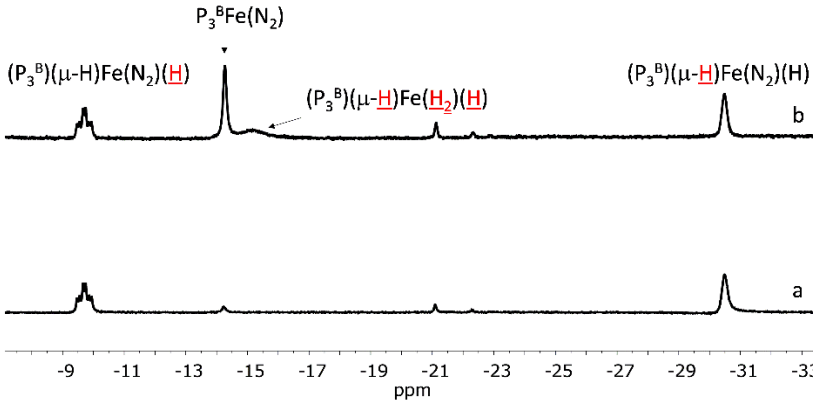

Figure 3.7. Hydride region of ^{1}H NMR spectrum of a toluene-d_8 solution of (P_3^B)(μ-H)Fe(N_2)(H) pre-photolysis (bottom) and after 10 minutes of Hg lamp photolysis at -78 °C (top). The proton(s) corresponding to the ^{1}H resonance are depicted in red and are underlined.

A similar experiment using the aforementioned hydride/borohydride complex (P_3^B)(μ-H)Fe(N_2)(H), observed during catalysis with $P_3^BFe(N_2)^-$ by freeze quenched Mössbauer studies,[20] provided more tractable spectroscopic results. Thus, a toluene-d_8 solution of (P_3^B)(μ-H)Fe(N_2)(H) was subjected to mercury lamp photolysis at -78 °C in an NMR tube,

[b] Unpublished work.

leading to the formation of $P_3^BFe(N_2)$ and $(P_3^B)(\mu\text{-}H)Fe(H_2)(H)$, as discerned by ^1H NMR spectroscopy (Figure 3.7). This observation can be explained as follows: Reductive elimination of H_2 from $(P_3^B)(\mu\text{-}H)Fe(N_2)(H)$ can form $P_3^BFe(N_2)$. Remaining $(P_3^B)(\mu\text{-}H)Fe(N_2)(H)$ may then undergo H_2 for N_2 substitution to generate known $(P_3^B)(\mu\text{-}H)Fe(H_2)(H)$. These observations suggest that an irradiation strategy may also lead to increased NH_3 catalysis efficiency by $P_3^BFe(N_2)^-$. Accordingly, at high acid and reductant loadings, a substantial increase in the equivalents of ammonia was observed, with up to 94 equiv of ammonia being detected (88.1 ± 8.0 with light versus 60.0 ± 3.7 with no light, entries 12 and 13). We also performed the catalysis using $(P_3^B)(\mu\text{-}H)Fe(N_2)(H)$ and found that more ammonia was generated in the presence of light (entries 14 and 15); in addition, hydrazine was detected, 3.5 ± 1.0 with light versus 0.7 ± 0.4 with no light.[c]

3.3 Conclusions

We have synthesized and characterized a new diiron(I) $[P_2^{PPh}Fe(H)]_2(\mu\text{-}N_2)$ complex that is active for catalytic N_2-to-NH_3 conversion. This species partially dissociates into an *S* = ½ $[P_2^{PPh}Fe(N_2)(H)]$ species in solution under N_2, as established by Mössbauer, EPR, and ENDOR spectroscopies. A monomeric dihydride complex, $P_2^{PPh}Fe(N_2)(H)_2$, forms under conditions that model the catalysis, and its N_2-to-NH_3 conversion activity is also enhanced under photolysis, consistent with its observed photoinstability. These observations lead us to speculate that photoinduced release of H_2 is beneficial to the catalysis, perhaps via generation of "$P_2^{PPh}Fe^0(N_2)$''. While mechanistic studies are needed to explore this hypothesis further,

[c] Unpublished work.

the previously reported $P_3^BFe(N_2)^-$ system, where an off-path $(P_3^B)(\mu\text{-}H)Fe(N_2)(H)$ species appears to limit catalytic efficiency, also shows enhanced NH_3 yields under irradiation. Accordingly, irradiation of $(P_3^B)(\mu\text{-}H)Fe(N_2)(H)$ generates (in part) previously characterized $P_3^BFe^0(N_2)$.

The $[P_2^{PPh}Fe(H)]_2(\mu\text{-}N_2)$ system described herein expands on the few well-defined iron systems that mediate catalytic nitrogen fixation against a backdrop of many related iron complexes that have not shown catalytic efficacy under the conditions discussed herein.[17] Dinuclear $[P_2^{PPh}Fe(H)]_2(\mu\text{-}N_2)$ differs from tetradentate P_3^EFe catalysts,[17,20] and also a recently reported bis(phosphine)pyrrole system, through its use of a trisphosphine donor auxiliary that doesn't present other heteroatom donors to the iron center.[15] In this context, Ashley and co-workers have recently reported an iron system supported by only phosphine donors that is selective for N_2-to-N_2H_4 conversion;[44] the present $[P_2^{PPh}Fe(H)]_2(\mu\text{-}N_2)$ system does not generate catalytic quantities of hydrazine under the conditions employed here, or with Ashley's reported conditions (see appendix). The factors that control the N_2-fixing abilities and product profiles of these various iron systems are rich and present a fascinating topic for comparative studies.

3.4 Experimental Section

3.4.1 General Information

All manipulations were carried out using standard Schlenk or glovebox techniques under an N_2 atmosphere. Unless otherwise noted, solvents were deoxygenated and dried by thoroughly sparging with N_2, followed by passage through an activated alumina column in a solvent purification system by SG Water, USA LLC. Solvents were tested with a standard purple solution of sodium benzophenone ketyl in tetrahydrofuran in order to confirm effective moisture removal. Deuterated solvents were purchased from Cambridge Isotope Laboratories, Inc., degassed, filtered through an alumina plug, and dried over 3Å molecular sieves prior to use. Bis(*o*-diisopropylphosphino-phenyl)-chlorophosphine,[41] [Na][BAr^F_4] (BAr^F_4 = tetrakis(3,5-bis(trifluoromethyl)phenyl)borate),[45] [$H(OEt_2)_2$][BAr^F_4],[45] KC_8 (potassium graphite)[46], $P_3^BFe(N_2)$,[29a] and $(P_3^B)(\mu\text{-}H)Fe(N_2)(H)$[55] were prepared according to literature procedures. All other reagents were purchased from commercial vendors and used without further purification unless otherwise stated.

Physical Methods. Elemental analyses were performed by Midwest Microlabs, LLC (Indianapolis, IN) or by the Beckman Institute X-Ray Crystallography Facility (Pasadena, CA) on a PerkinElmer 2400 Series II CHN Elemental Analyzer. ^1H and ^{13}C NMR chemical shifts are reported in ppm relative to proton and carbon resonances from solvents as internal standards. Solution phase magnetic moments were acquired using the Evans method.[47] Optical spectroscopy measurements were taken on a Cary 50 UV-Vis spectrophotometer using a 1-cm two-window quartz cell. Fourier transform infrared ATR spectra were collected

on a Thermo Scientific Nicolet iS5 Spectrometer with diamond ATR crystal (utilized iD5 ATR insert).

X-ray Crystallography. XRD studies were carried out by the Beckman Institute X-Ray Crystallography Facility (Pasadena, CA) on a Bruker AXS KAPPA APEX II diffractometer coupled to an APEX II CCD detector with graphite monochromated Mo K_a radiation (λ = 0.71073 Å) for the structure of compound **3.2-FeBr$_2$** (CCDC 1521910) or on a Bruker AXS D8 VENTURE KAPPA diffractometer coupled to a PHOTON 100 CMOS detector with Mo K_a radiation (λ = 0.71073 Å) for the structure of compound **3.3** (CCDC 1521909). The structures were solved by direct methods using SHELXS[48] and refined against F^2 on all data by full-matrix least squares with SHELXL-2014[49] using established refinement techniques.[50] All non-hydrogen atoms were refined anisotropically. All hydrogen atoms were included into the model at geometrically calculated positions and refined using a riding model. The isotropic displacement parameters of all hydrogen atoms were fixed to 1.2 times the U value of the atoms they are linked to (1.5 times for methyl groups). For **3.3**, all disordered atoms were refined with the help of similarity restraints on the 1,2- and 1,3-distances and displacement parameters as well as rigid bond restraints for anisotropic displacement parameters. Compound **3.3** crystallizes in the triclinic space group P-1 with two molecules in the asymmetric unit along with two half occupied pentane molecules. One phosphorous ligand on each molecule was disordered. In the second molecule (Fe11 and Fe12), one of the P^{i}Pr$_2$ moieties was disordered over three positions. Attempts to refine a two component disorder led to ^{i}Pr moieties with incorrect geometries and high residual electron density maxima. Refinement of the second molecule required stronger restraints on the anisotropic

displacement parameters and the disordered aromatic rings were restrained to be flat. The two half occupied pentane molecules are located near crystallographic inversion centers and disordered appropriately.

Mössbauer Spectroscopy. Mössbauer spectra were recorded on a spectrometer from SEE Co. (Edina, MN) operating in the constant acceleration mode in a transmission geometry. The sample was kept in an SVT-400 cryostat from Janis (Wilmington, MA). The quoted isomer shifts are relative to the centroid of the spectrum of a metallic foil of α-Fe at room temperature. Solid samples were prepared by grinding solid material into a fine powder and then mounting in a Delrin cup fitted with a screw-cap as a boron nitride pellet. Solution samples were transferred to a sample cup and chilled to 77 K inside of the glovebox, and unless noted otherwise, quickly removed from the glovebox and immersed in liquid N_2 until mounted in the cryostat. Data analysis was performed using version 4 of the program WMOSS (www.wmoss.org) and quadrupole doublets were fit to Lorentzian lineshapes. Unless otherwise noted, Mössbauer spectra were collected with an applied 50mT parallel field at 80K.

CW EPR Spectroscopy. X-band EPR spectra were obtained on a Bruker EMX spectrometer at 77 K in a liquid nitrogen immersion dewar using Bruker Win-EPR software (ver. 3.0). Samples were prepared as 3-17 μM solutions prepared as frozen glasses in 2-methyltetrahydrofuran. Samples were collected at powers ranging from 6 to 7 mW and

modulation amplitudes of 1-2 Gauss. Spectra were simulated using the EasySpin[51] simulation toolbox (release 5.1.8) with Matlab 2016b.

Pulse EPR Spectroscopy. All pulse Q-band (≈ 33.7 GHz) EPR and electron nuclear double resonance (ENDOR) experiments were aquired using a Bruker (Billerica, MA) ELEXSYS E580 pulse EPR spectrometer equipped with a Bruker D2 resonator. Temperature control was achieved using an ER 4118HV-CF5-L Flexline Cryogen-Free VT cryostat manufactured by ColdEdge (Allentown, PA) equipped with an Oxford Instruments Mercury ITC.

Pulse Q-band electron spin-echo detected EPR (ESE-EPR) field-swept spectra were acquired using the 2-pulse "Hahn-echo" sequence ($\pi/2 - \tau - \pi -$ echo) and subsequently, each field swept echo-detected EPR absorption spectrum was modified using a pseudo-modulation function (modulation amplitude = 1.5 mT) to approximate the effect of field modulation and produce the CW-like 1st derivative spectrum.[52]

Pulse Q-band ENDOR was acquired using the Davies pulse sequence ($\pi - T_{RF} - \pi_{RF} - T_{RF} - \pi/2 - \tau - \pi -$ echo), where T_{RF} is the delay between mw pulses and RF pulses, π_{RF} is the length of the RF pulse and the RF frequency is randomly sampled during each pulse sequence. For the ^{2}D Davies ENDOR experiments collected from 0.5 – 20.5 MHz, an LP-2500 low-pass filter (Vectronics, Starkville, MS) with a cutoff frequency of 35 MHz was used to eliminate signals from ^{1}H harmonics.

In general, the ENDOR spectrum for a given nucleus with spin I= ½ (^{1}H, ^{31}P) coupled to the S = ½ electron spin exhibits a doublet at frequencies

$$\nu_{\pm} = \left|\frac{A}{2} \pm \nu_N\right| \quad (1)$$

where ν_N is the nuclear Larmor frequency and A is the hyperfine coupling. For nuclei with $I \geq 1$ (^{14}N, ^{2}D), an additonal splitting of the $\nu_{\pm}$ manifolds is produced by the nuclear quadrupole interaction (P)

$$\nu_{\pm,m_I} = \left| \nu_N \pm \frac{3P(2m_I - 1)}{2} \right| \quad (2)$$

Pulse Q-band Electron spin echo envelope modulation (ESEEM) spectra were collected using the three pulse sequence ($\pi/2 - \tau - \pi/2 - T - \pi/2 - \tau$ – echo) with a four step phase cycle.

Simulations of all pulse EPR data were achieved using the EasySpin simulation toolbox (release 5.1.8) with Matlab 2016 using the following Hamiltonian:

$$\hat{H} = \mu_B \vec{B}_0 g \hat{S} + \mu_N g_N \vec{B}_0 \hat{I} + h\hat{S} \cdot \boldsymbol{A} \cdot \hat{I} + h\hat{I} \cdot \boldsymbol{P} \cdot \hat{I} \quad (3)$$

In this expression, the first term corresponds to the electron Zeeman interaction term where μ_B is the Bohr magneton, g is the electron spin g-value matrix with principle components g = [g_{xx} g_{yy} g_{zz}], and $\hat{S}$ is the electron spin operator; the second term corresponds to the nuclear Zeeman interaction term where μ_N is the nuclear magneton, g_N is the characteristic nuclear g-value for each nucleus (e.g. ^{1}H,^{2}D,^{31}P) and $\hat{I}$ is the nuclear spin operator; the third term corresponds to the electron-nuclear hyperfine term, where $\boldsymbol{A}$ is the hyperfine coupling tensor with principle components $\boldsymbol{A}$ = [A_{xx} A_{yy} A_{zz}]; and for nuclei with $I \geq 1$, the final term corresponds to the nuclear quadrupole (NQI) term which arises from the interaction of the nuclear quadrupole moment with the local electric field gradient (efg) at the nucleus, where

$\boldsymbol{P}$ is the quadrupole coupling tensor. In the principle axis system (PAS), $\boldsymbol{P}$ is traceless and parametrized by the quadrupole coupling constant e^2Qq/h and the asymmetry parameter η such that:

$$\boldsymbol{P} = \begin{pmatrix} P_{xx} & 0 & 0 \\ 0 & P_{yy} & 0 \\ 0 & 0 & P_{zz} \end{pmatrix} = \frac{e^2Qq/h}{4I(2I-1)} \begin{pmatrix} -(1-\eta) & 0 & 0 \\ 0 & -(1+\eta) & 0 \\ 0 & 0 & 2 \end{pmatrix} \quad (4)$$

where $\frac{e^2Qq}{h} = 2I(2I-1)P_{zz}$ and $\eta = \frac{P_{xx}-P_{yy}}{P_{zz}}$. The asymmetry parameter may have values between 0 and 1, with 0 corresponding to an electric field gradient with axial symmetry and 1 corresponding to a fully rhombic efg.

The orientations between the hyperfine and NQI tensor principle axis systems and the g-matrix reference frame are defined by the Euler angles (α, β, γ).

^{14}N ENDOR/ESEEM. The low-intensity features between 5 and 10 MHz which appear in the ^{2}D Davies ENDOR of both **3.4** and **3.4D** (Figure A3.49) arise from the hyperfine coupling from the proximal ^{14}N of the bound N_2 moiety. The presence of this ^{14}N hyperfine coupling was corroborated by the use of Q-band 3-pulse ESEEM, which is particularly sensitive to hyperfine couplings to $I = 1$ nuclei near cancellation ($A = 2\nu_I$). These features are well simulated by an axial hyperfine tensor with A = [5.4 5.8 9.0] MHz and a fairly large quadrupole coupling constant of 3.6 MHz with a very small asymmetry parameter η = 0.08, consistent with the ^{14}N nucleus being in a bonding environment with axial symmetry. Simulations of the experimental data also indicate a rotation of the hyperfine and quadrupole

tensors relative to the g-matrix reference frame by $\beta = 90°$, (rotation of the PAS z-axis about the x-axis). These results confirm that N_2 remains bound in species **3.4.**

Ammonia Quantification. The catalytic reaction mixture was cooled to 77 K and allowed to freeze. The reaction vessel was opened to the atmosphere and to the frozen solution was slowly added a fourfold excess (with respect to acid) solution of a NaO^{t}Bu in MeOH (0.25 M) over 1–2 minutes. The solution was allowed to freeze, then the tube was sealed and allowed to warm to room temperature and stirred at room temperature for 10 minutes. An additional Schlenk tube was charged with HCl (3 mL of a 2.0 M solution in Et_2O, 6 mmol) to serve as a collection flask. The volatiles of the reaction mixture were vacuum transferred into the collection flask. After completion of the vacuum transfer, the collection flask was sealed and warmed to room temperature. Solvent was removed *in vacuo*, and the remaining residue dissolved in H_2O (1 mL) to make a stock solution that was used for both the ammonia ad hydrazine quantification. An aliquot of this solution (20 μL) was then analyzed for the presence of NH_3 (present as NH_4Cl) by the indophenol method.[53] Quantification was performed with UV−Vis spectroscopy by analyzing the absorbance at 635 nm.

Hydrazine Quantification. Hydrazine quantification was performed using the same stock solution from the ammonia quantification. An aliquot of the stock solution (20 μL) was analyzed for the presence of N_2H_4 (present as N_2H_5Cl) by a standard spectrophotometric method.[54] Quantification was performed with UV−Vis spectroscopy by analyzing the absorbance at 458 nm. *Note that no hydrazine was observed under the reaction conditions.

Standard NH_3 Generation Reaction Procedure for $[P_2^{PPh}Fe(H)]_2(\mu\text{-}N_2)$ (3.3). All solvents were stirred with Na/K for ≥1 hours and filtered through alumina prior to use. In a nitrogen-filled glovebox, a stock solution of the catalyst in THF (3.4 mM) was prepared. (Note: a fresh stock solution was prepared for each experiment and used immediately.) An aliquot of this stock solution (18 or 90 μL, 0.06 or 0.30 μmol) was added to a Schlenk tube and evaporated to dryness under vacuum to give a thin film of **3.3**. The tube was allowed to cool to 77 K in the glovebox cold well. To the cold tube was added a solution of $[H(OEt_2)_2][BAr^F{}_4]$ (93 mg, 0.092 mmol) in Et_2O (0.5 mL). This solution was allowed to freeze before the vial that contained the $[H(OEt_2)_2][BAr^F{}_4]$ was rinsed with an additional 0.5 mL of Et_2O and added to the tube. After the acid layer had frozen, a suspension of KC_8 (15 mg, 0.11 mmol, 1.2 equiv relative to $[H(OEt_2)_2][BAr^F{}_4]$) in 0.5 mL of Et_2O was added to the cold tube. The temperature of the system was allowed to equilibrate for 5 minutes. A stir bar was added to the tube before it was sealed with a Teflon screw-valve. The Schlenk tube was passed out of the box into a liquid N_2 bath and transported to a fume hood. The reaction vessel was then transferred to a dry ice/acetone bath where it thawed to -78 °C and was allowed to stir for at least 1 hour. The tube was then allowed to warm to room temperature with stirring, and stirred at room temperature for 5 minutes.

Standard NH_3 Generation Reaction with Hg Lamp Photolysis Procedure for $[P_2^{PPh}Fe(H)]_2(\mu\text{-}N_2)$ (3.3). All solvents were stirred with Na/K for ≥1 hours and filtered through alumina prior to use. In a nitrogen-filled glovebox, a stock solution of the catalyst in THF (3.4 mM) was prepared. (Note: a fresh stock solution was prepared for each experiment

and used immediately.) An aliquot of this stock solution (18 or 90 μL, 0.06 or 0.30 μmol) was added to a Quartz Schlenk tube and evaporated to dryness under vacuum to give a thin film of **3.3**. The tube was allowed to cool to 77 K in the glovebox cold well. To the cold tube was added a solution of $[H(OEt_2)_2][BAr^F{}_4]$ (93 mg, 0.092 mmol) in Et_2O (0.5 mL). This solution was allowed to freeze before the vial that contained the $[H(OEt_2)_2][BAr^F{}_4]$ was rinsed with an additional 0.5 mL of Et_2O and added to the tube. After the acid layer had frozen, a suspension of KC_8 (15 mg, 0.111 mmol, 1.2 equiv relative to $[H(OEt_2)_2][BAr^F{}_4]$ in 0.5 mL of Et_2O was added to the cold tube. The temperature of the system was allowed to equilibrate for 5 minutes. A stir bar was added to the tube before it was sealed with a Teflon screw-valve. The Schlenk tube was passed out of the box into a liquid N_2 bath and transported to a fume hood. The reaction vessel was then transferred to a dry ice/isopropanol bath which was positioned under a Hg lamp and turned on 1 minute prior to transfer of the Schlenk tube to the bath. The entire reaction apparatus was surrounded by foil and the reaction vessel was allowed to stir for at least 1 hour before the Hg lamp was turned off and the Schlenk tube was allowed to warm to room temperature with stirring, and stirred at room temperature for 5 minutes.

Standard NH_3 Generation Reaction Procedure for $[P_2^{PPh}Fe(H)]_2(\mu\text{-}N_2)$ (3.3) Allowed to Warm to Room Temperature Overnight. The procedure was identical to that of the standard catalytic reaction protocol with the changes noted. The reaction was allowed to warm from -78 °C to room temperature overnight (approximately 16 hours).

Standard NH_3 Generation Reaction Procedure for P_2^{PPh} (3.1). The procedure was identical to that of the standard catalytic reaction protocol with the changes noted. A stock solution of **3.1** in THF (3.4 mM) was prepared. (Note: a fresh stock solution was prepared for each experiment and used immediately.) An aliquot of this stock solution (180 μL, 0.62 μmol) was used.

Standard NH_3 Generation Reaction with Hg Lamp Photolysis Procedure for P_2^{PPh} (3.1). The procedure was identical to that of the standard catalytic reaction protocol with Hg lamp photolysis with the changes noted. A stock solution of **3.1** in THF (3.4 mM) was prepared. (Note: a fresh stock solution was prepared for each experiment and used immediately.) An aliquot of this stock solution (180 μL, 0.62 μmol) was used.

Standard NH_3 Generation Reaction Procedure for $[P_2^{PPh}Fe(H)]_2(\mu\text{-}N_2)$ (3.3) Using 2-MeTHF as the Solvent, Instead of Et_2O. The procedure was identical to that of the standard catalytic reaction protocol with the changes noted. The reaction solvent was 2-MeTHF.

Standard NH_3 Generation Reaction Procedure for $P_2^{PPh}Fe(N_2)(H)_2$ (3.5). The procedure was identical to that of the standard catalytic reaction protocol with the changes noted. A stock solution of **3.5** in THF (3.4 mM) was prepared. (Note: a fresh stock solution was prepared for each experiment and used immediately.) An aliquot of this stock solution (180 μL, 0.62 μmol) was used.

Standard NH_3 Generation Reaction with Hg Lamp Photolysis Procedure for $P_2^{PPh}Fe(N_2)(H)_2$ (3.5). The procedure was identical to that of the standard catalytic reaction protocol with Hg lamp photolysis with the changes noted. A stock solution of **3.5** in THF (3.4 mM) was prepared. (Note: a fresh stock solution was prepared for each experiment and used immediately.) An aliquot of this stock solution (180 μL, 0.62 μmol) was used.

Standard NH_3 Generation Reaction Procedure for $P_3^BFe(N_2^-)$. The procedure was identical to that of the standard catalytic reaction protocol with the changes noted. A stock solution of **$P_3^BFe(N_2^-)$** in THF (9.5 mM) was prepared. (Note: a fresh stock solution was prepared for each experiment and used immediately.) An aliquot of this stock solution (12 μL, 0.11 μmol) was used.

Standard NH_3 Generation Reaction with Hg Lamp Photolysis Procedure for $P_3^BFe(N_2^-)$. The procedure was identical to that of the standard catalytic reaction protocol with Hg lamp photolysis with the changes noted. A stock solution of **$P_3^BFe(N_2^-)$** in THF (9.5 mM) was prepared. (Note: a fresh stock solution was prepared for each experiment and used immediately.) An aliquot of this stock solution (12 μL, 0.11 μmol) was used.

Standard NH_3 Generation Reaction with Blue LED Photolysis Procedure for $[P_2^{PPh}Fe(H)]_2(\mu\text{-}N_2)$ (3.3). The procedure was identical to that of the standard catalytic reaction protocol with Hg lamp photolysis with the changes noted. A blue LED was used in place of a Hg lamp.

Standard NH_3 Generation Reaction Procedure for $(P_3^B)(\mu\text{-}H)Fe(N_2)(H)$. The procedure was identical to that of the standard catalytic reaction protocol with the changes noted. A stock solution of **$(P_3^B)(\mu\text{-}H)Fe(N_2)(H)$** in THF (9.6 mM) was prepared. (Note: a fresh stock solution was prepared for each experiment and used immediately.) An aliquot of this stock solution (64 μL, 0.61 μmol) was used. In addition, due to the insolubility of the iron hydride borohydride species, a 3:1 mixture of Et_2O:toluene was used as the solvent for the catalytic reaction.

Standard NH_3 Generation Reaction with Hg Lamp Photolysis Procedure for $(P_3^B)(\mu\text{-}H)Fe(N_2)(H)$. The procedure was identical to that of the standard catalytic reaction protocol with Hg lamp photolysis with the changes noted. A stock solution of **$(P_3^B)(\mu\text{-}H)Fe(N_2)(H)$** in THF (9.6 mM) was prepared. (Note: a fresh stock solution was prepared for each experiment and used immediately.) An aliquot of this stock solution (64 μL, 0.61 μmol) was used. In addition, due to the insolubility of the iron hydride borohydride species, a 3:1 mixture of Et_2O:toluene was used as the solvent for the catalytic reaction.

3.4.2 Synthesis

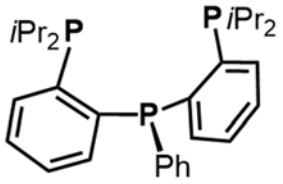

P_2^{PPh} **(3.1)**

P_2^{PPh} (3.1). To a stirring solution of bis(*o*-diisopropylphosphino-phenyl)-chlorophosphine (0.304 g, 0.671 mmol) in THF (5 mL) was added dropwise phenyl magnesium chloride (3 M in Et_2O, 0.24 mL, 0.705 mmol) at -78 °C. The yellow reaction mixture was stirred for 2 hours at -78 °C and then allowed to warm to room temperature. After stirring for an additional 15 minutes at room temperature, the reaction was concentrated to 3 mL. To the concentrated solution, dioxane (3 mL) was added which resulted in the precipitation of an off white solid ($MgCl_2$ salts). The heterogeneous mixture was filtered through celite, the salts washed with pentane (3 x 5 mL), the filtrate collected and solvent removed *in vacuo* to provide a pale yellow oil. The oil was triturated with pentane (5 mL) and resuspended in pentane, which resulted in the precipitation of a white crystalline solid. The solid was isolated, washed with pentane (3 x 5 mL), and dried under vacuum to give P_2^{PPh} (**3.1**) (0.307 g, 0.432 mmol) in 64% yield. ^{1}H NMR (C_6D_6, 400 MHz) δ ppm 7.49 – 7.40 (m, 2H), 7.39 – 7.31 (m, 2H), 7.08 (t, J = 6.7 Hz, 7H), 6.97 (t, J = 7.5 Hz, 2H), 2.11 (td, J = 7.0, 2.6 Hz, 2H), 1.98 (hept, J = 7.1 Hz, 2H), 1.18 (td, J = 13.8, 7.0 Hz, 12H), 0.92 (ddd, J = 32.8, 11.5, 7.0 Hz, 12H). ^{31}P{^{1}H} (C_6D_6, 162 MHz) δ ppm -2.17 (dd, J = 152.5, 6.0 Hz, 2P, P-Ar), -14.26 (dt, J = 158.7, 147.0 Hz, 1P, P-Ph). ^{13}C NMR (C_6D_6, 101 MHz) δ ppm 148.42 (m), 142.42 (m), 139.73 (dt), 135.64 (d), 134.88 (m), 132.44 (m), 128.91 (s), 128.45 (d), 24.94 (m), 20.56 (m), 19.88 (m). ESI-MS (electrospray): calcd for $C_{30}H_{41}AgP_3^+$ 601.15 *m/z*, found: 601.27 *m/z*.

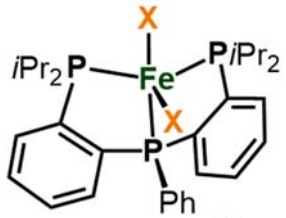

3.2-$FeBr_2$ or 3.2-$^{57}FeCl_2$

$P_2^{PPh}FeBr_2$ (3.2-$FeBr_2$). P_2P^{Ph} (**3.1**) (0.306 g, 0.619 mmol) and ferrous bromide (0.140 g, 0.649 mmol) were combined in THF (20 mL) in the glovebox. The dark black-purple solution was stirred vigorously over two hours. The crude reaction mixture was concentrated *in vacuo* until 10 mL of THF remained and then filtered through celite. To the concentrated stirring black-purple solution, 10 mL of pentane was added dropwise, resulting in the precipitation of a dark black-purple solid. The dark solid was isolated on a frit, washed with pentane (3 x 1 mL), and dried under dynamic vacuum to give $P_2^{PPh}FeBr_2$ (**3.2-$FeBr_2$**) (0.3822 g, 0.538 mmol) in 87% yield. ^{1}H NMR (THF-d_8, 400 MHz) δ ppm 133.90, 56.82, 9.86, 9.00, 8.14, 7.81, 7.65, 7.25, 7.12, 6.70, 5.06, 4.09, 3.90, 3.70, 3.56, 2.88, 2.23, 1.72, and 0.96 ppm. μ_{eff} (THF-d_8, Evans' method, 298K): 3.92μ_B. UV-Vis (THF, nm {$cm^{-1}M^{-1}$}): 486 {1,300}, 591 {980}. Anal calcd for $C_{30}H_{41}Br_2FeP_3$: C, 50.73; H, 5.82. Found: C, 50.82; H, 5.92.

3.2-$^{57}FeCl_2$ was synthesized using an identical procedure, except with $^{57}FeCl_2$ in place of $FeBr_2$, and gave similar features by ^{1}H NMR: ^{1}H NMR (C_6D_6, 400 MHz) δ ppm 120.81, 108.39, 16.39, 11.43, 10.08, 9.02, 8.63, 3.58, 3.28, 3.26, 1.63, 142, 1.25, 1.12, 0.88, 0.28, -2.90 ppm.

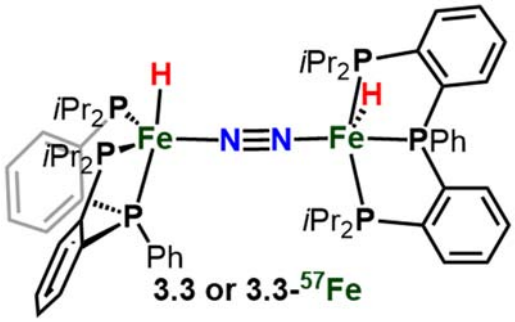

3.3 or 3.3-^{57}Fe

[P_2^{PPh}Fe(H)]$_2$(μ-N_2) (3.3). To a dark purple solution of $P_2^{PPh}FeBr_2$ (**3.2-FeBr$_2$**) (0.0522 g, 0.073 mmol) in THF (5 mL) at -78 °C was added sodium triethylborohydride (1 M in toluene, 0.13 mL, 0.14 mmol) dropwise. The reaction mixture was stirred at -78 °C for 4 hours. The dark green solution was allowed to warm to room temperature, stirred for an additional hour, and then concentrated *in vacuo*. The resultant green oil was resuspended in pentane (3 mL), filtered through celite, and the reaction vessel and salts washed with pentane (3 x 1 mL). The concentrated intense green filtrate slowly precipitated **3.3** (0.0275 g, 0.024 mmol) overnight as dark green crystalline needles in 64 % yield. IR (KBr; cm^{-1}): 1833 (ν_{FeH}), 1734 (ν_{FeH}). (Note: Weak coupling of the Fe-H vibration to a symmetry allowed N-N vibration is plausible; however, we have not been able to unambiguously assign the N-N vibration through $^{15}N_2$ labeling studies. We expect admixed $^{14}N_2$ in the sample owing to technical challenges with its synthesis. We have included the IR spectrum of the $^{15}N_2$ labeled data below.) ^{1}H NMR (THF-d_8, 500 MHz) δ ppm 8.15 (d, J = 7.5 Hz, 2H), 7.52 (d, J = 7.5 Hz, 2H), 7.43 (t, J = 7.3 Hz, 2H), 7.26 (t, J = 7.3 Hz, 2H), 7.14 (t, J = 7.3 Hz, 2H), 6.63 (d, J = 7.4 Hz, 2H), 6.12 (t, J = 7.5 Hz, 1H), 2.99 (broad s, 2H), 2.59 (broad s, 2H), 0.72 (m, 6H), 0.42 (m, 6H). ^{31}P{^{1}H} (THF-d_8, 202 MHz) δ ppm -44.32 (very broad singlet). UV-vis (THF, nm {cm^{-1}M^{-1}}): 338 {1,200}, 655 {380}. Anal calcd for $C_{125}H_{180}Fe_4N_4P_{12}$: C, 64.33; H, 7.77;

N, 2.40. Found: C, 63.94; H, 7.92; N, 2.71. (*Note: **3.3** crystallizes as 2 dinuclear complexes with 1 pentane molecule.)

[P_2^{PPh}Fe(D)]$_2$(μ-N_2) (3.3D). 3.3D was prepared using the synthetic procedure for **3.3** with the following changes noted. Toluene was used as the reaction solvent and $LiDBEt_3$ was used instead of $NaHBEt_3$. IR (KBr; cm^{-1}): 1839 (ν_{NN}), 1734 (ν_{NN}), 1324 (ν_{FeD}), 1256 (ν_{FeD}) (predicted ν_{FeD} = 1309, 1237 cm^{-1}. The ^{1}H NMR spectrum of **3.3D** matched that of **3.3**.

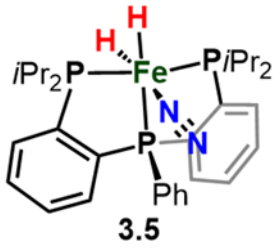

3.5

P_2^{PPh}Fe(N_2)($H)_2$ (3.5). A Schlenk tube containing **3.3** (0.020 g, 17.1 μmol) in THF (2 mL) was freeze-pump-thawed (3X) and exposed to 1 atmosphere of H_2. The reaction tube was stirred vigorously at room temperature for 24 hours before it was freeze-pump-thawed (2X), re-exposed to 1 atmosphere of N_2, and stirred for another 24 hours, during which the reaction turned mustard yellow. The reaction mixture was then concentrated *in vacuo* and the resultant thin film was suspended in pentane and filtered through celite. The yellow solid was washed with pentane (3 x 1mL) and dried under vacuum. ^{1}H NMR (C_6D_6, 400 MHz) δ ppm 7.90 (t, *J* = 6.5 Hz, 2H), 7.46–7.41 (m, 4H), 7.05 (q, *J* = 7.8, 7.3 Hz, 5H), 6.95–6.92 (m, 1H) (1 C-H_{Ar} overlapped with C_6H_6 peak, but all 13 C-H_{Ar} can be resolved with THF-d_8), 2.47–2.42 (m, 4H), 1.56 (q, *J* = 6.9 Hz, 6H), 1.26 (q, *J* = 7.2 Hz, 6H), 1.13 (q, *J* = 6.6, 6H), 0.59 (q, *J* =

6.9, 6H), -8.82 (broad singlet, 1H), -20.43 (broad singlet, 1H). ^{1}H NMR (THF-d_8, 500 MHz) δ ppm 8.09 (t, J = 6.4 Hz, 2H), 7.77 (d, J = 7.2 Hz, 2H), 7.40 (p, J = 7.2 Hz, 4H), 7.22–7.15 (m, 5H), 2.67 (h, J = 6.8 Hz, 2H), 2.56–2.50 (m, 2H), 1.43 (q, J = 7.0 Hz, 6H), 1.15–1.19 (m, 12H), 0.46 (q, J = 6.9, 6H). The coupling of the two hydride resonances can be resolved in the ^{1}H NMR at low temperature (THF-d_8, 500 MHz, -78 °C) δ ppm -9.43 (m, 1H), -20.71 (m, 1H). ^{1}H{^{31}P δ 110 ppm} (THF-d_8, 500 MHz, -78 °C) δ ppm -9.43 (td, J = 38.2 , 15.7 Hz, 1H), -20.71 (td, J = 43.2 , 15.6 Hz, 1H). ^{1}H{^{31}P δ 120 ppm} (THF-d_8, 500 MHz, -78 °C) δ ppm -9.43 (dd, J = 30.6 , 15.7 Hz, 1H), -20.71 (dd, J = 24.0 , 15.6 Hz, 1H). ^{31}P{^{1}H} (C_6D_6, 162 MHz) δ ppm 119.07 (m, 2P, PiPr$_2$), 110.22 (m, 1P, PPh). ^{31}P{^{1}H} (THF-d_8, 202 MHz) δ ppm 120.79 (m, 2P, PiPr$_2$), 111.95 (m, 1P, PPh). ^{13}C NMR (C_6D_6, 101 MHz) δ ppm 150.72 (m), 149.52 (m), 141.31 (d), 132.33 (d), 130.86 (t), 129.50 (d), 31.68 (t), 27.54 (td), 20.36 (t), 19.80 (dd). IR (KBr; cm^{-1}): 2058 (ν_{NN}), 1812 (ν_{FeH}). IR (thin film from evaporation of C_6D_6; cm^{-1}): 2071 (ν_{NN}), 1796 (ν_{FeH}). UV-Vis (THF, nm {cm^{-1}M^{-1}}): 335 {4,600}, 386 {4,000}. Anal calcd for $C_{30}H_{43}FeN_2P_3$: C, 62.08; H, 7.47; N, 4.83. Found: C, 61.16; H, 7.85; N, 4.82.

3.4.3 Miscellaneous Experiments

GC Analysis of the headspace of addition of 2 equiv of MeOTf to [P$_2^{PPh}$Fe(H)]$_2$(μ-N$_2$). In a nitrogen filled glovebox, a solution of **3.3** (5.0 mg, 4.3 μmol) in toluene (2 mL) was prepared in a 70 mL Schlenk tube containing a 14/20 joint. The 14/20 joint was sealed with a rubber septum at room temperature and subsequently chilled to -78 °C in the glovebox coldwell. In a separate vial, a stock solution of MeOTf (10 μL of MeOTf in 2 mL of toluene,

46 mM in toluene) was prepared. To the Schlenk tube containing **3.3**, 200 μL of the MeOTf stock solution was added at -78 °C through the rubber septum using a 1 mL disposable syringe and the rubber septum was quickly covered with tape. After 20 minutes of stirring at -78 °C, the reaction was allowed to warm to room temperature and stirred for an additional 1.5 hours before the headspace was analyzed for methane by GC chromatography (97% yield methane).

IR and NMR Spectral Analysis of addition of 10 equiv of $[H(OEt_2)_2][BAr^F{}_4]$) to $[P_2{}^{PPh}Fe(H)]_2(\mu\text{-}N_2)$ followed by 12 equiv of KC_8 per Fe Center. To a 20 mL scintillation vial was added **3.3** (0.006 g, 5.1 μmol) in THF (500 μL) and the solvent removed in vacuo to generate a dark emerald green thin film (in order to mimic the catalytic run procedure). The 20 mL vial containing the thin film of **3.3** was charged with a stir bar. In a separate 4 mL vial, a solution of $[H(OEt_2)_2][BAr^F{}_4]$ (103 mg, 102 μmol) in Et_2O (1 mL) was made. Finally, in another 4 mL vial, a suspension of KC_8 (16.5 mg, 122 μmol) in Et_2O (1 mL) was prepared. All three vials were chilled in the glovebox coldwell at -78 °C for 30 minutes. The solution of $[H(OEt_2)_2][BAr^F{}_4]$ was quickly added to the vial containing the thin film of **3.3**. Residual $[H(OEt_2)_2][BAr^F{}_4]$ in the 4 mL vial was rinsed using pre-chilled Et_2O (0.5 mL). The red-orange reaction mixture was stirred at -78 °C for 5 minutes, after which the suspension of KC_8 in Et_2O was added rapidly. Residual KC_8 in the 4 mL vial was rinsed using pre-chilled Et_2O (0.5 mL). The reaction mixture was then stirred for 45 minutes at -78 °C before it was allowed to warm to room temperature and stirred for an additional 15 minutes. The reaction mixture was then filtered through glass filter paper into a 20 mL vial containing

triphenylphosphine (0.003 g, 11.4 μmol) as a ^{31}P NMR internal standard and the resultant crude mixture was concentrated to ½ the original volume and transferred to an NMR tube. The integration of the ^{31}P resonances suggested the formation of $P_2^{PPh}Fe(N_2)(H)_2$ in approximately 93% yield. The NMR solution was then transferred to a 20 mL vial in the glovebox and concentrated to provide an orange thin film which was subsequently analyzed by ^{1}H and ^{31}P NMR spectroscopies in C_6D_6 and matched the data reported above.

NMR Spectral Analysis of addition of 3 equiv of KC_8 to $[P_2^{PPh}Fe(H)]_2(\mu\text{-}N_2)$ yields $[P_2^{PPh}Fe(N_2)(H)]K$. A 20 mL vial containing **3.3** (0.016 g, 13.8 μmol) in THF-d_8 (500 μL) was chilled to -78 °C in the glovebox coldwell. In a separate 4 mL vial, KC_8 (5.6 mg, 41.6 μmol) was chilled to -78 °C. Both vials were allowed to cool for 20 min before the KC_8 was added to the vial containing **3.3** as a solid. The reaction mixture was stirred vigorously at -78 °C for 1 hour before PPh_3 (3.6 mg, 13.8 μmol) was added to the vial as a solid. The vial containing the PPh_3 was rinsed with THF-d_8 (2 × 50 μL) and the rinsings added to the reaction vial. The reaction mixture was then filtered to a J. Young tube and the reaction vial rinsed with THF-d_8 (2 × 100 μL) and the rinsings added to the tube. The tube was frozen at 77K until it was warmed back to -78 °C for NMR analysis. ^{1}H NMR (THF-d_8, 500 MHz, -78 °C) δ ppm 7.78 (q, J = 4.4 Hz, 2H), 7.53–7.45 (m, 2H), 7.11–6.99 (m, 9H), 2.51–2.42 (m, 2H), 2.42–2.32 (m, 2H), 1.20–1.05 (m, 18H), 0.35 (p, J = 8.5, 7.5, 6H), -10.21 (td, J = 68.1, 26.6, 1H). *Accurate integrations of the aromatic C-H region are precluded by the presence of triphenylphosphine. $^{31}P\{^{1}H\}$ (THF-d_8, 202 MHz, -78 °C) δ ppm 121.92 (t, J = 41.8 Hz,

1P, PPh), 116.96 (d, J = 39.9 Hz, 2P, PiPr$_2$). IR (thin film from evaporation of THF-d$_8$; cm^{-1}): 1857 (ν_{NN}), 1718 (ν_{FeH}).

NMR Spectral Analysis of addition of 2 equiv of [H(OEt$_2$)$_2$][BAr$^F_4$] to [P$_2^{PPh}$Fe(H)]$_2$(μ-N$_2$) yields [P$_2^{PPh}$Fe(N$_2$)(H)]BAr$^F_4$. A 20 mL vial containing **3.3** (0.011 g, 9.4 μmol) in diethyl ether (1 mL) was chilled to -78 °C in the glovebox coldwell. In a separate 4 mL vial, a diethyl ether solution of HBAr$^F_4$ (0.019 g, 18.4 μmol, 250 μL diethyl ether) was chilled to -78 °C. Both solutions were allowed to cool for 20 min before the HBAr$^F_4$ solution was added to the vial containing **3.3** at -78 °C in one shot. The vial containing HBAr$^F_4$ was subsequently rinsed one time with 250 μL of pre-chilled diethyl ether and the rinsings were quickly added to the vial containing **3.3**. The reaction mixture was stirred vigorously at -78 °C for 1 hour and 15 minutes before it was allowed to warm to room temperature and stirred for an additional 10 minutes. The reaction mixture was then concentrated in vacuo and the resultant orange thin film was suspended in THF-d$_8$ (300 μL) and filtered through a cotton plug to a vial containing hexamethylbenzene as a ^{1}H internal standard (0.003 g, 18.9 μmol). The reaction vial was then rinsed with THF-d$_8$ (2 × 200 μL) and filtered to the vial containing hexamethylbenzene. The orange solution was then transferred to an NMR tube for spectral analysis. ^{1}H NMR (THF-d$_8$, 400 MHz) δ ppm 8.22–8.10 (m), 7.85–7.69 (m), 7.59–7.50 (m), 7.36 (t, J = 7.9, 1H), 7.30–7.27 (m), 7.27–7.21 (m), 6.60 (t, J = 9.3 Hz, 2H), 3.14–2.92 (m, 4H), 1.56–1.41 (m), 1.35–1.14 (m), -16.85 (dt (q), J = 54.9, 1H). *Note that the presence of a paramagnetic species and BAr$^F_4$ prevents the accurate integration of the arene and alkyl –CH$_3$ peaks. ^{31}P{^{1}H} (THF-d$_8$, 162 MHz) δ ppm 113.41 (overlapping dt, J = 34.6, 25.0 Hz,

1P, PPh), 95.75 (dd, J = 29.5, 7.5 Hz, 2P, PiPr$_2$). ^{11}B NMR (THF-d_8, 128 MHz) δ ppm -4.68 (s). ^{19}F NMR (THF-d_8, 376 MHz) δ ppm -61.51 (s). IR (thin film from evaporation of THF-d_8; cm^{-1}): 2193 (ν_{NN}), 2162 (ν_{NN}), 2069 (ν_{FeH}).

EPR Spectral Analysis of Photolysis of [P_2^{PPh}Fe(H)]$_2$(μ-N_2). To two EPR tubes was added 200 μL each of a 3.4 μM stock solution of [P_2^{PPh}Fe(H)]$_2$(μ-N_2) in 2-MeTHF. The samples were frozen at 77 K and an EPR spectrum was collected for each tube. The samples were then carefully thawed to -78 °C in a dry ice/isopropanol bath and photolyzed for different amounts of time at -78 °C: 10 minutes and 1 hour. The samples were then quickly transferred to a liquid nitrogen bath and a second spectrum collected for each tube.

Experimental conditions: microwave frequency = 9.409 GHz; microwave power = 6.423 mW; modulation frequency = 100 kHz; modulation amplitude = 1 G; conversion time = 82 ms; time constant = 20.5 ms; temperature = 77 K. Simulation parameters: g = [2.0980 2.0900 2.0019]; ^{31}P1 A = [70 70 62] MHz, colinear with g; ^{31}P2 A = [76 76 66] MHz, colinear with g; ^{31}P3 A = [142 144 158] MHz, Euler angle β of 20° relative to g tensor; Hydride ^{1}H A = [18 64 52] MHz, Euler angle β of 20° relative to g tensor, Deuteride ^{2}D A = ^{1}H A*(g_n(^{2}D)/ g_n (^{1}H)) = [2.8 9.8 8.0] MHz.

NMR Spectral Analysis of Photolysis of P_2^{PPh}Fe(N_2)($H)_2$. To a quartz J. Young tube was added a solution of **3.5** (9.5 mg, 16.0 μmol) in 200 μL toluene-d_8 using a micropipettor. The vial containing the solution of **3.5** was subsequently washed (3 x 200 μL toluene-d_8). In a

separate vial, a toluene-d_8 stock solution of dioxane was prepared (1.17 M, 10 μL of dioxane in 90 μL of toluene-d_8). To the J. Young tube was added 14 μL of the dioxane solution and the tube quickly capped. Initial ^{31}P and ^{1}H NMR analysis of the solution pre-photolysis were collected at -78 °C. The J. Young tube was then cooled to -78 °C in an isopropanol/dry ice bath and subjected to varying amounts of Hg lamp photolysis. *All spectra were collected at -78 °C. Consumption of starting material was confirmed by comparing the relative integrations of the hydride protons to an internal standard (dioxane). A sample photo (Figure A3.43) is provided to show the drastic color change after 30 minutes of photolysis at -78 °C.

UV-Vis Spectral Analysis of Photolysis of $P_2^{PPh}Fe(N_2)(H)_2$. To a 1 cm cuvette was added 500 μL of a stock solution of **3.5** (1 mg, 0.8 μmol, in 3 mL THF). An additional 2.5 mL of THF was added to the cuvette before it was capped and removed from the glovebox. The cuvette was then chilled to -78 °C in the UV-Vis instrument and a spectrum acquired. The cuvette was then removed from the instrument and cooled to -78 °C in an isopropanol/dry ice bath and subjected to Hg lamp photolysis for 10 min. The cuvette was then carried quickly to the UV-Vis spectrometer in the -78 °C bath and inserted into the instrument where it was allowed to equilibrate for 2 minutes before a spectrum was acquired.

Mössbauer Analysis of Photolysis of $(P_2^{PPh})^{57}Fe(N_2)(H)_2$. To a Mössbauer cup was added 200 μL each of a 3.4 μM stock solution of **$(P_2^{PPh})^{57}Fe(N_2)(H)_2$** in 2-MeTHF. The sample was frozen at 77 K and a Mössbauer spectrum was collected of the starting material. The

sample was then photolyzed for different amounts of time at 77K: 10 minutes, 1 hour, and 4 hours and Mössbauer spectra collected after each time point.

EPR Spectral Analysis of Photolysis of $P_2^{PPh}Fe(N_2)(H)_2$. To two EPR tubes was added 200 μL each of a 3.4 μM stock solution of the **$P_2^{PPh}Fe(N_2)(H)_2$** in 2-MeTHF. The samples were frozen at 77 K and an EPR spectrum was collected for each tube. The samples were then carefully thawed to -78 °C in a dry ice/isopropanol bath and photolyzed for different amounts of time at -78 °C: 10 minutes and 30 minutes. The samples were then quickly transferred to a liquid nitrogen bath and a second EPR spectrum collected for each tube.

NMR Spectral Analysis of Photolysis of $(P_3^B)(\mu\text{-}H)FeN_2(H)$. Due to the instability of $(P_3^B)(\mu\text{-}H)FeN_2(H)$ to dynamic vacuum, the iron hydride-borohydride complex was generated in situ according to known methods.[56] To a Schlenk tube was added a suspension of $TPBFeN_2$ (26.8 mg, 39.7 μmol) in 1 mL of toluene-d_8 using a micropipettor. The vial containing the solution of $TPBFeN_2$ was subsequently washed (3 x 500 μL toluene-d_8) and the washings pipetted into the Schlenk tube. The tube was freeze-pump-thawed (3X), and an atmosphere of H_2 added. After stirring the reaction mixture overnight, the tube was freeze-pump-thawed (3X) again, and exposed to an atmosphere of N_2, before it was allowed to stir for 24 hours. The tube was then freeze-pump-thawed (3X) to get rid of any residual H_2 and exposed to an atmosphere of N_2. An 800 μL aliquot of the reaction mixture was pipetted into a J. Young NMR tube. Initial ^{31}P and ^{1}H NMR analysis of the light orange $(P_3^B)(\mu\text{-}H)FeN_2(H)$ solution pre-photolysis revealed no remaining $(P_3^B)(\mu\text{-}H)FeH_2(H)$ adduct. The J.

Young tube was cooled to -78 °C in an isopropanol/dry ice bath and subjected to Hg lamp photolysis for 10 min. Room temperature ^{1}H and ^{31}P NMR spectra of the reaction were obtained and revealed the growth of $(P_3^B)(\mu\text{-}H)FeH_2(H)$ and $P_3^BFeN_2$ in addition to remaining $(P_3^B)(\mu\text{-}H)FeN_2(H)$.

3.5 References

1. J. B. Howard, D. C. Rees, *Chem. Rev.* **1996**, *96*, 2965–2982.
2. B. K. Burgess, D. J. Lowe, *Chem. Rev.* **1996**, *96*, 2983–3012.
3. B. M. Hoffman, D. Lukoyanov, Z.-Y. Yang, D. R. Dean, L. C. Seefeldt, *Chem. Rev.* **2014**, *114*, 4041–4062.
4. S. J. Yoo, H. C. Angove, V. Papaefthymiou, B. K. Burgess, E. Münck, *J. Am. Chem. Soc.* **2000**, *122*, 4926–4936.
5. O. Einsle, F. A. Tezcan, S. L. A. Andrade, B. Schmid, M. Yoshida, J. B. Howard, D. C. Rees, *Science* **2002**, *297*, 1696–1700.
6. T. Spatzal, M. Aksoyoglu, L. Zhang, S. L. A. Andrade, E. Schleicher, S. Weber, D. C. Rees, O. Einsle, *Science* **2011**, *334*, 940.
7. B. M. Hoffman, D. Lukoyanov, D. R. Dean, L. C. Seefeldt, *Acc. Chem. Res.* **2013**, *46*, 587–595.
8. J. Kowalska, S. DeBeer, *Biochim. Biophys. Acta, Mol. Cell Res.* **2015**, *1853*, 1406–1415.
9. (a) P. E. M. Siegbahn, J. Westerberg, M. Svensson, R. H. Crabtree, *J. Phys. Chem. B* **1998**, *102*, 1615–1623. (b) I. Dance, *Dalton Trans.* **2010**, *39*, 2972–2983. (c) D. Smith, K. Danyal, S. Raugei, L. C. Seefeldt, *Biochem.* **2014**, *53*, 2278–2285. (d) P. E. M. Siegbahn, *J. Am. Chem. Soc.* **2016**, *138*, 10485–10495.
10. T. A. Bazhenova, A. E. Shilov, *Coord. Chem. Rev.* **1995**, *144*, 69–145.
11. D. V. Yandulov, R. R. Schrock, *Science* **2003**, *301*, 76–78.
12. V. Ritleng, D. V. Yandulov, W. Weare, R. R. Schrock, A. S. Hock, W. M. Davis, *J. Am. Chem. Soc.* **2004**, *126*, 6150–6163.
13. K. Arashiba, Y. Miyake, Y. Nishibayashi, *Nat. Chem.* **2011**, *3*, 120–125.
14. K. Arashiba, E. Kinoshita, S. Kuriyama, A. Eizawa, K. Nakajima, H. Tanaka, K. Yoshizawa, Y. Nishibayashi, *J. Am. Chem. Soc.* **2015**, *137*, 5666–5669.
15. S. Kuriyama, K. Arashiba, K. Nakajima, Y. Matsuo, H. Tanaka, K. Ishii, K. Yoshizawa, Y. Nishibayashi, *Nat. Commun.* **2016**, *7*, 12181–12189.
16. (a) S. Kuriyama, K. Arashiba, H. Tanaka, Y. Matsuo, K. Nakajima, K. Yoshizawa, Y. Nishibayashi, *Angew. Chem. Int. Ed.* **2016**, *55*, 14291–14295.
17. J. S. Anderson, J. Rittle, J. C. Peters, *Nature* **2013**, *501*, 84–87.
18. (a) G. Ung, J. C. Peters, *Angew. Chem. Int. Ed.* **2015**, *54*, 532–535. (b) G. Ung, J. C. Peters, *Angew. Chem.* **2015**, *127*, 542–545.
19. T. J. Del Castillo, N. B. Thompson, D. L. Suess, G. Ung, J. C. Peters, *Inorg. Chem.* **2015**, *137*, 7803–7809.
20. T. J. Del Castillo, N. B. Thompson, J. C. Peters, *J. Am. Chem. Soc.* **2016**, *138*, 5341–5350.
21. D. J. Lowe, R. N. F. Thorneley, *Biochem. J.* **1984**, *224*, 877–886.
22. G. Ertl, *J. Vac. Sci. Technol., A* **1983**, *1*, 1247–1253.
23. G. J. Leigh, M. Jimenez-Tenorio, *J. Am. Chem. Soc.* **1991**, *113*, 5862–5863.

24. S. Komiya, M. Akita, A. Yoza, N. Kasuga, A. Fukuoka, Y. Kai, *J. Chem. Soc., Chem. Commun.* **1993**, 787–788.
25. J. L. Crossland, D. R. Tyler, *Coord. Chem. Rev.* **2010**, *254*, 1883–1894.
26. L. C. Field, N. Hazari, H. L. Li, *Inorg. Chem.* **2015**, *54*, 4768–4776.
27. S. F. McWilliams, P. L. Holland, *Acc. Chem. Res.* **2015**, *48*, 2059–2065.
28. Y. Lee, N. P. Mankad, J. C. Peters, *Nat. Chem.* **2010**, *2*, 558–565.
29. (a) M.-E. Moret, J. C. Peters, *Angew. Chem. Int. Ed.* **2011**, *50*, 2063–2067. (b) M.-E. Moret, J. C. Peters, *J. Am. Chem. Soc.* **2011**, *133*, 18118–18121.
30. J. S. Anderson, M.-E. Moret, J. C. Peters. *J. Am. Chem. Soc.* **2013**, *135*, 534–537.
31. S. E. Creutz, J. C. Peters, *J. Am. Chem. Soc.* **2014**, *136*, 1105–1115.
32. M. J. Chalkley, T. J. Del Castillo, B. D. Matson, J. R. Roddy, J. C. Peters. *ACS Cent. Sci.*, **2017**, *3*, 217–223.
33. R. Y. Igarashi, M. Laryukhin, P. C. Dos Santos, H.-I. Lee, D. R. Dean, L. C. Seefeldt, B. M. Hoffman, *J. Am. Chem. Soc.* **2005**, *127*, 6231–6241.
34. F. B. Simpson, R. H. Burris. *Science* **1984**, *224*, 1095–1097.
35. (a) D. Lukoyanov, N. Khadka, Z.-Y. Yang, D. R. Dean, L. C. Seefeldt, B. M. Hoffman, *J. Am. Chem. Soc.* **2016**, *138*, 10674–10683. (b) D. Lukoyanov, N. Khadka, Z.-Y. Yang, D. R. Dean, L. C. Seefeldt, B. M. Hoffman, *J. Am. Chem. Soc.* **2016**, *138*, 1320–1327.
36. A. Sacco, M. Aresta, *Chem. Commun.* **1968**, 1223–1224.
37. M. Aresta, P. Giannoccaro, M. Rossi, A. Sacco, *Inorg. Chim. Acta* **1971**, *5*, 115–118.
38. M. K. Whittlesey, R. J. Mawby, R. Osman, R. N. Perutz, L. D. Field, M. P. Wilkinson, M. W. George, *J. Am. Chem. Soc.* **1993**, *115*, 8627–8637.
39. L. S. Van Der Sluys, J. Eckert, O. Eisenstein, J. H. Hall, J. C. Huffman, S. A. Jackson, T. F. Koetzle, G. J. Kubas, P. J. Vergamini, K. G. Caulton, *J. Am. Chem. Soc.* **1990**, *112*, 4831–4841.
40. J. Ballmann, R. F. Munha, M. D. Fryzuk, *Chem. Commun.* **2010**, *46*, 1013–1025.
41. N. P. Mankad, E. Rivard, S. B. Harkins, J. C. Peters. *J. Am. Chem. Soc.* **2005**, *127*, 16032–16033.
42. A. W. Addison, T. N. Rao, J. Reedijk, J. van Rijn, G. C. Verschoor, *J. Chem. Soc., Dalton Trans.* **1984**, 1349–1356.
43. T. A. Betley, J. C. Peters. *J. Am. Chem. Soc.* **2004**, *126*, 6252–6254.
44. P. J. Hill, L. R. Doyle, A. D. Crawford, W. K. Myers, A. E. Ashley, *J. Am. Chem. Soc.* **2016**, *138*, 13521–13524.
45. M. Brookhart, B. Grant, A. F. Volpe Jr., *Organometallics* **1992,** *11*, 3920-3922.
46. I. S. Weitz, M. Rabinovitz., *J. Chem. Soc., Perkin Trans. 1* **1993,** 1, 117-120.
47. D. F. Evans, *J. Chem. Soc.*, **1959**, 2003.
48. G. M. Sheldrick, *Acta Cryst.* **1990**, A46, 467-473.
49. G. M. Sheldrick, *Acta Cryst.* **2008**, A64, 112-122.
50. P. Müller, *Crystallography Reviews* **2009**, *15*, 57-83.
51. S. Stoll, A. Schweiger, EasySpin, a comprehensive software package for spectral simulation and analysis in EPR. *Journal of Magnetic Resonance* **2006,** *178*, *1*, 42-55.
52. J. S. Hyde, M. Pasenkiewicz-Gierula, A. Jesmanowicz, W. E. Antholine, Pseudo field modulation in EPR spectroscopy. *Applied Magnetic Resonance* **1990,** *1* (3), 483-496.

53. M. W. Weatherburn, *Anal. Chem.* **1967**, *39*, 971-974.
54. G. W. Watt, J. D. Crisp, *Anal Chem.* **1952**, *24*, 2006.
55. H. Fong, M.-E. Moret, Y. Lee, J. C. Peters, *Organometallics,* **2015**, *32*, 3053.

Chapter 4

NOVEL LIGAND FRAMEWORKS FOR HETEROBIMETALLIC COMPLEXES

4.1 Introduction

In this chapter, the synthesis and reactivity of heterobimetallic complexes supported by novel ligand frameworks is discussed. Although bimetallic complexes have been studied in the past,[1-3] only recently has their application to catalytic transformations been explored.[4-10] Herein, we describe the synthesis of two structurally related dinucleating ligands, P_2^{SiCp} and P_2^{PCp}, designed to accommodate both an early and late metal center using asymmetric metal binding sites. In this context, both Fe and Zr can be site-specifically installed. Preliminary reactivity studies with these two ligand platforms suggests that the P_2^{PCp} system is more amenable towards achieving cooperative reactivity.

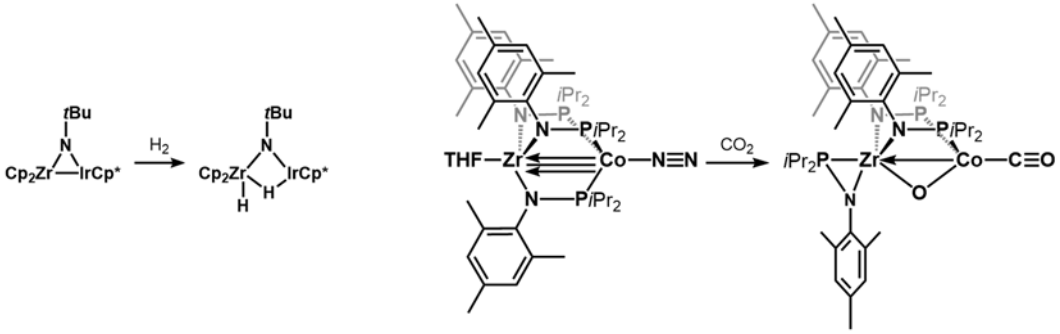

Figure 4.1. Examples of small molecule activation by heterobimetallic complexes. (Left) H_2 activation[11] and (right) CO_2 activation.[12]

While many monometallic catalysts have been described in the literature, heterobimetallic catalysts systems are less common. A bimetallic approach may lead to divergent reactivities, mechanisms, and transformations not possible with mononuclear systems. Early–late heterobimetallic complexes containing both Lewis acidic and Lewis basic metal centers have been reported to exhibit cooperative

activation of non-polar small molecules, such as N_2,[13] H_2,[8] and CO_2 (Figure 4.1).[12] Unlike systems with one transition metal center and a metalloid, such as Na, Al, or B, bimetallic complexes containing two transition metals provide additional d-orbitals for ligand interactions.[14] The incorporation of two different metals may impart unique characteristics, including redox properties,[13, 15] metal-metal bonding,[11, 16] and cooperative substrate binding.[17]

Studying the small molecule binding and reactivity of heterobimetallic model complexes may also provide insight into the nature of small molecule binding and activation in biological systems, which often contain heterometallic active sites.[18-21] For instance, the observation that N_2 fixation occurs most efficiently at an enzyme active site containing multiple Fe centers and a Mo center (in FeMo nitrogenase) suggests that more than one of these metals participates in N_2 activation. In fact, out of the three known types of nitrogenases (FeFe, FeV, and FeMo), the FeMo nitrogenase is the most efficient for N_2 reduction to NH_3 under ambient conditions.[22] Interestingly, FeV nitrogenase is the most effective for CO reduction to C_2 and other hydrocarbon products.[23] Although the mechanism by which these active sites mediate substrate reduction is unknown, but the differing nature of the metals in the active site may lead to different substrate selectivities. Many monometallic Fe and Mo complexes are capable of catalytic N_2 reduction to NH_3,[24-26] such as the examples discussed in Chapters 1 and 3, but no hetereobimetallic complexes capable of catalytic N_2 fixation have been reported. These observations merit the development of simplified heterobimetallic complexes capable of substrate binding and reduction,

such as with N_2. Studying the binding modes supported by these complexes as well as their catalytic properties may help guide our analysis of more complex systems.

Herein, we describe the synthesis of dinucleating ligands designed to accommodate small molecule binding between an early and late metal center. Given the wealth of metallocene chemistry,[27] we chose to incorporate a cyclopentadienyl (Cp) fragment to bind the early metal center in our dinucleating framework and phosphine ligands to bind the late metal center. To demonstrate that the dinucleating ligand framework accommodates two different metals and allows for substrate binding between the two metals, we targeted FeZr complexes.

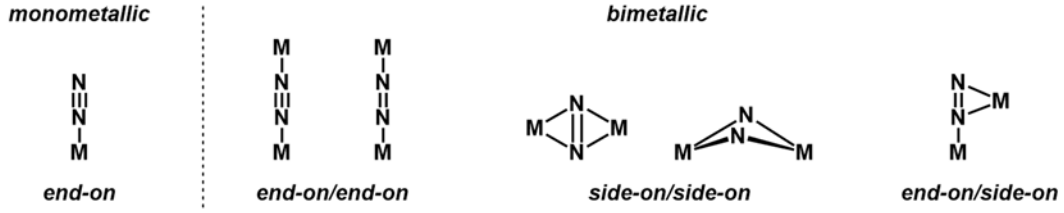

Figure 4.2. Previously reported binding modes for monometallic and bimetallic metal complexes.

Zr was of particular interest due to its ability to bind N_2 through different coordination modes (Figure 4.2); for example, zirconocene complexes are capable of bridging dinitrogen in the common end-on/end-on fashion as well as in a side-on/side-on and side-on/end-on fashion, depending on the nature of the Cp ligand.[28-30] Unlike Zr, Fe has only been reported to bind N_2 in an end-on fashion either terminally or by bridging the N_2 ligand to a second metal center.[31-33] Since the relationship between the nature of N_2 binding and functionalization are still being explored,[34] we hoped to design a dinucleating ligand that could accommodate all

three binding-modes. By incorporating both Zr and Fe, it may be possible to access new N_2 binding modes for Fe as well as access new reactivities towards small molecules such as CO_2, H_2, and olefins.

In the first part of the chapter, a P-Si-P ligand containing a pendant Cp group is discussed. This particular ligand supports [Fe(μ-H)$_2$Zr(X)] units with two bridging hydride ligands that hold the two metals in close proximity; however, no Fe–Zr interaction is observed. These complexes are diamagnetic and were characterized using a variety of spectroscopic techniques and X-ray crystallography. Although this ligand platform showed that an early and late metal could be accommodated by the novel dinucleating ligand, the formation of bridging hydrides between the two metal centers hindered additional reactivity studies. In the second part of the chapter, a related P-P'-P ligand platform with a pendant Cp group is discussed in which the formation of an FeZr complex without bridging hydrides is achieved. Along the way, the reactivity of the monometallic P_2^{PCp}Fe complex was explored.

4.2 Results and Discussion

4.2.1 Synthesis and Reactivity of P_2^{SiCp}-Supported Complexes

To achieve site selective metalation of two different metals, a novel ligand containing a cyclopentadienyl fragment for binding of an early metal center and a SiP_2 fragment for binding of a late metal center was synthesized (Scheme 4.1). The previously reported $HSiP_2Cl$ precursor[35] was treated with 5 equivalents of LiCp in THF with gentle heating to provide P_2^{SiHCp} (**4.1**) in 63% yield on gram scales.

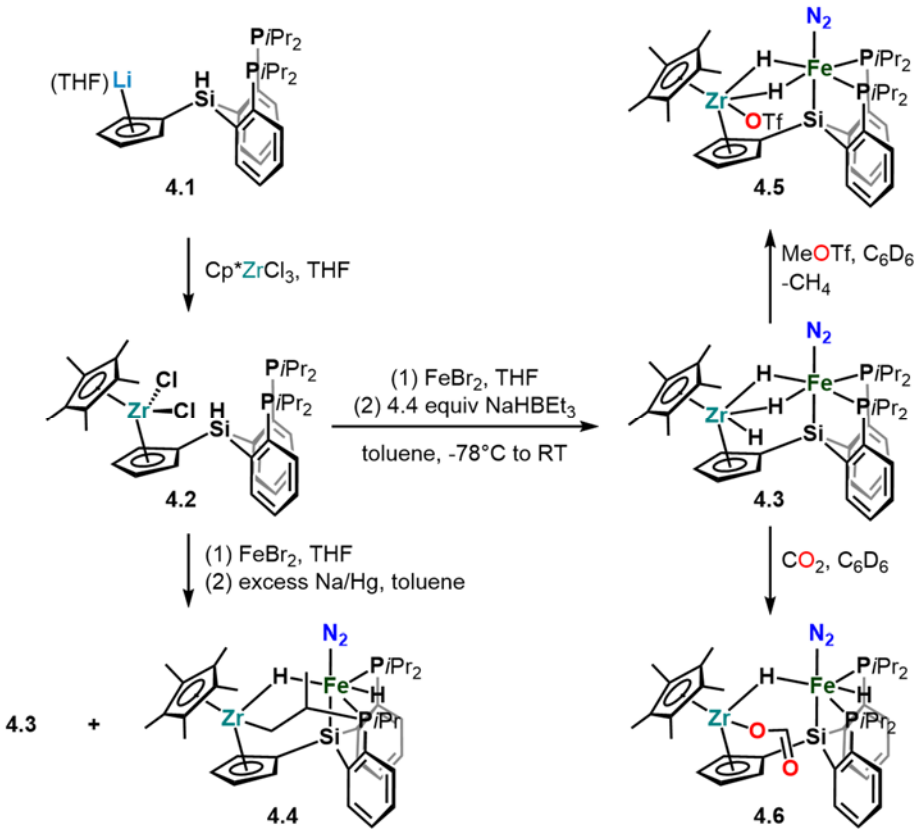

Scheme 4.1. Synthesis of P_2^{SiCp} and P_2^{SiCp}-supported complexes.

The resonances corresponding to the protons on the Cp portion of the ligand are observed in the ^{1}H NMR spectrum as a doublet of triplets at 6.57 ppm. This resonance splits into two distinct triplet resonances at 6.79 and 6.05 ppm when **4.1** is treated with commercially available Cp*ZrCl$_3$ in THF at room temperature (see appendix). In addition, a new singlet at 1.82 ppm in the ^{1}H NMR spectrum, corresponding to the incorporation of the 15 protons of the Cp*–Me substituents, confirms the formation of **4.2** in 66% yield (Scheme 4.1). An X-ray crystal structure of **4.2** is shown in Figure 4.3. Interestingly, in the solid-state structure of the complex, there is no interaction between the phosphorus atoms of the ligand and the Zr center. This can be attributed to the unfavorable steric interaction that would arise between

the methyl substituents on the Cp* ligand and the isopropyl groups on the phosphorus atoms.

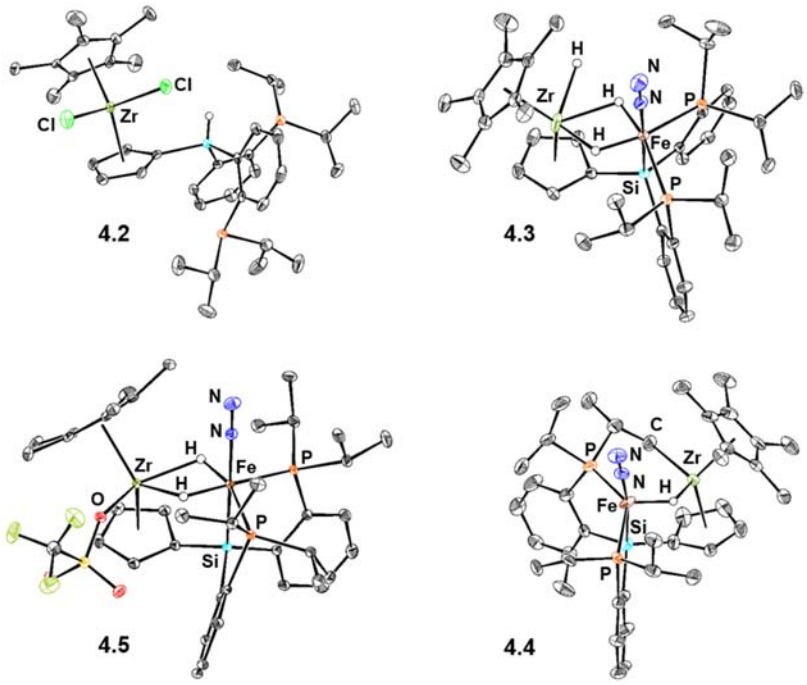

Figure 4.3. X-ray crystal structures of P_2^{SiCp}-supported complexes. Ellipsoids are shown at 50% probability.

Recently reported syntheses of homobimetallic diiron complexes from our group provided insight into possible Fe metalation strategies at the Si–H binding site.[36-37] Complexation of **4.2** with 1.1 equivalents of $FeBr_2$, followed by reduction with six equivalents of sodium amalgam provided a mixture of products from which **4.3** and **4.4** could be identified (Scheme 4.1, Figure 4.3). The X-ray structure of **4.3** (Figure 4.3) shows two bridging hydride ligands between the Fe and Zr centers as well as a terminal hydride ligand on the Zr center in the Fourier difference map. One of the hydride ligands is a result of the Si–H bond activation upon Fe metalation.

Because the complexation of $FeBr_2$ does not go to completion, given the lability of $FeBr_2$ in the bisphosphine framework, the other two hydride ligands could come from C–H activation of the Cp*–Me groups or the isopropyl groups of a zirconocene species. C–H activation of the solvent is also a possibility. All three hydride resonances are detected in the ^1H NMR spectrum and the expected coupling between the hydride ligands is confirmed by the COSY NMR spectrum (see appendix). Two inequivalent phosphine resonances are observed in the ^{31}P spectrum, consistent with the C_1 symmetry of the complex. An N_2 stretch of 2065 cm^{-1} is observed in the solid state IR spectrum and a *d*(N–N) of 1.114 Å is observed in the X-ray crystal structure, consistent with weak activation.

One potential mechanism by which complex **4.4** is formed upon reduction of the $Zr(IV)Cl_2$ fragment to a Zr(II) intermediate, which could undergo an intramolecular C–H bond activation of the ligand. The solid state structure of **4.4** shows the presence of one bridging hydride, consistent with one of the two hydridic resonances observed in the ^1H NMR spectrum at -15.60 and -18.70 ppm. The COSY NMR of the crude reaction mixture confirms the coupling between these two hydride signals (see appendix). Although the second hydride could not be located by X-ray crystallography, the doublet of triplets at -18.70 ppm in the ^1H NMR is consistent with the second hydride coupling to the bridging hydride ligand and two 'equivalent' phosphine ligands, suggesting that the second hydride is located between the two phosphorus atoms. Decoupling experiments, ^1H (^{31}P decoupled) and ^{31}P (^1H decoupled), as well as HMBC NMR spectroscopy corroborate the structural assignment of **4.4** (see appendix). The wider P–Fe–P' bond angle of 133.32°

observed in the solid state structure of **4.4** relative to the 106.82° bond angle observed for **4.3** is also consistent with this structural assignment (Figure 4.3).

A reproducible synthetic route to **4.3** was accessed by complexation of **4.2** with 1.1 equivalents of $FeBr_2$, followed by the addition of 4.4 equivalents of $NaHBEt_3$,[38-39] providing **4.3** in 28% yield as the major Fe-containing species by ^1H and ^{31}P NMR spectroscopy (Scheme 4.1). The diamagnetism of **4.3** allows for the formal oxidation state of the two metal centers to be assigned as Fe(II) and Zr(IV), with both metals having an 18 electron count. Furthermore, the internuclear Fe–Zr distance of 2.97 Å, determined in the solid state structure of **4.3**, indicates that there is no Fe–Zr bond. Although there is no Fe–Zr bond, the two metal centers could still communicate electronically. To determine whether the metals interact electronically, the terminal hydride ligand on the Zr center was replaced with an electron withdrawing triflate group. Treatment of **4.3** with methyl triflate provided **4.5** as a dark turquoise crystalline solid in 70% yield. An X-ray structure of **4.5** is shown in Figure 4.3 and confirms the replacement of the terminal Zr hydride ligand with an electron-withdrawing triflate ligand. Given the different electronic and steric profiles of the terminal ligands on the Zr center in **4.3** and **4.5**, a less activated N_2 ligand of **4.5** might be expected. Indeed, a stretch of 2077 cm^{-1} in the solid state IR spectrum of **4.5** was determined, suggesting that the electron withdrawing triflate group on the Zr center results in a less activated N_2 on the more electron deficient Fe center.

As seen in the solid state structure of the complexes above, the desired side-on or side-on/end-on coordination modes of N_2 were not achieved. To learn whether the heterobimetallic complex could bridge other substrates, **4.3** was treated with CO_2.

CO_2 reduction to formate and other reduced products is thought to proceed by hydride insertion. Although **4.3** has three M-H bonds only one insertion event occurs with the terminal Zr-H (Scheme 4.1, compound **4.6**). The bridging hydride ligands do not react in the presence of excess CO_2. Other small molecules, such as CO and and tBuNC led to displacement of N_2 on the Fe center. Overall, cooperative reactivity between the two metals was not observed. From this point, a new ligand system was targeted.

4.2.2 Synthesis and Reactivity of P_2^{PCp}-Supported Complexes

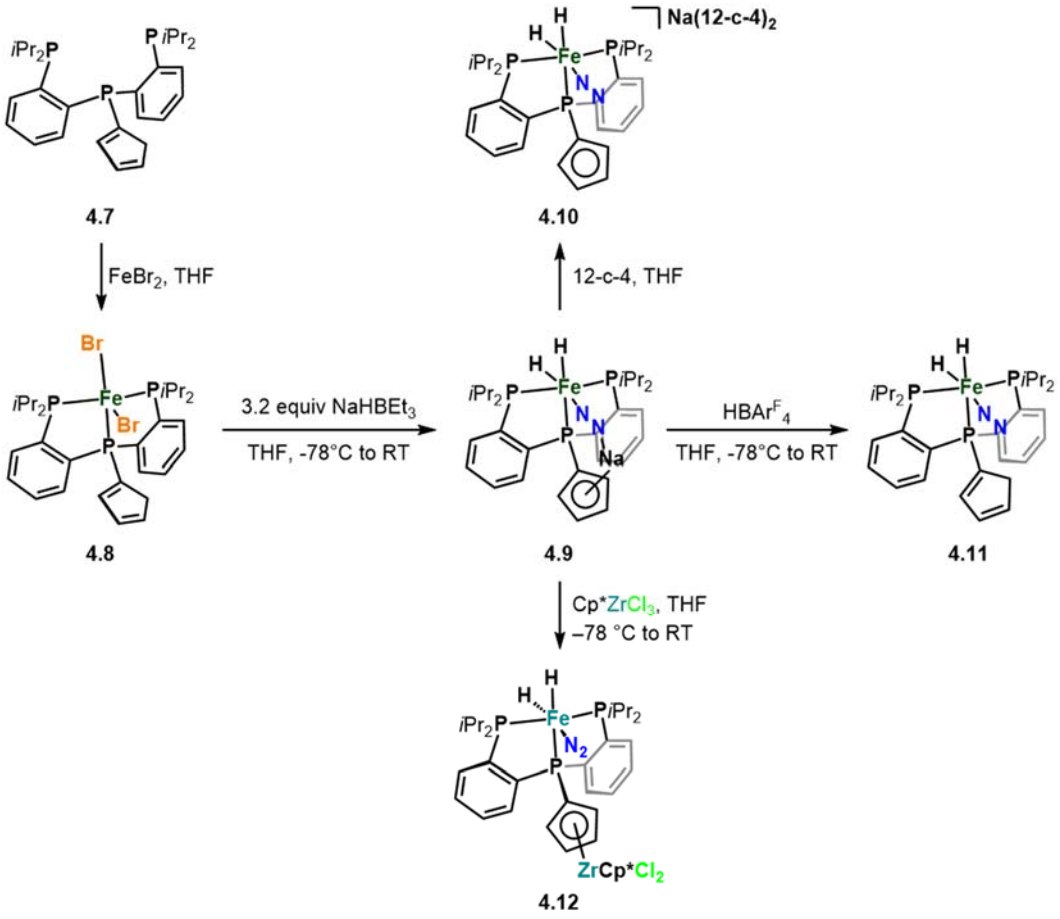

Scheme 4.2. Synthesis of P_2^{PCp} and P_2^{PCp}-supported complexes.

P_2^{PCp} (**4.7**) was synthesized by the addition of LiCp to the known bis(*o*-diisopropylphosphino-phenyl)-chlorophosphine[40] and exhibits a doublet at δ = -1.9 ppm and two overlapping triplets centered at δ = -28.9 ppm by ^{31}P NMR spectroscopy, suggesting a mixture of rotamers (see appendix). Complexation of **4.7** with one equivalent of $FeBr_2$ yielded paramagnetic $P_2^{PCp}FeBr_2$ **4.8** as a purple-black crystalline solid (Scheme 4.2). Treatment of **4.8-FeBr$_2$** with three equivalents of $NaHBEt_3$ in THF at low temperature under an N_2 atmosphere provided the diamagnetic $[P_2^{PCp}Fe(N_2)(H)_2]Na$ complex (**4.9**).

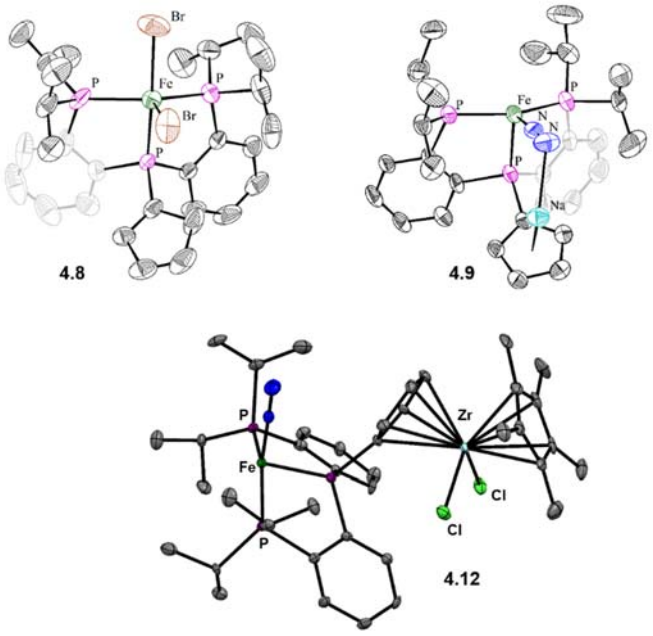

Figure 4.4. X-ray crystal structures of P_2^{PCp}-supported complexes. Ellipsoids are shown at 50% probability.

Excitingly, the solid-state structure of **4.9** demonstrated that the P_2^{PCp} ligand was capable of supporting N_2 between the two metal binding sites (Figure 4.4, upper right). Complex **4.9** exhibits an N_2 stretch of 1993 cm^{-1} in the solid state IR. The

neutral complex **4.11** could be generated by treating **4.9** with an equivalent of $HBAr^F_4$ and exhibits an N_2 stretch of 2068 cm^{-1}. Upon treatment of **4.9** with two equiv of 12-c-4, a shift in the N-N vibration to 2031 cm^{-1} was observed. **4.9** serves as a good starting material for the generation of heterobimetallic complex **4.12** (Scheme 4.2). As expected, the Cp ring is oriented down to avoid steric interactions between the isopropyl groups on the phosphines ligated to iron and the ligands on Zr in the solid state structure (Figure 4.4 bottom).

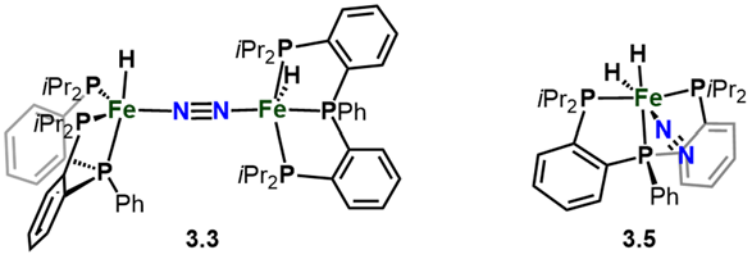

Figure 4.5. Catalysts discussed in Chapter 3.

Ligand **4.7** differs from ligand **3.1** (discussed in Chapter 3) by the replacement of the phenyl group with a cyclopentadienyl group. Given the similarities of catalysts **3.5** (Figure 4.5), and **4.9**, we anticipated that the latter would catalyze the reduction of dinitrogen to ammonia. To our delight, we observed catalytic amounts of ammonia upon treatment of **4.9** with $HBAr^F_4$ and KC_8. Mononuclear **4.9** gives a comparable yield to dinuclear complex **3.3** (discussed in Chapter 3), both in the absence and presence of light (entries 1-4). Performing the catalysis in the presence of a blue LED increases the amount of ammonia formed (entry 5). Interestingly, the structurally similar $P_2^{PPh}Fe(N_2)(H)_2$ (**3.5**), which contains a –Ph group in place of the "NaCp" group, provides a lower yield of ammonia (2.6 ± 0.1 equiv when 150 equiv of $HBAr^F_4$ and 180 equiv of KC_8 used). The crown ether

encapsulated Na salt **4.10** is also a competent catalyst for dinitrogen reduction (entries 7). Most interestingly, the hetereobimetallic complex **4.12** yields slightly more ammonia (6.4 equiv) than the Fe-only analogue (4.1 ± 0.3 equiv). Although additional studies are needed to fully understand the nature of this enhancement, Zr appears to benefit the catalysis. It would be interesting to look at other reaction conditions to determine whether the improved yield using the heterobimetallic catalyst can be enhanced further. Additional reductants, such as Na/Hg and Cp^*_2Co, in place of KC_8, were also attempted but did not lead to ammonia formation.

Table 4.1. Catalytic dinitrogen reduction to ammonia with synthetic iron complexes.[a]

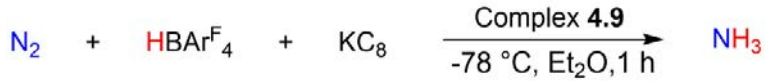

	Variation	$HBAr^F_4$ (equiv)	KC_8 (equiv)	Mean ± SD (equiv NH_3)
1	None	41	49	4.1 ± 0.3
2	Hg Lamp	41	49	5.9 ± 0.4
3	None	136	170	5.0 ± 0.6
4	Hg Lamp	136	170	8.4 ± 0.1
5[b]	Blue LED	136	170	10.8
6[c]	**4.10** instead of **4.9**	150	180	4.8 ± 0.2
7[b]	**4.12** instead of **4.9**	46	50	6.4

[a] All entries are an average of 3 runs unless otherwise noted.
[b] Result of a single run.
[c] Average of 2 runs.

Iron-catalyzed olefin hydrogenations have been previously reported.[41-46] In the case of the triphos-supported **4.9**, we speculated that the NaCp moiety of the complex could mediate proton delivery to the olefin by acting as a proton relay.

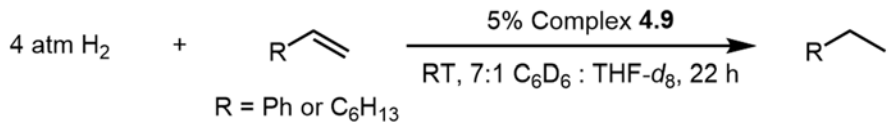

Scheme 4.3. Catalytic hydrogenation of styrene using **4.9**.

Upon addition of an excess of styrene and 4 atm of H_2 to complex **4.9** at room temperature, we observed the formation of ethylbenzene (Scheme 4.3). The disappearance of styrene and the appearance of the hydrogenated product was detected by ^{1}H NMR spectroscopy (see appendix) and the product confirmed by GC-MS. An unactivated olefin, 1-octene, could also be successfully hydrogenated using **4.9**. Stoichiometric experiments with the olefin and H_2 substrates were conducted to gain mechanistic insights. Although treatment of **4.9** with 1.1 equiv of styrene led to no observable reaction by ^{1}H NMR spectroscopy (see appendix), the addition of H_2 to **4.9** led to the formation of an H_2 adduct (see appendix). Additional studies are required to determine what role the NaCp unit plays in catalysis.

4.3 Conclusions

Heterobimetallic complexes containing an early metal and late metal center could lead to the cooperative binding and activation of non-polar substrates. Progress towards ligand frameworks that can support Lewis acidic and Lewis basic metal centers has been made. In part one of this chapter, we describe **[Fe(μ-H)$_2$Zr(X)]**

complexes which support two bridging hydride ligands between the Fe and Zr metal centers. In the second part of chapter four, we describe a structurally related P_2^{PCp} ligand capable of supporting Fe and Na which are bridged by dinitrogen. Using **4.9**, Zr can be installed to yield a heterobimetallc complex, **4.12**, which also catalyzes the reduction of dinitrogen to ammonia. Beyond nitrogen reduction, we discovered that **4.9** is also a catalyst for olefin hydrogenation.

4.4 Experimental Section

4.4.1 General Information

General Considerations. All manipulations were carried out using standard Schlenk or glovebox techniques under an N_2 atmosphere. Unless otherwise noted, solvents were deoxygenated and dried by thoroughly sparging with N_2, followed by passage through an activated alumina column in a solvent purification system by SG Water, USA LLC. Solvents were tested with a standard purple solution of sodium benzophenone ketyl in tetrahydrofuran in order to confirm effective moisture removal. Deuterated solvents were purchased from Cambridge Isotope Laboratories, Inc., degassed, filtered through an alumina plug, and dried over 3 Å molecular sieves prior to use. Bis(*o*-diisopropylphosphino-phenyl)-chlorosilane,[35] bis(*o*-diisopropylphosphino-phenyl)-chlorophosphine,[40] $[Na][BAr^F{}_4]$,[47] $[H(OEt_2)_2][BAr^F{}_4]$,[47] and KC_8[48] were prepared according to literature procedures. All other reagents were purchased from commercial vendors and used without further purification unless otherwise stated.

Physical Methods. Elemental analyses were performed by Midwest Microlabs, LLC (Indianapolis, IN) or at the Beckman Institute Crystallography facility on a PerkinElmer 2400 Series II CHN Elemental Analyzer. ^1H and ^{13}C NMR chemical shifts are reported in ppm relative to proton and carbon resonances from solvents as internal standards. Solution phase magnetic moments were acquired using the Evans method.[49] Optical spectroscopy measurements were taken on a Cary 50 UV-vis

spectrophotometer using a 1-cm two-window quartz cell. Fourier transform infrared ATR spectra were collected on a Bruker ATR Spectrometer with diamond ATR crystal (utilized iD5 ATR insert).

Mössbauer Spectroscopy. Mössbauer spectra were recorded on a spectrometer from SEE Co. (Edina, MN) operating in the constant acceleration mode in a transmission geometry. The sample was kept in an SVT-400 cryostat from Janis (Wilmington, MA). The quoted isomer shifts are relative to the centroid of the spectrum of a metallic foil of α-Fe at room temperature. Solid samples were prepared by grinding solid material into a fine powder and then mounting in a Delrin cup fitted with a screw-cap as a boron nitride pellet. Solution samples were transferred to a sample cup and chilled to 77 K inside of the glovebox, and unless noted otherwise, quickly removed from the glovebox and immersed in liquid N_2 until mounted in the cryostat. Data analysis was performed using version 4 of the program WMOSS (www.wmoss.org) and quadrupole doublets were fit to Lorentzian lineshapes. Unless otherwise noted, Mössbauer spectra were collected with an applied 50 mT parallel field at 80 K.

X-ray crystallography. XRD studies were carried out at the Beckman Institute Crystallography facility on a Bruker Kappa Apex II diffractometer (Mo Kα radiation). Structures were solved using OLEX and refined against F2 on all data by full-matrix least squares with SHELXL. The crystals were mounted on a glass fiber or a nylon loop with paratone N oil.

Ammonia Quantification. The catalytic reaction mixture was cooled to 77 K and allowed to freeze. The reaction vessel was opened to the atmosphere and to the frozen solution was slowly added a fourfold excess (with respect to acid) solution of a NaO^{t}Bu in MeOH (0.25 M) over 1–2 minutes. The solution was allowed to freeze, then the tube was sealed and allowed to warm to room temperature and stirred at room temperature for 10 minutes. An additional Schlenk tube was charged with HCl (3 mL of a 2.0 M solution in Et_2O, 6 mmol) to serve as a collection flask. The volatiles of the reaction mixture were vacuum transferred into the collection flask. After completion of the vacuum transfer, the collection flask was sealed and warmed to room temperature. Solvent was removed *in vacuo*, and the remaining residue dissolved in H_2O (1 mL) to make a stock solution that was used for both the ammonia ad hydrazine quantification. An aliquot of this solution (20 μL) was then analyzed for the presence of NH_3 (present as NH_4Cl) by the indophenol method.[50] Quantification was performed with UV−Vis spectroscopy by analyzing the absorbance at 635 nm.

Standard NH_3 Generation Reaction Procedure for 4.9. All solvents were stirred with Na/K for ≥1 hours and filtered through alumina prior to use. In a nitrogen-filled glovebox, a stock solution of the catalyst in THF (10 mM) was prepared. (Note: a fresh stock solution was prepared for each experiment and used immediately.) An aliquot of this stock solution (60–200 μL, 0.68–2.3 μmol) was added to a Schlenk tube and evaporated to dryness under vacuum to give a thin film of **4.9**. The tube was

allowed to cool to 77 K in the glovebox cold well. To the cold tube was added a solution of $[H(OEt_2)_2][BAr^F{}_4]$ (93 mg, 0.092 mmol) in Et_2O (0.5 mL). This solution was allowed to freeze before the vial which contained the $HBAr^F{}_4$ was rinsed with an additional 0.5 mL of Et_2O and added to the tube. After the acid layer froze, a suspension of KC_8 (15 mg, 0.111 mmol) in 0.5 mL of Et_2O (1.2 equiv relative to $[H(OEt_2)_2][BAr^F{}_4]$) was added to the cold tube. The temperature of the system was allowed to equilibrate for 5 minutes. A stir bar was added to the tube and the tube sealed with a Teflon screw-valve. The Schlenk tube was passed out of the box into a liquid N_2 bath and transported to a fume hood. The reaction vessel was then transferred to a dry ice/acetone bath where it thawed to -78 °C and was allowed to stir for at least 1 hour. The tube was then warmed to room temperature with stirring, and stirred at room temperature for 5 minutes.

Standard NH_3 Generation Reaction with Hg Lamp Photolysis Procedure for 4.9. All solvents were stirred with Na/K for ≥1 hours and filtered through alumina prior to use. In a nitrogen-filled glovebox, a stock solution of the catalyst in THF (10 mM) was prepared. (Note: a fresh stock solution was prepared for each experiment and used immediately.) An aliquot of this stock solution (60–200 μL, 0.68–2.3 μmol) was added to a Quartz Schlenk tube and evaporated to dryness under vacuum to give a thin film of **3.9**. The tube was allowed to cool to 77 K in the glovebox cold well. To the cold tube was added a solution of $[H(OEt_2)_2][BAr^F{}_4]$ (93 mg, 0.092 mmol) in Et_2O (0.5 mL). This solution was allowed to freeze before the vial that contained the $[H(OEt_2)_2][BAr^F{}_4]$ was rinsed with an additional 0.5 mL of Et_2O and added to the

tube. After the acid layer had frozen, a suspension of KC_8 (15 mg, 0.111 mmol, 1.2 equiv relative to $[H(OEt_2)_2][BAr^F{}_4]$ in 0.5 mL of Et_2O was added to the cold tube. The temperature of the system was allowed to equilibrate for 5 minutes. A stir bar was added to the tube before it was sealed with a Teflon screw-valve. The Schlenk tube was passed out of the box into a liquid N_2 bath and transported to a fume hood. The reaction vessel was then transferred to a dry ice/isopropanol bath which was positioned under a Hg lamp and turned on 1 minute prior to transfer of the Schlenk tube to the bath. The entire reaction apparatus was surrounded by foil and the reaction vessel was allowed to stir for at least 1 hour before the Hg lamp was turned off and the Schlenk tube was allowed to warm to room temperature with stirring, and stirred at room temperature for 5 minutes.

Standard NH_3 Generation Reaction with Blue LED Photolysis Procedure with 4.9. The procedure was identical to that of the standard catalytic reaction protocol with Hg lamp photolysis with the changes noted. A blue LED was used in place of a Hg lamp.

Standard NH_3 Generation Reaction Procedure with 4.10. The procedure was identical to that of the standard catalytic reaction protocol with the changes noted. A suspension of **4.10** (1.9 mg, 2.0 μmol) was prepared in THF (300 μL). An addition 300 μL was used to the rinse the vial containing **4.10** and the solvent removed *in vacuo*.

Standard NH_3 Generation Reaction Procedure with 4.12. The procedure was identical to that of the standard catalytic reaction protocol with the changes noted. A stock solution of **4.12** in THF was prepared. (Note: a fresh stock solution was prepared for each experiment and used immediately.)

Standard NH_3 Generation Reaction Procedure for 4.9 and Cp_2^*Co as the Reductant. The procedure was identical to that of the standard catalytic reaction protocol with the changes noted. Cp_2^*Co was used as the reductant.

Standard NH_3 Generation Reaction Procedure for 4.9 and Na (Hg) as the Reductant. The procedure was identical to that of the standard catalytic reaction protocol with the changes noted. Na/Hg was used as the reductant.

4.4.2 Synthesis Details

P_2^{SiCp}-Supported Complexes

P_2^{SiHCp} (4.1, Cp'). $HSi(Cl)(P^{iPr})_2$ (5.19 g, 11.5 mmol) and LiCp (3.5 g, 48.6 mmol) were combined in THF (40 mL), removed from the glovebox, and heated to 62°C. After two days, the reaction mixture was cooled to room temperature and concentrated. The crude orange oil was introduced to the dry box, resuspended in C_6H_6 (40 mL) and filtered through celite. The orange filtrate was concentrated, triterated with pentane (3 x 15 mL), concentrated, and resuspended in pentane (10 mL), resulting in the precipitation of an off-white solid. The suspension was allowed to sit at -35°C overnight. The off-white precipitate was collected on a glass-frit (F) and washed with pentane (3 x mL). The resulting off-white powder, $HSi(Cp)(P^{iPr})_2$ (**4.1**, 3.51 g, 7.22 mmol, 63%), was dried under vacuum. ^{1}H NMR (5 : 1 C_6D_6 : THF-d_8, 400 MHz, ppm): δ 7.94 (d, J = 7.6 Hz, 2H, Ar-H), 7.44 (dd, J = 7.8, 2.7 Hz, Ar-H), 7.25 (m, 2H, Ar-H), 7.15 (t, J = 7.4 Hz, 2H, Ar-H), 6.76 (t, J = 4.9 Hz, 1H, Si-H), 6.57 (dt, J = 15.1, 2.4 Hz, 4H, Cp-H), 2.19 (m, 2H, methine C-H), 2.09 (m, 2H, methine C-H), 1.16 (m, 12H, methyl C-H), 1.04 (m, 12H, methyl C-H). ^{13}C NMR (5 : 1 C_6D_6 : THF-d_8, 100.6 MHz, ppm): δ 148.25 (dd, J = 41.0, 2.5 Hz), 142.96 (d, J = 13.3 Hz), 139.07 (dd, J = 13.4, 1.5 Hz), 131.26 (d, J = 2.3 Hz), 128.23 (s), 127.89 (d, J = 1.4 Hz), 115.22 (s), 108.29 (s), 25.25 (dd, J = 13.6, 2.3 Hz), 24.73 (d, J = 13.5 Hz), 20.42 (m). ^{31}P NMR (5 : 1 C_6D_6 : THF-d_8, 161.9 MHz, ppm) δ -0.18. ^{29}Si NMR (5 : 1 C_6D_6 : THF-d_8, 79.47 MHz, ppm): δ -32.6 (t, J_{Si-P} = 20.4 Hz, Si–H). IR

(solid): ν(Si-H) = 2137, 2107 cm^{-1}. ESI-MS (electrospray): calcd for $C_{29}H_{41}AgP_2Si$ *m/z* 586.2, found (M+) 587.1 *m/z*.

Cp*Cp'ZrCl$_2$ (4.2). Cp*ZrCl$_3$ (605 mg, 1.82 mmol) and **4.1** (884 mg, 1.82 mmol) were combined in THF (5 mL) in the glovebox, After two hours, the reaction mixture was concentrated, and the crude yellow oil was resuspended in C_6H_6 (8 mL) and filtered through celite. The yellow filtrate was concentrated, triterated with pentane (3 x 15 mL), concentrated, and resuspended in ether (10 mL), resulting in the precipitation of a yellow powder. The suspension was allowed to sit at room temperature overnight. The yellow precipitate was collected on a glass-frit (M) and washed with pentane (3 x mL). The resulting yellow powder, Cp*Cp'ZrCl$_2$ (**4.2**, 937 mg, 1.21 mmol, 66%), was dried under vacuum. ^{1}H NMR (C_6D_6, 400 MHz, ppm): δ 8.49 (d, J = 8.7 Hz, 2H, Ar-H), 7.29 (m, 4H, Ar-H), 7.18 (m, 2H, Ar-H), 6.79 (t, J = 2.5 Hz, 2H, Cp-H), 6.54 (t, J = 6.8 Hz, 1H, Si-H), 6.05 (t, J = 2.5 Hz, 2H, Cp-H), 1.90 (m, 2H, methine C-H), 1.82 (s, 15H, Cp* C-H), 1.72 (m, 2H, methine C-H), 1.03 (m, 12H, methyl C-H), 0.74 (m, 12H, methyl C-H). ^{13}C NMR (C_6D_6, 100.6 MHz, ppm): 145.24 (d, J = 16.7 Hz), 145.26 (d, J = 2.2 Hz), 144.83 (d, J = 2.1 Hz), 140.35 (dd, J = 14.4, 6.8 Hz), 131.78 (d, J = 2.4 Hz), 129.26 (s), 126.49 (d, 2.7 Hz), 124.27 (s), 123.80 (t, J = 6.6 Hz) 117.24 (s), 26.51 (d, J = 14.9 Hz), 24.67 (d, J = 14.2 Hz), 21.8 (d, J = 15.1 Hz), 20.32 (m), 12.48 (s). ^{31}P NMR (C_6D_6, 161.9 MHz, ppm): δ 0.12 (s). ^{29}Si NMR (C_6D_6, 79.47 MHz): δ -27.7 (t, J_{Si-P} = 18.2 Hz, Si–H). IR (solid): ν(Si-H) = 2154 cm^{-1}. Elemental: Anal. Calcd for $C_{39}H_{55}Cl_2P_2SiZr$: C, 60.36; H, 7.14. Found: C, 59.98; H, 7.13.

[Fe(μ-H)$_2$Zr(H)] (4.3). Cp*Cp'ZrCl$_2$, **4.2**, (1.77 g, 2.28 mmol) and ferrous bromide (540 mg, 2.51 mmol) were combined in THF (15 mL) in the glovebox, After 30 min, the reaction mixture was concentrated, and the yellow oil was triterated with pentane (3 x 5 mL) to provide a yellow powder. The yellow powder was suspended in toluene (35 mL) and cooled to -78 °C. To this stirring solution, Na•HBEt$_3$ (1.0M in toluene, 9.6 mL) was added. The reaction mixure was allowed to warm to room temperature overnight, concentrated, resuspended in benzene (10 mL), and filtered through celite, and the brown filtrate concentrated. The brown residue was then resupsended in ether and allowed to sit overnight, resulting in the precipitation of a magenta solid. The magenta powder was collected on a glass-frit (M), washed with pentane (3 x mL), resuspended in THF, and cooled to -78 °C. To the chilled THF solution, pentane was added dropwise, resulting in the precipitation of a magenta powder. The magenta powder, [Fe(μ-H)$_2$Zr(H)] (**4.3**, 500 mg, 0.64 mmol, 28%), was collected on a glass-frit (M), washed with pentane (3 x mL), and dried under vacuum. ^{1}H NMR (C$_6$D$_6$, 400 MHz, ppm): δ 8.40 (m, Ar-H), 7.55 (m, 2H, Ar-H), 6.79 (s, 1H, Ar-H), 5.41 (d, J = 21.0 Hz, 2H, Cp-H), 4.99 (s, 1H, Cp-H), 4.61 (m, 1H, Zr-H), 2.44 (m, 2H, methine C-H), 2.12 (s, 15H, Me-H), 1.84 (m, 2H, methine C-H), 1.52 (m, 6H, Me-H), 1.22 (m, 6H, methyl C-H), 0.58 (dd, J = 14.0, 6.7, 3H, methyl C-H), 0.06 (dd, J = 13.2, 6.7, 3H, methyl C-H), -17.26 (m, 1H, Fe-H-Zr), -20.69 (m, 1H, Fe-H-Zr). ^{13}C NMR (THF-d_8, 100.6 MHz, ppm): 156.07 (d, J = 49.04 Hz), 154.70 (d, J = 43.90 Hz), 150.36 (d, J = 40.5 Hz), 149.06 (d, J = 46.9 Hz), 149.06 (d, J = 46.9 Hz), 133.12 (dd, J = 18.4, 12.5 Hz), 128.96 (s), 128.83 (s), 128.53 (s), 128.26 (s), 127.68 (d, J = 4.4 Hz), 126.88 (dd, J = 8.7, 3.7 Hz), 117.06 (s), 113.06 (s), 111.73 (s), 110.95 (s),

110.41 (s), 34.88 (s), 32.31 (d, J = 7.7 Hz), 29.47 (d, J = 9.2 Hz), 28.43 (d, J = 19.0 Hz), 26.68 (d, J = 18.2 Hz), 26.2 (s), 23.88 (d, J = 6.5 Hz), 23.02 (s), 20.67 (s), 20.18 (d, J = 4.1 Hz), 19.55 (d, J = 2.9 Hz), 19.16 (dd, J = 8.5, 5.4 Hz), 18.51 (d, J = 5.8 Hz), 18.15 (d, J = 4.9 Hz), 14.21 (s), 12.69 (s). ^{31}P NMR (C_6D_6, 161.9 MHz, ppm): δ 100.94 (m), 91.43 (m). IR (solid): ν(N-N) = 2065 cm^{-1}. Elemental: Anal. Calcd for $C_{39}H_{58}FeN2P_2SiZr$: C, 59.14; H, 7.38; N, 3.54. Found: C, 58.71; H, 7.14; N, 3.17.

[Fe(μ-H)$_2$Zr(CH$_2$)] (4.4). Cp*ZrCl$_3$ (136.8 mg, 0.411 mmol) and **4.1** (200 mg, 0.411 mmol) were combined in THF (5 mL) in the glovebox. After two hours, ferrous bromide (97.5 mg, 0.452 mmol) was added. The reaction was stirred for 30 min, concentrated, and the yellow oil was triterated with pentane (3 x 5 mL) to provide a yellow powder. The yellow powder was suspended in toluene (8 mL). To this solution, freshly prepared Na(Hg) amalgam (174.4 mg Na, mmol, 17 g Hg) was added and the reaction mixure was stirred vigorously overnight. After 1 day, additional freshly prepared Na(Hg) amalgam (55 mg Na, mmol, 7.5 g Hg) was added to the reaction and stirred overnight. The reaction solution was then decanted, filtered through celite, and the filtrate concentrated. Slow evaporation of ether provided a mixture of **4.3** and **4.4** as magenta and purple x-ray quality crystals respectively.

[Fe(μ-H)$_2$Zr(OTf)] (4.5). To a stirring solution of [Fe(μ-H)$_2$Zr(H)], **4.3**, (50 mg, 0.063 mmol) in benzene, methyl triflate (7.0 μL, 0.063 mmol) was added. After 1 hour, crystals formed and the resulting suspension was allowed to sit at room temperature for 12 hours. The blue-green crystals were collected on a glass-frit (M)

and washed with pentane (3 x 1 mL), furnishing [Fe(μ-H)$_2$Zr(OTf)] (**4.5**, 41.4 mg, 0.044 mmol, 70%). ^{1}H NMR (toluene-d_8, 400 MHz, ppm): δ 8.20 (m, 2H, Ar-H), 7.52 (dd, J = 7.8, 4.1 Hz, 1H, Ar-H) 7.31 (td, J = 7.3, 2.4 Hz, 1H, Ar-H) 7.21 (td, J = 7.2, 2.6 Hz, 1H, Ar-H) 7.08 (m, 3H, Ar-H), 6.77 (q, J = 2.2 Hz, 1H, Cp-H), 6.02 (q, J = 2.5 Hz, 1H, Cp-H), 5.88 (dq, J = 2.5 Hz, 1H, Cp-H), 4.78 (q, J = 2.4 Hz, 1H, Cp-H), 2.41 (m, 2H, methine C-H), 2.07 (m, 2H, methine C-H), 1.96 (s, 15H, Me-H), 1.60 (m, 3H, Me-H), 1.33 (m, 12H, Me-H), 0.86 (m, 2H, Me-H), 0.65 (dd, J = 9.5, 6.6 Hz, 3H, Me-H), 0.43 (dd, J = 14.2, 7.0 Hz, 2H, Me-H), -0.23 (dd, J = 13.7, 6.8 Hz, 2H, Me-H), -16.85 (ddd, J = 35.3, 15.7, 10.7 Hz, 1H, Zr-H-Fe), -20.58 (ddd, J = 24.6, 10.8, 7.0 Hz, 1H, Zr-H-Fe). ^{13}C NMR (toluene-d_8, 100.6 MHz, ppm): 155.25 (d, J = 50.3 Hz), 151.16 (d, J = 42.7 Hz), 149.15 (d, J = 41.2 Hz), 147.47 (d, J = 48.8 Hz), 132.05 (m), 129.62 (s), 126.57 (s), 126.23 (s), 125.86 (s) 123.78 (s), 121.28 (s), 118.09 (s), 111.80 (s), 32.20 (s), 30.91 (s), 28.25 (d, J = 12.1 Hz), 25.17 (s), 24.07 (s), 17.73 (m), 12.09 (q, J = 128.9 Hz). ^{31}P NMR (toluene, 161.9 MHz, ppm): δ 100.46 (m), 86.21 (m). ^{19}F NMR (toluene, 376.4 MHz): δ -73.78 (t, J_{Si-P} = 18.2 Hz, Si–H). IR (solid): ν(N-N) = 2077 cm^{-1}. Elemental: Anal. Calcd for $C_{40}H_{57}F_3FeN_2O_3P_2SSiZr$: C, 51.11; H, 6.11, N, 2.98. Found: C, 50.78; H, 5.86, N, 2.97.

P_2^{PCp}-Supported Complexes

P_2^{PCp} (4.7). Lithium cyclopentadienide was prepared by treating freshly cracked cyclopentadiene (10 mL, 121.8 mmol) with *n*-BuLi (1.6 M in hexanes, 116 mmol) in THF (130 mL) at -78 °C. The reaction was warmed to room temperature overnight. The reaction vessel was brought into the glovebox where the white solid was filtered, washed with pentane, and dried under vacuum.

To a stirring solution of bis(*o*-diisopropylphosphino-phenyl)-chlorophosphine (**4.7**) (2.5 g, 5.52 mmol) in THF (10 mL) was added dropwise lithium cyclopentadienide (0.44 g, 6.07 mmol) in THF (4 mL) at -78 °C. The reaction was stirred for 2 hours at -78 °C and then warmed to room temperature. After stirring for an additional 15 minutes at room temperature, the solvent was removed *in vacuo*. The crude oil was resuspended in benzene (10 mL), filtered through celite, concentrated, and the resultant oil triterated with pentane (3 x 2 mL) to provide a cream colored solid. The cream colored solid was washed with pentane (3 x 5 mL) and dried under vacuum to give P_2^{PCp} (**4.7**) (2.18 g, 4.53 mmol) in 82% yield. ^{1}H NMR (400 MHz, C_6D_6, data reported for major regioisomer) δ 7.33 (dtd, *J* = 8.8, 5.0, 4.4, 2.6 Hz, 2H), 7.18 (d, *J* = 4.1 Hz, 2H), 7.13 – 7.06 (m, 2H), 7.02 (q, *J* = 9.2, 7.5 Hz, 2H), 6.47 (dd, *J* = 3.1, 1.6 Hz, 1H), 6.42 (t, *J* = 4.5 Hz, 2H), 3.05 (s, 2H), 2.13 (pd, *J* = 6.9, 3.0 Hz, 2H), 2.07 – 1.93 (m, 2H), 1.26 – 1.11 (m, 12H), 0.95 (ddd, *J* = 12.5, 6.9, 3.3 Hz, 12H). ^{31}P (C_6D_6, 400 MHz, ppm, data reported for major regioisomer): -1.80 (d, *J* = 149.0 Hz, 2P), -28.5 (t, *J* = 149.0 Hz, 1P). ^{13}C NMR (101 MHz, C_6D_6) δ 149.19 (ddd, *J* = 33.6,

11.5, 6.4 Hz), 148.63 – 147.94 (m), 145.88 (dt, *J* = 17.5, 7.1 Hz), 144.35 (d, *J* = 17.2 Hz), 143.20 (d, *J* = 12.0 Hz), 142.92 – 141.83 (m), 137.60 (d, *J* = 6.2 Hz), 136.81 (d, *J* = 18.6 Hz), 134.76 – 134.39 (m), 134.39 – 134.02 (m), 133.28 (d, *J* = 4.6 Hz), 133.05 (d, *J* = 5.4 Hz), 132.33 (dd, *J* = 6.0, 2.3 Hz), 128.82 (d, *J* = 2.4 Hz), 46.56 (d, *J* = 19.6 Hz), 43.29 (d, *J* = 5.3 Hz), 26.00 – 23.43 (m), 21.40 – 19.36 (m). ESI-MS (electrospray): calcd for $C_{29}H_{41}AgP_3^+$ 589.15 *m/z*, found: 589.11 *m/z*; Ligand + MeCN was also found: calcd for $C_{31}H_{44}NP_3$ 523.27 *m/z*, found: 523.87 *m/z*

$P_2^{PCp}FeBr_2$ (4.8-$FeBr_2$). P_2^{PCp} (**4.7**) (0.338 g, 0.700 mmol) and ferrous bromide (0.166 g, 0.770 mmol) were combined in THF (20 mL) in the glovebox. The dark black purple solution was stirred vigorously over two hours. The crude reaction mixture was filtered through celite and the filtrate evaporated *in vacuo* to give a midnight purple crystalline solid. The purple solid was isolated on a frit, washed with pentane (3 x 5 mL), and dried under dynamic vacuum to give $P_2^{PCp}FeBr_2$ (**4.8-$FeBr_2$**) (0.481 g, 0.689 mmol) in 98% yield. ^{1}H NMR (400 MHz, C_6D_6) δ 142.04, 33.92, 16.59, 15.48, 11.28, 6.99, 6.08, 4.45, 3.82, 2.48, 1.52, -2.07, -2.71. μ_{eff} (THF-d_8, Evans' method, 298K): 3.82 μ_B. Anal calcd for $C_{29}H_{41}Br_2FeP_3$: C, 49.89; H, 5.92. Found: C, 49.64; H, 5.81.

4.8-$^{57}FeCl_2$ was synthesized using an identical procedure, except with $^{57}FeCl_2$ in place of $FeBr_2$, and gave similar features by ^{1}H NMR: ^{1}H NMR (400 MHz, C_6D_6) δ 125.84, 79.64, 18.00, 11.28, 8.61, 7.60, 4.07, -0.22.

[P_2^{PCp}Fe(N_2)(H_2)]Na (4.9). To a dark purple solution of **4.8-FeBr$_2$** (0.0578 g, 0.083 mmol) in THF (5 mL) at -78 °C was added sodium triethylborohydride (1 M in toluene, 0.18 mL, 0.18 mmol). The reaction mixture was stirred at -78 °C for 1.5 hours before a final portion of sodium triethylborohydride (0.05 mL, 0.05 mmol) was added and the solution stirred for an additional 1.5 hours at -78 °C. The brown reaction mixture was warmed to room temperature, stirred for 2 hours, and concentrated *in vacuo*. The resultant brown oil was resuspended in benzene (2 mL), filtered through celite, and the reaction vessel and salts washed with benzene (3 x 1 mL). The brown filtrate was concentrated in vacuo and the brown powder resuspended in 5 mL of Et_2O, which resulted in the precipitation of the yellow crystalline solid **4.9** (0.0181 , 0.027 mmol) in 36% yield. ^{1}H NMR (400 MHz, C_6D_6) δ 8.40 (q, *J* = 4.9 Hz, 2H), 7.48 (d, *J* = 5.9 Hz, 2H), 6.33 (s, 2H), 5.92 (s, 2H), 2.50 (dp, *J* = 14.2, 7.1 Hz, 4H), 1.59 (q, *J* = 7.2 Hz, 6H), 1.42 (dd, *J* = 13.9, 6.4 Hz, 6H), 1.18 (q, *J* = 6.7 Hz, 6H), 0.61 (q, *J* = 6.9 Hz, 6H), -9.02 (bs, 1H), -19.34 (bs, 1H). ^{31}P (THF-d_8, 400 MHz, ppm): 121.3 (bs, 2P), 108.23 (t, *J* = 17.1 Hz, 1P). ^{13}C NMR (101 MHz, THF-d_8) δ 154.93 – 153.41 (m), 149.12 (dt, *J* = 44.1, 17.6 Hz), 131.72 (t, *J* = 6.5 Hz), 129.12 – 126.88 (m), 112.35 (d, *J* = 13.0 Hz), 109.60 (d, *J* = 49.5 Hz), 106.30 (d, *J* = 11.1 Hz), 66.14, 32.82 (t, *J* = 3.0 Hz), 21.40 – 18.27 (m), 15.51. IR (KBr; cm^{-1}): 1993 (N–N), 1775 (Fe–H). Anal calcd for $C_{29}H_{42}FeN_2NaP_3$: C, 58.99; H, 7.17; N, 4.74. Found: C, 58.87; H, 7.20; N, 4.54.

[(P_2^{PCp})($H)_2$Fe-N_2]Na(12-c-4)$_2$ (4.10). The 12-c-4 salt of **4.9** was synthesized in an analogous manner as **4.9** using **4.8** (169 mg, 0.242 mmol), except once the crude

material was suspended in benzene, two equiv of 12-c-4 (0.080 mL, 0.484 mmol) was added, which led to the precipitation of a yellow solid. The yellow solid was isolated on a frit and rinsed with benzene, yielding **4.10** (157 mg, 69% yield). IR (KBr; cm^{-1}): 2031 (N–N), 1774 (Fe–H). Anal calcd for $C_{45}H_{74}FeN_2NaO_8P_3$: C, 57.33; H, 7.91; N, 2.97. Found: C, 57.21; H, 7.75; N, 2.88. **4.10** has not been characterized in solution yet, because it is not soluble in common organic solvents.

$P_2^{PCp}Fe(N_2)(H_2)$ (4.11). To a yellow solution of **4.9** (0.018 g, 0.027 mmol) in THF (1 mL) at -78 °C was added $HBAr^F{}_4$ (0.0274 g, 0.027 mmol). The reaction mixture was stirred at -78 °C for 1 hour, then at room temperature for 1 hour. The orange reaction mixture was subsequently concentrated *in vacuo* and the resultant orange oil resuspended C_6D_6 for NMR analysis. A purification procedure has not yet been developed given the high solubility of the compound in numerous solvents. ^{1}H NMR (400 MHz, C_6D_6) δ 8.34 (s, 2H), 7.91 (d, *J* = 6.5 Hz, 2H), 7.41 (s, 2H), 7.12 – 6.99 (m, 2H), 6.36 (d, *J* = 5.3 Hz, 2H), 6.30 (s, 2H), 3.08 (s, 2H), 2.44 (dt, *J* = 13.9, 6.9 Hz, 4H), 1.57 (q, *J* = 7.3 Hz, 6H), 1.27 (q, *J* = 7.3 Hz, 6H), 1.08 (dq, *J* = 12.2, 6.8, 6.4 Hz, 6H), 0.60 (q, *J* = 6.9 Hz, 6H), -8.38 – -9.75 (m, 1H), -20.49 (s, 1H). ^{31}P NMR (162 MHz, C_6D_6) δ 119.25 (d, *J* = 46.7 Hz, 2P), 98.01 (s, 1P). IR (thin film; cm^{-1}): 2068 (N–N), 1790 (Fe–H).

$(P_2^{PCp})Fe(N_2)(H)_2Cp^*ZrCl_2$ (4.12). To a yellow solution of **4.9** (0.0403 g, 0.061 mmol) in THF (5 mL) at -78 °C was added Cp^*ZrCl_3 (0.0202 g, 0.061 mmol). The reaction mixture was stirred at -78 °C for 1 hour, then at room temperature for 2

hours. The orange reaction mixture was subsequently concentrated *in vacuo* and the resultant orange oil resuspended in diethyl ether (2 mL). The crude solution was filtered through celite, and the reaction vessel and salts washed with diethyl ether (3 x 1 mL). The red/orange filtrate was concentrated *in vacuo* again and dried under vacuum for 2 hours before it was resuspended in 1 mL of Et_2O, which resulted in the precipitation of red orange crystals of **4.12** (0.0426 g, 0.0453 mmol) in 74% yield. ^{1}H NMR (400 MHz, toluene-d_8) δ 9.19 (t, J = 6.8 Hz, 2H), 7.37 (d, J = 7.7 Hz, 2H), 7.24 (t, J = 7.5 Hz, 2H), 7.09 (q, J = 8.0, 7.5 Hz, 2H), 6.55 (q, J = 2.9 Hz, 2H), 5.26 (d, J = 2.9 Hz, 2H), 2.55 – 2.28 (m, 4H), 1.63 (s, 15H), 1.50 (q, J = 7.1 Hz, 6H), 1.27 – 1.11 (m, 12H), 0.48 (p, J = 8.8, 6.9 Hz, 6H), -8.90 (q, J = 50.3, 46.8 Hz, 1H), -20.57 (dt, J = 62.7, 43.1 Hz, 1H). ^{31}P NMR (162 MHz, toluene-d_8) δ 118.34 (d, J = 56.0 Hz, 2P), 105.24 (s, 1P). IR (KBr; cm^{-1}): 2065 (N–N), 1786 (Fe–H).

4.4.3 Reactivity Studies

[Fe(μ-H)$_2$Zr(OCHO)] (4.6). 4.6 was generated in situ for spectral analysis. To a magenta solution of **4.3** (0.030 g, 0.038 mmol) in a J. Young tube (C_6D_6, 0.6 mL) at room temperature was added 1 atm of CO_2. The J. Young tube was rotated and spectra collected after 10 minutes of mixing and then 12 hours of mixing.

Olefin Catalysis ^{1}H NMR Spectroscopic Studies with 4.9. To a J. Young tube containing a mixture of complex **4.9** (4.1 mg, 6.9 μmol) and an excess of styrene (14.2 μL, 0.124 mmol) in 0.6 mL of 7:1 C_6D_6 : THF-d_8, was added 4 atm of H_2. The reaction was monitored over time using NMR spectroscopy. ^{31}P and ^{1}H NMR spectra were collected after 1 hour and 9 hours of mixing.

^{1}H NMR and IR Spectroscopic Investigation of H_2 Addition to 4.9. To a yellow solution of **4.9** (0.015 g, 0.025 mmol) in a J. Young tube (10: 1 toluene-d_8 :THF-d_8, 0.6 mL) at room temperature was added 4 atm of H_2. The J. Young tube was rotated and a spectrum collected after 22 hours of mixing.

^{1}H NMR Analysis of the Reaction Between Styrene and 4.9. To a yellow solution of **4.9** (4.1 mg, 6.9 μmol) in a J. Young tube (7:1 C_6D_6 : THF-d_8, 0.6 mL) at room temperature was added 1.0 equiv of styrene (0.8 μL, 6.9 μmol). The J. Young tube was rotated and spectra collected after 10 minutes and 1 hour of mixing.

4.5 References

1. Bullock, R. M.; Casey, C. P. *Acc. Chem. Res.* **1987,** *20*, 167.
2. Stephan, D. W. *Coord. Chem. Rev.* **1989,** *95*, 41.
3. Wheatley, N.; Kalck, P. *Chem. Rev.* **1999,** *99*, 3379.
4. Cooper, B. G.; Napoline, J. W.; Thomas, C. M. *Cat. Rev.-Sci. Eng.* **2012,** *54*, 1.
5. Mazzacano, T. J.; Mankad, N. P. *J. Am. Chem. Soc.* **2013,** *135*, 17258.
6. Uyeda, C.; Peters, J. C. *J. Am. Chem. Soc.* **2013,** *135*, 12023.
7. Zhou, W.; Marquard, S. L.; Bezpalko, M. W.; Foxman, B. M.; Thomas, C. M. *Organometallics* **2013,** *32*, 1766.
8. Cammarota, R. C.; Lu, C. C. *J. Am. Chem. Soc.* **2015,** *137*, 12486.
9. Bagherzadeh, S.; Mankad, N. P. *J. Am. Chem. Soc.* **2015,** *137*, 10898.
10. Chakraborty, A.; Kinney, R. G.; Krause, J. A.; Guan, H. *ACS Catal.* **2016,** *6*, 7855.
11. Baranger, A. M.; Bergman, R. G. *J. Am. Chem. Soc.* **1994,** *116*, 3822.
12. Krogman, J. P.; Foxman, B. M.; Thomas, C. M. *J. Am. Chem. Soc.* **2011,** *133*, 14582.
13. Kuriyama, S.; Arashiba, K.; Nakajima, K.; Tanaka, H.; Yoshizawa, K.; Nishibayashi, Y. *Chem. Sci.* **2015,** *6*, 3940.
14. Thomas, C. M. *Comments Inorg. Chem.* **2011,** *32*, 14.
15. Kuppuswamy, S.; Powers, T. M.; Krogman, J. P.; Bezpalko, M. W.; Foxman, B. M.; Thomas, C. M. *Chem. Sci.* **2013,** *4*, 3557.
16. Greenwood, B. P.; Forman, S. I.; Rowe, G. T.; Chen, C.-H.; Foxman, B. M.; Thomas, C. M. *Inorg. Chem.* **2009,** *48*, 6251.
17. Miyazaki, T.; Tanabe, Y.; Yuki, M.; Miyake, Y.; Nishibayashi, Y. *Organometallics* **2011,** *30*, 2394.
18. Volbeda, A.; Charon, M.-H.; Piras, C.; Hatchikian, E. C.; Frey, M.; Fontecilla-Camps, J. C. *Nature* **1995,** *373*, 580.
19. Jeoung, J.-H.; Dobbek, H. *Science* **2007,** *318*, 1461.
20. Spatzal, T.; Aksoyoglu, M.; Zhang, L.; Andrade, S. L. A.; Schleicher, E.; Weber, S.; Rees, D. C.; Einsle, O. *Science* **2011,** *334*, 940.
21. Sippel, D.; Einsle, O. *Nat. Chem. Biol.* **2017,** *advance online publication*.
22. Eady, R. R. *Chem. Rev.* **1996,** *96*, 3013.
23. Hu, Y.; Lee, C. C.; Ribbe, M. W. *Science* **2011,** *333*, 753.
24. Anderson, J. S.; Rittle, J.; Peters, J. C. *Nature* **2013,** *501*, 84.
25. Arashiba, K.; Miyake, Y.; Nishibayashi, Y. *Nat. Chem.* **2011,** *3*, 120.
26. Yandulov, D. V.; Schrock, R. R. *Science* **2003,** *301*, 76.
27. Togni, A.; Halterman, R. L., *Metallocenes: Synthesis Reactivity Applications*. Wiley-VCH: Weinheim, 1998.
28. Manriquez, J. M.; Bercaw, J. E. *J. Am. Chem. Soc.* **1974,** *96*, 6229.
29. Pool, J. A.; Lobkovsky, E.; Chirik, P. J. *Nature* **2004,** *427*, 527.
30. Pun, D.; Lobkovsky, E.; Chirik, P. J. *J. Am. Chem. Soc.* **2008,** *130*, 6047.
31. Smith, J. M.; Lachicotte, R. J.; Pittard, K. A.; Cundari, T. R.; Lukat-Rodgers, G.; Rodgers, K. R.; Holland, P. L. *J. Am. Chem. Soc.* **2001,** *123*, 9222.

32. O'Donoghue, M. B.; Zanetti, N. C.; Davis, W. M.; Schrock, R. R. *J. Am. Chem. Soc.* **1997,** *119*, 2753.
33. Crossland, J. L.; Tyler, D. R. *Coord. Chem. Rev.* **2010,** *254*, 1883.
34. Burford, R. J.; Fryzuk, M. D. *Nat. Chem. Rev.* **2017,** *1*, 1.
35. Takaoka, A.; Mankad, N. P.; Peters, J. C. *J. Am. Chem. Soc.* **2011,** *133*, 8440.
36. Rittle, J.; McCrory, C. C. L.; Peters, J. C. *J. Am. Chem. Soc.* **2014,** *136*, 13853.
37. Creutz, S. E.; Peters, J. C. *J. Am. Chem. Soc.* **2015,** *137*, 7310.
38. Tainturier, G.; Fahim, M.; Gautheron, B. *J. Organomet. Chem.* **1989,** *373*, 193.
39. Jones, S. B.; Petersen, J. L. *Inorg. Chem.* **1981,** *20*, 2889.
40. Mankad, N. P.; Rivard, E.; Harkins, S. B.; Peters, J. C. *J. Am. Chem. Soc.* **2005,** *127*, 16032.
41. Bart, S. C.; Lobkovsky, E.; Chirik, P. J. *J. Am. Chem. Soc.* **2004,** *126*, 13794.
42. Daida, E. J.; Peters, J. C. *Inorg. Chem.* **2004,** *43*, 7474.
43. Trovitch, R. J.; Lobkovsky, E.; Chirik, P. J. *Inorg. Chem.* **2006,** *45*, 7252.
44. Russell, S. K.; Milsmann, C.; Lobkovsky, E.; Weyhermüller, T.; Chirik, P. J. *Inorg. Chem.* **2011,** *50*, 3159.
45. Fong, H.; Moret, M.-E.; Lee, Y.; Peters, J. C. *Organometallics* **2013,** *32*, 3053.
46. Chirik, P. J. *Acc. Chem. Res.* **2015,** *48*, 1687.
47. Brookhart, M.; Grant, B.; Volpe, A. F. *Organometallics* **1992,** *11*, 3920.
48. Weitz, I. S.; Rabinovitz, M. *J. Chem. Soc., Perkin Trans. 1* **1993**, 117.
49. Evans, D. F. *J. Chem. Soc.* **1959**, 2003.
50. Weatherburn, M. W. *Anal. Chem.* **1967,** *39*, 971.

Chapter 2 Appendix.

Pd Chemistry: NMR Spectra

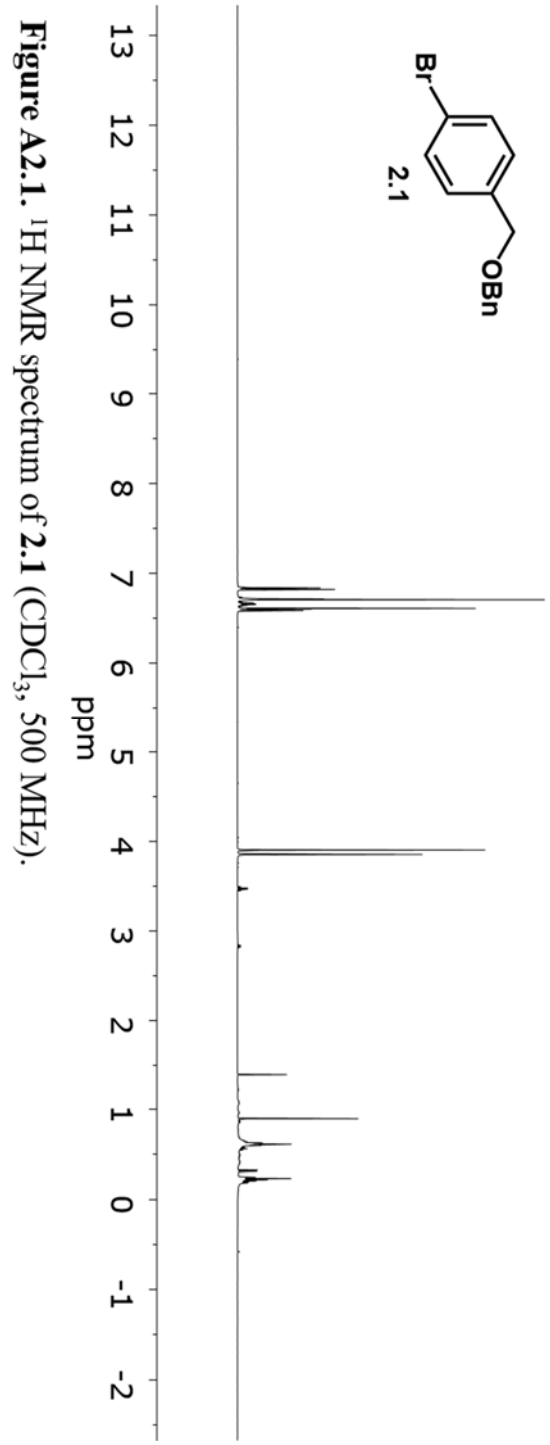

Figure A2.1. ^{1}H NMR spectrum of **2.1** ($CDCl_3$, 500 MHz).

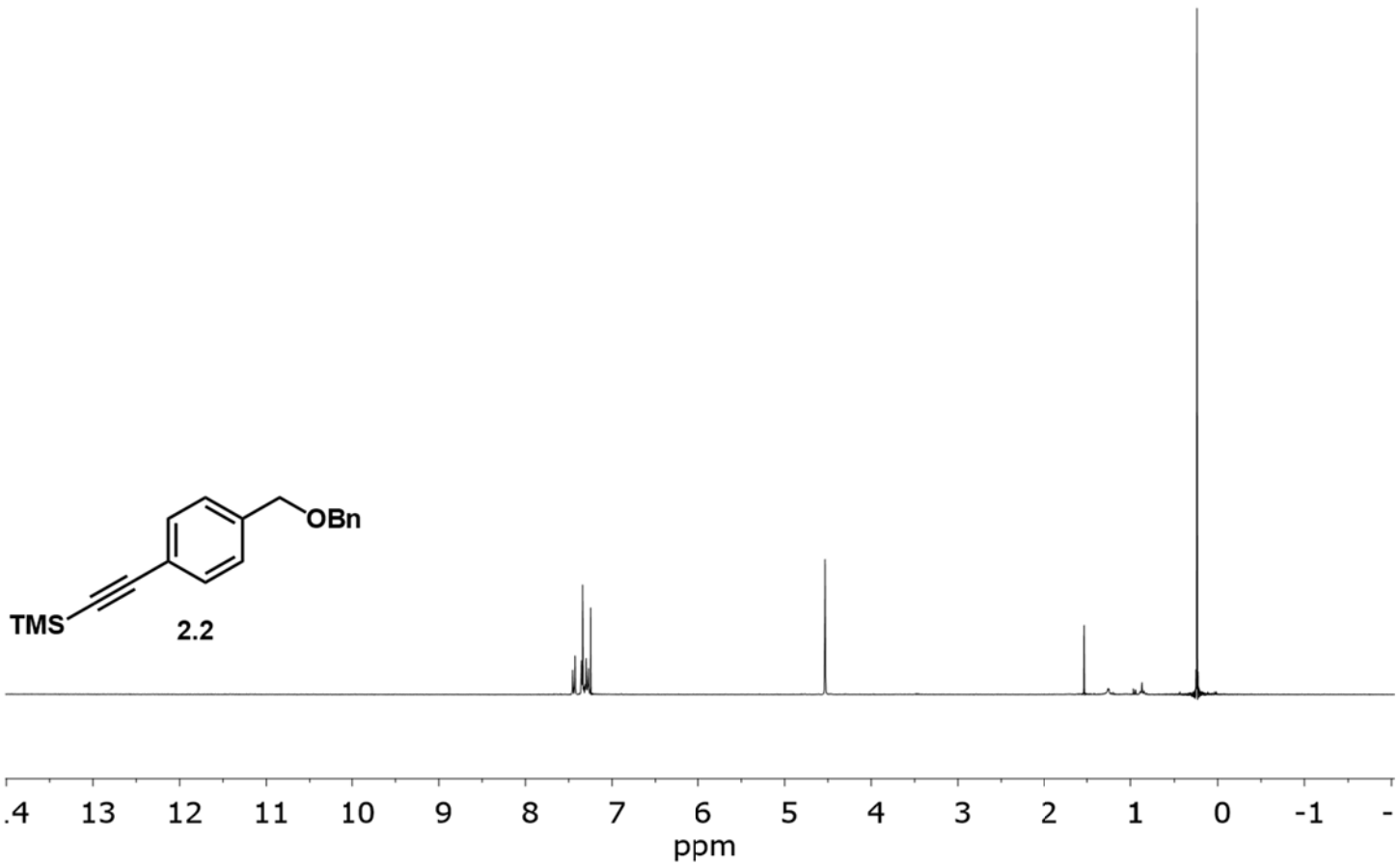

Figure A2.2. ^{1}H NMR spectrum of **2.2** ($CDCl_3$, 300 MHz).

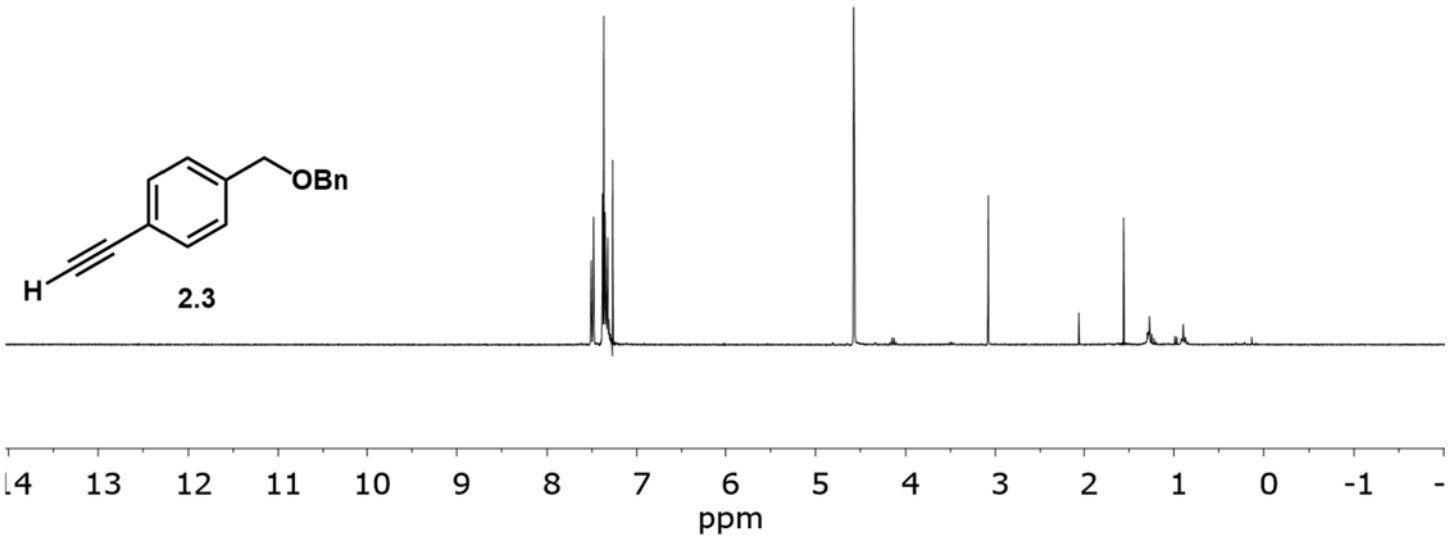

Figure A2.3. ^{1}H NMR spectrum of **2.3** ($CDCl_3$, 300 MHz).

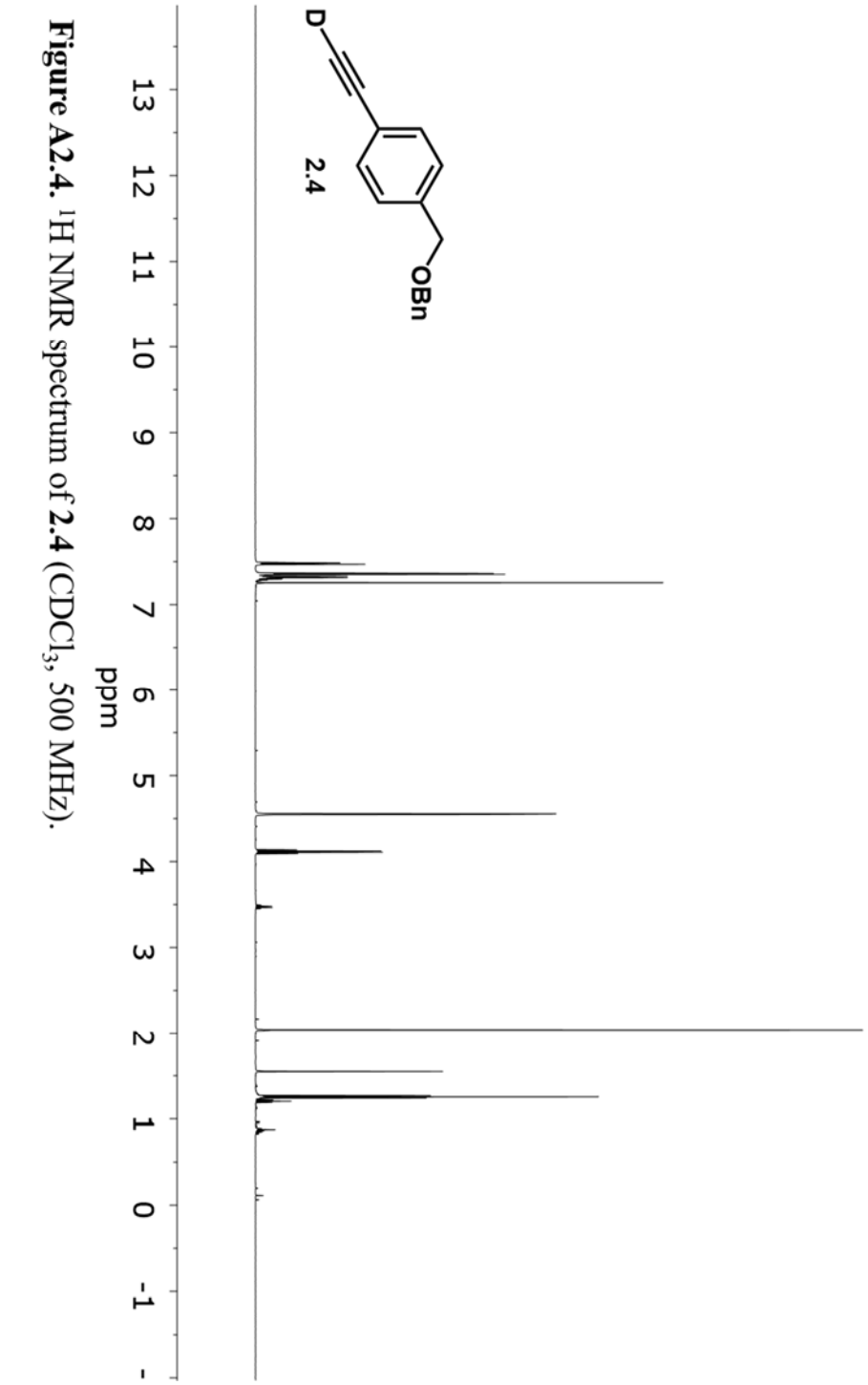

Figure A2.4. ^{1}H NMR spectrum of **2.4** ($CDCl_3$, 500 MHz).

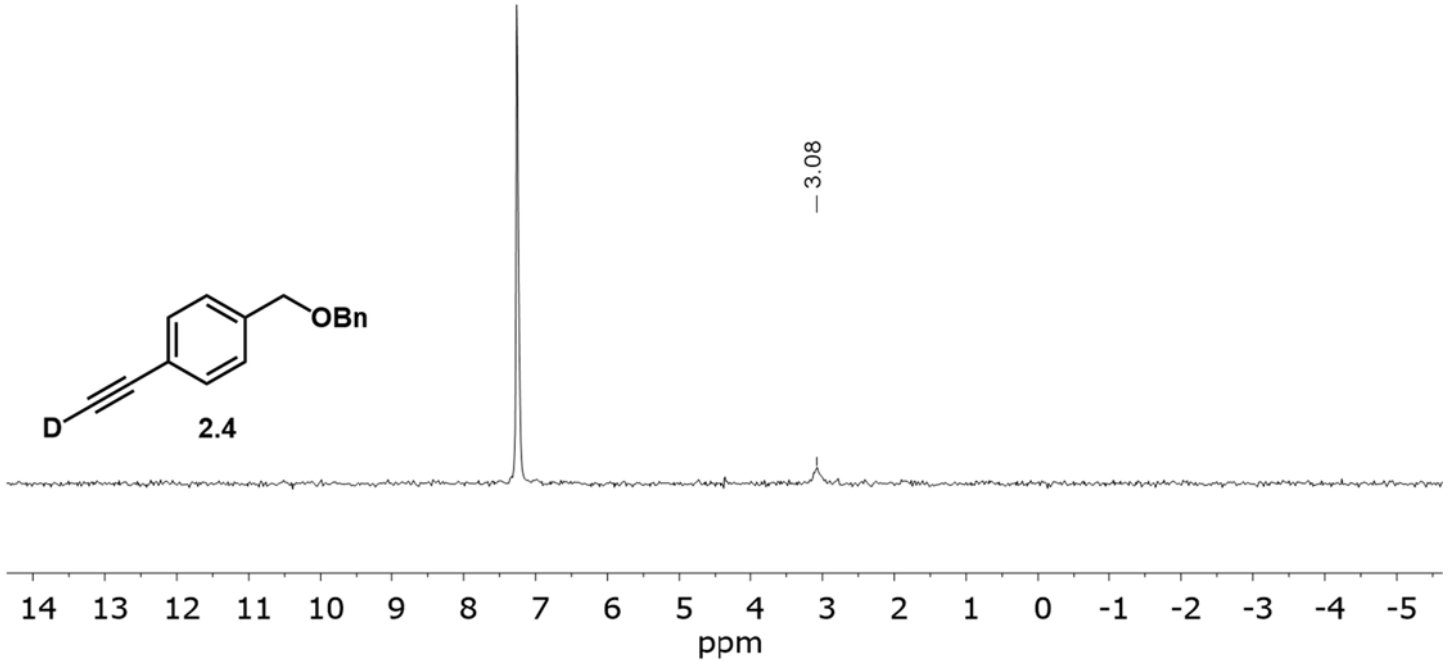

Figure A2.5. ^{2}D NMR spectrum of **2.4** ($CHCl_3$, 400 MHz).

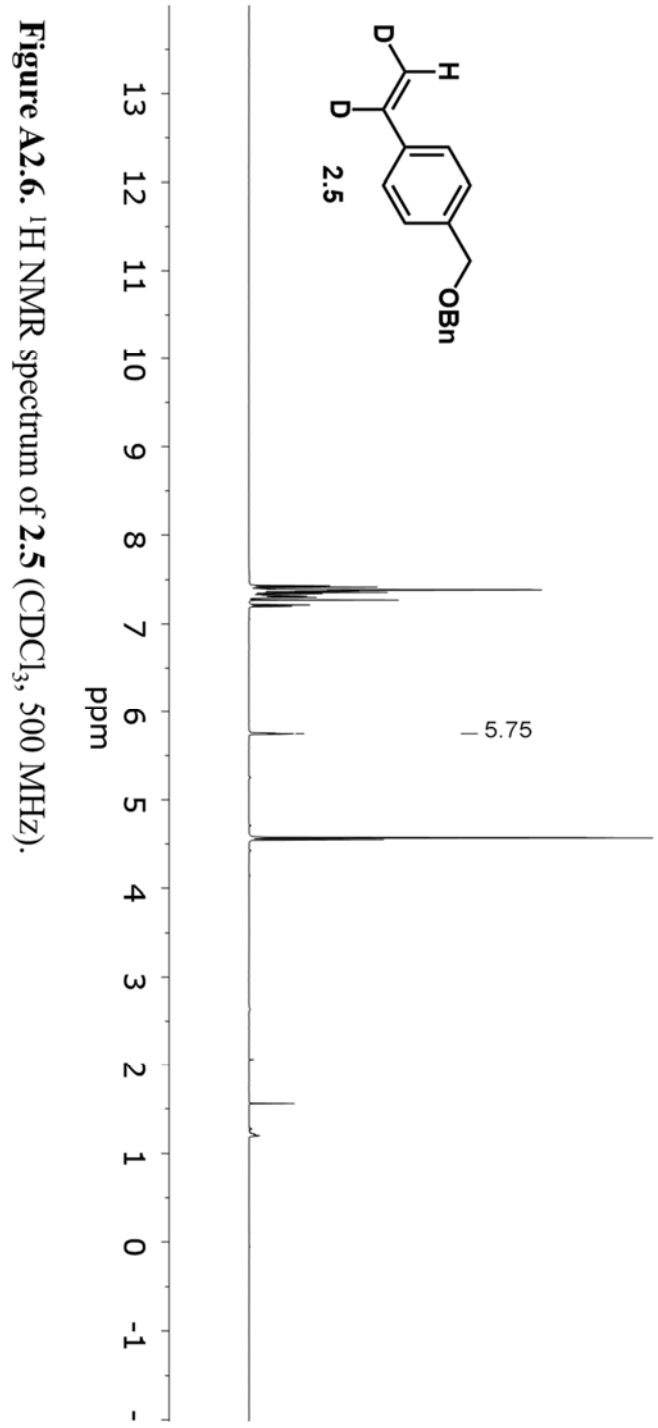

Figure A2.6. ^{1}H NMR spectrum of **2.5** ($CDCl_3$, 500 MHz).

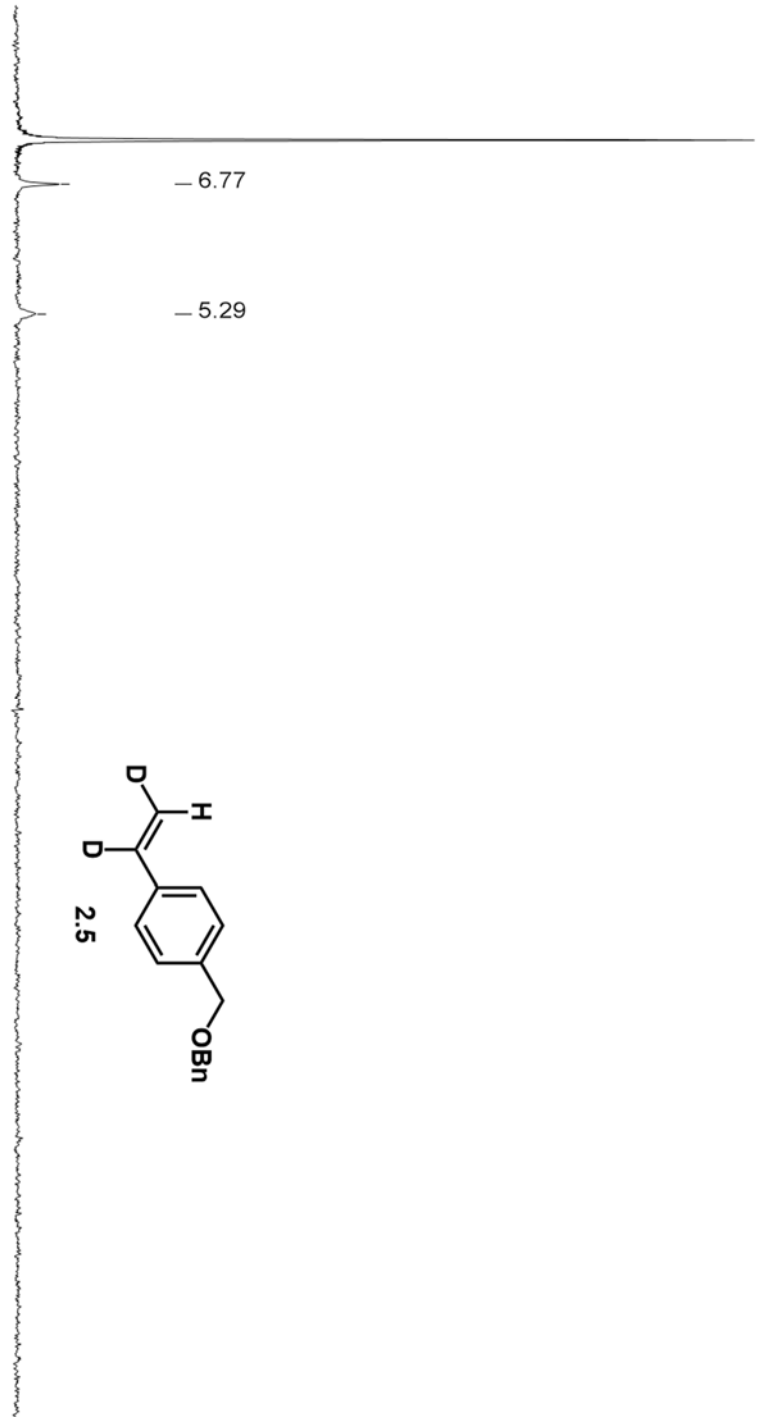

Figure A2.7. ^{2}D NMR spectrum of **2.5** ($CHCl_3$, 400 MHz).

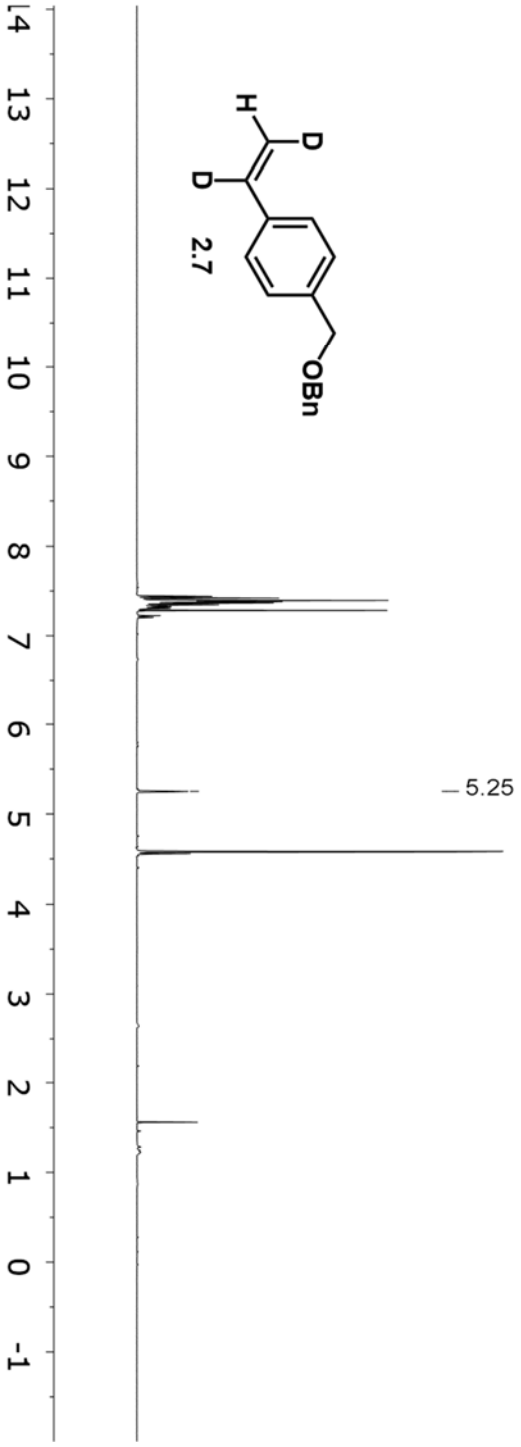

Figure A2.8. ^{1}H NMR spectrum of **2.7** ($CDCl_3$, 400 MHz).

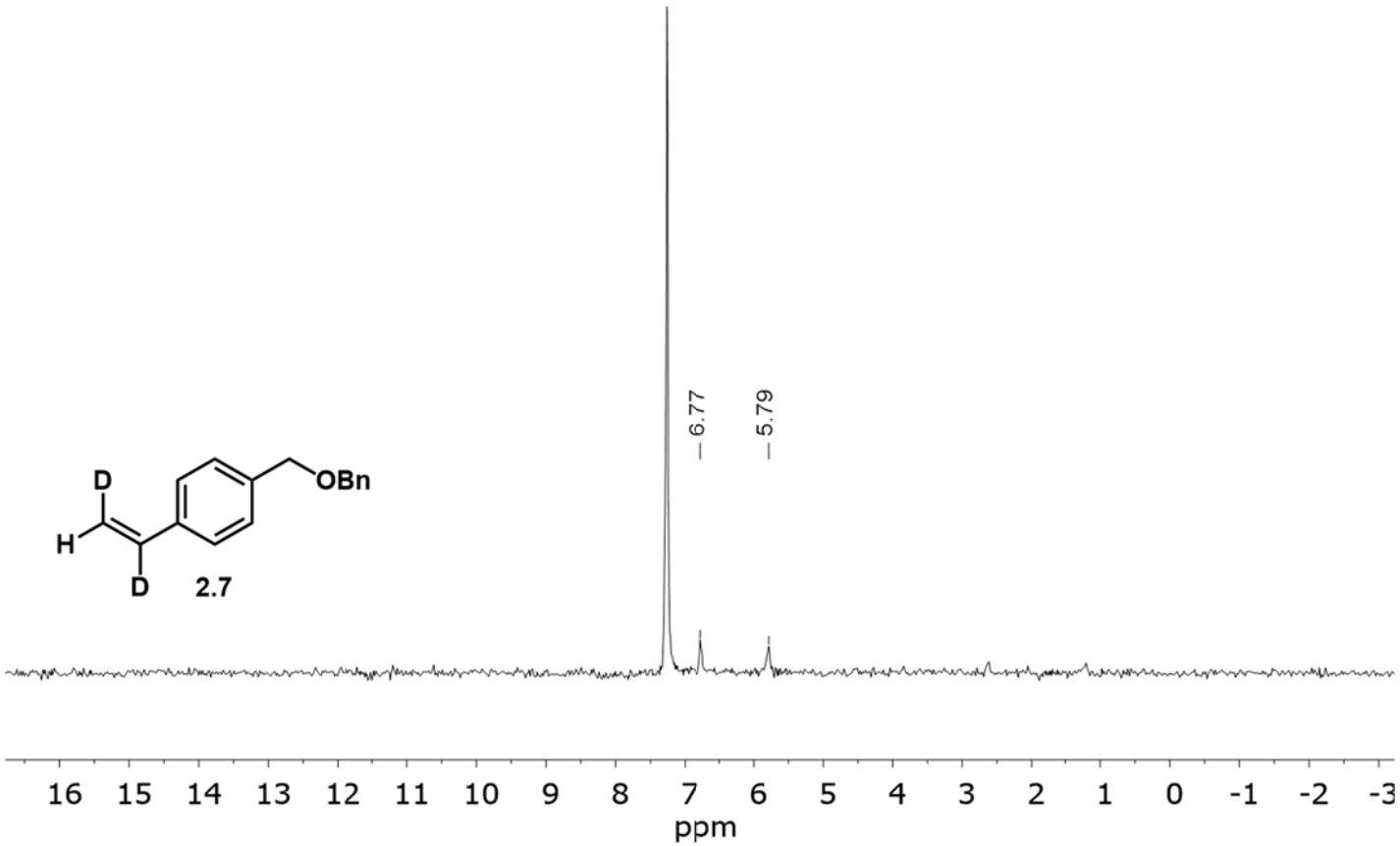

Figure A2.9. ^{2}D NMR spectrum of **2.7** ($CHCl_3$, 400 MHz).

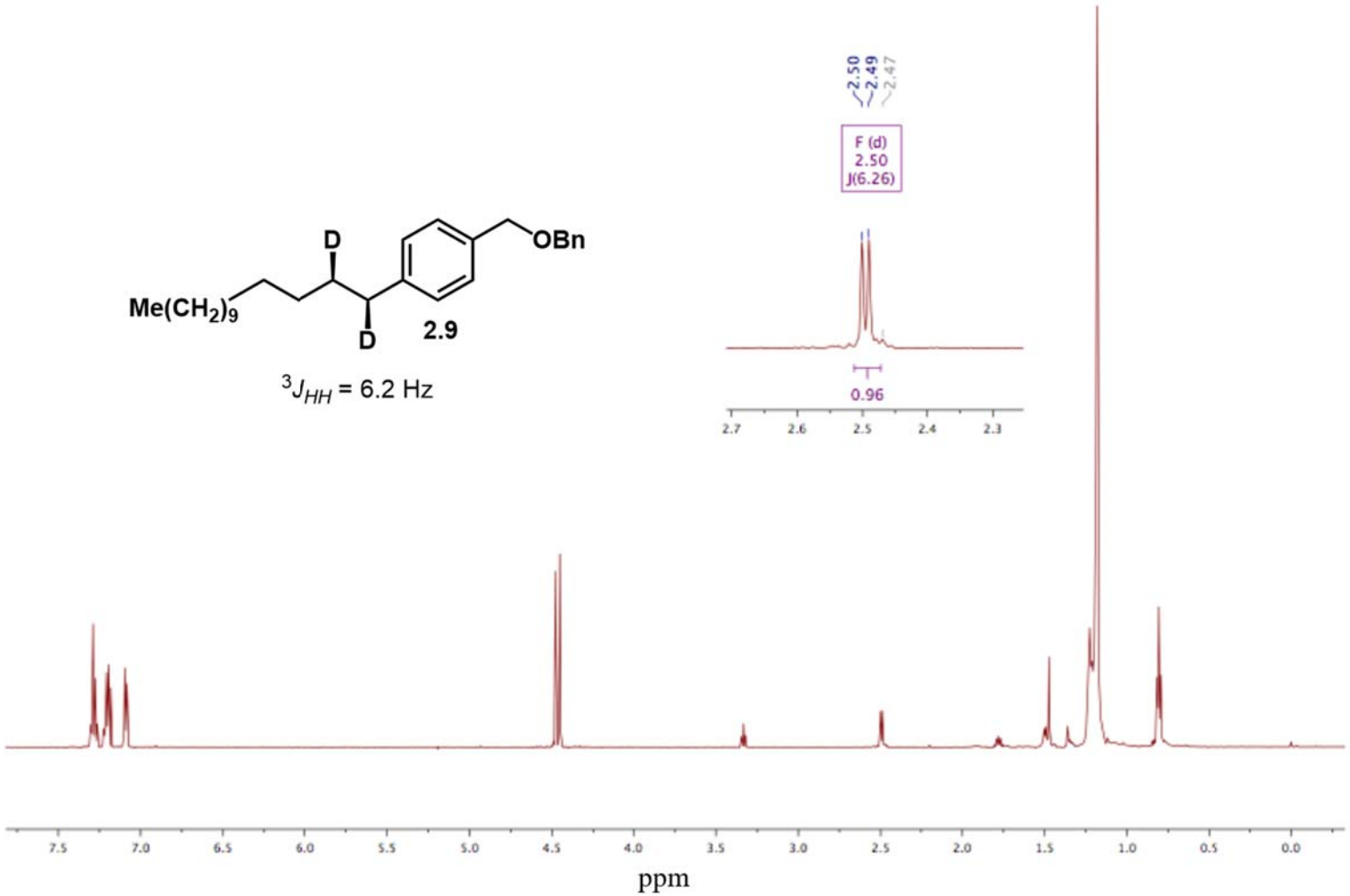

Figure A2.10. ^{1}H (deuterium decoupled) NMR spectrum of **2.9** ($CDCl_3$, 600 MHz).

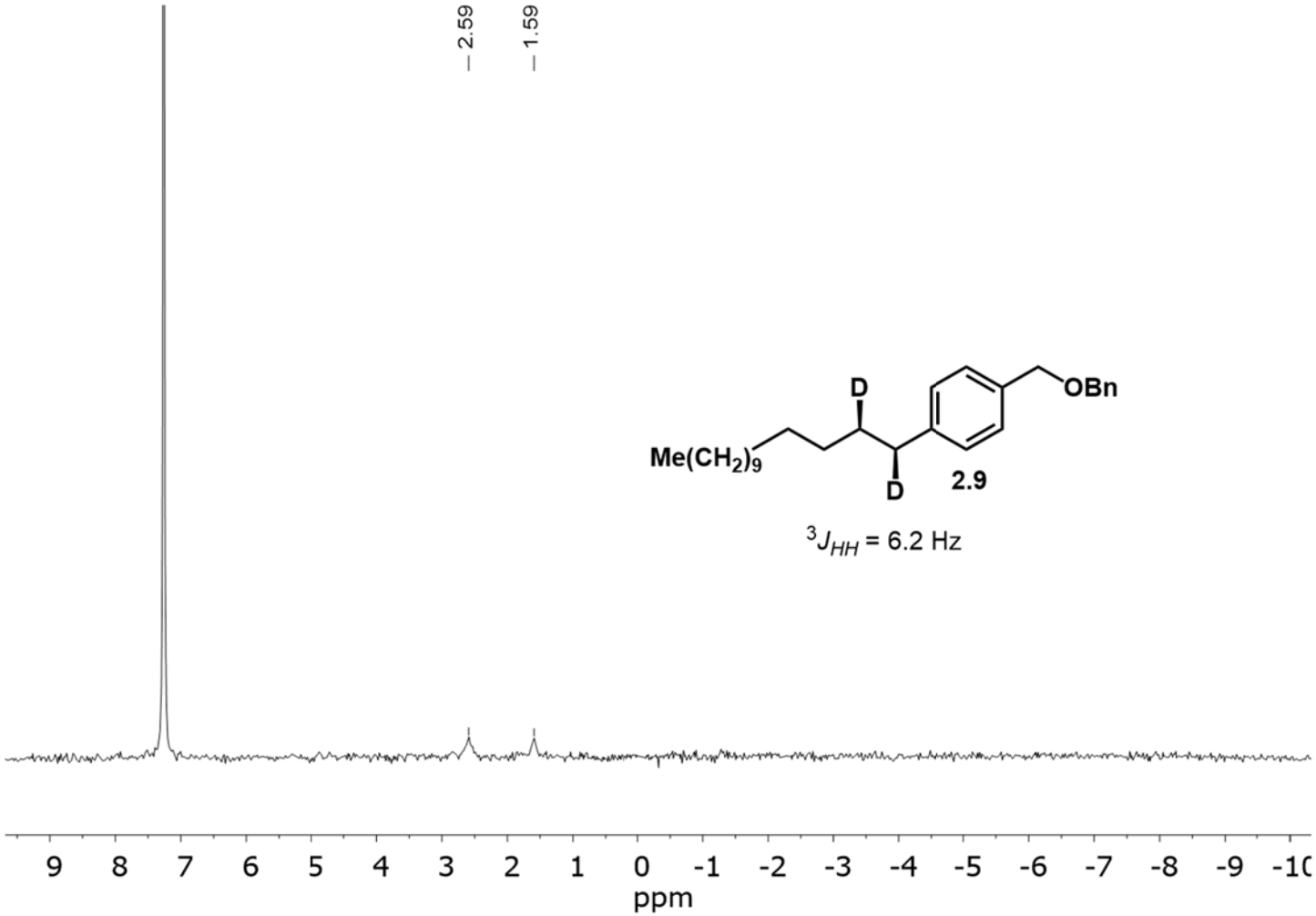

Figure A2.11. ^{2}D NMR spectrum of **2.9** ($CHCl_3$, 400 MHz).

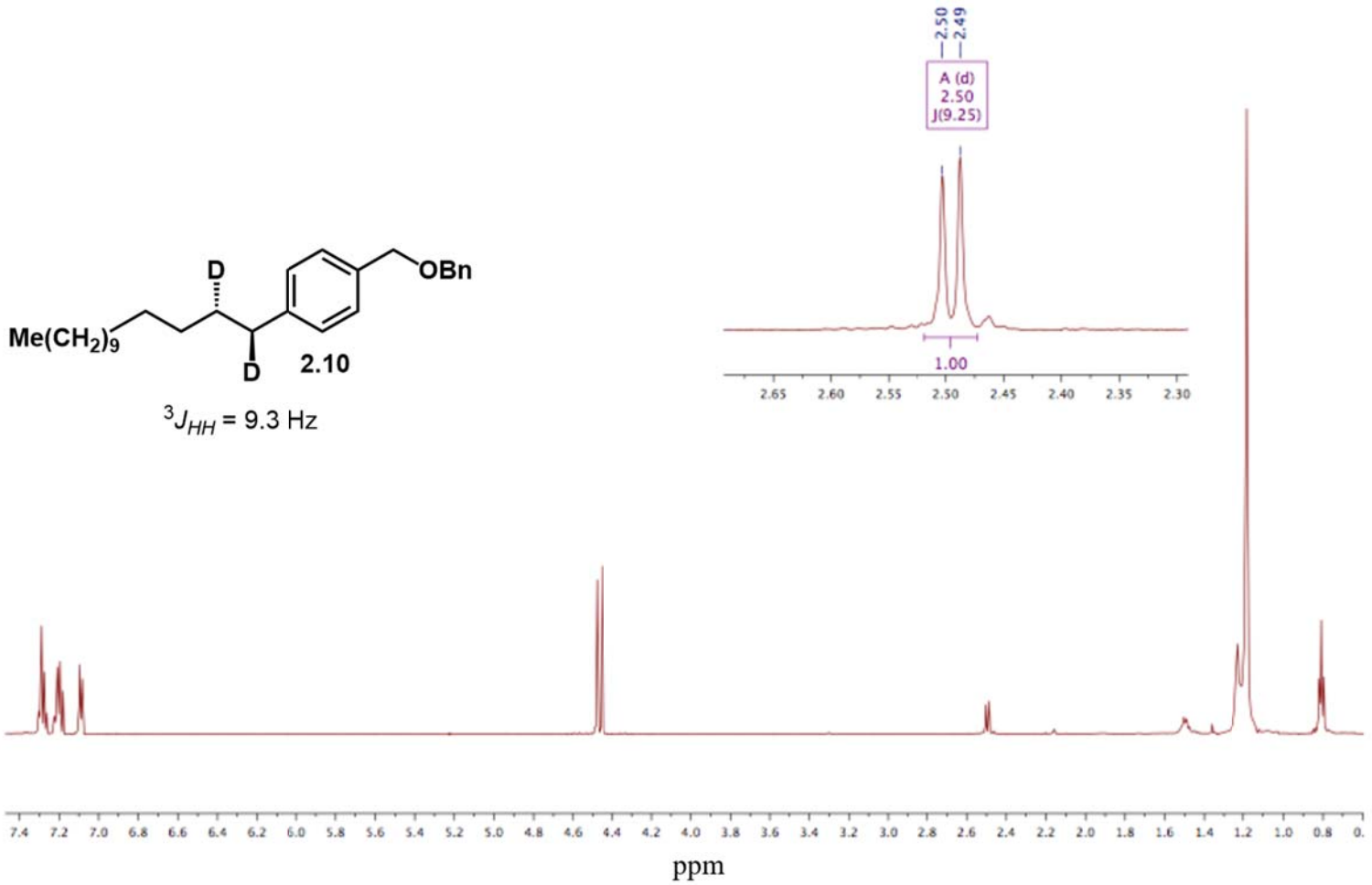

Figure A2.12. ^{1}H (deuterium decoupled) NMR spectrum of **2.10** ($CDCl_3$, 600 MHz).

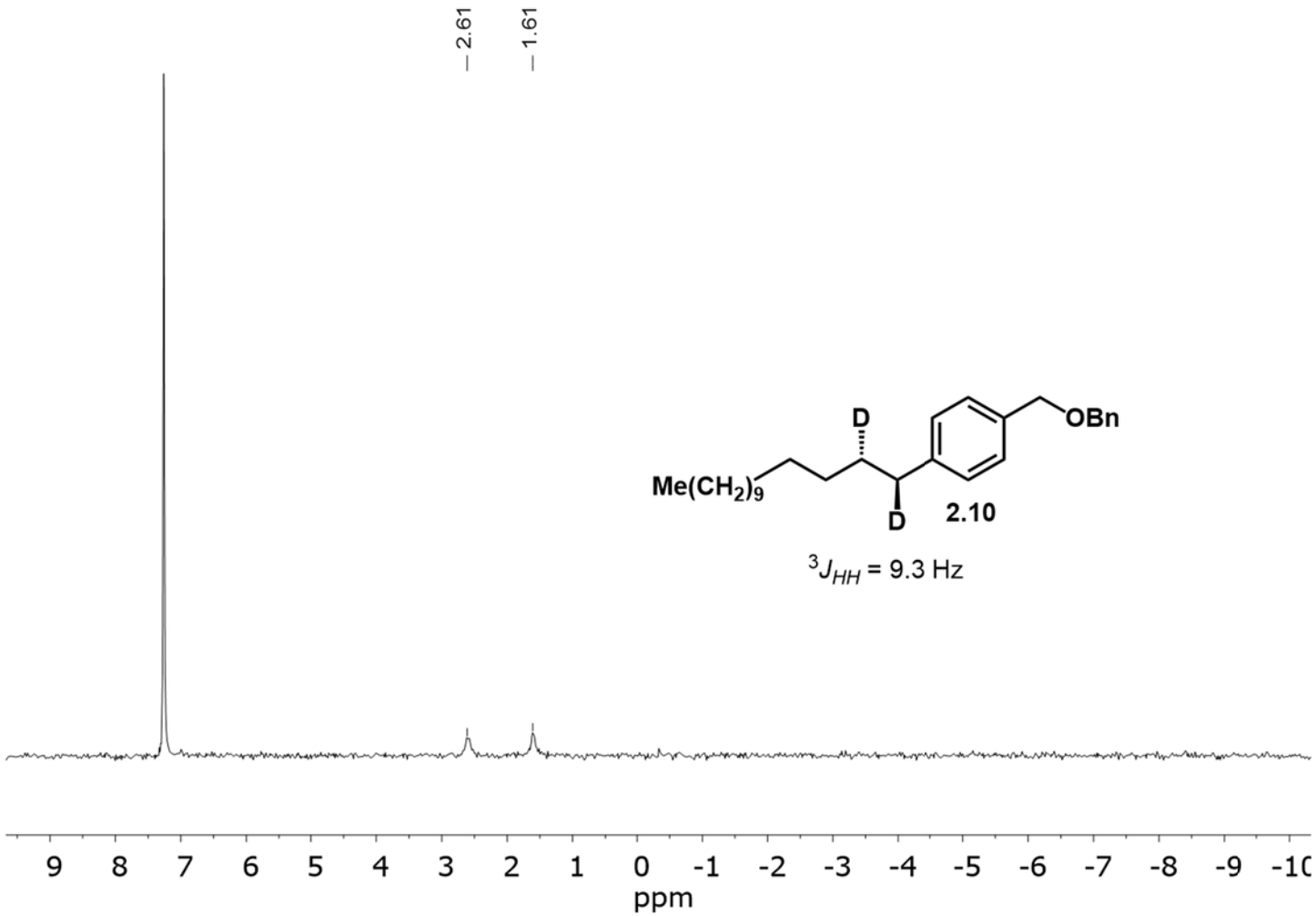

Figure A2.13. ^{2}D NMR spectrum of **2.10** ($CHCl_3$, 400 MHz).

Ni Chemistry Spectra

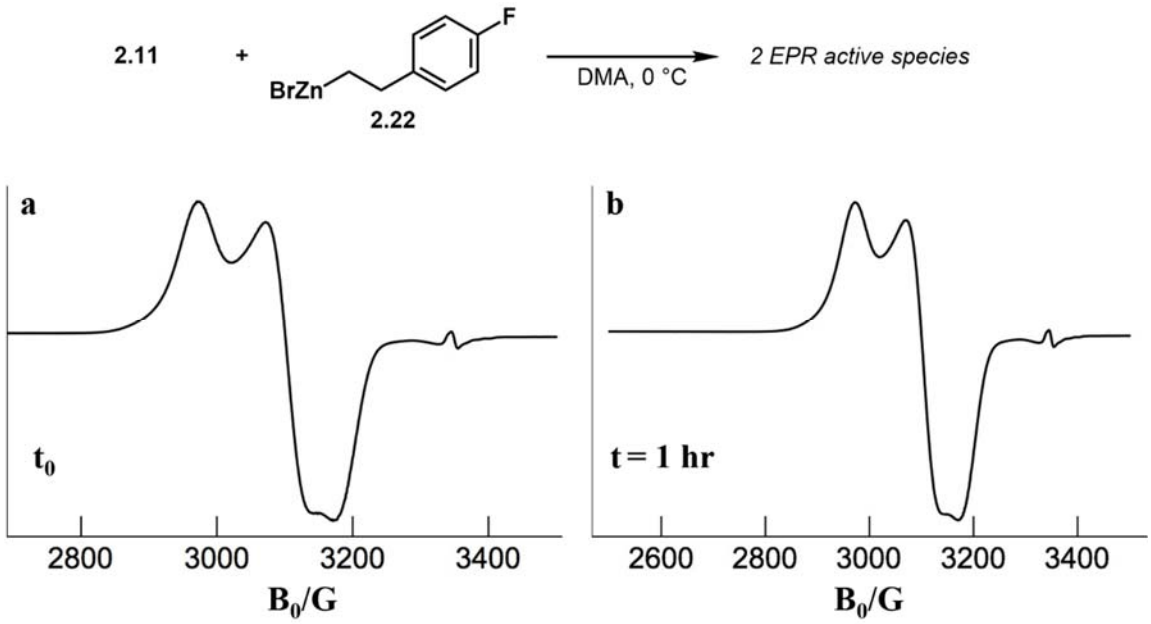

Figure A2.14. EPR Study of Complex 2.11 with (4-fluorophenethyl)zinc(II) bromide. (a) Experimental parameters; Microwave power, 2.026 mW; microwave frequency, 9.405 GHz; modulation amplitude, 2 G; gain, 5020; time constant, 40.960 (b) Experimental parameters; Microwave power, 2.036 mW; microwave frequency, 9.404 GHz; modulation amplitude, 2 G; gain, 5020; time constant, 40.960.

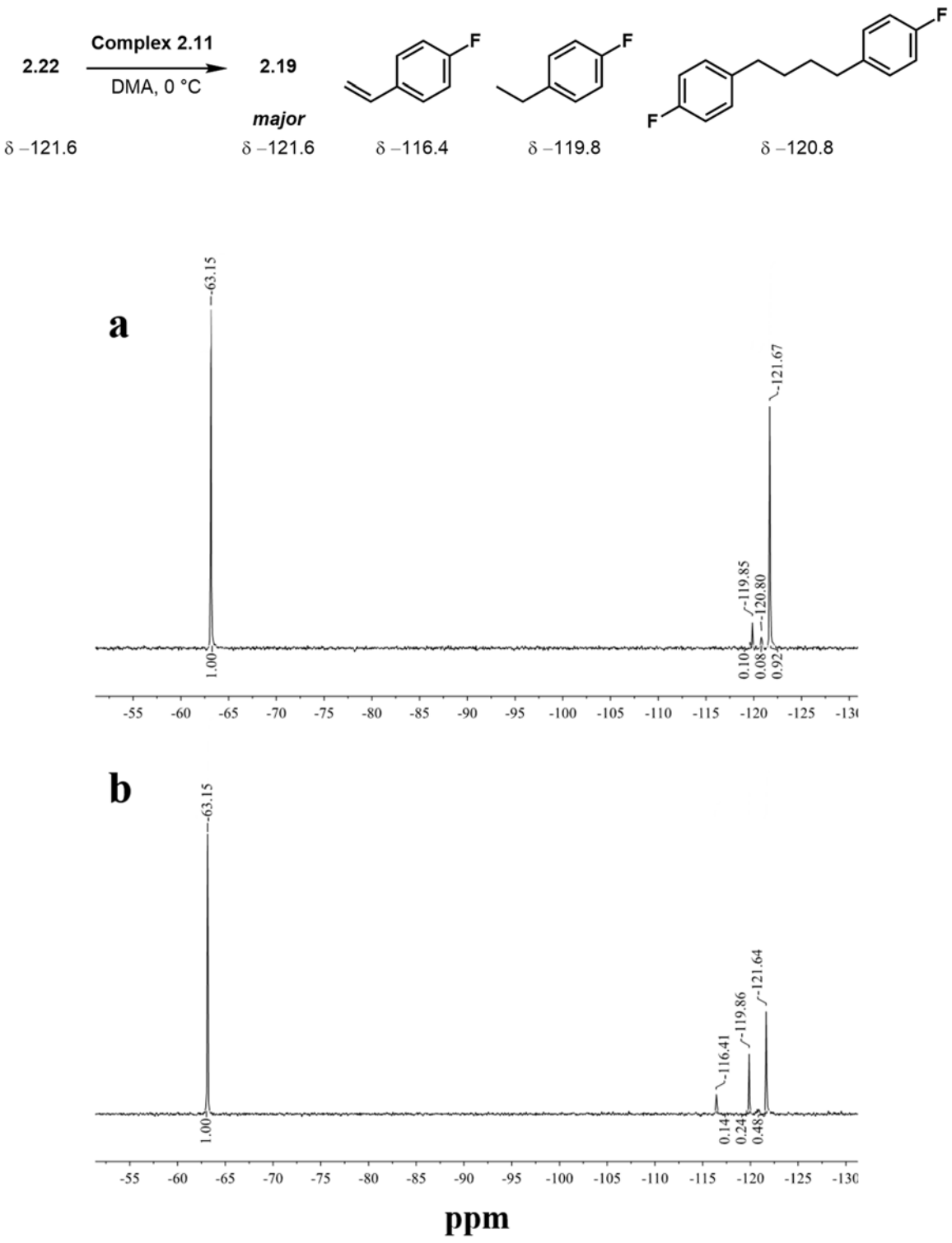

Figure A2.15 ^{19}F NMR spectra (DMA, 376 MHz, 0 °C) of **2.11** with (4-fluorophenethyl)zinc(II) bromide **2.22** (a) after 2 min and (b) after 3 hr. Reaction of **2.11**

provides predominantly starting material **2.22**. Other products formed are shown with their respective ^{19}F NMR chemical shifts.

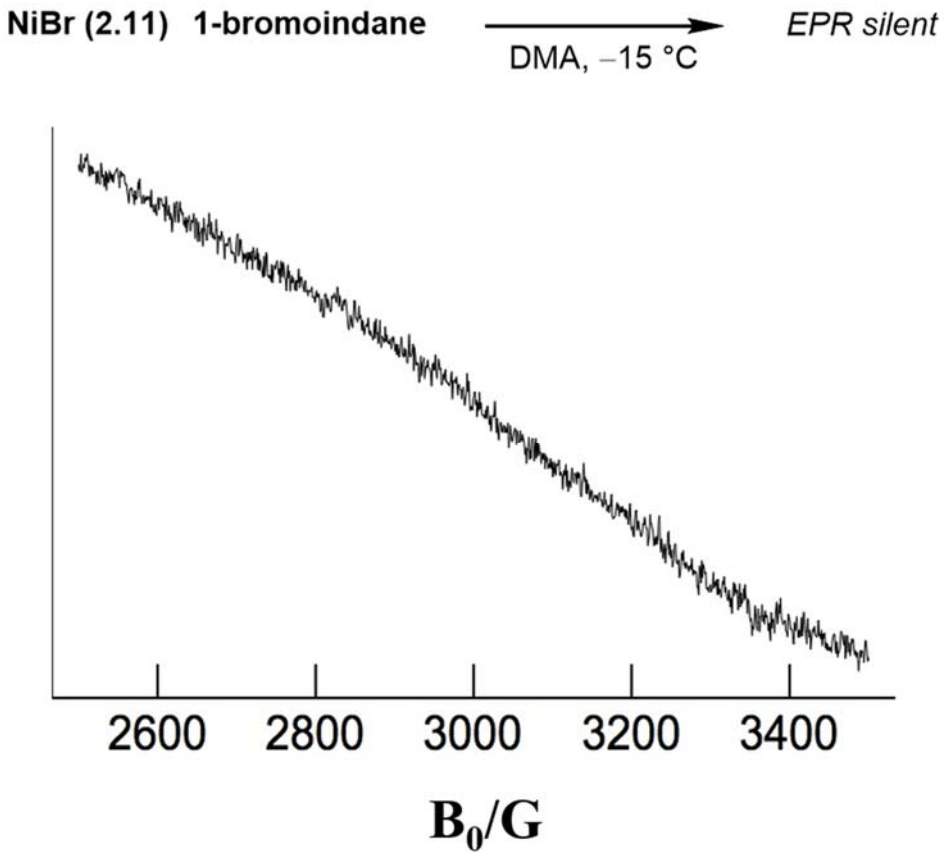

Figure A2.16. EPR Study of Complex **2.11** with 1-bromoindane. Experimental parameters; Microwave power, 2.041 mW; microwave frequency, 9.499 GHz; modulation amplitude, 2 G; gain, 5020; time constant, 40.960.

X-ray Data

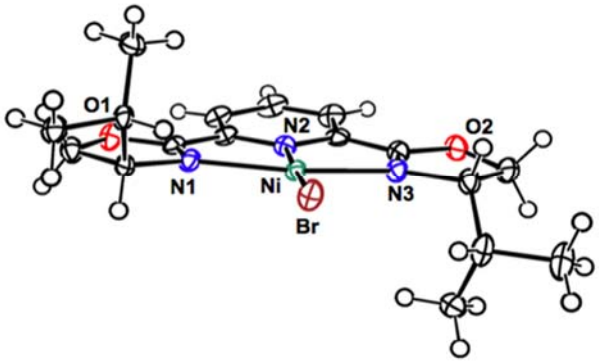

Thermal ellipsoid representation of **2.11-NiBr**. *A second molecule and a THF molecule have been omitted for clarity.*

Table A2.1 Crystal data and structure refinement for **2.11** (tmb05)

Identification code	tmb05
Empirical formula	$C_{19}H_{27}BrN_3NiO_{2.5}$
Formula weight	476.05
Temperature/K	100.15
Crystal system	monoclinic
Space group	$P2_1$
a/Å	5.8729(2)
b/Å	18.1779(7)
c/Å	18.9801(9)
α/°	90
β/°	95.041(3)
γ/°	90
Volume/Å^3	2018.42(14)
Z	4
ρ_{calc}mg/mm^3	1.567
m/mm^{-1}	2.962
F(000)	980.0
Crystal size/mm^3	0.3 × 0.17 × 0.01
Radiation	MoKα (λ = 0.71073)

2Θ range for data collection	4.482 to 75.392°
Index ranges	$-9 \leq h \leq 9, -27 \leq k \leq 27, -28 \leq l \leq 31$
Reflections collected	72097
Independent reflections	16187 [R_{int} = 0.0542, R_{sigma} = 0.0763]
Data/restraints/parameters	16187/1/486
Goodness-of-fit on F^2	0.984
Final R indexes [I>=2σ (I)]	R_1 = 0.0359, wR_2 = 0.0582
Final R indexes [all data]	R_1 = 0.0710, wR_2 = 0.0643
Largest diff. peak/hole / e $Å^{-3}$	0.75/-0.75
Flack parameter	0.009(3)

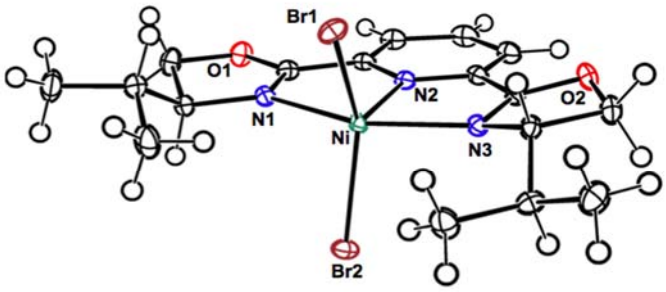

Thermal ellipsoid representation of **2.12-NiBr$_2$**. *A second molecule and a THF molecule have been omitted for clarity.*

Table A2.2. Crystal data and structure refinement for **2.12-NiBr$_2$** (tmb08).

Identification code	tmb08
Empirical formula	$C_{19}H_{27}Br_2N_3NiO_{2.5}$
Formula weight	555.96
Temperature/K	100.15
Crystal system	monoclinic
Space group	$P2_1$
a/Å	13.2569(5)
b/Å	10.8461(4)
c/Å	16.1968(6)
α/°	90
β/°	107.367(2)

γ/°	90
Volume/Å^3	2222.70(15)
Z	4
ρ_{calc}mg/mm^3	1.661
m/mm^{-1}	4.489
F(000)	1120.0
Crystal size/mm^3	0.41 × 0.32 × 0.18
Radiation	MoKα (λ = 0.71073)
2Θ range for data collection	4.588 to 83.28°
Index ranges	-24 ≤ h ≤ 24, -20 ≤ k ≤ 20, -29 ≤ l ≤ 30
Reflections collected	189417
Independent reflections	29929 [R_{int} = 0.0438, R_{sigma} = 0.0488]
Data/restraints/parameters	29929/1/504
Goodness-of-fit on F^2	1.009
Final R indexes [I>=2σ (I)]	R_1 = 0.0313, wR_2 = 0.0548
Final R indexes [all data]	R_1 = 0.0496, wR_2 = 0.0583
Largest diff. peak/hole / e Å^{-3}	1.03/-0.75
Flack parameter	0.0113(18)

Table A2.3 Crystal data and structure refinement for **2.17**.

Identification code	tmb14	
Empirical formula	$C_{28}H_{33}N_4NiO_4$	
Formula weight	548.29	
Temperature	296.15 K	
Wavelength	0.71073 Å	
Crystal system	Monoclinic	
Space group	P 1 21 1	
Unit cell dimensions	a = 14.7477(7) Å	α = 90°
	b = 5.6865(3) Å	β = 112.189(3)°
	c = 19.1442(9) Å	γ = 90°
Volume	1486.59(13) Å^3	
Z	2	
Density (calculated)	1.225 Mg/m^3	
Absorption coefficient	0.689 mm^{-1}	
F(000)	578	
Crystal size	0.11 x 0.14 x 0.04 mm^3	
Theta range for data collection	1.491 to 34.552°.	

Index ranges	$-22 \leq h \leq 23$, $-9 \leq k \leq 8$, $-30 \leq l \leq 28$
Reflections collected	43380
Independent reflections	11456 [R(int) = 0.0724]
Completeness to theta = 25.242°	100.0 %
Absorption correction	None
Max. and min. transmission	1.0000 and 0.8917
Refinement method	Full-matrix least-squares on F^2
Data / restraints / parameters	11456 / 1 / 383
Goodness-of-fit on F^2	1.053
Final R indices [I>2sigma(I)]	$R_1 = 0.0526$, $wR_2 = 0.1175$
R indices (all data)	$R_1 = 0.0878$, $wR_2 = 0.1366$
Absolute structure parameter	0.019(7)
Extinction coefficient	n/a
Largest diff. peak and hole	0.830 and -0.697 e $Å^{-3}$

NMR Spectra

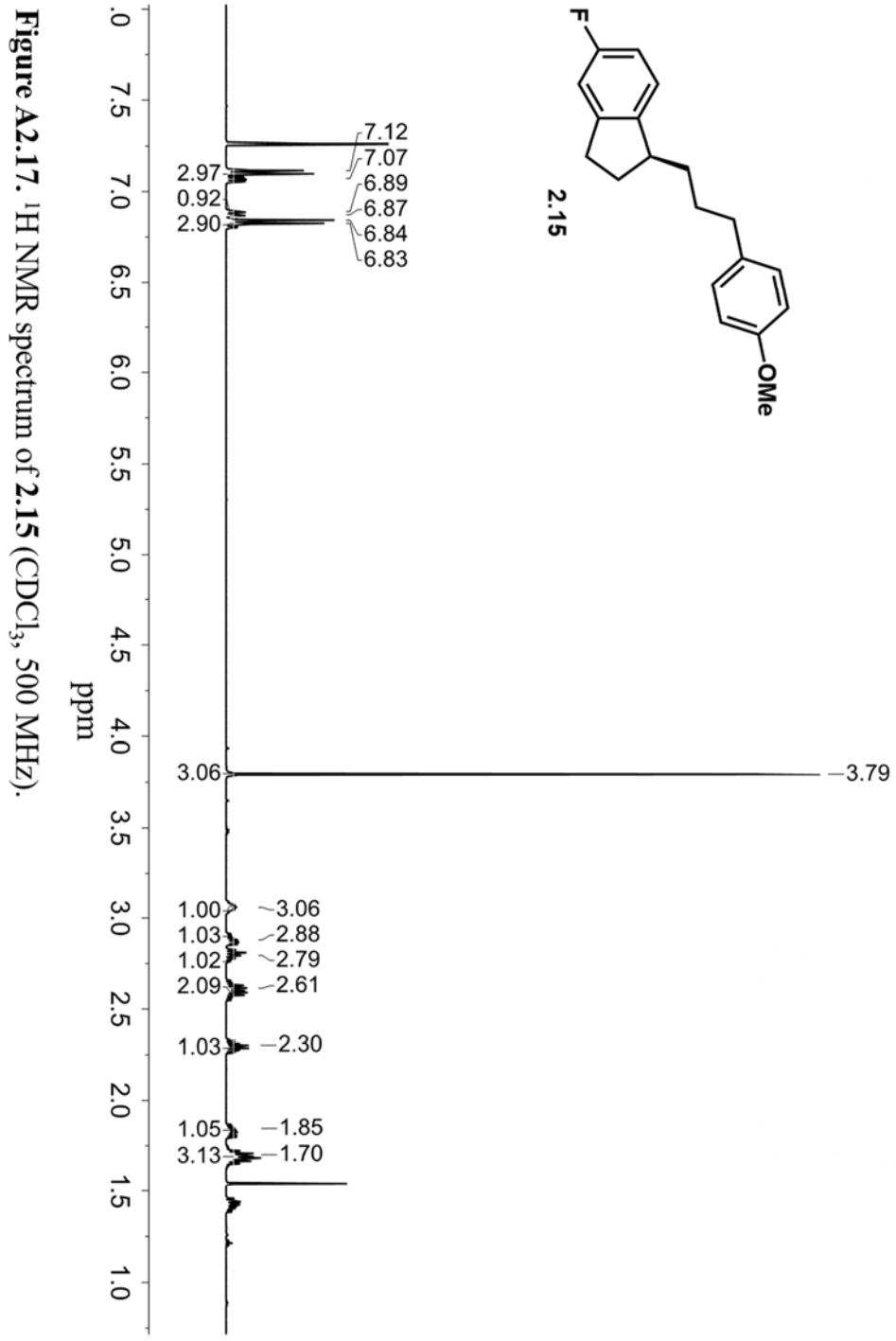

Figure A2.17. ^{1}H NMR spectrum of **2.15** ($CDCl_3$, 500 MHz).

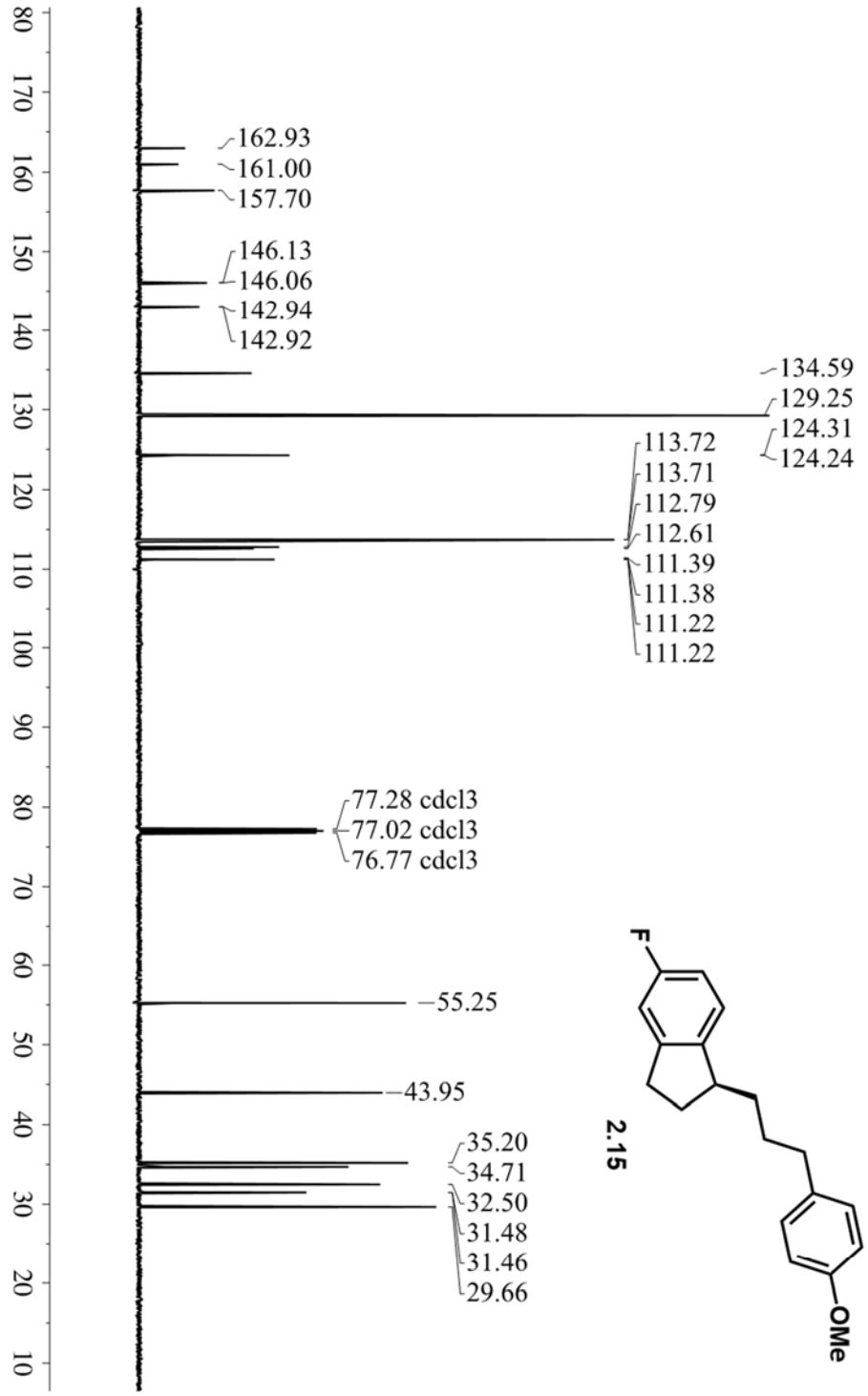

Figure A2.18. ^{13}C NMR spectrum of **2.15** ($CDCl_3$, 126 MHz).

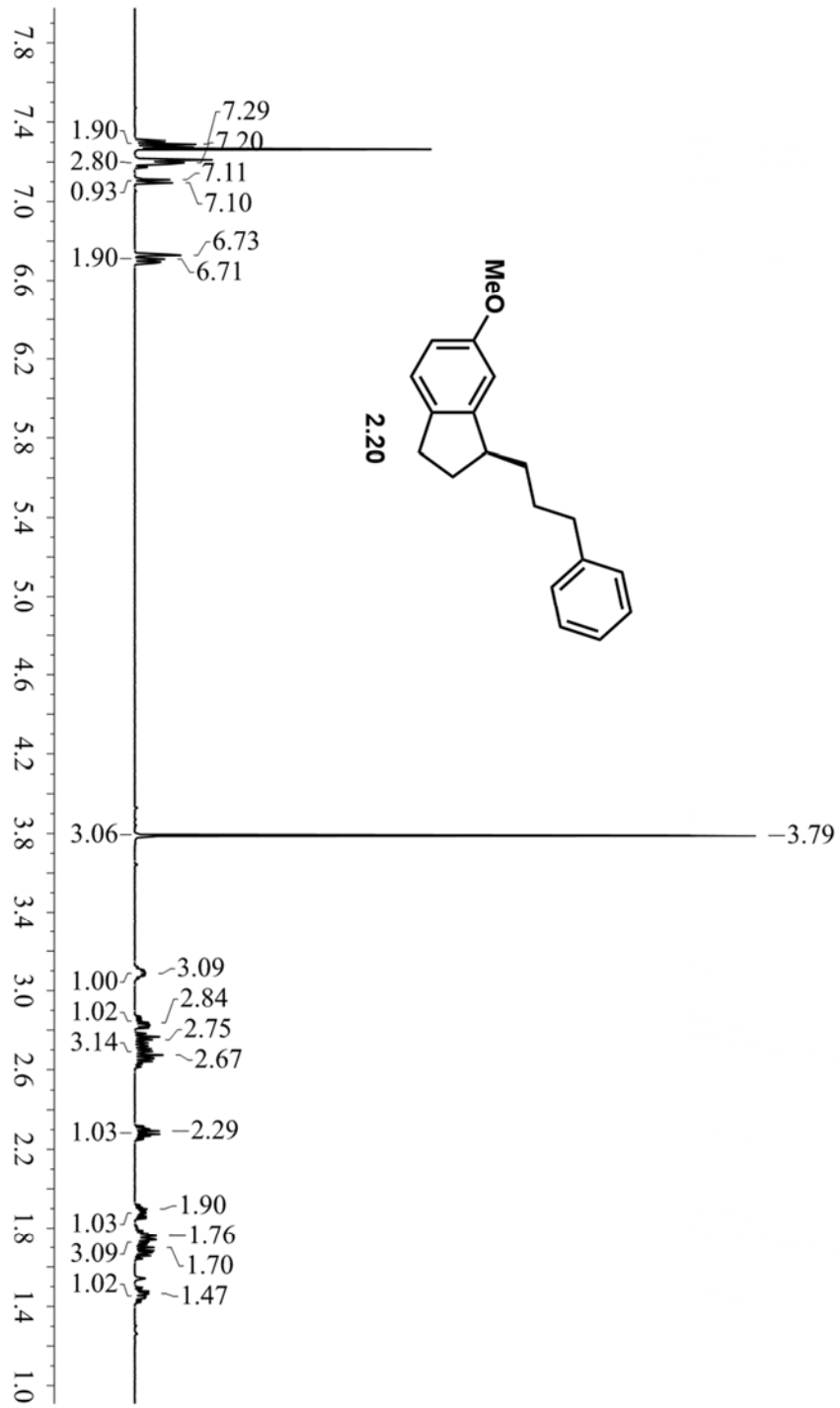

Figure A2.19. ^{1}H NMR spectrum of **2.20** ($CDCl_3$, 500 MHz).

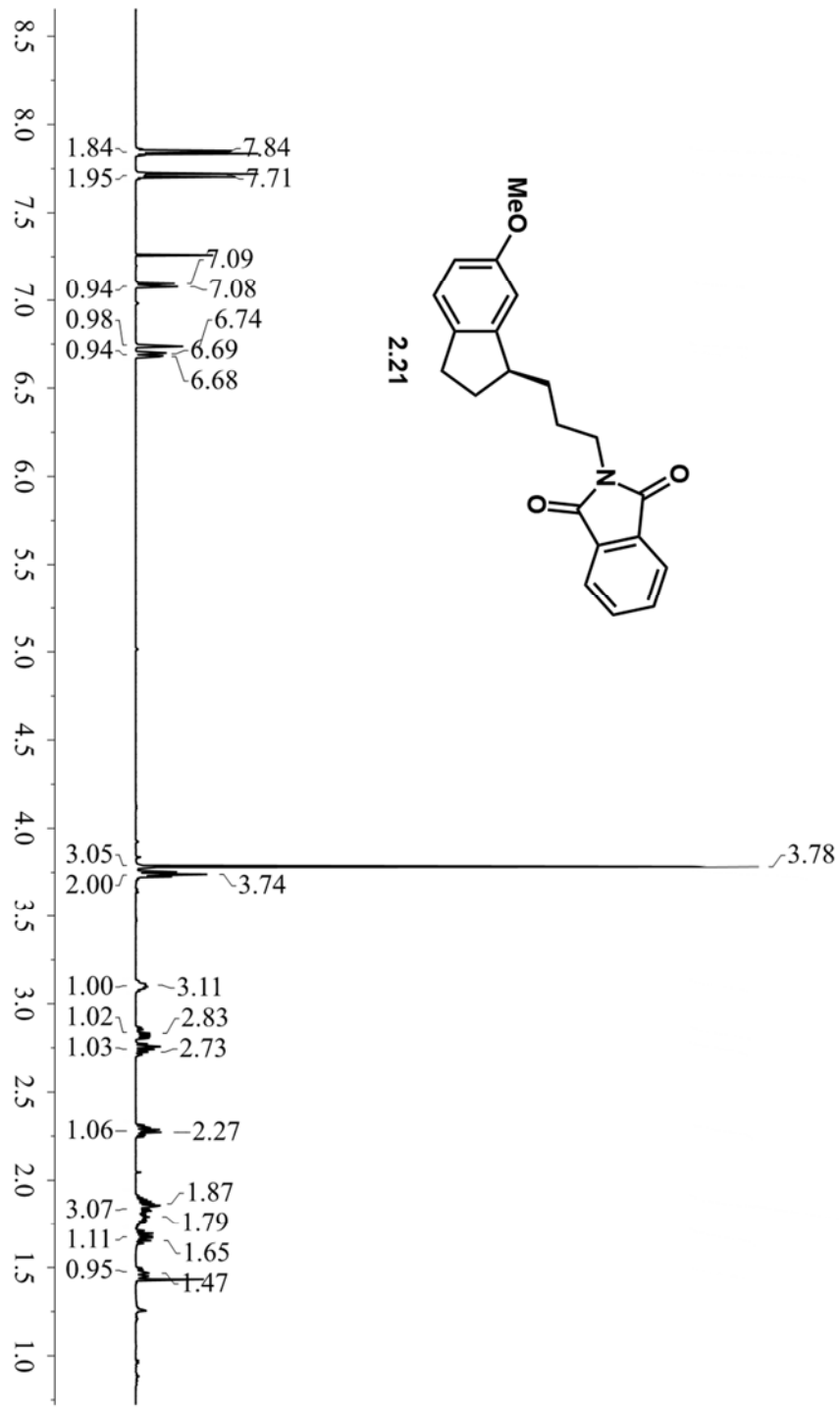

Figure A2.20. ^{1}H NMR spectrum of **2.21** ($CDCl_3$, 500 MHz).

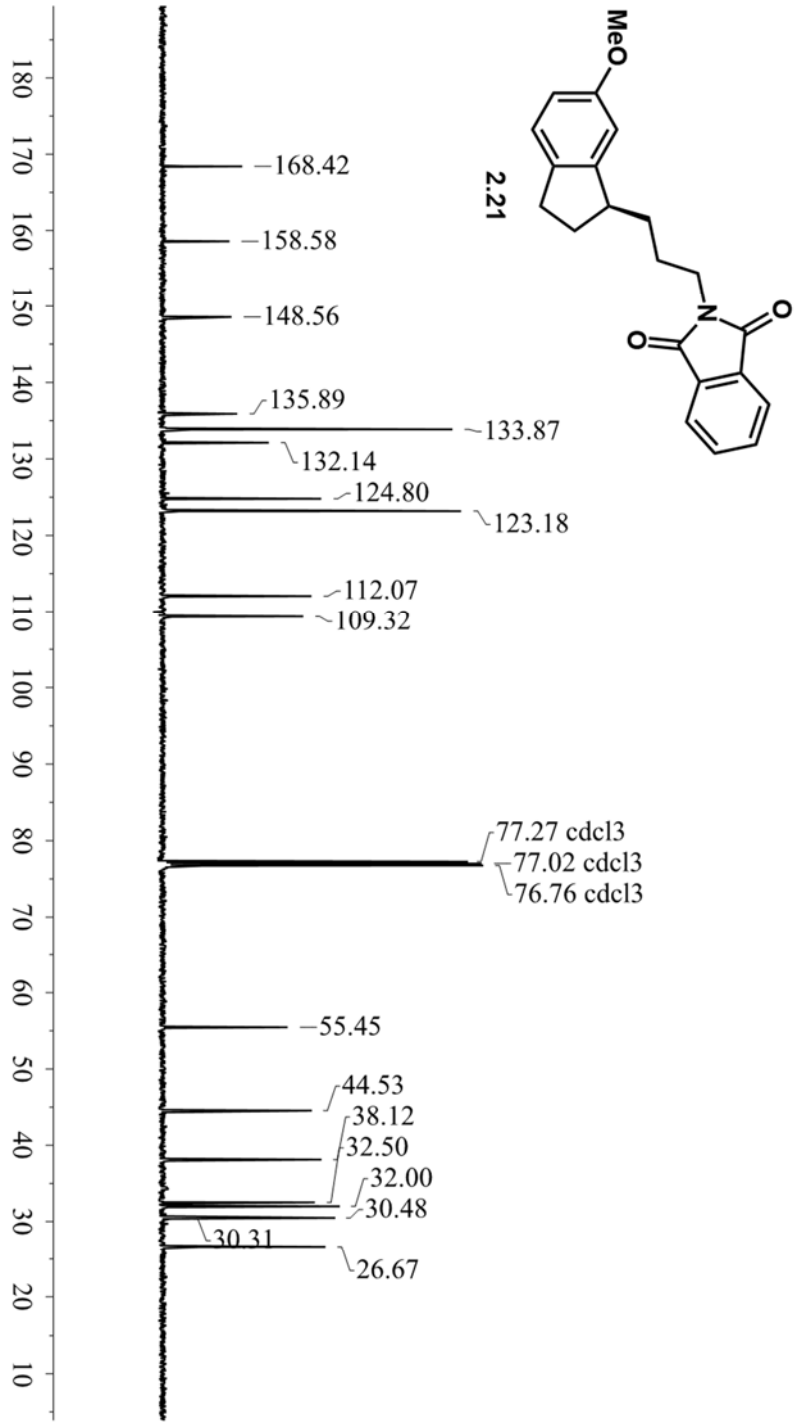

Figure A2.21. ^{13}C NMR spectrum of **2.21** ($CDCl_3$, 126 MHz).

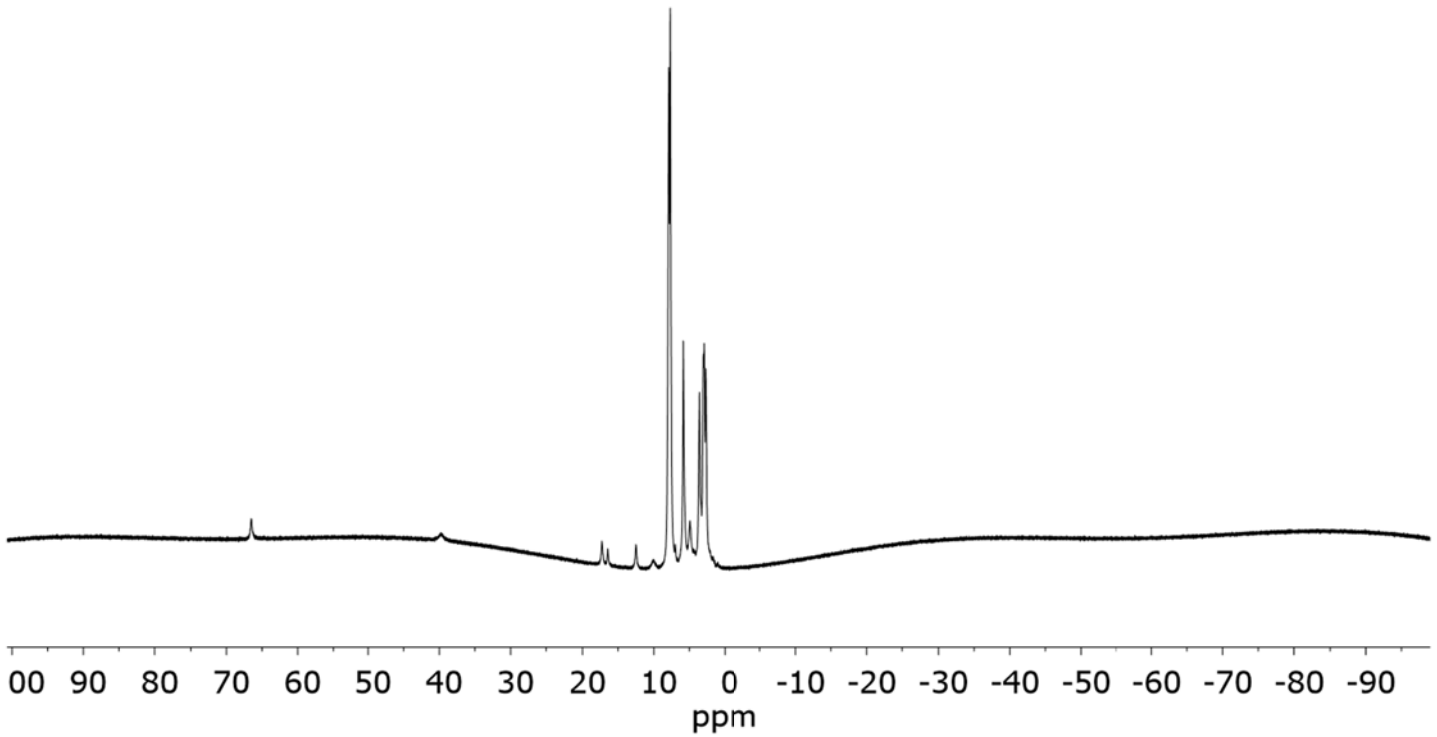

Figure A2.22. ^{1}H NMR spectrum of **2.12** generated by the reaction of **2.11** and 1-bromoindane (C_6D_6, 300 MHz).

Chapter 3 Appendix.

A3.1 Catalysis Details

Table A3.1. Results of individual runs using **3.3** at 300 equiv acid loading per complex with no photolysis.

Run	Absorbance	Equiv NH_3/Complex	% Yield (Based on H^+)
A	0.123	8.91	9.0
B	0.111	7.98	8.0
C	0.092	6.53	6.6

Table A3.2. Results of individual runs using **3.3** at 300 equiv acid loading per complex with no photolysis, allowed to warm to room temperature overnight.

Run	Absorbance	Equiv NH_3/Complex	% Yield (Based on H^+)
A	0.126	9.17	9.2
B	0.113	8.13	8.2

Table A3.3. Results of individual runs using **3.3** at 300 equiv acid loading per complex with Hg lamp photolysis.

Run	Absorbance	Equiv NH_3/Complex	% Yield (Based on H^+)
A	0.274	18.4	20.6
B	0.252	18.8	18.9
C	0.232	17.2	17.3

Table A3.4. Results of individual runs using **3.1** at 150 equiv acid loading per complex with no photolysis.

Run	Absorbance	Equiv NH_3/Complex	% Yield (Based on H^+)
A	0.005	-0.04	0
B	0.002	-0.16	0

Table A3.5. Results of individual runs using **3.1** at 150 equiv acid loading per complex with Hg lamp photolysis.

Run	Absorbance	Equiv NH_3/Complex	% Yield (Based on H^+)
A	0.009	0.10	0.2
B	0.007	0.01	0.02

Table A3.6. Results of individual runs using **3.3** at 300 equiv acid loading per complex with no photolysis and 2-MeTHF instead of Et_2O as the reaction solvent.

Run	Absorbance	Equiv NH_3/Complex	% Yield (Based on H^+)
A	0.009763	0.26	0.3
B	0.014944	0.56	0.7

Table A3.7. Results of individual runs using **3.3** at 3000 equiv acid loading per complex with no photolysis.

Run	Absorbance	Equiv NH_3/Complex	% Yield (Based on H^+)
A	0.068	23.5	2.4
B	0.074	25.9	2.7
C	0.069	24.1	2.5

Table A3.8. Results of individual runs using **3.3** at 3000 equiv acid loading per complex with Hg lamp photolysis.

Run	Absorbance	Equiv NH_3/Complex	% Yield (Based on H^+)
A	0.183	67.4	6.9
B	0.191	70.6	7.3
C	0.169	62.0	6.3

Table A3.9. Results of individual runs using **3.5** at 150 equiv acid loading per complex with no photolysis.

Run	Absorbance	Equiv NH_3/Complex	% Yield (Based on H^+)
A	0.074	2.56	5.2
B	0.074	2.58	5.2

Table A3.10. Results of individual runs using **3.5** at 150 equiv acid loading per complex with Hg lamp photolysis.

Run	Absorbance	Equiv NH_3/Complex	% Yield (Based on H^+)
A	0.224	8.27	16.3
B	0.257	9.53	19.3

Table A3.11. Results of individual runs using **$P_3^BFe(N_2^-)$** at 1500 equiv acid loading per complex with no photolysis.

Run	Absorbance	Equiv NH_3/Complex	% Yield (Based on H^+)
A	0.294	59.2	11.8
B	0.317	64.1	12.8
C	0.281	56.7	11.2

Table A3.12. Results of individual runs using **$P_3^BFe(N_2^-)$** at 1500 equiv acid loading per complex with Hg lamp photolysis.

Run	Absorbance	Equiv NH_3/Complex	% Yield (Based on H^+)
A	0.390	79.1	15.8
B	0.450	91.5	18.2
C	0.462	93.9	18.7

Table A3.13. Results of individual runs using **3.3** at 300 equiv acid loading per complex with Blue LED photolysis.

Run	Absorbance	Equiv NH_3/Complex	% Yield (Based on H^+)
A	0.281	21.01	21
B	0.289	21.58	22

Table A3.14. Results of individual runs using **$(P_3^B)(\mu\text{-}H)Fe(N_2)(H)$** at 150 equiv acid loading per complex with no photolysis. *Yield based on all nitrogenous products.

Run	Absorbance (NH_3)	Equiv NH_3/Complex	Absorbance (N_2H_4)	Equiv N_2H_4/Complex	% Yield (Based on H^+)
A	0.158	5.81	0.032	0.44	14
B	0.168	6.17	0.078	0.97	13

Table A3.15. Results of individual runs using **$(P_3^B)(\mu\text{-}H)Fe(N_2)(H)$** at 150 equiv acid loading per complex with Hg lamp photolysis. *Yield based on all nitrogenous products.

Run	Absorbance (NH_3)	Equiv NH_3/Complex	Absorbance (N_2H_4)	Equiv N_2H_4/Complex	% Yield (Based on H^+)
A	0.247	9.2	0.232	2.76	24
B	0.211	7.85	0.360	4.24	24

*A3.2 Spectroscopic characterization of compounds **3.1**, **3.2**, **3.3** and **3.5**.*

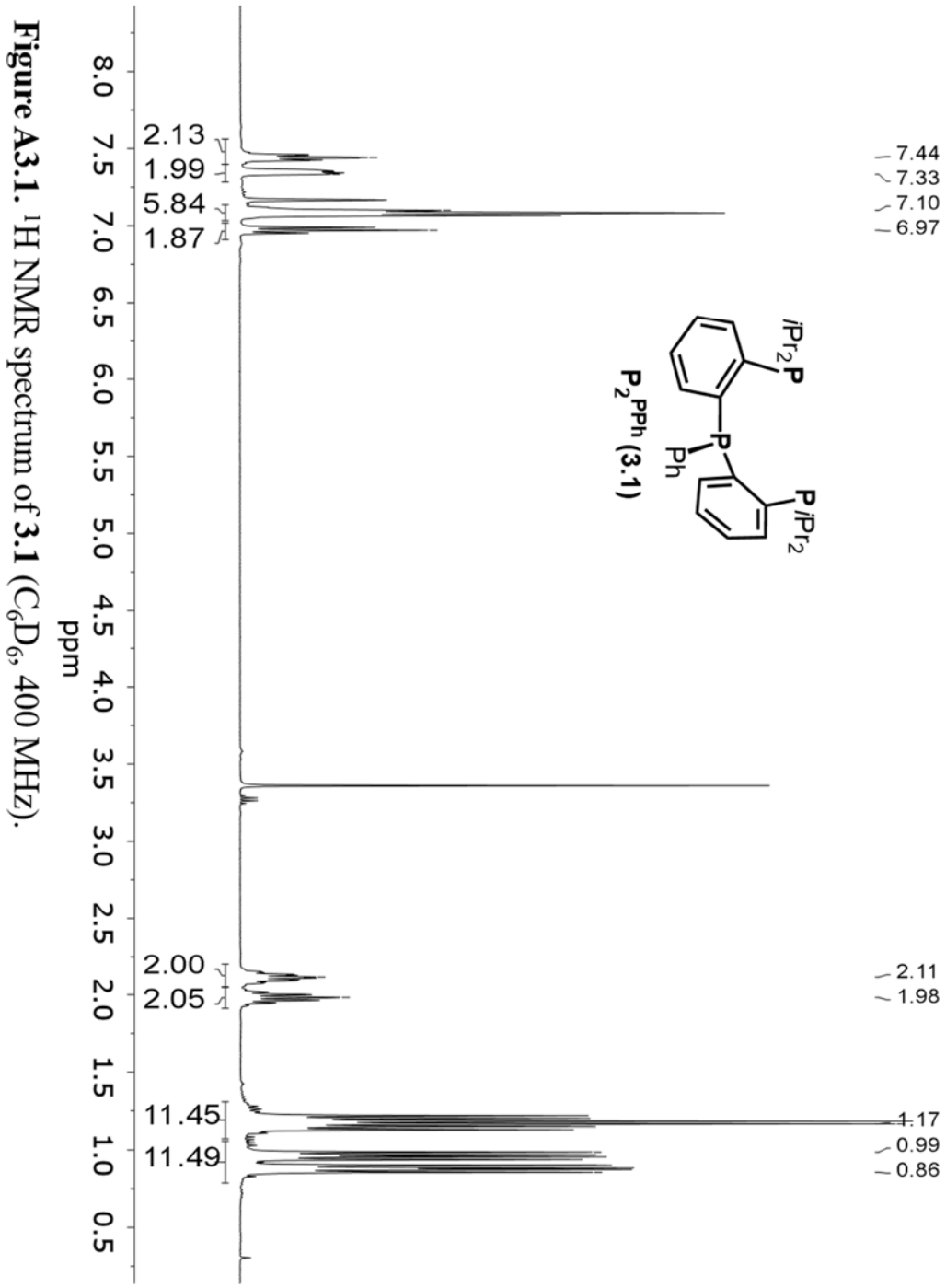

Figure A3.1. ^{1}H NMR spectrum of **3.1** (C_6D_6, 400 MHz).

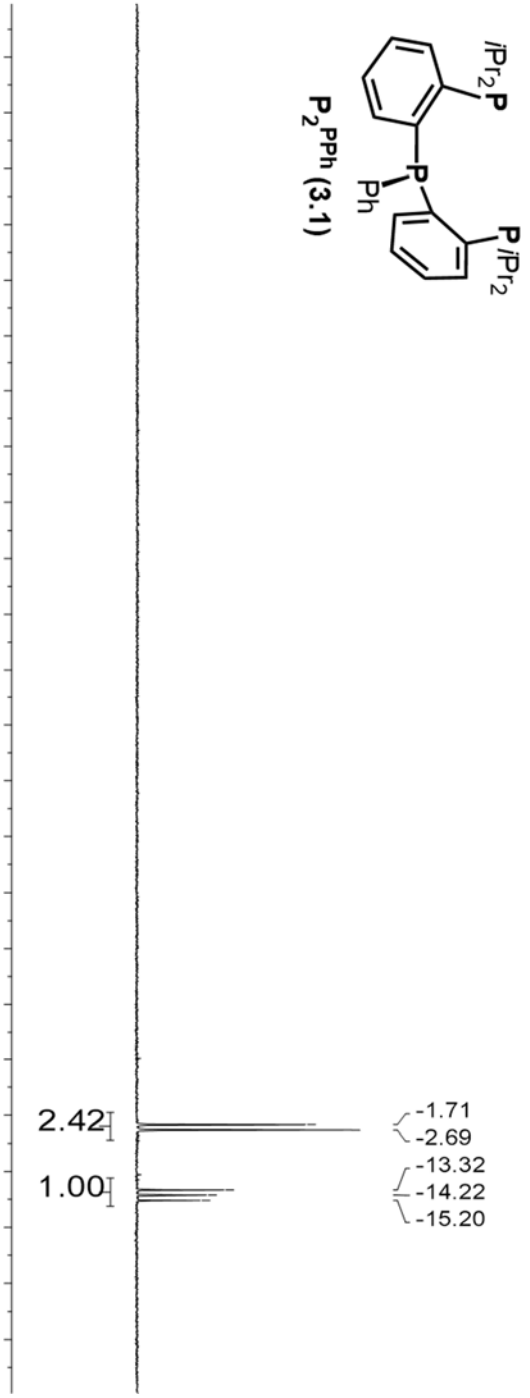

Figure A3.2. ^{31}P NMR spectrum of **3.1** (C_6D_6, 162 MHz).

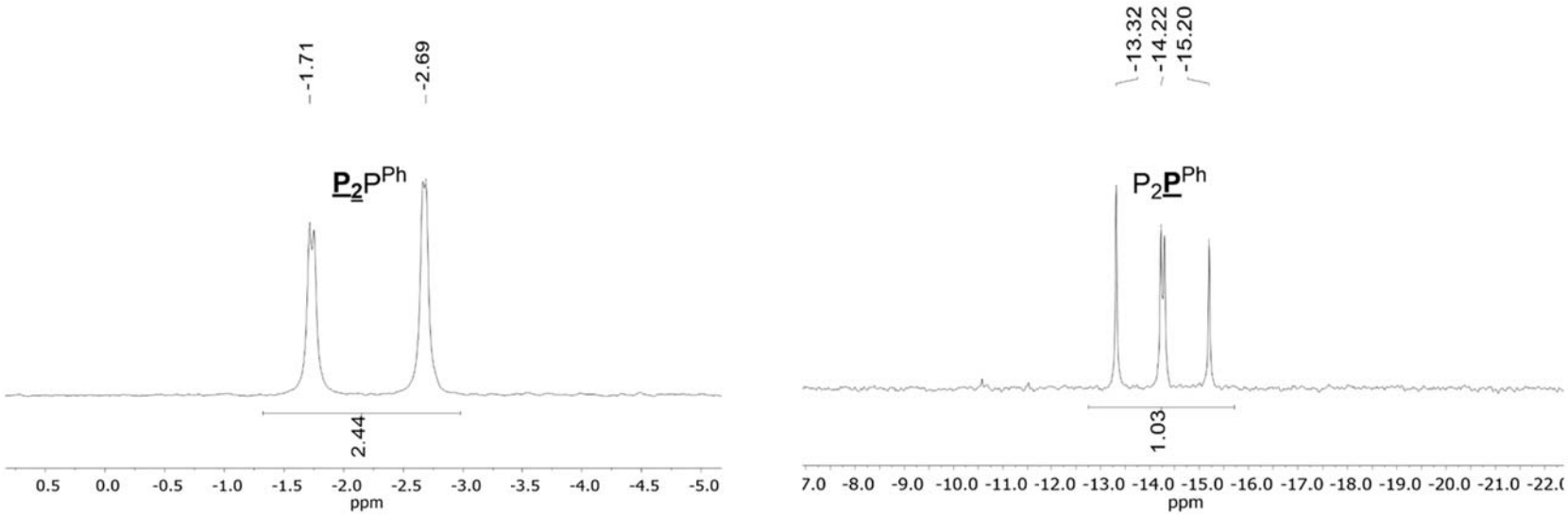

Figure A3.3. ^{31}P NMR spectrum of **3.1** (C_6D_6, 162 MHz) (magnified).

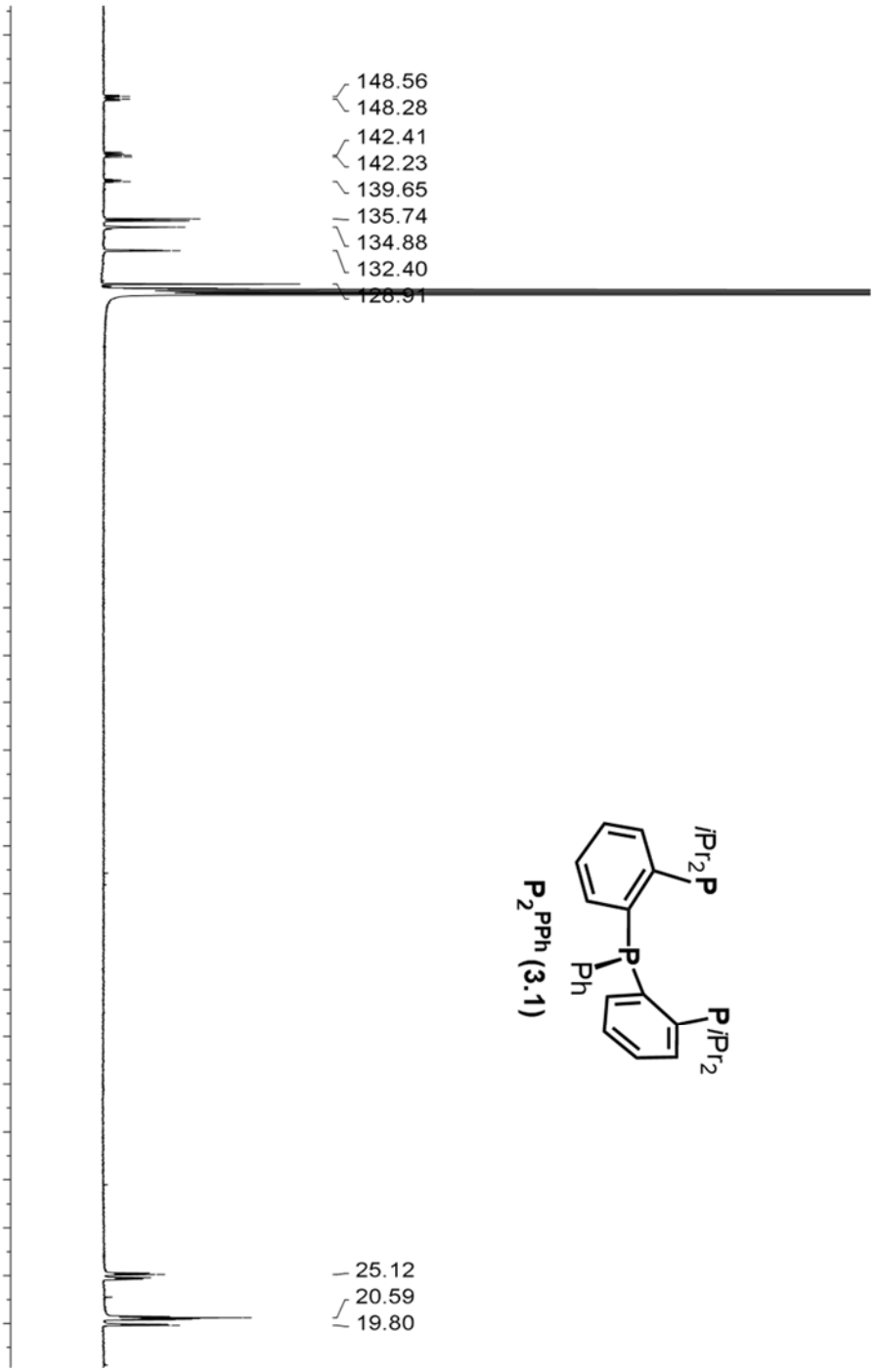

Figure A3.4. ^{13}C NMR spectrum of **3.1** (C_6D_6, 101 MHz).

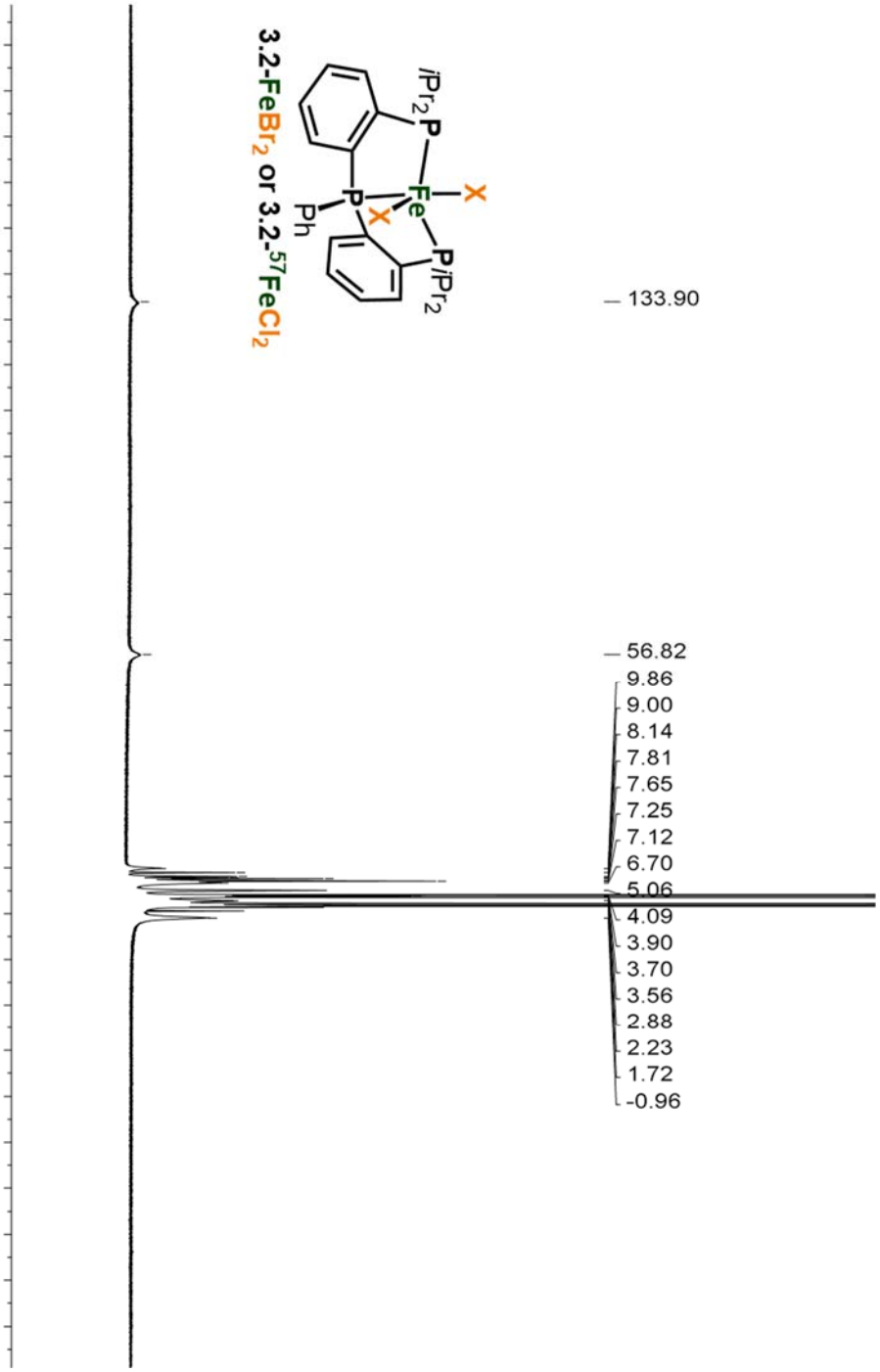

Figure A3.5. ^{1}H NMR spectrum of **3.2-FeBr$_2$** (THF-d_8, 400 MHz).

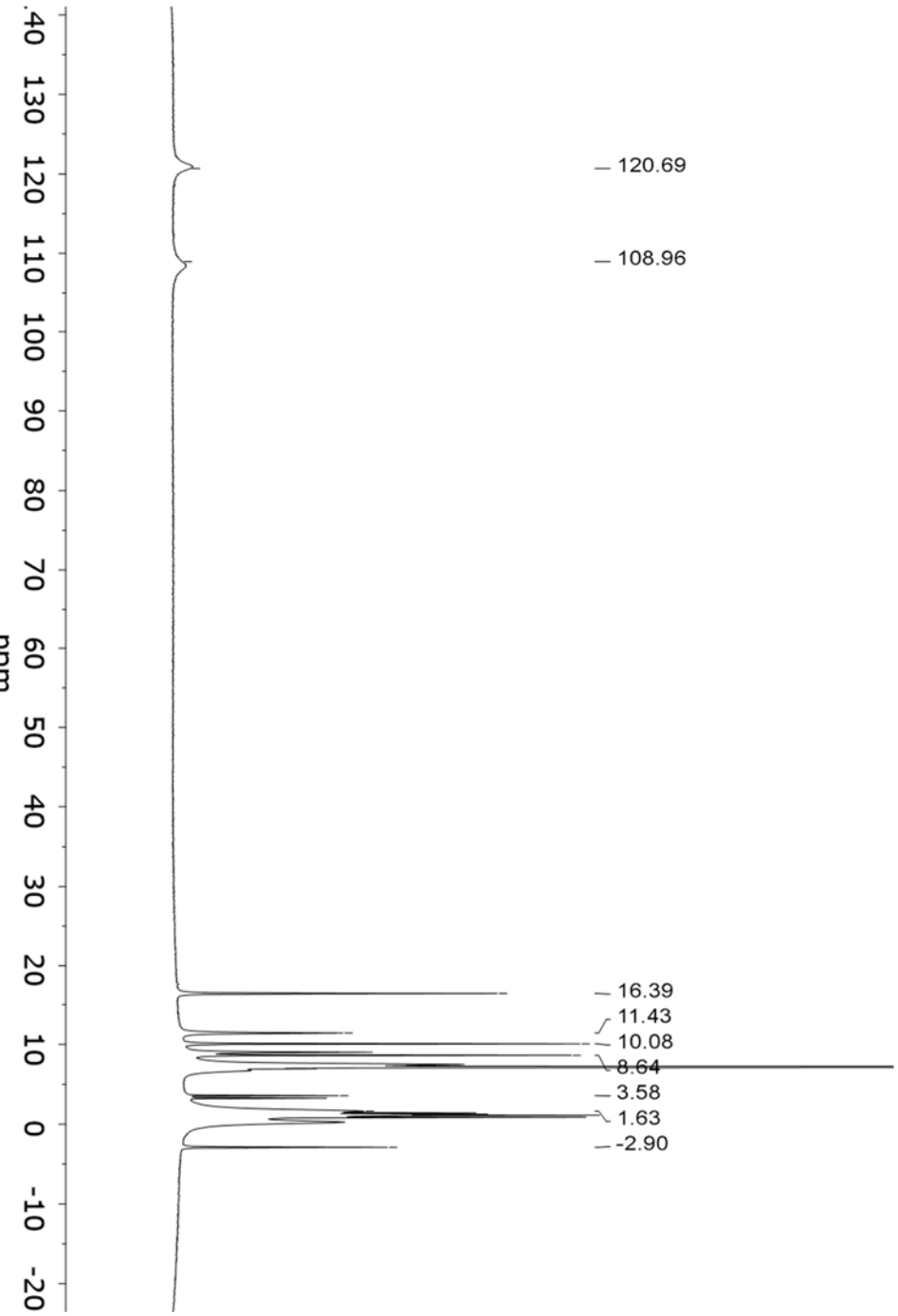

Figure A3.6. ^{1}H NMR spectrum of **3.2-^{57}FeCl$_2$** (THF-d_8, 400 MHz).

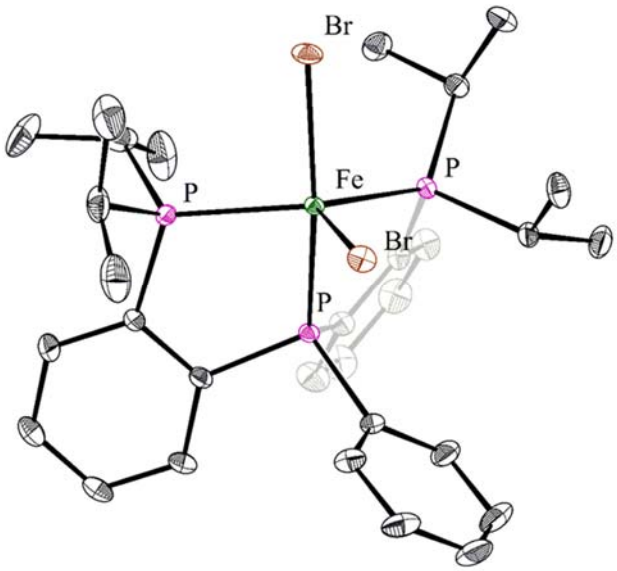

Figure A3.7. X-ray crystal structure of **3.2-FeBr$_2$** with thermal ellipsoids shown at 50% probability.

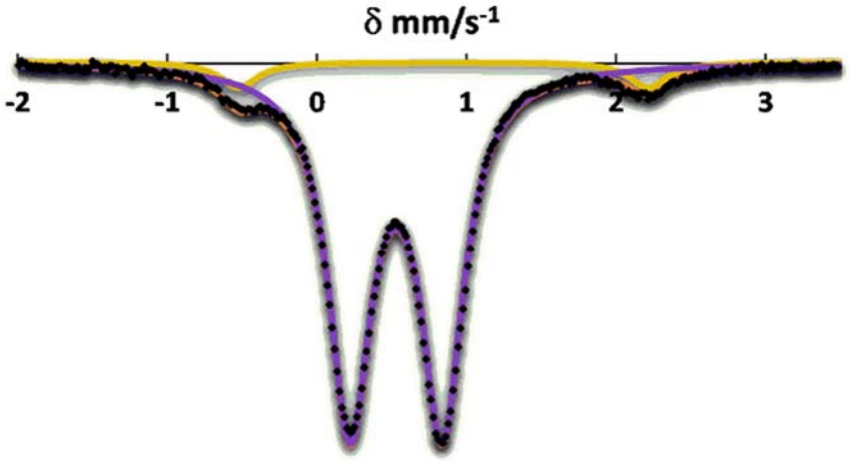

Figure A3.8. Solid-state ^{57}Fe Mössbauer spectrum of **3.2-^{57}FeCl$_2$**. Data presented in black points, simulation represented by solid orange line, major $S = 1$ component (95 % of the total Fe) represented with purple line (fit with $\delta =$ 0.53 mm s^{-1}, $\Delta E_Q =$ 0.62 mm s^{-1}, $\Gamma_R =$ 0.35 mm s^{-1} and $\Gamma_L =$ 0.35 mm s^{-1}), and minor $S = 2$ component (5 % of the total Fe) represented by yellow line (fit with $\delta =$ 0.85 mm s^{-1}, $\Delta E_Q =$ 2.74 mm s^{-1}, $\Gamma_R =$ 0.29 mm s^{-1} and $\Gamma_L =$ 0.29 mm s^{-1}).

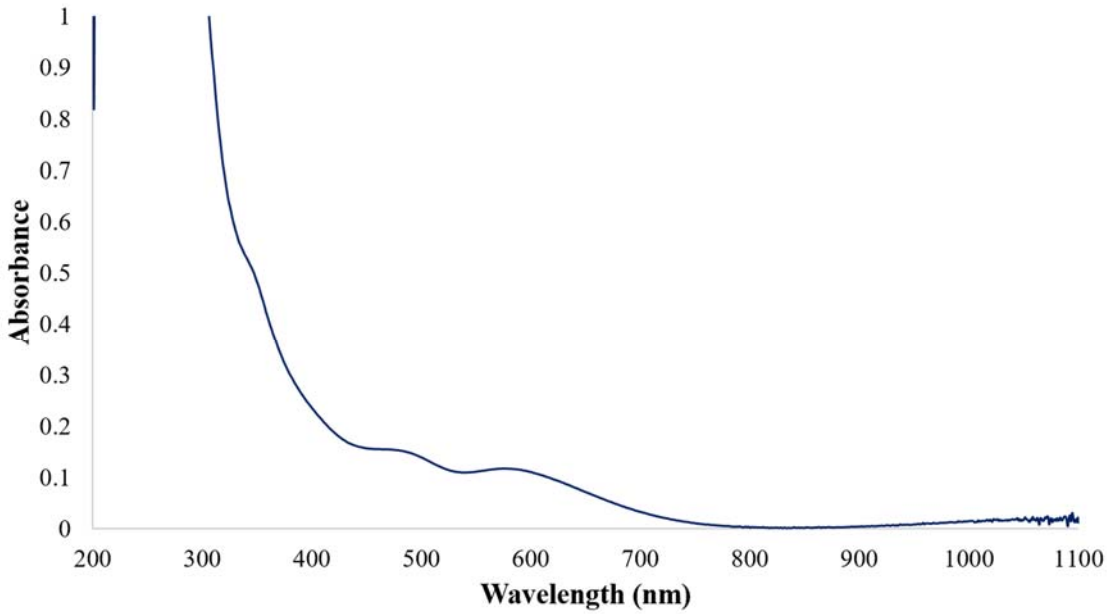

Figure A3.9. UV-Vis of **3.2-FeBr$_2$** in THF (l = 1 cm, c = 0.12 μM).

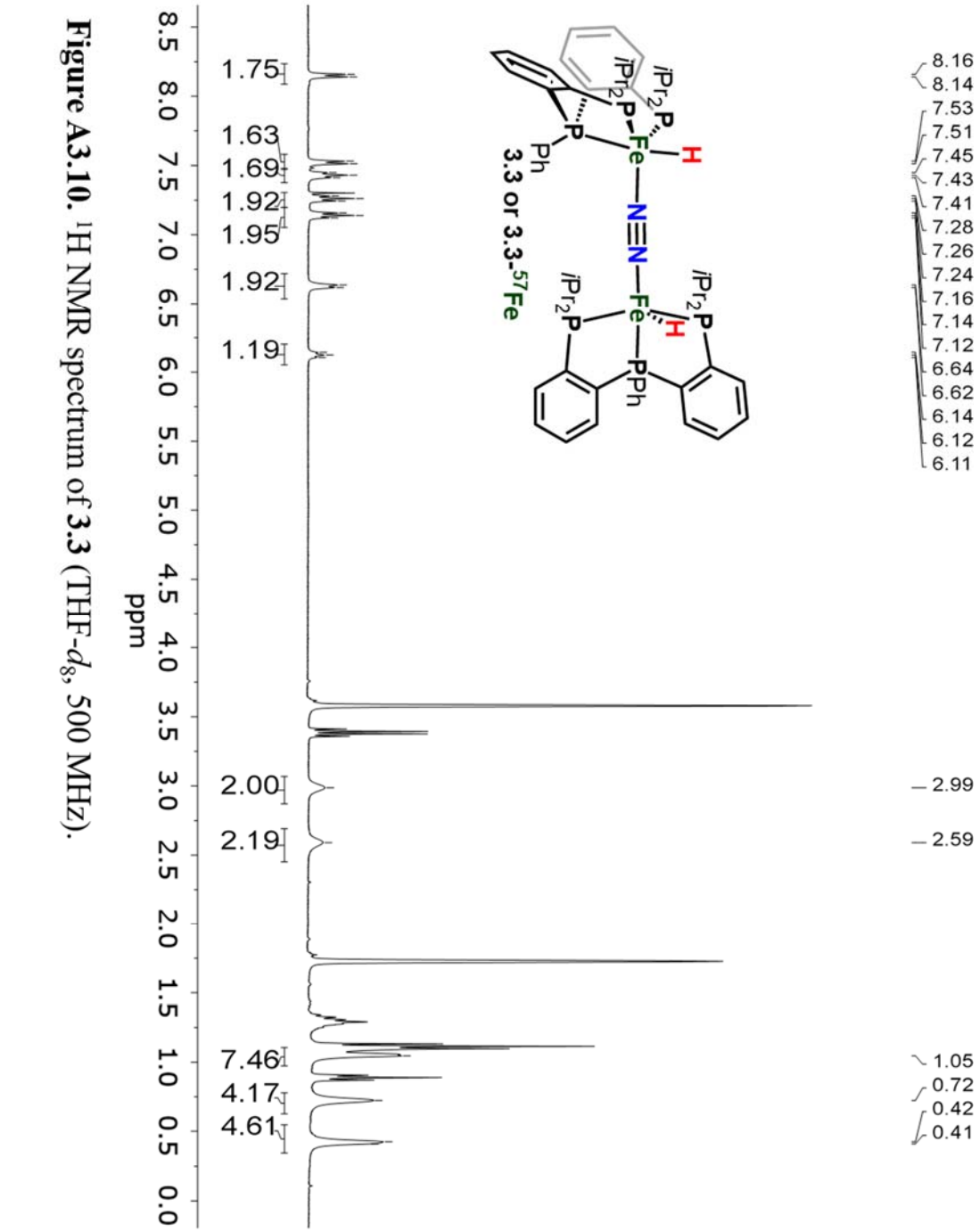

Figure A3.10. ^{1}H NMR spectrum of **3.3** (THF-d_8, 500 MHz).

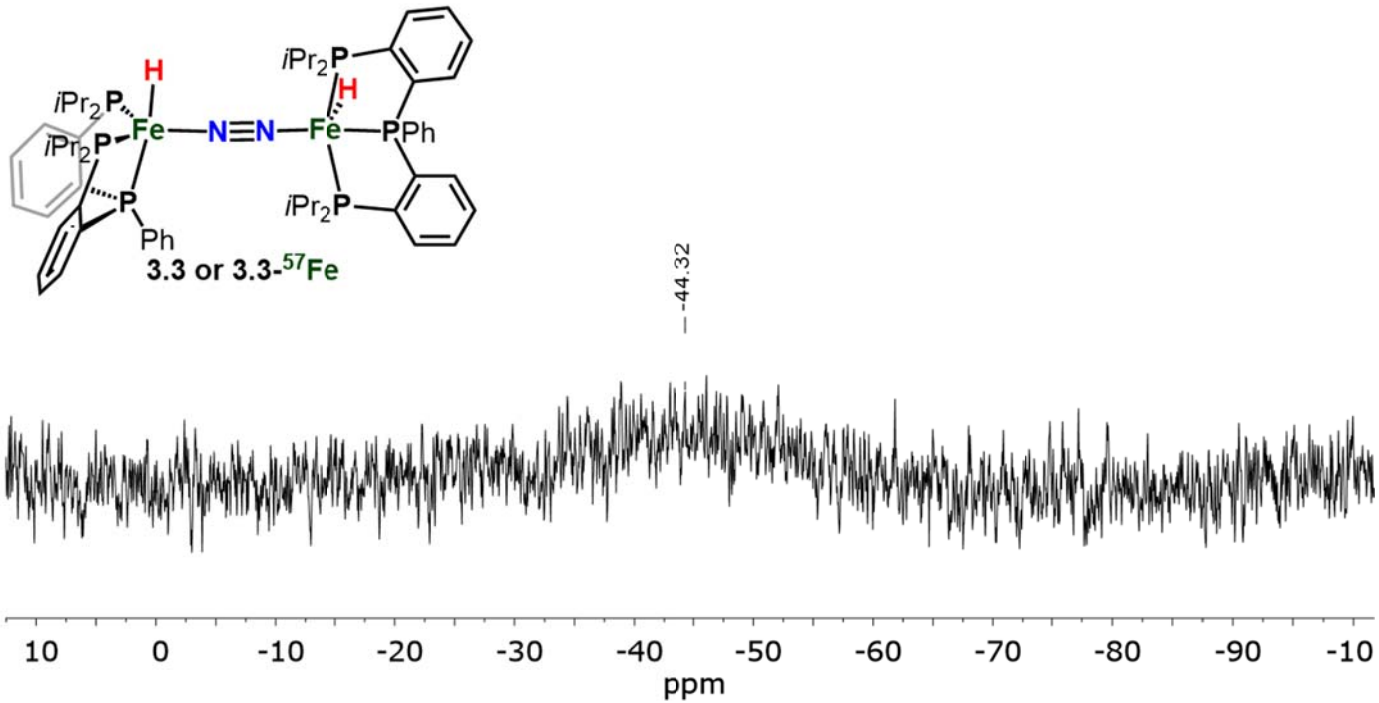

Figure A3.11. ^{31}P NMR spectrum of **3.3** (THF-d_8, 202 MHz).

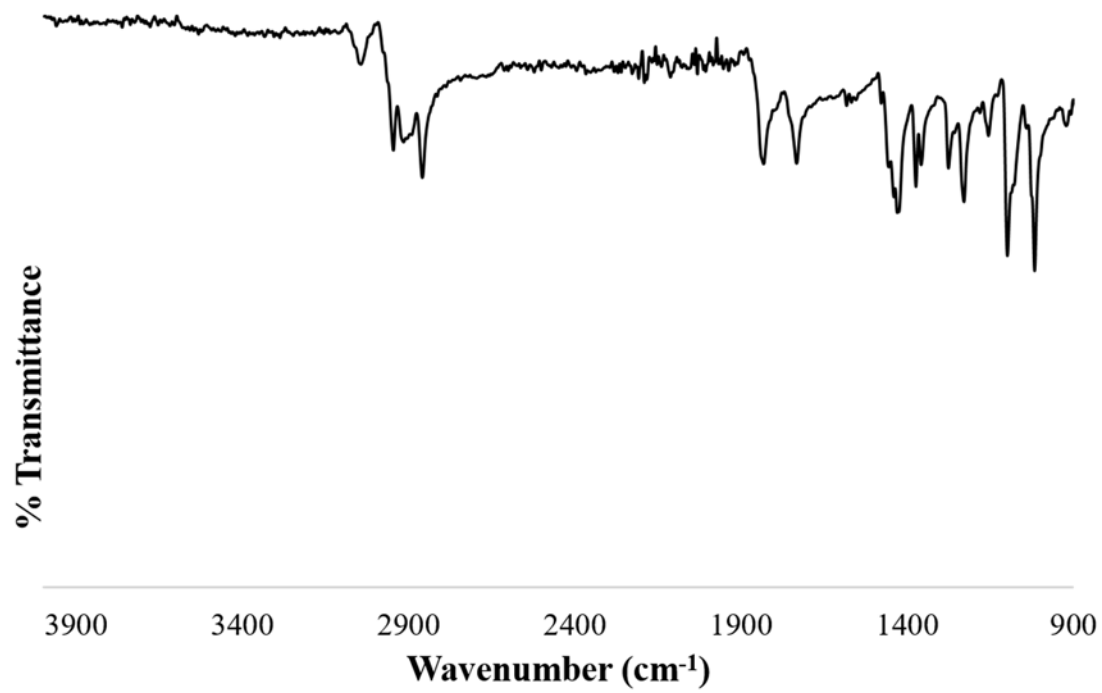

Figure A3.12. Solid-state IR spectrum of **3.3** (KBr); $\nu_{Fe\text{-}H}$ = 1833 cm^{-1}; $\nu_{Fe\text{-}H}$ = 1734 cm^{-1}.

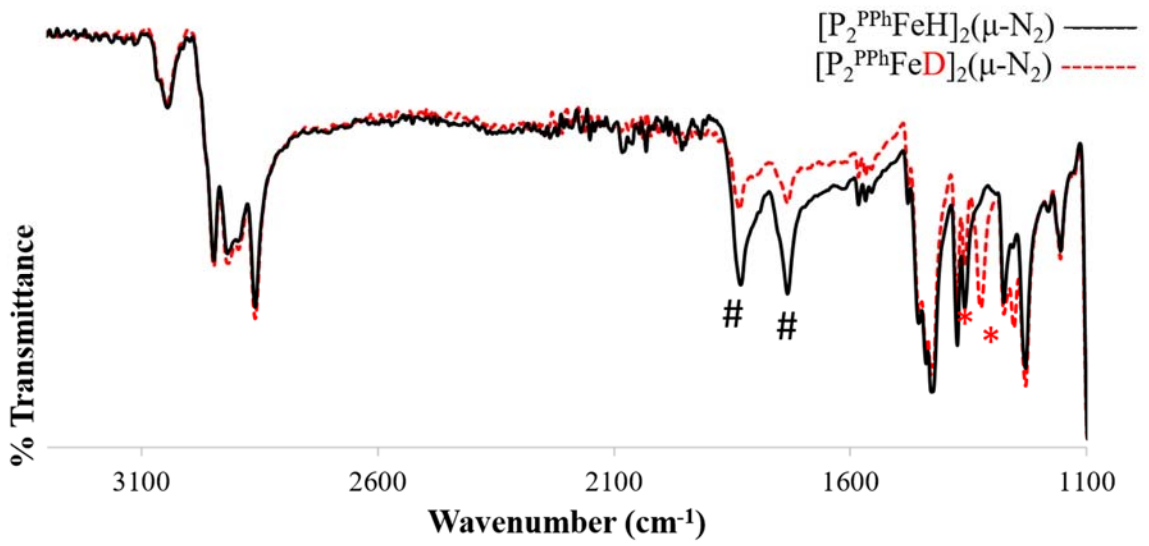

Figure A3.13. Infrared spectrum of solid **3.3** and **3.3D** overlaid. Astericks indicate Fe-D vibrations and hashtags indicate Fe-H vibrations. **3.3** exhibited expected peak shifts in the Fe-H(D) vibrations from 1833 and 1734 cm^{-1} for **3.3** to 1324 cm^{-1} and 1256 cm^{-1} for **3.3D**.

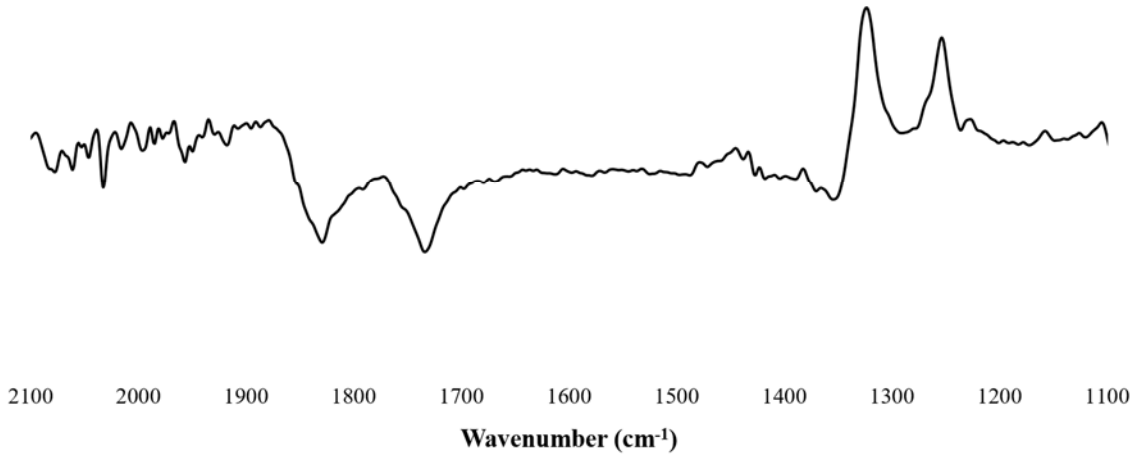

Figure A3.14. Solid-state IR difference spectrum of **3.3D** and **3.3**.

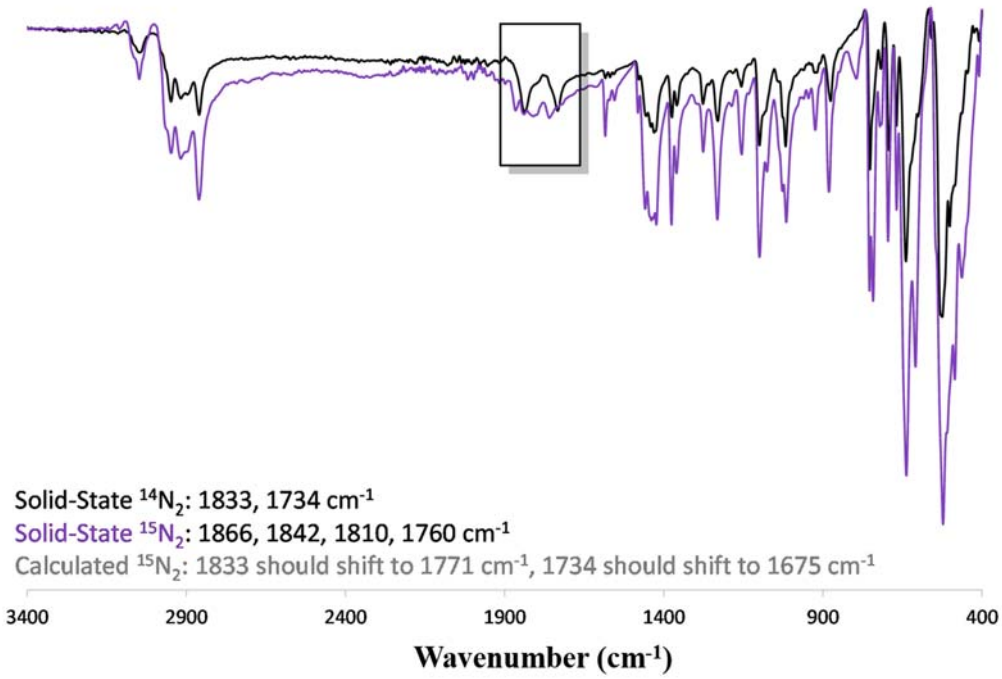

Figure A3.15. Solid-state IR difference spectrum of **3.3** and **3.3-$^{15}N_2$** overlaid.

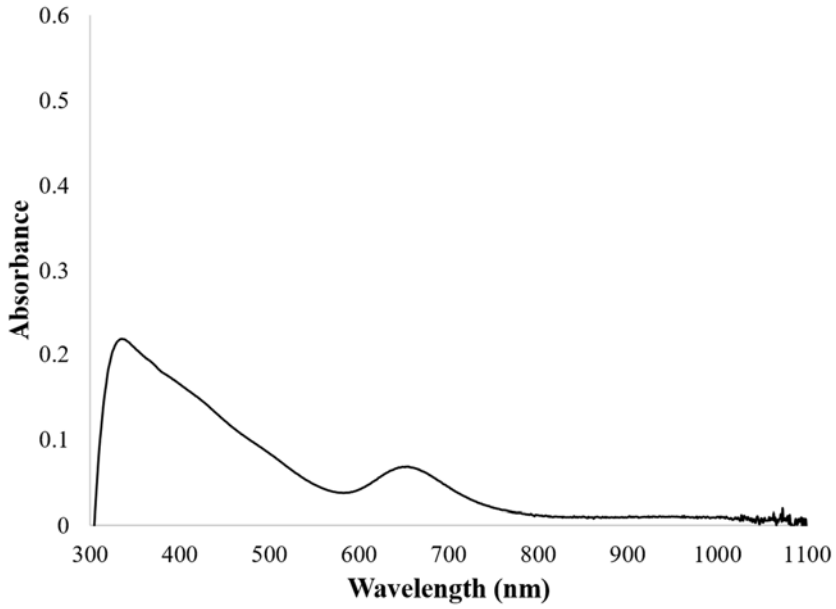

Figure A3.16. UV-Vis of **3.3** in THF (l = 1 cm, c = 0.18 μM).

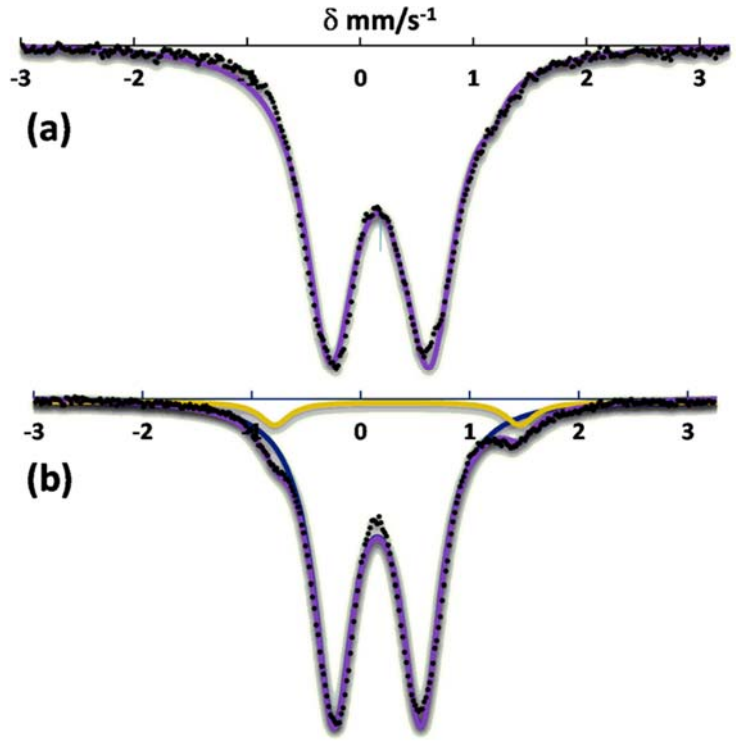

Figure A3.17. (a) Solid-state ^{57}Fe Mössbauer spectrum of **3.3**. Data presented in black points, simulation represented by solid purple line (fit with δ = 0.15 mm s^{-1}, ΔE_Q = 0.78 mm s^{-1}, Γ_R = 0.71 mm s^{-1} and Γ_L = 0.71 mm s^{-1}) **(b)** ^{57}Fe Mossbauer spectrum of a 4.2 mM solution of **3.3** in 2-MeTHF. Data presented in black points, simulation represented by solid purple,

major $S = 0$ component (95 % of the total Fe) represented with blue line (fit with $\delta =$ 0.15 mm s^{-1}, ΔE_Q = 0.80 mm s^{-1}, Γ_R = 0.43 mm s^{-1} and Γ_L = 0.43 mm s^{-1}), and minor $S = 1/2$ component (5 % of the total Fe) represented by yellow line (fit with $\delta =$ 0.34 mm s^{-1}, ΔE_Q = 2.25 mm s^{-1}, Γ_R = 0.33 mm s^{-1} and Γ_L = 0.33 mm s^{-1}).

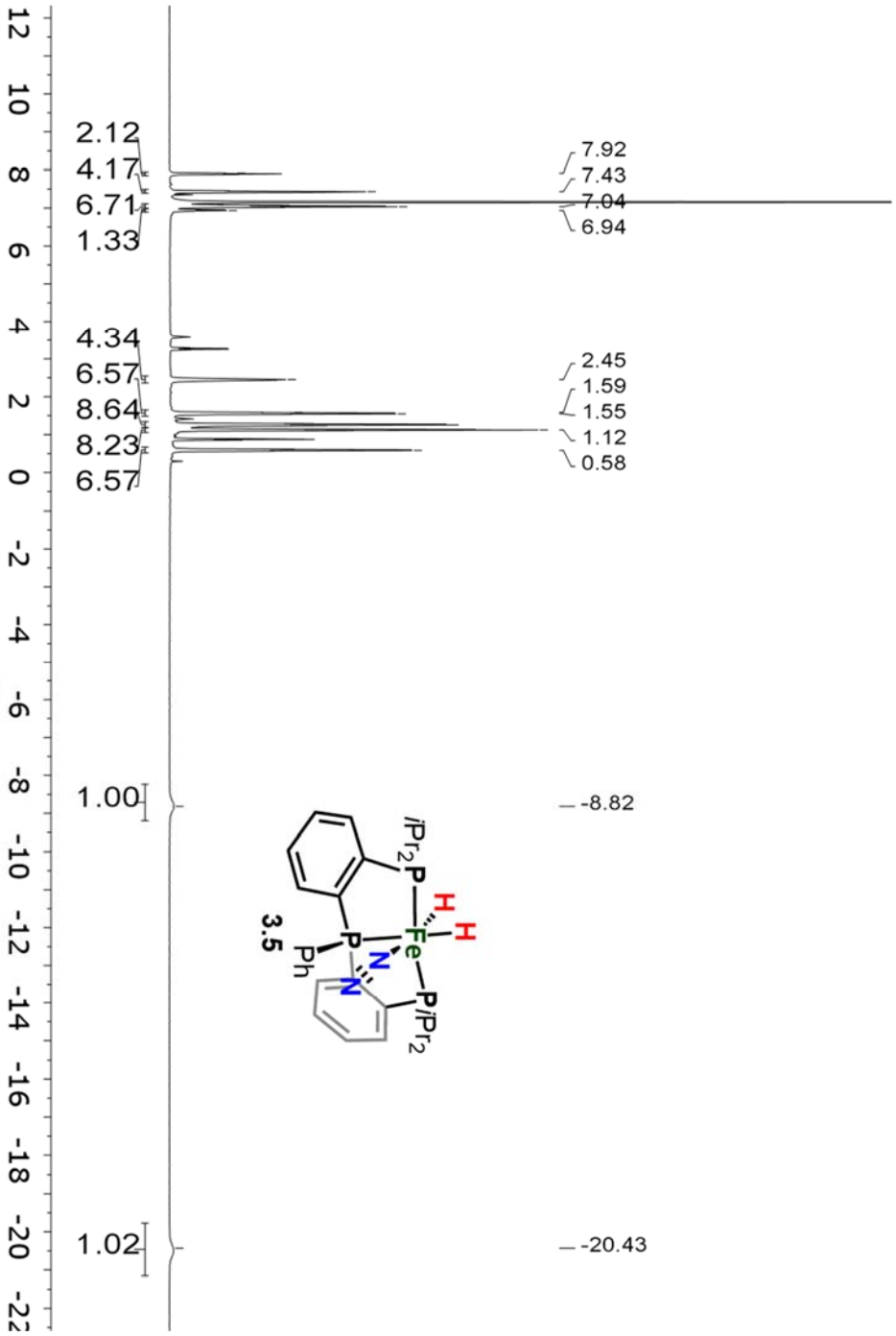

Figure A3.18. ^{1}H NMR spectrum of **3.5** (C_6D_6, 400 MHz).

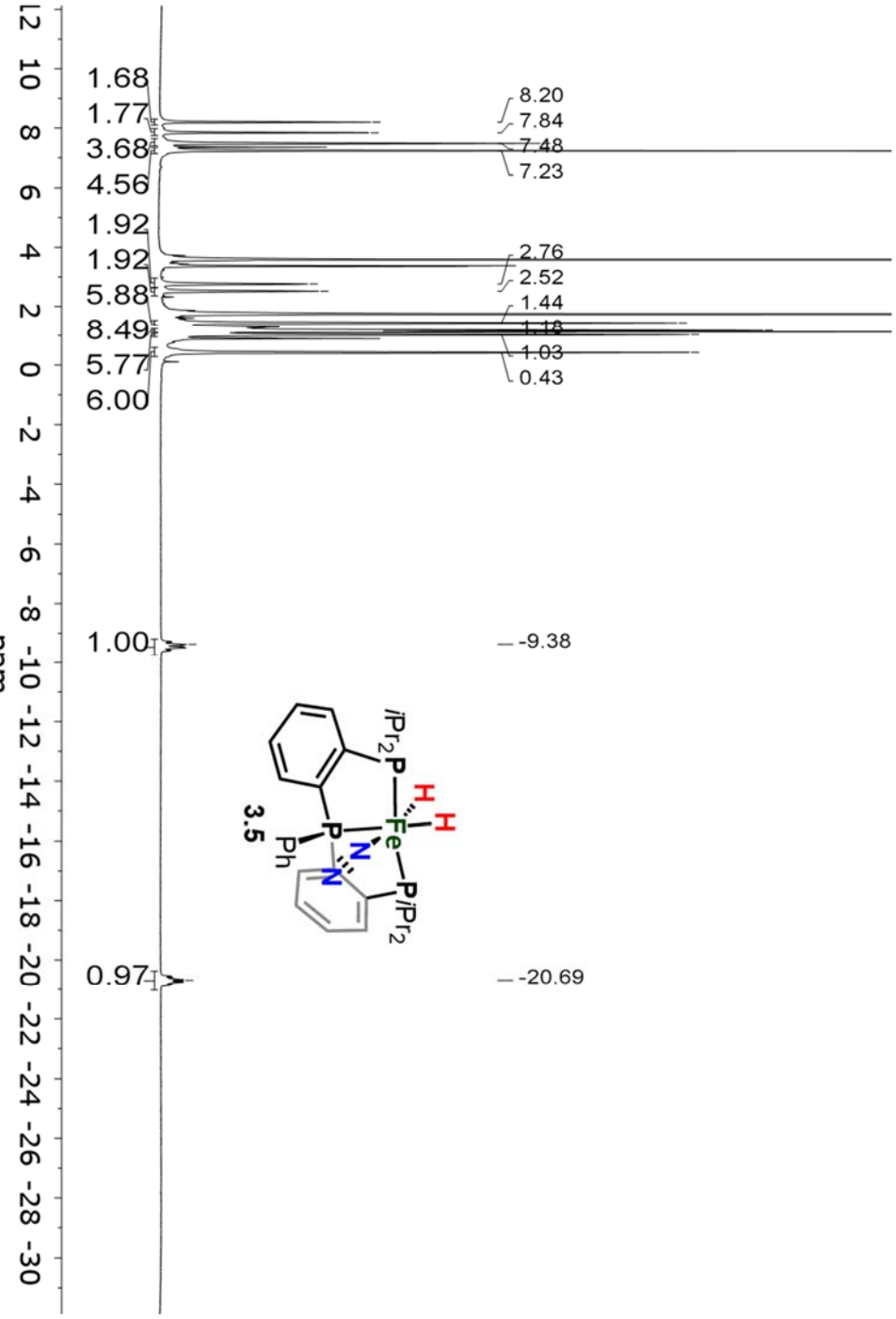

Figure A3.19. ^{1}H NMR of **3.5** (THF-d_8, 500 MHz, -78 °C).

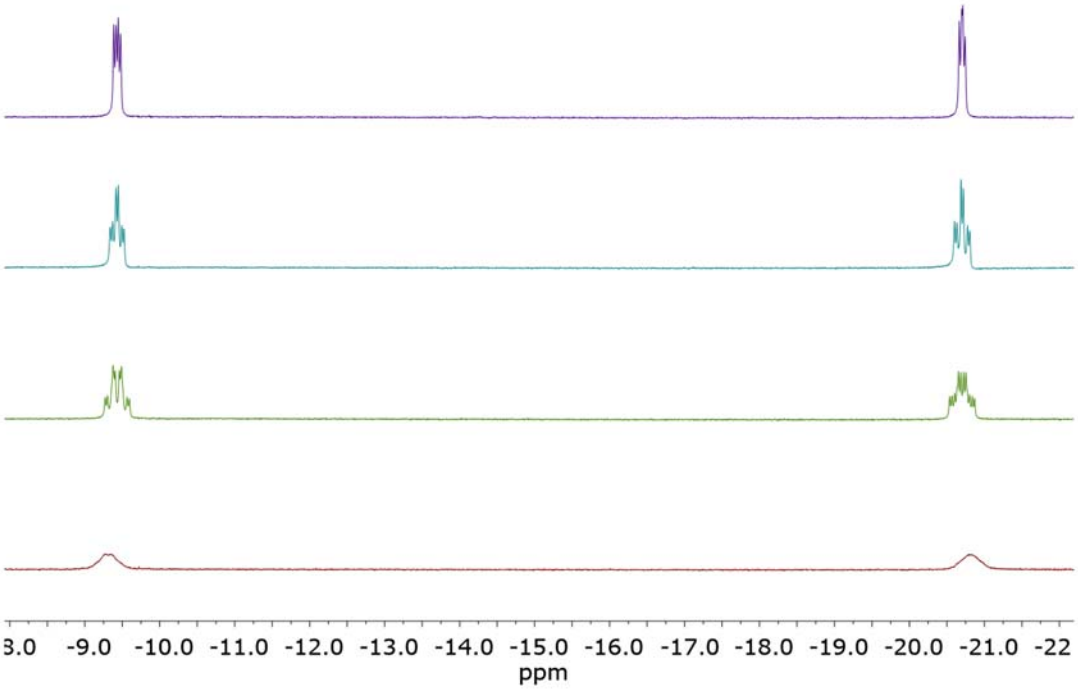

Figure A3.20. ^{1}H NMR of **3.5** (THF-d_8, 500 MHz, vt). Red: room temperature; green: -78 °C; blue: -78 °C and decoupled ^{31}P δ 110 ppm; purple: -78 °C and decoupled ^{31}P δ 120 ppm.

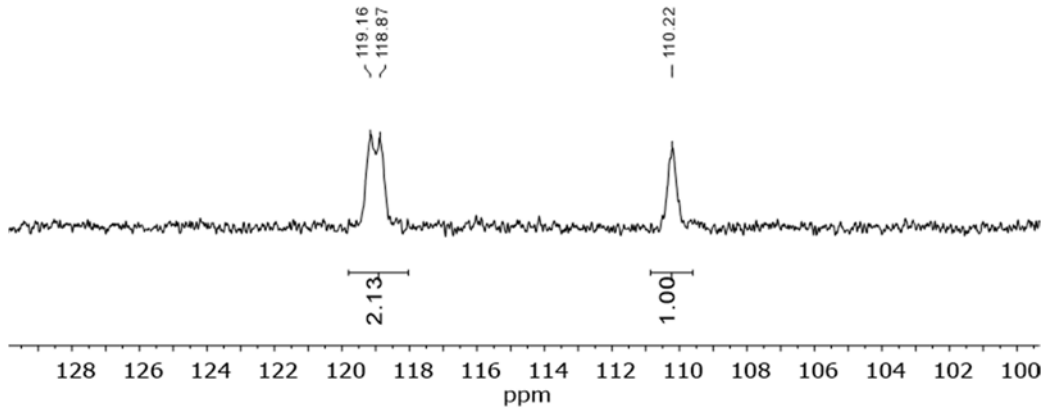

A3.21. ^{31}P NMR of **3.5** (C_6D_6, 162 MHz).

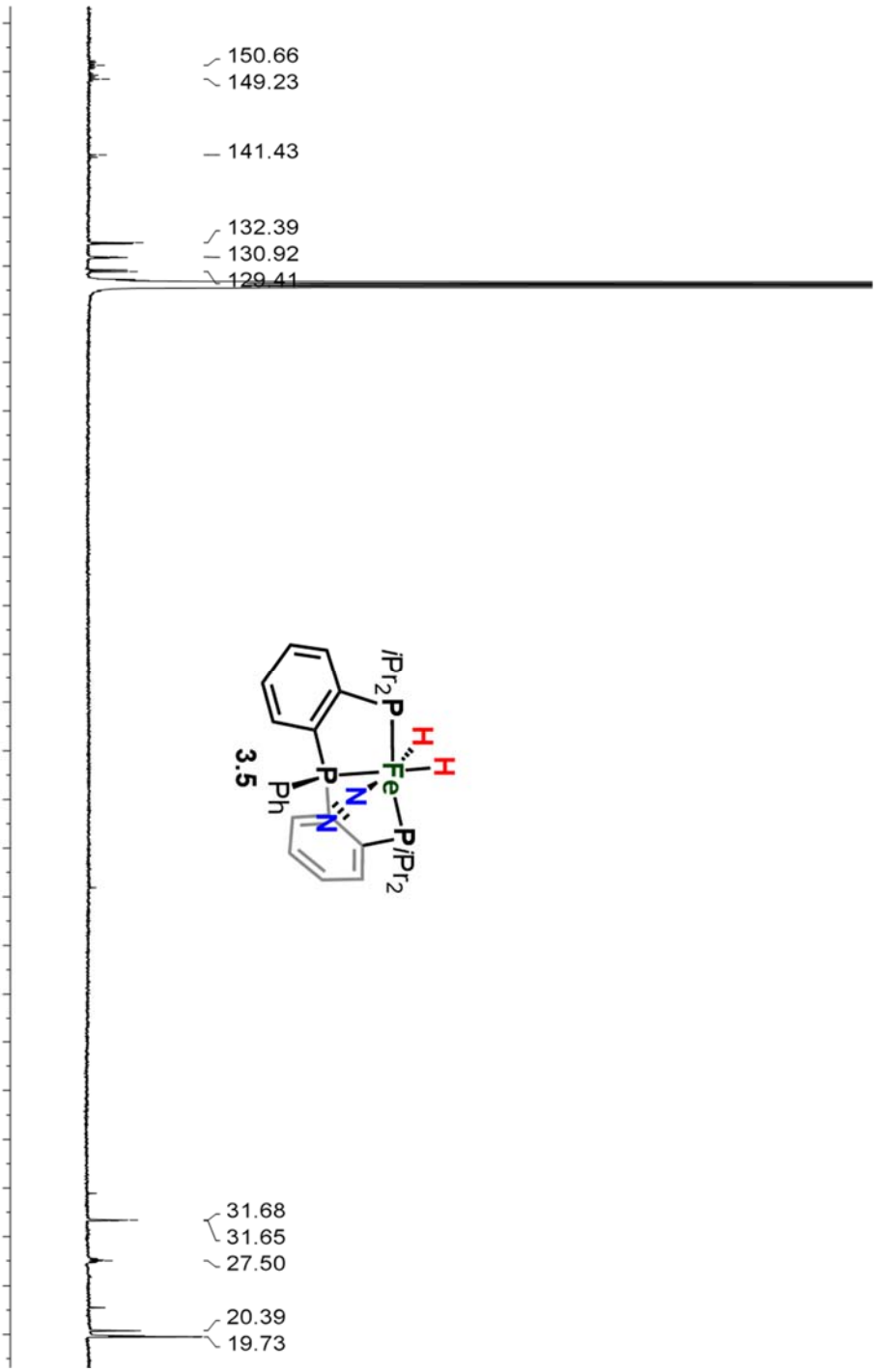

Figure A3.22. ^{13}C NMR spectrum of **3.5** (C_6D_6, 101 MHz).

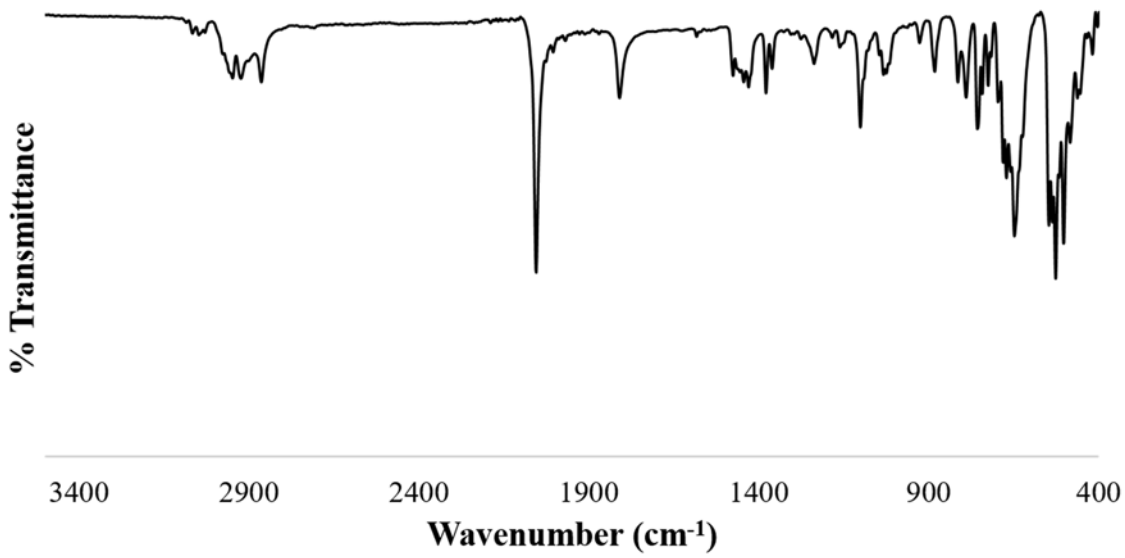

Figure A3.23. IR (KBr) of **3.5**; ν_{NN} = 2058 cm^{-1}; ν_{FeH} = 1812 cm^{-1}.

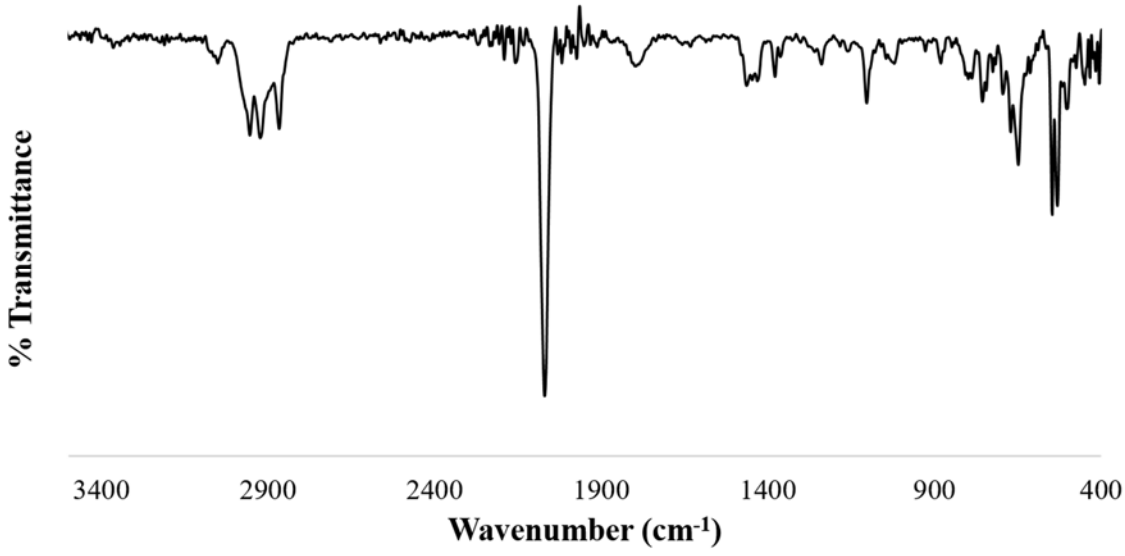

Figure A3.24. IR (thin film deposited from C_6D_6) of **3.5**; ν_{NN} = 2071 cm^{-1};ν_{FeH} = 1796 cm^{-1}.

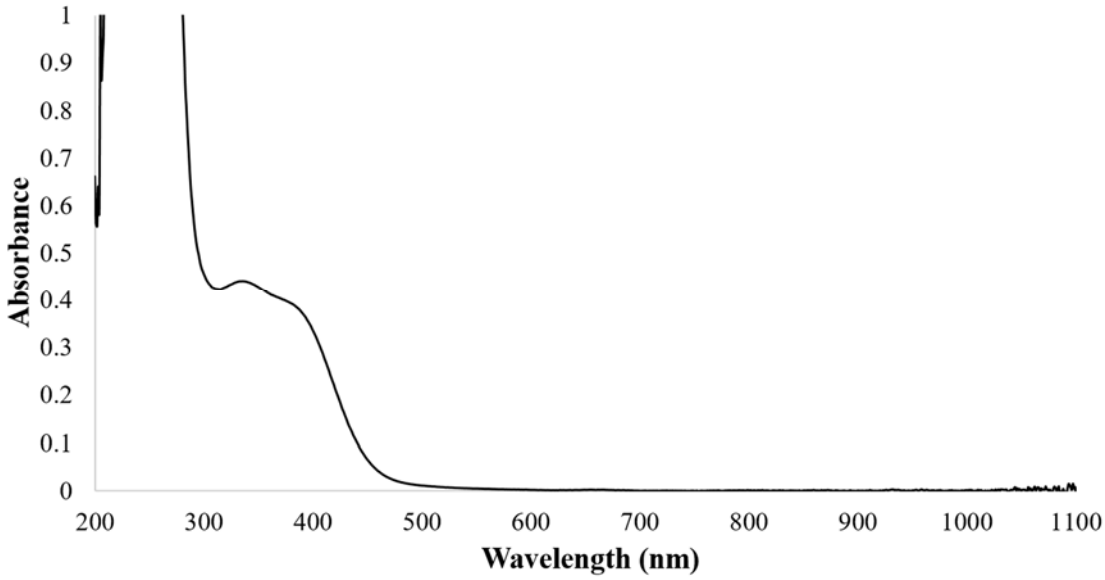

Figure A3.25. UV-Vis of **3.5** in THF (l = 1 cm, c = 0.1 μM).

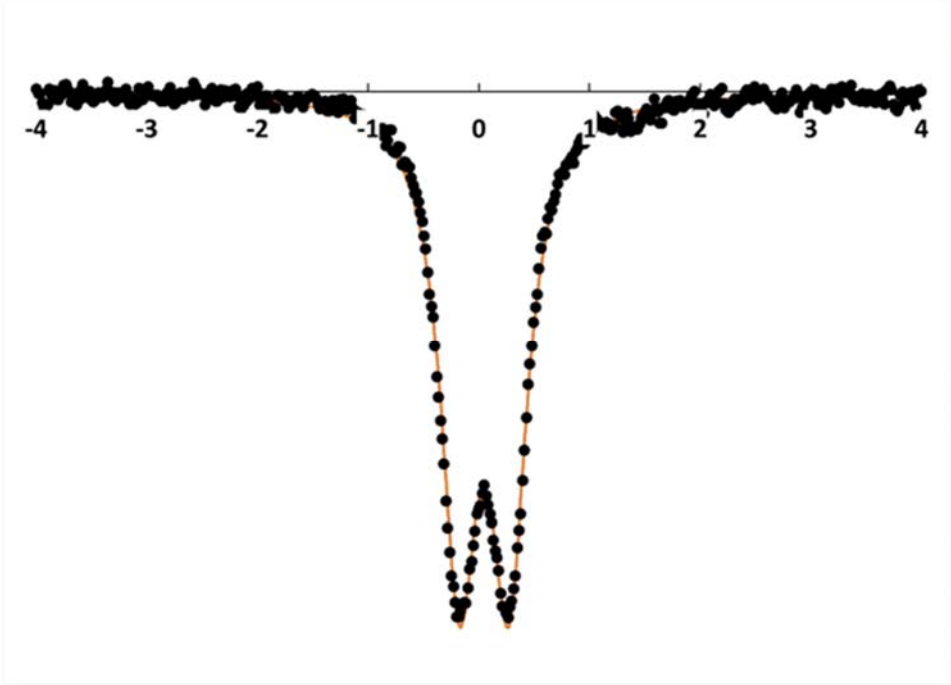

Figure A3.26. 0 mT, ^{57}Fe Mössbauer spectrum of a 4.5 mM solution of **3.5** in 2-MeTHF. Fit with δ = 0.05 mm s^{-1}, ΔE_Q = 0.45 mm s^{-1}, Γ_R = 0.39 mm s^{-1} and Γ_L = 0.39 mm s^{-1}. Data presented in black points, simulation represented by solid orange line.

A3.3 Miscellaneous Experiments

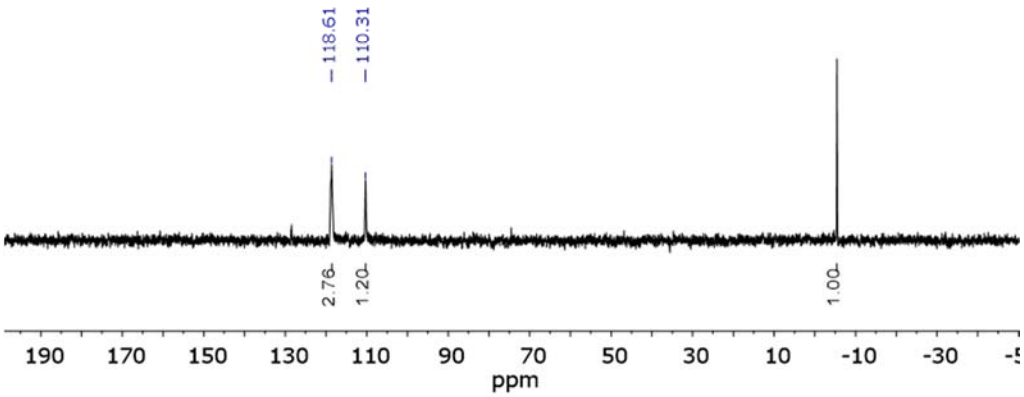

Figure A3.27. ^{31}P NMR of **3.5** (C_6D_6, 162 MHz).

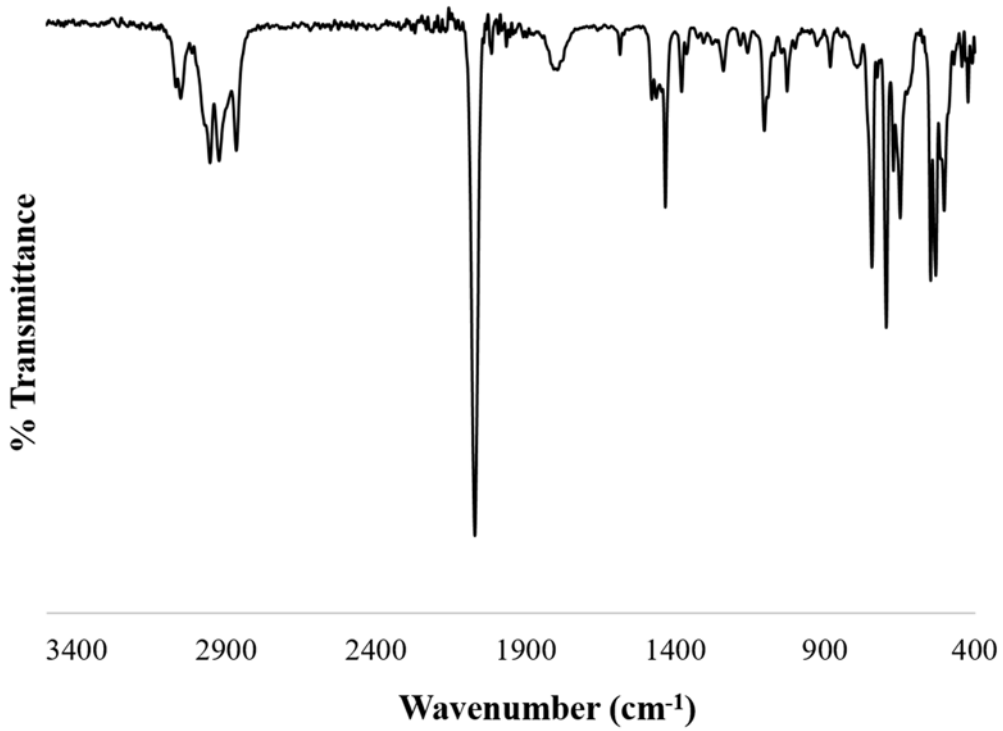

Figure A3.28. IR (thin film deposited from C_6D_6) of **3.5**; ν_{NN} = 2071 cm^{-1};

$\nu_{Fe\text{-}H}$ = 1794 cm^{-1}.

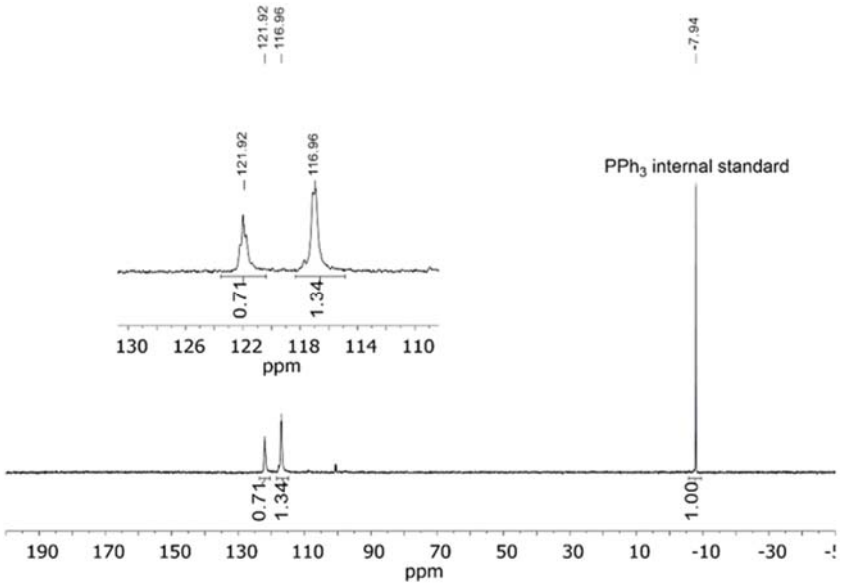

Figure A3.29. ^{31}P NMR spectrum of the crude reaction between dinuclear **3.3** and KC_8 (THF-d_8, 202 MHz, -78 °C). The triplet centered at δ 121.92 ppm and the doublet centered at δ 116.96 ppm are consistent with a molecule that has two distinct phosphines, both of which couple to each other. Coupling to the proton resonance corresponding to the hydride ligand could not be resolved.

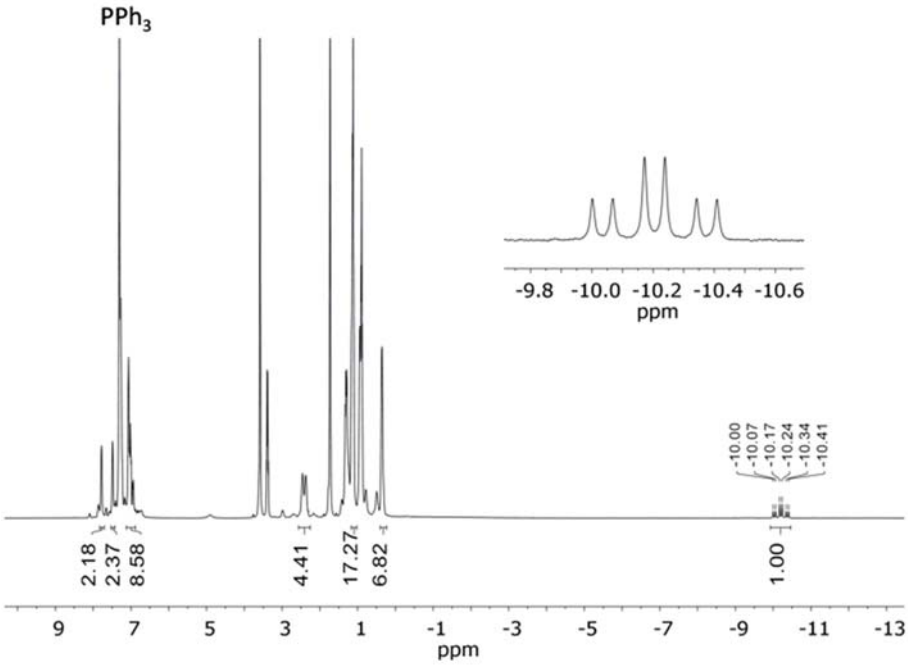

Figure A3.30. ^{1}H NMR spectrum of the crude reaction between dinuclear **3.3** and KC_8 (THF-d_8, 500 MHz, -78 °C). The triplet of doublets centered at δ -10.21 ppm is consistent with the presence of one hydride ligand which couples to two distinct phosphines.

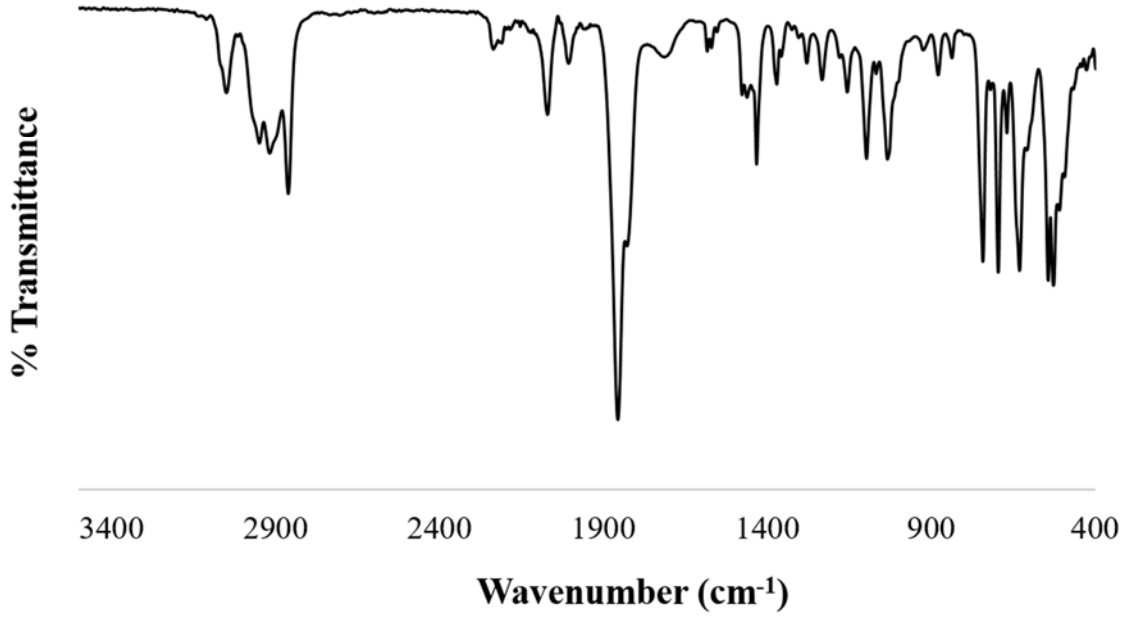

Figure A3.31. IR spectrum of the crude reaction between dinuclear **3.3** and KC_8. The N-N vibration at 1857 cm^{-1} is consistent with an anionic FeN_2^- moiety.

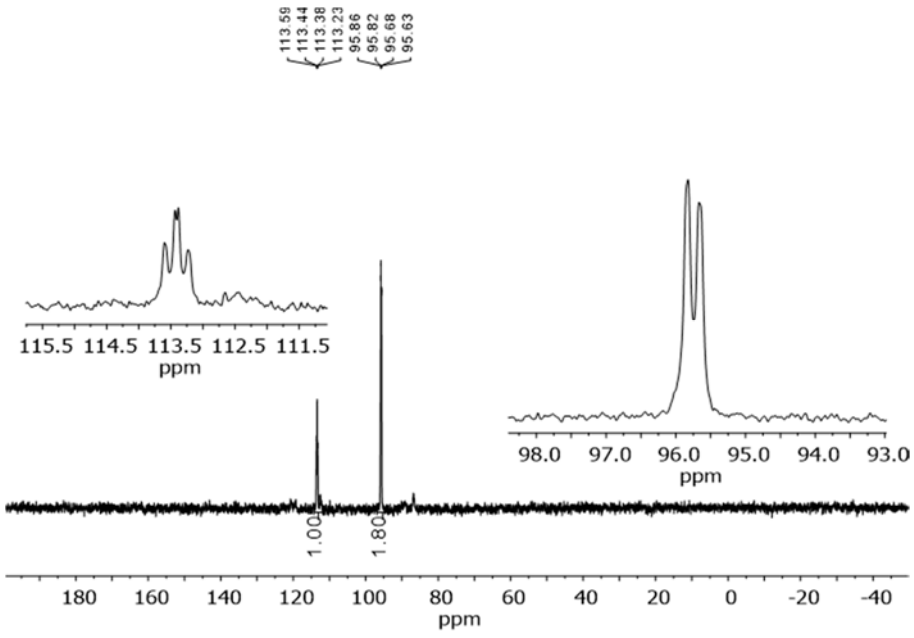

Figure A3.32. ^{31}P NMR spectrum of the crude reaction between dinuclear **3.3** and $HBAr^F_4$ (THF-d_8, 162 MHz). The triplet of doublets centered at δ 113.41 ppm and the doublet of

doublets centered at δ 95.75 ppm are consistent with a molecule that has two distinct phosphines, both of which couple to each other and a hydride ligand.

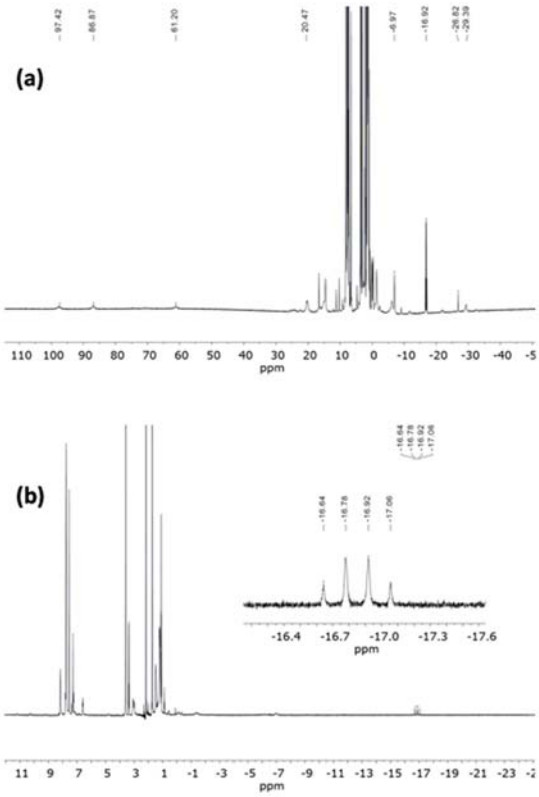

Figure A3.33. ^{1}H NMR spectrum of the crude reaction between dinuclear **3.3** and $HBAr^{F}_{4}$ (THF-d_8, 400 MHz). The two overlapping triplet of doublets centered at δ -16.85 ppm is consistent with the presence of one hydride ligand which couples to two distinct phosphines. (a) Full spectrum and (b) zoomed in diamagnetic region.

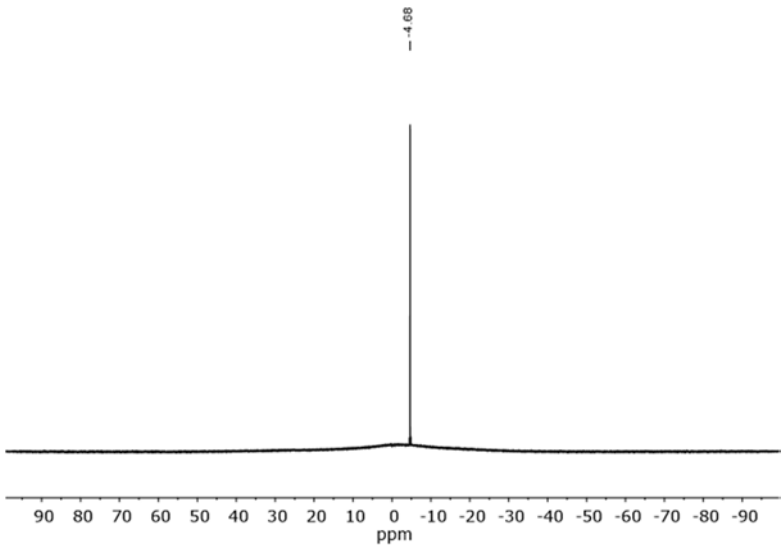

Figure A3.34. ^{11}B NMR spectrum of the crude reaction between dinuclear **3.3** and HBAr$^{F}_{4}$ (THF-d_8, 162 MHz).

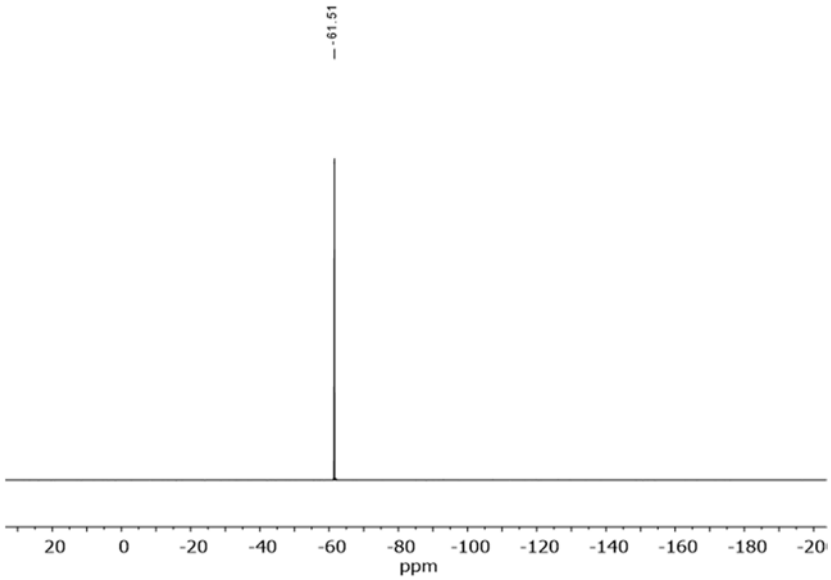

Figure A3.35. ^{19}F NMR spectrum of the crude reaction between dinuclear **3.3** and HBAr$^{F}_{4}$ (THF-d_8, 376 MHz).

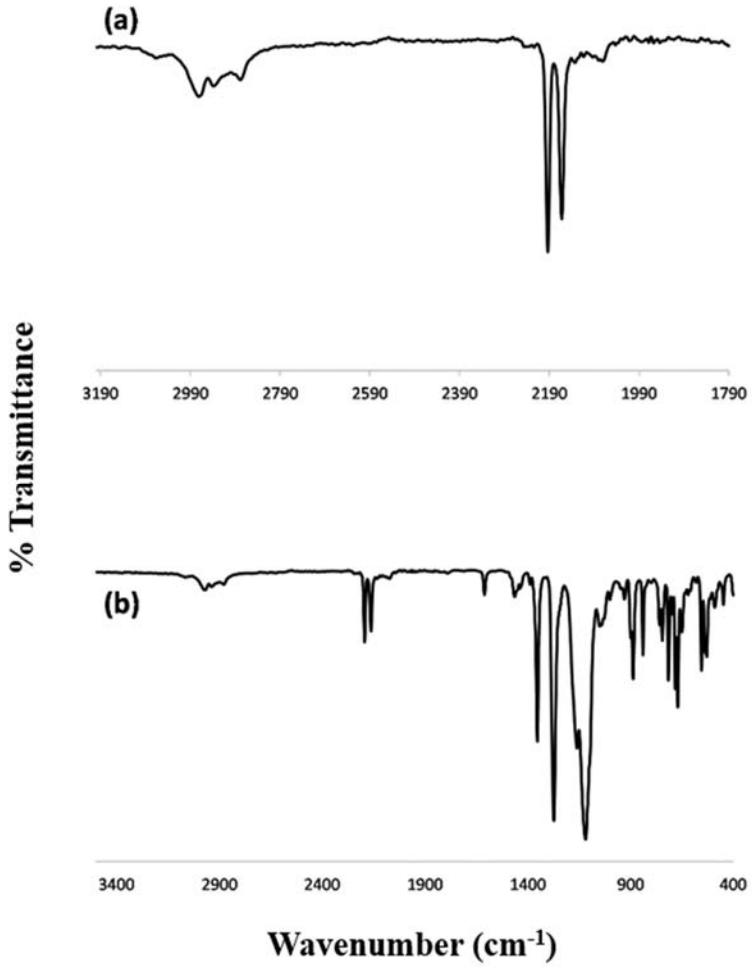

Figure A3.36. (a) Magnified IR spectrum of the crude reaction between dinuclear **3.3** and $HBAr^{F}_{4}$ and **(b)** full IR spectrum. The N-N stretches located at 2194 and 2264 cm^{-1} are consistent with a cationic FeN_2 complex. The high intensity peaks in the fingerprint are from BAr^{F}_{4}.

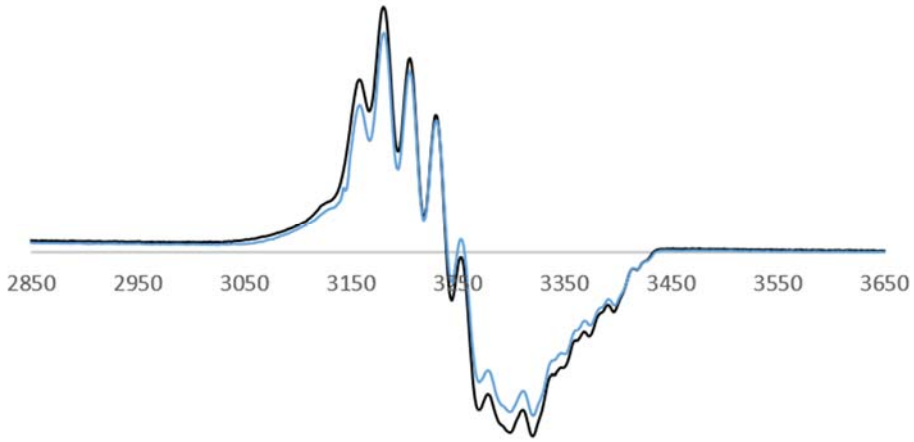

Figure A3.37. EPR spectra of **3.3** in 2-MeTHF before (blue) and after **10 min** of photolysis (black).

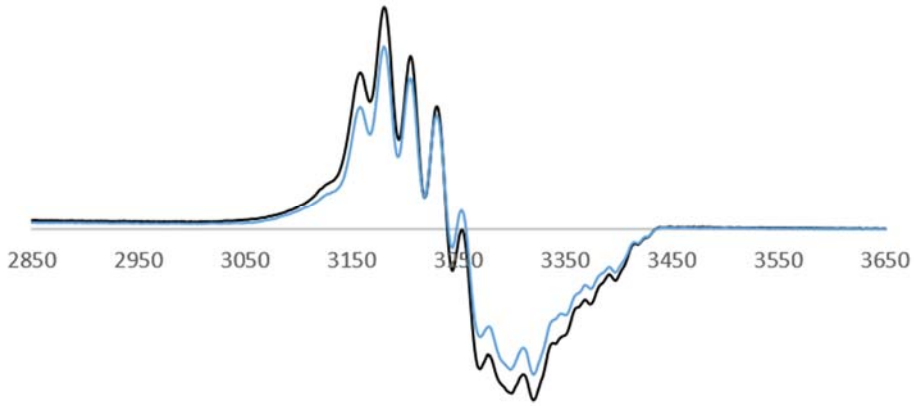

Figure A3.38. EPR spectra of **3.3** in 2-MeTHF before (blue) and after **1 hour** of photolysis (black).

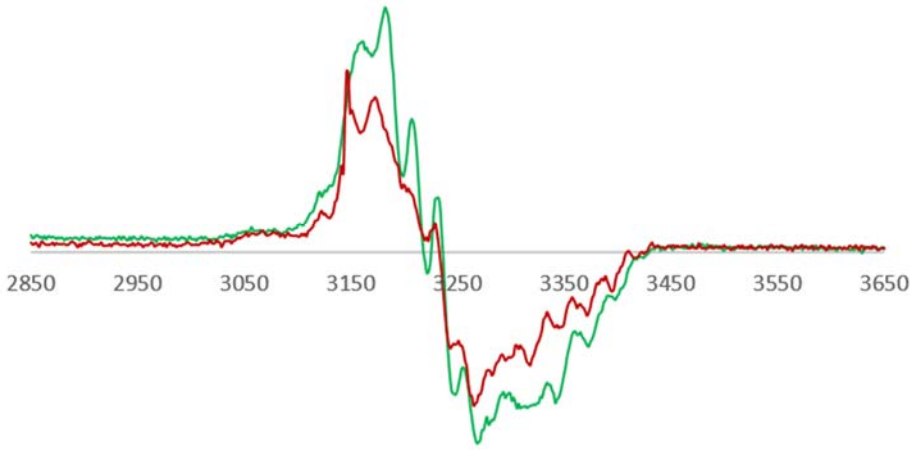

Figure A3.39. Difference EPR spectra derived from Figures **A3.37** and **A3.36** above in 2-MeTHF after 10 minutes (red) and 1 hour of photolysis (green).

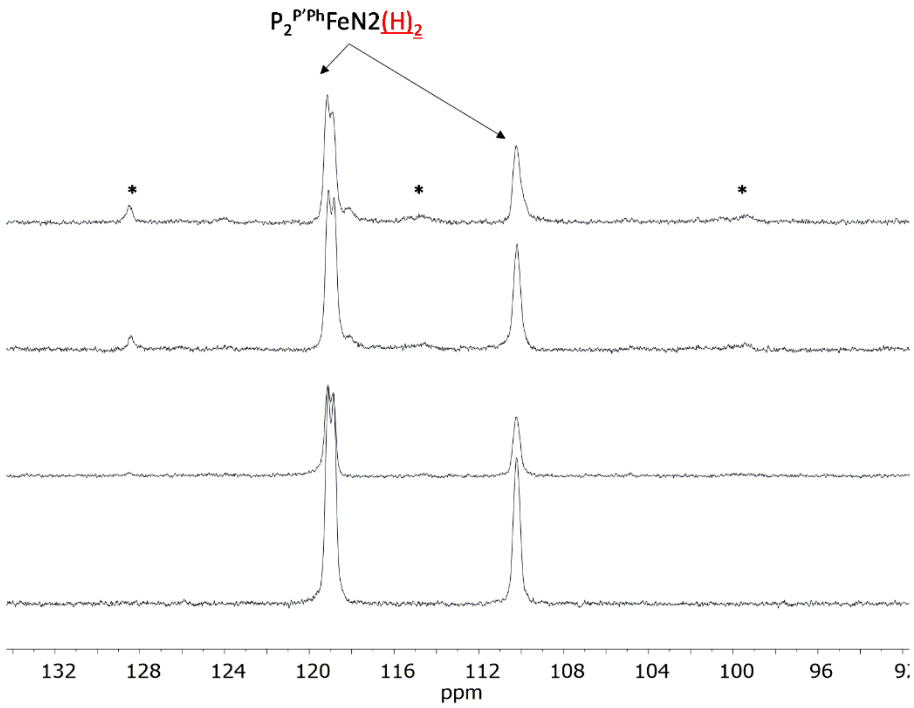

Figure A3.40. ^{31}P NMR spectra (toluene-d_8 , 202 MHz) of $P_2^{PPh}Fe(N_2)(H)_2$ before photolysis (spectrum a), after 5 minutes of Hg lamp photolysis at -78 °C (spectrum b), after 30 minutes total of Hg lamp photolysis at -78 °C (spectrum c), and after 1 hour total of Hg lamp photolysis at -78 °C (spectrum d).

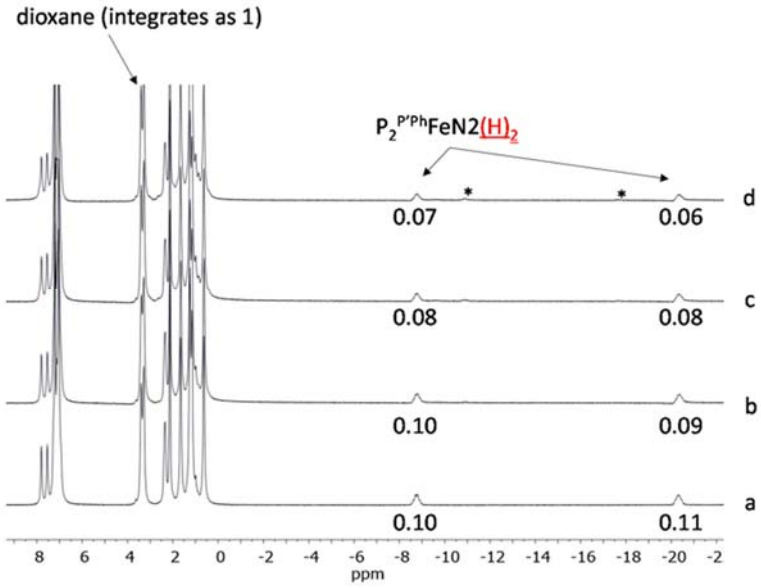

Figure A3.41. ^{1}H NMR spectra (500 MHz, toluene-d_8) of $P_2^{PPh}Fe(N_2)(H)_2$ before photolysis (spectrum a), after 5 minutes of Hg lamp photolysis at -78 °C (spectrum b), after 30 minutes total of Hg lamp photolysis at -78 °C (spectrum c), and after 1 hour total of Hg lamp photolysis at -78 °C (spectrum d). *new signal; note that integrations are relative to a dioxane internal standard, which integrates as 1.

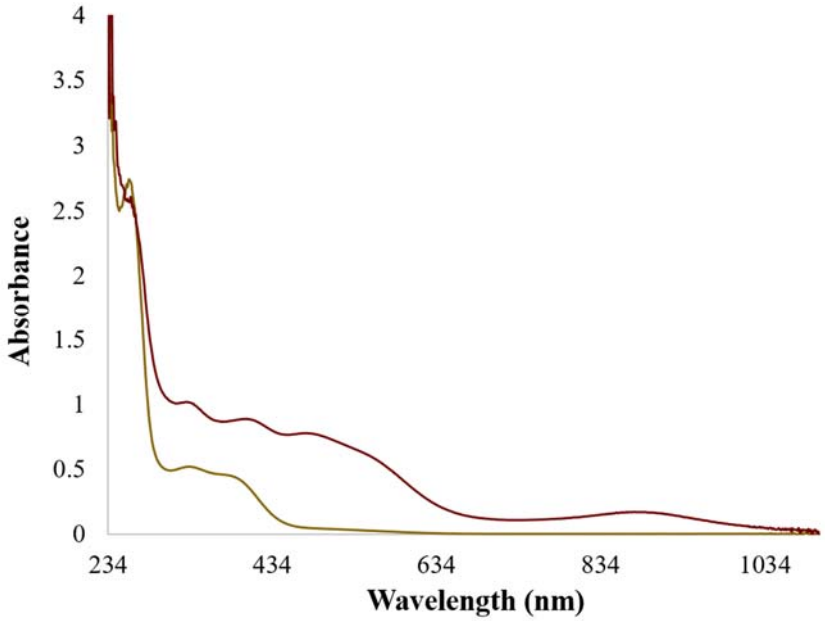

Figure A3.42. UV-Vis of **3.5** (golden yellow) in THF and **3.5** after 10 minutes of photolysis at -78 °C (wine red).

Figure A3.43. Photograph showing qualitative color change of **3.5** pre- (left) and post-photolysis (right).

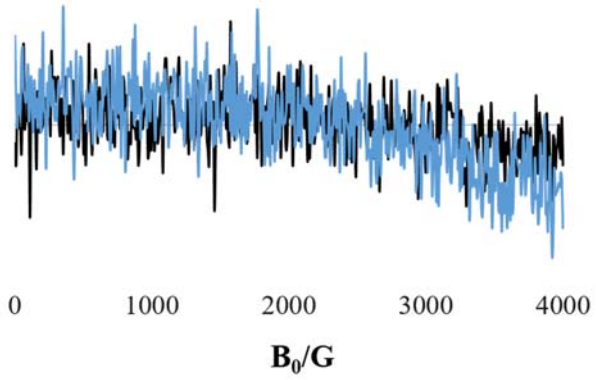

Figure A3.44. EPR spectra of **3.5** in 2-MeTHF before (black trace) and after 10 minutes of Hg lamp photolysis (blue trace) at -78 °C.

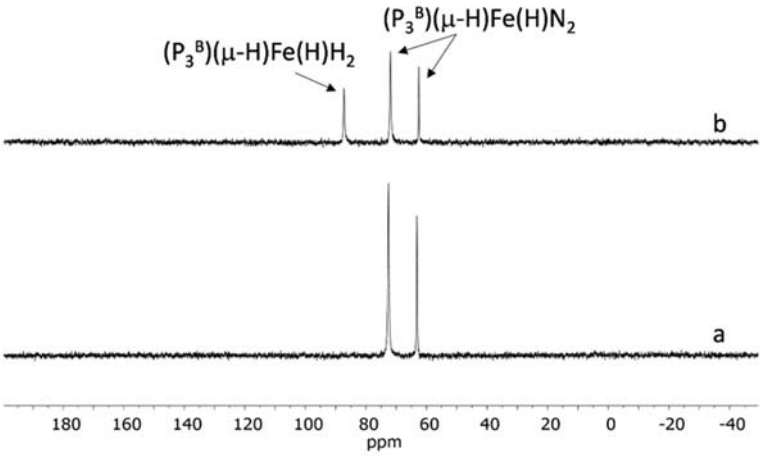

Figure A3.45. ^{31}P NMR spectra (toluene-d_8 , 162 MHz) of $(P_3^B)(\mu\text{-H})Fe(H)N_2$ (spectrum a) and after 10 minutes of Hg lamp photolysis (spectrum b).

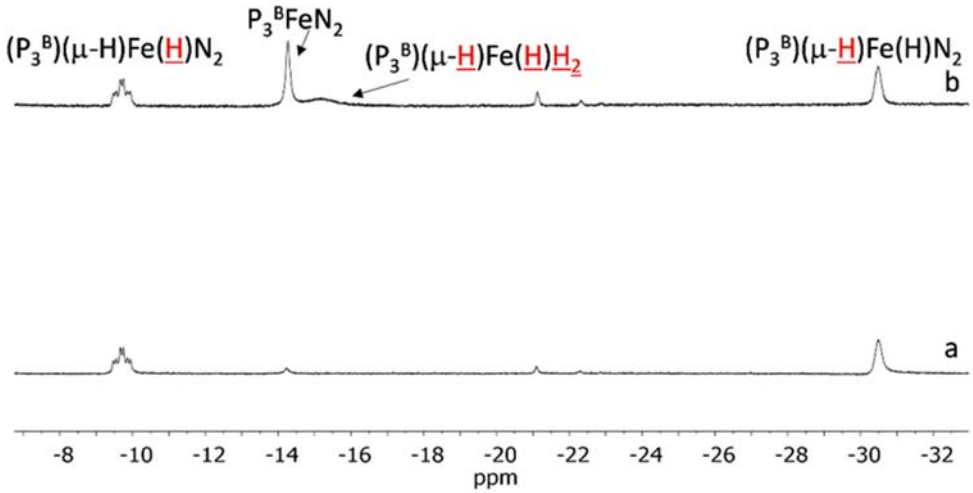

Figure A3.46. Hydride region of the ^{1}H NMR spectra (toluene-d_8 , 400 MHz) of $(P_3^B)(\mu\text{-H})Fe(H)N_2$ (spectrum a) and after 10 minutes of Hg lamp photolysis (spectrum b).

A3.4 Pulsed EPR Data

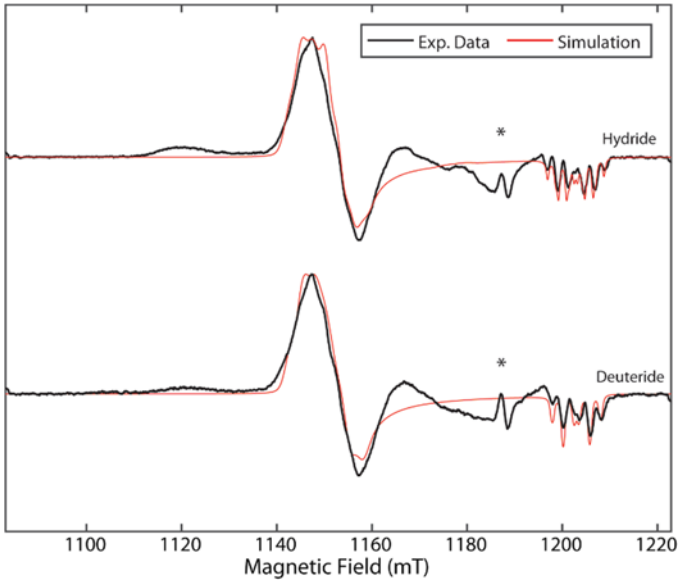

Figure A3.47. Q-band Pseudomodulated Electron Spin-Echo (ESE) detected EPR spectra (black) of **3.4** (top trace) and **3.4D** (bottom trace) in 2-MeTHF with simulations of each (red). Experimental conditions: microwave frequency = 33.702 GHz; π pulse length = 40 ns; interpulse delay τ = 300ns; pseudmodulation function amplitude = 1.5 mT; shot repitition time (srt) = 7 ms; temperature = 12 K. Simulation parameters are as described in Table A3.16. Asterisks indicate the position of a background signal from the resonator.

Table A3.16. EPR Simulation parameters for **3.4** and **3.4D**.

Parameter	**1**	**2**	**3**	**Euler Angles (α,β,γ)° between A and g matrices**
g-value	2.0980	2.0900	2.0019	N/A
^{31}P 1 A (MHz)	70	70	62	(0, 0, 0)
^{31}P 1 A (MHz)	76	76	66	(0, 0, 0)
^{31}P 1 A (MHz)	142	144	158	(0, 20, 0)
Hydride ^{1}H A (MHz)	18	64	52	(0, 20, 0)
Deuteride ^{2}H A (MHz)	2.8	9.8	8.0	(0, 20, 0)

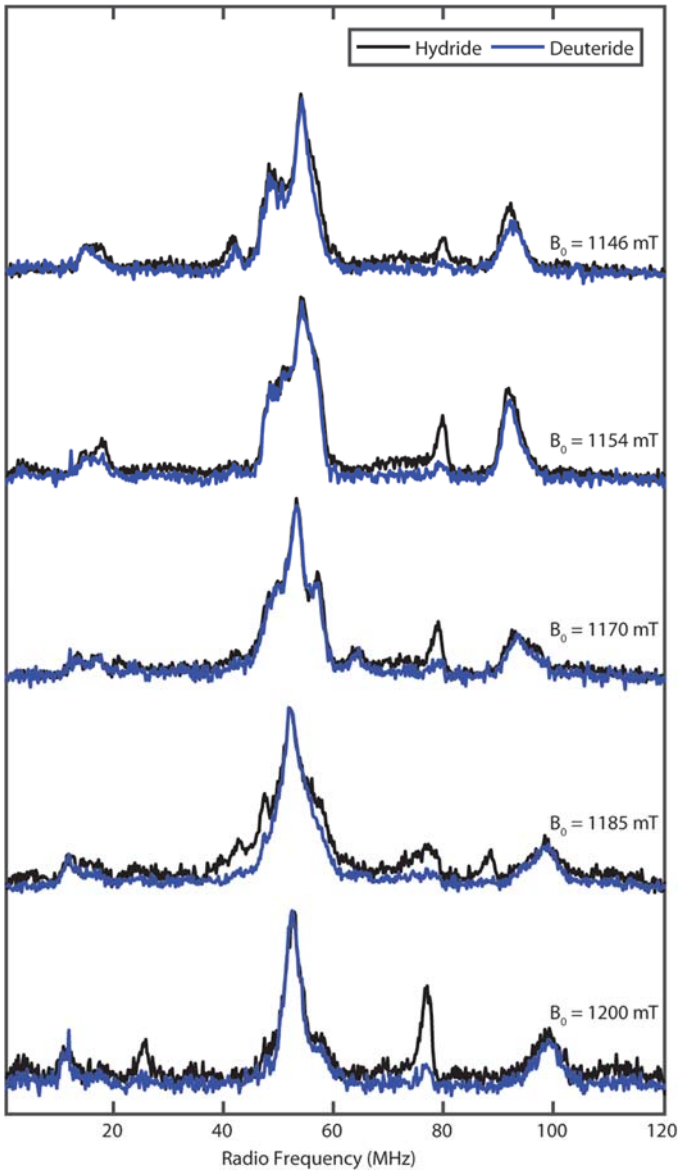

Figure A3.48. Comparison of field-dependent Q-band ^{1}H Davies ENDOR of **3.4** (black) and **3.4D** (blue) in 2-MeTHF. Experimental conditions: microwave frequency = 33.702 GHz; MW π pulse length = 40 ns; interpulse delay τ = 300ns; pulse length = 15 μs; T_{RF} delay = 1 μs; shot repitition time (srt) = 7 ms; temperature = 12 K; RF frequency randomly sampled.

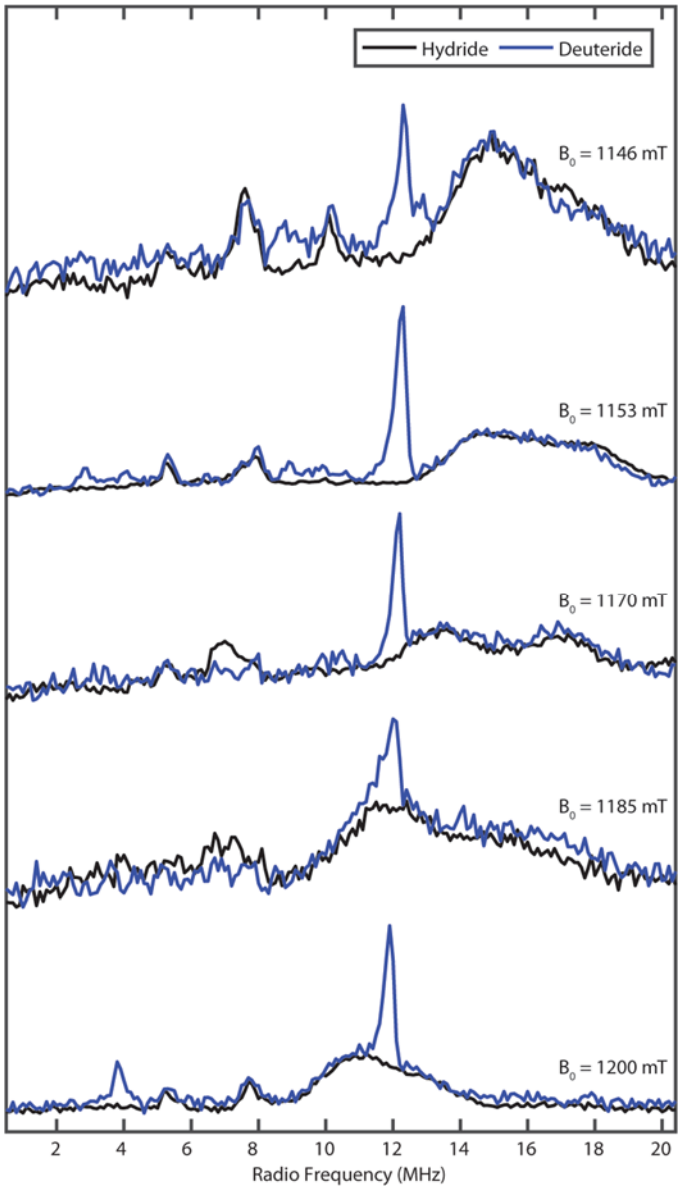

Figure A3.49. Comparison of field-dependent Q-band ^{2}H Davies ENDOR of **3.4** (black) and **3.4D** (blue) in 2-MeTHF. Experimental conditions: microwave frequency = 33.702 GHz; MW π pulse length = 80 ns; interpulse delay τ = 300ns; RF π pulse length = 40 μs; T_{RF} delay = 1 μs; shot repitition time (srt) = 7 ms; temperature = 12 K; RF frequency randomly sampled.

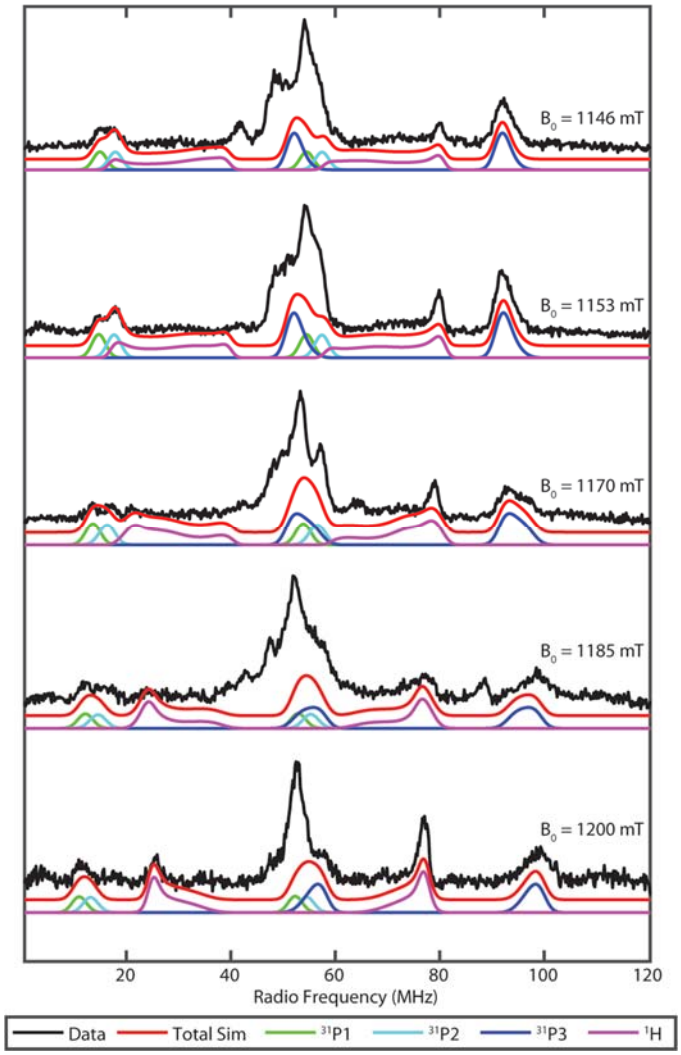

Figure A3.50. Field-dependent Q-band ^{1}H Davies ENDOR of **3.4** (black) in 2-MeTHF with simulations of three ^{31}P (green, cyan, and blue) and one Hydride ^{1}H (purple) hyperfine couplings. Summation of individual component ENDOR simulations is displayed in red. Remaining unsimulated peaks centered around the ^{1}H Larmor frequency (c.a. 48-51 MHz) stem from weak couplings from the isopropyl groups of the $P_2^{P'Ph}$ ligand and the bulk solvent. Simulation parameters are listed in Table A3.16. Experimental conditions: microwave frequency = 33.702 GHz; MW π pulse length = 40 ns; interpulse delay τ = 300 ns; π_{RF} pulse length = 15 μs; T_{RF} delay = 1 μs; shot repitition time (srt) = 7 ms; temperature = 12 K; RF frequency randomly sampled.

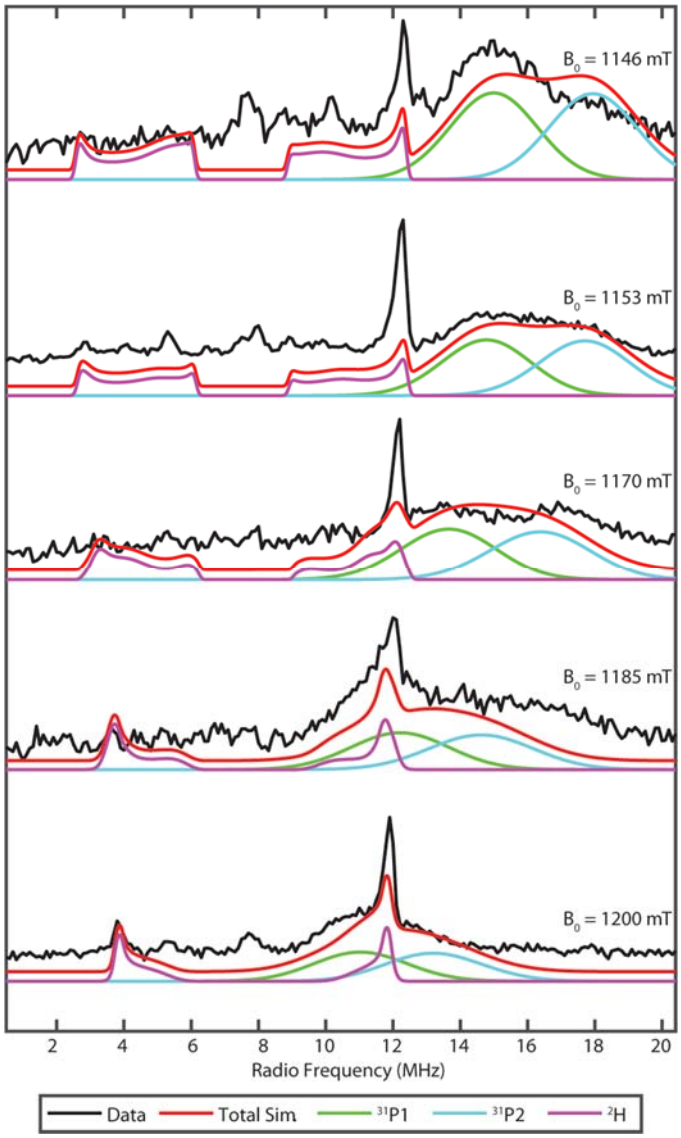

Figure A3.51. Field-dependent Q-band ^{2}H Davies ENDOR of **3.4D** (black) in 2-MeTHF with simulations of two weaker ^{31}P (green, cyan) couplings and one deuteride ^{2}H (purple) hyperfine coupling. Summation of individual component ENDOR simulations is displayed in red. Simulation parameters are listed in Table A3.16. Experimental conditions: microwave frequency = 33.702 GHz; MW π pulse length = 80 ns; interpulse delay τ = 300ns; π_{RF} pulse length = 40 μs; T_{RF} delay = 1 μs; shot repitition time (srt) = 7 ms; temperature = 12 K; RF frequency randomly sampled.

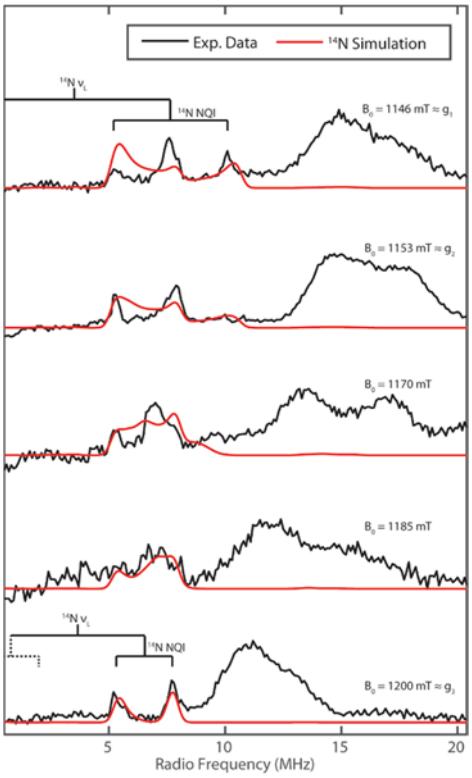

Figure A3.52. Field-dependent Q-band Davies ENDOR of **3.4** (black) in 2-MeTHF with simulations of the ^{14}N hyperfine coupling and nuclear quadrupole interaction (red). Though only the higher frequency peaks are observed, ^{14}N couplings are centered at the ^{14}N Larmor frequency split by the hyperfine coupling A and further split by the nuclear quadrupole interaction (NQI) (denoted by goal posts at the two most extreme field positions). Simulation parameters: ^{14}N A = [5.4 5.8 9.0] MHz; e^2qQ/h = 3.6 MHz, η = 0.08 with both the hyperfine and nuclear quadrupole tensors rotated by β = 90° relative to the g-tensor. Experimental conditions: microwave frequency = 33.702 GHz; MW π pulse length = 80 ns; interpulse delay τ = 300ns; π_{RF} pulse length = 40 µs; T_{RF} delay = 1 µs; shot repitition time (srt) = 7 ms; temperature = 12 K; RF frequency randomly sampled.

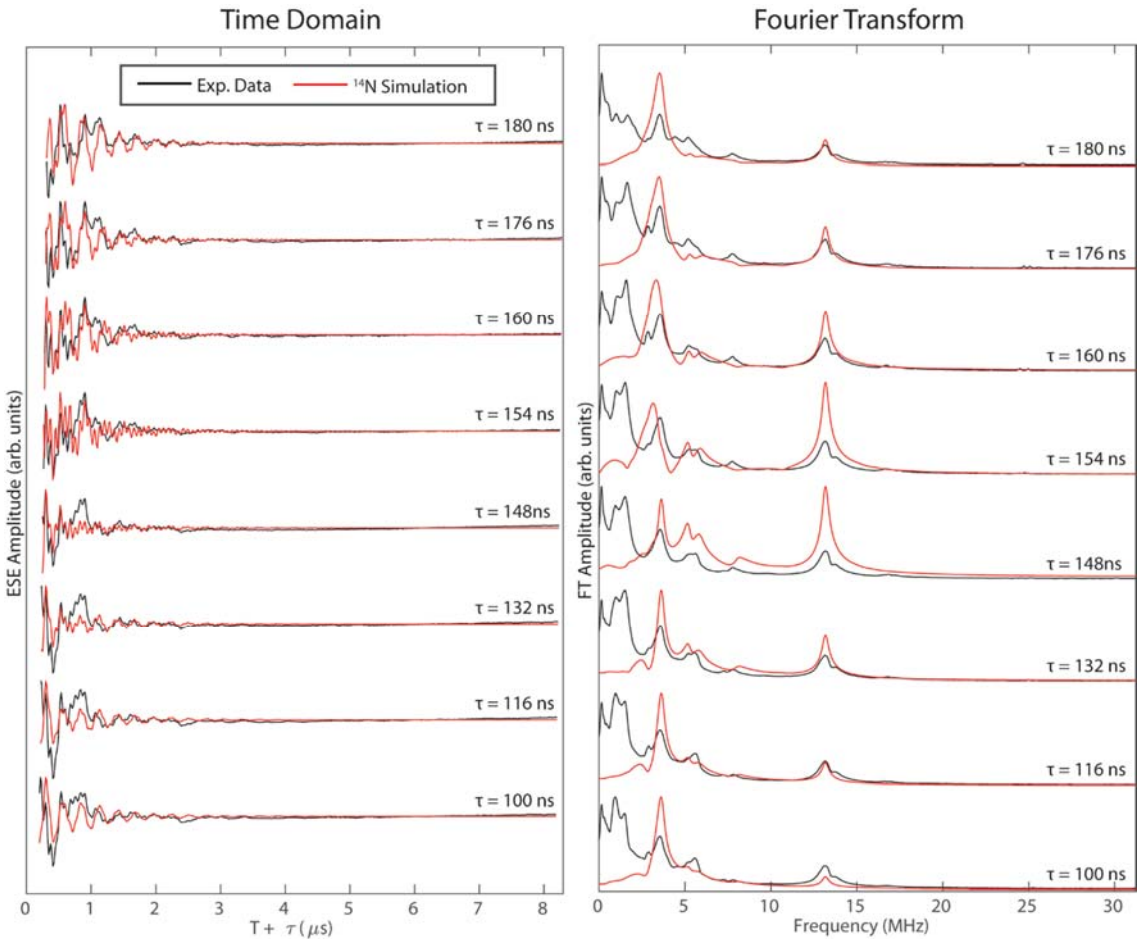

Figure A3.53. Three pulse ESEEM waveforms (left) and corresponding Fourier-transform spectra of **3.4** (black) in 2-MeTHF collected at 1153 mT with simulations of the ^{14}N hyperfine coupling and nuclear quadrupole interaction (red). Simulation parameters: ^{14}N A = [5.4 5.8 9.0] MHz; e^2qQ/h = 3.6 MHz, η = 0.08 with both the hyperfine and nuclear quadrupole tensors rotated by β = 90° relative to the g-tensor. Experimental conditions: microwave frequency = 33.702 GHz; MW π pulse length = 20 ns; interpulse delay τ = 100-180 ns; Initial delay T = 100 ns incremented by dT = 16 ns; shot repitition time (srt) = 7 ms; temperature = 12 K.

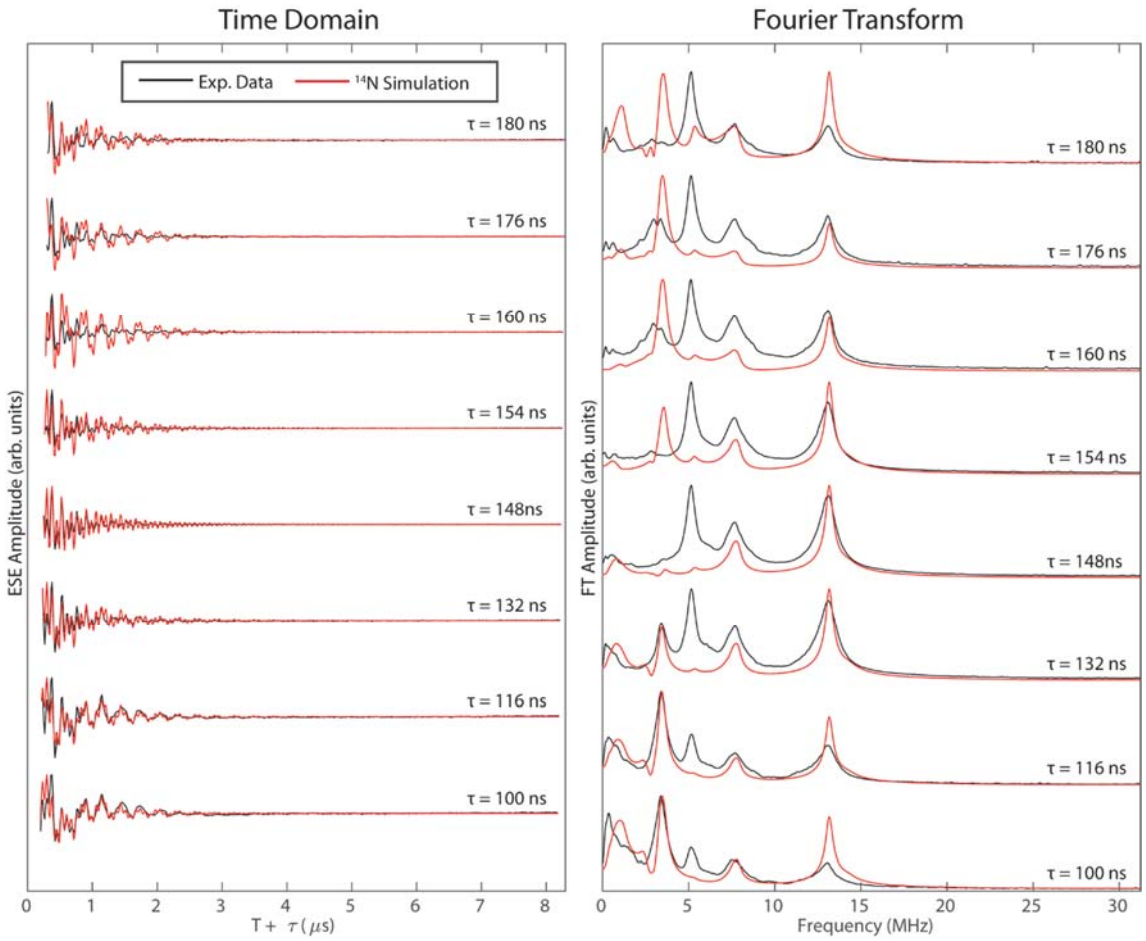

Figure A3.54. Three pulse ESEEM waveforms (left) and corresponding Fourier-transform spectra of **3.4** (black) in 2-MeTHF collected at 1200 mT with simulations of the ^{14}N hyperfine coupling and nuclear quadrupole interaction (red). Simulation parameters: ^{14}N A = [5.4 5.8 9.0] MHz; e^2qQ/h = 3.6 MHz, η = 0.08 with both the hyperfine and nuclear quadrupole tensors rotated by β = 90° relative to the g-tensor. Experimental conditions: microwave frequency = 33.702 GHz; MW π pulse length = 20 ns; interpulse delay τ = 100-180 ns; Initial delay T = 100 ns incremented by dT = 16 ns; shot repitition time (srt) = 7 ms; temperature = 12 K.

A3.5 X-Ray Diffraction Data

Table A3.17. Crystal data and structure refinement for **3.2-FeBr$_2$**.

Identification code	a16018_a
Empirical formula	$C_{30}H_{41}Br_2FeP_3$
Formula weight	710.21
Temperature/K	100.0
Crystal system	orthorhombic
Space group	$P2_12_12_1$
a/Å	11.0296(15)
b/Å	16.3022(12)
c/Å	17.4950(13)
α/°	90
β/°	90
γ/°	90
Volume/Å^3	3145.7(5)
Z	4
ρ_{calc}g/cm^3	1.500
μ/mm^{-1}	3.190
F(000)	1448.0
Crystal size/mm^3	0.44 × 0.35 × 0.3
Radiation	MoKα (λ = 0.71073)
2Θ range for data collection/°	5.514 to 87.492
Index ranges	$-20 \leq h \leq 21$, $-31 \leq k \leq 31$, $-33 \leq l \leq 33$
Reflections collected	127248
Independent reflections	24009 [R_{int} = 0.0566, R_{sigma} = 0.0385]
Data/restraints/parameters	24009/0/333
Goodness-of-fit on F^2	0.980
Final R indexes [I>=2σ (I)]	R_1 = 0.0245, wR_2 = 0.0512
Final R indexes [all data]	R_1 = 0.0330, wR_2 = 0.0525
Largest diff. peak/hole / e Å^{-3}	0.86/-0.49
Flack parameter	-0.0048(16)

Table A3.18. Crystal data and structure refinement for **3.3**.

Identification code	P16044	
Empirical formula	$C_{62.50}H_{88}Fe_2N_2P_6$	
Formula weight	1164.86	
Temperature	100(2) K	
Wavelength	0.71073 Å	
Crystal system	Triclinic	
Space group	P-1	
Unit cell dimensions	a = 12.2816(7) Å	α = 72.8813(19)°
	b = 19.2311(12) Å	β = 77.5344(19)°
	c = 27.8255(17) Å	γ = 80.1633(19)°
Volume	6092.2(6) $Å^3$	
Z	4	
Density (calculated)	1.270 Mg/m^3	
Absorption coefficient	0.673 mm^{-1}	
F(000)	2476	
Crystal size	0.200 x 0.150 x 0.100 mm^3	
Theta range for data collection	2.143 to 38.568°.	
Index ranges	$-21 \leq h \leq 21$, $-33 \leq k \leq 33$, $-48 \leq l \leq 48$	
Reflections collected	499030	
Independent reflections	68875 [R(int) = 0.0921]	
Completeness to theta = 25.242°	99.9 %	
Absorption correction	Semi-empirical from equivalents	
Max. and min. transmission	0.7481 and 0.7111	
Refinement method	Full-matrix least-squares on F^2	
Data / restraints / parameters	68875 / 3763 / 1824	
Goodness-of-fit on F^2	1.023	
Final R indices [I>2sigma(I)]	R1 = 0.0573, wR2 = 0.1282	
R indices (all data)	R1 = 0.1148, wR2 = 0.1492	
Extinction coefficient	n/a	
Largest diff. peak and hole	1.754 and -1.489 e $Å^{-3}$	

Table A3.19 Crystal structure and refinement data for $[P_2^{PPh}Fe(N_2)(H)]Na$ anion.

Empirical formula	$C_{30}H_{41}FeN_2NaO_2P_3$	
Formula weight	613.28	
Temperature	100(2) K	
Wavelength	0.71073 Å	
Crystal system	Triclinic	
Space group	P-1	
Unit cell dimensions	a = 18.3186(19) Å	α = 76.428(5)°
	b = 18.4812(14) Å	β = 72.660(5)°
	c = 26.336(4) Å	γ = 60.990(3)°
Volume	7399.5(15) $Å^3$	
Z	8	
Density (calculated)	1.101 Mg/m^3	
Absorption coefficient	0.563 mm^{-1}	
F(000)	2587	
Crystal size	0.12 x 0.15 x 0.29 mm^3	
Theta range for data collection	2.170 to 30.758°.	
Index ranges	$-26 \le h \le 26$, $-26 \le k \le 26$, $-36 \le l \le 37$	
Reflections collected	503698	
Independent reflections	42658 [R(int) = 0.1196]	
Completeness to theta = 26.000°	100.0 %	
Refinement method	Full-matrix least-squares on F^2	
Data / restraints / parameters	42658 / 0 / 1627	
Goodness-of-fit on F^2	0.848	
Final R indices [I>2sigma(I)]	$R_1 = 0.0606$, $wR_2 = 0.1511$	
R indices (all data)	$R_1 = 0.0971$, $wR_2 = 0.1772$	
Extinction coefficient	n/a	
Largest diff. peak and hole	3.025 and -1.052 e $Å^{-3}$	

Chapter 4 Appendix.

A4.1 Catalysis Details

Table A4.1. Results of individual runs using **4.9** at 41 equiv acid loading per complex with no photolysis.

Run	Absorbance	Equiv NH_3/Complex	% Yield (Based on H^+)
A	0.372	3.91	28
B	0.421	4.45	32
C	0.385	4.06	29

Table A4.2. Results of individual runs using **4.9** at 41 equiv acid loading per complex with Hg lamp photolysis. *10 μL aliquots (instead of 20 μL aliquots) of 1 mL water stock solution used for ammonia stock solution.

Run	Absorbance	Equiv NH_3/Complex	% Yield (Based on H^+)
A	0.277	5.79	42
B	0.265	5.54	40
C	0.304	6.36	46

Table A4.3. Results of individual runs using **4.9** at 136 equiv acid loading per complex with no photolysis. *10 μL aliquots (instead of 20 μL aliquots) of 1 mL water stock solution used for ammonia stock solution.

Run	Absorbance	Equiv NH_3/Complex	% Yield (Based on H^+)
A	0.072	4.59	10
B	0.087	5.62	12
C	0.074	4.67	10

Table A4.4. Results of individual runs using **4.9** at 136 equiv acid loading per complex with Hg lamp photolysis. *10 μL aliquots (instead of 20 μL aliquots) of 1 mL water stock solution used for ammonia stock solution.

Run	Absorbance	Equiv NH_3/Complex	% Yield (Based on H^+)
A	0.126	8.39	19
B	0.125	8.29	18
C	0.248	8.42	19

Table A4.5. Results of individual runs using **4.9** at 136 equiv acid loading per complex with blue LED photolysis.

Run	Absorbance	Equiv NH_3/Complex	% Yield (Based on H^+)
A	0.317	10.82	24

Table A4.6. Results of individual runs using **4.10** at 46 equiv acid loading per complex with no photolysis.

Run	Absorbance	Equiv NH_3/Complex	% Yield (Based on H^+)
A	0.404	4.65	29
B	0.428	4.93	32

Table A4.7. Results of individual runs using **4.12** at 46 equiv acid loading per complex with no photolysis.

Run	Absorbance	Equiv NH_3/Complex	% Yield (Based on H^+)
A	0.540	6.4	39

A4.2 Spectroscopic Characterization of ***4.1-4.12***

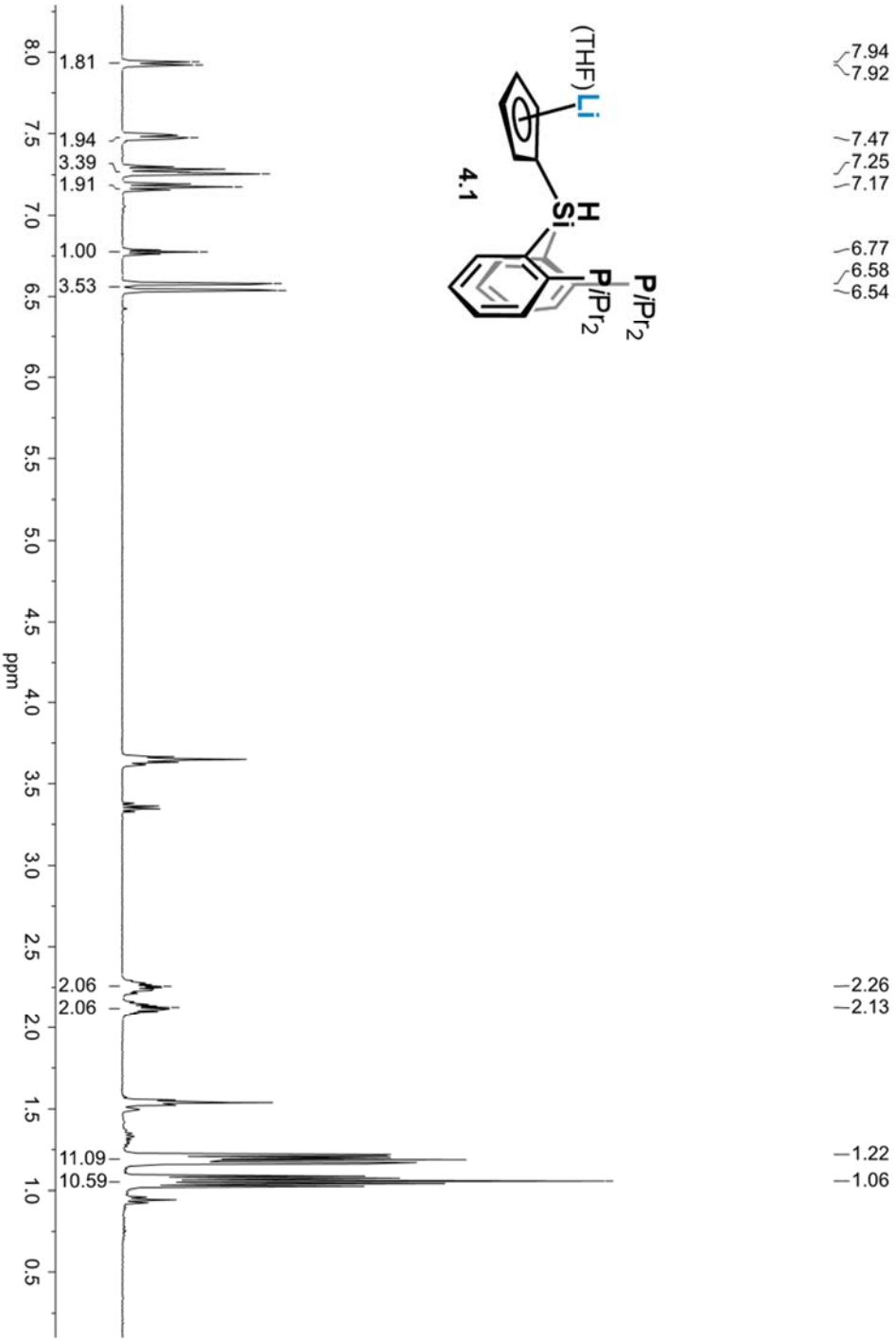

Figure A4.1. ^{1}H NMR Spectrum (5:1 C_6D_6:THF-d_8, 400 MHz) of LiCp' **(4.1)**.

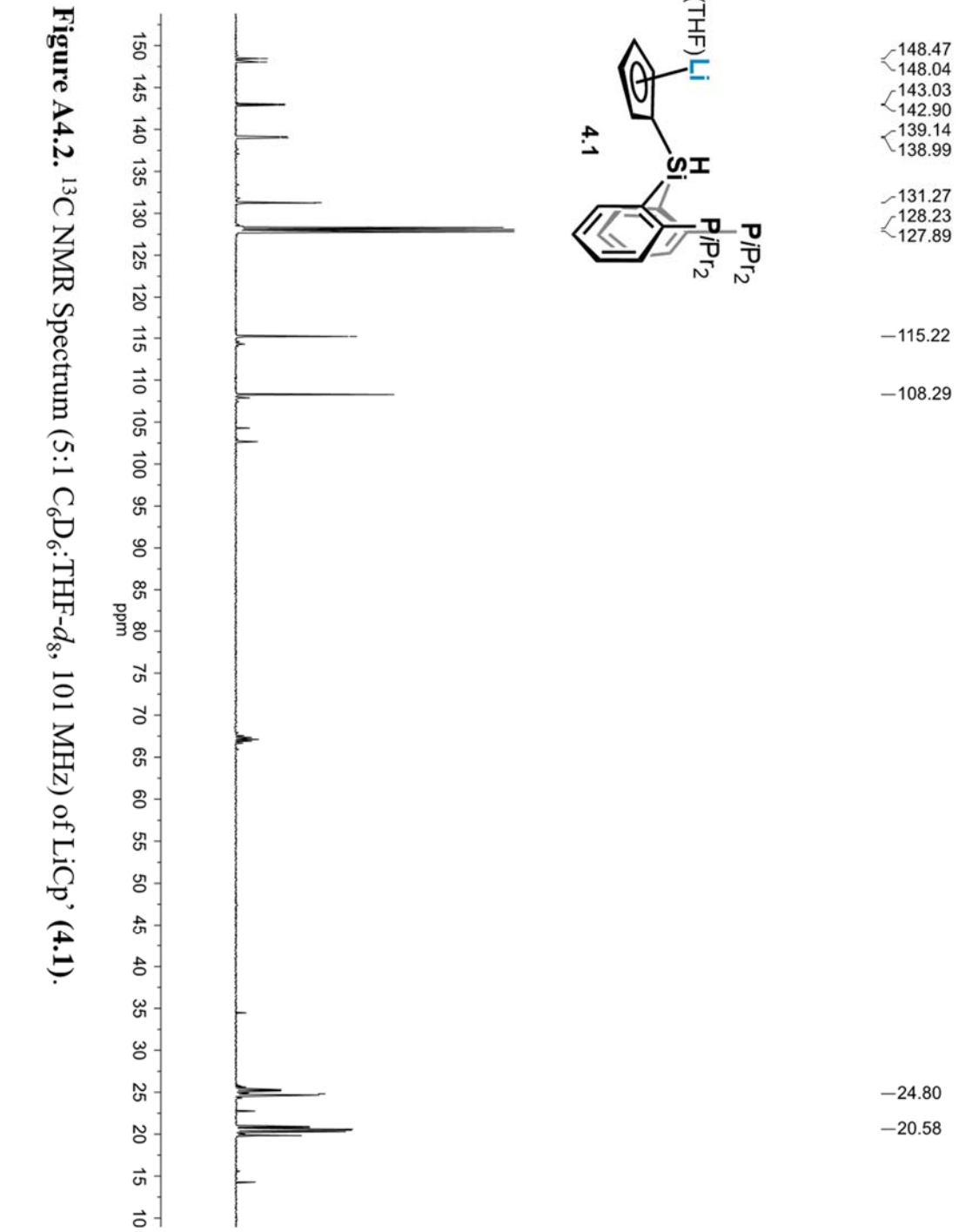

Figure A4.2. ^{13}C NMR Spectrum (5:1 C_6D_6:THF-d_8, 101 MHz) of LiCp' **(4.1)**.

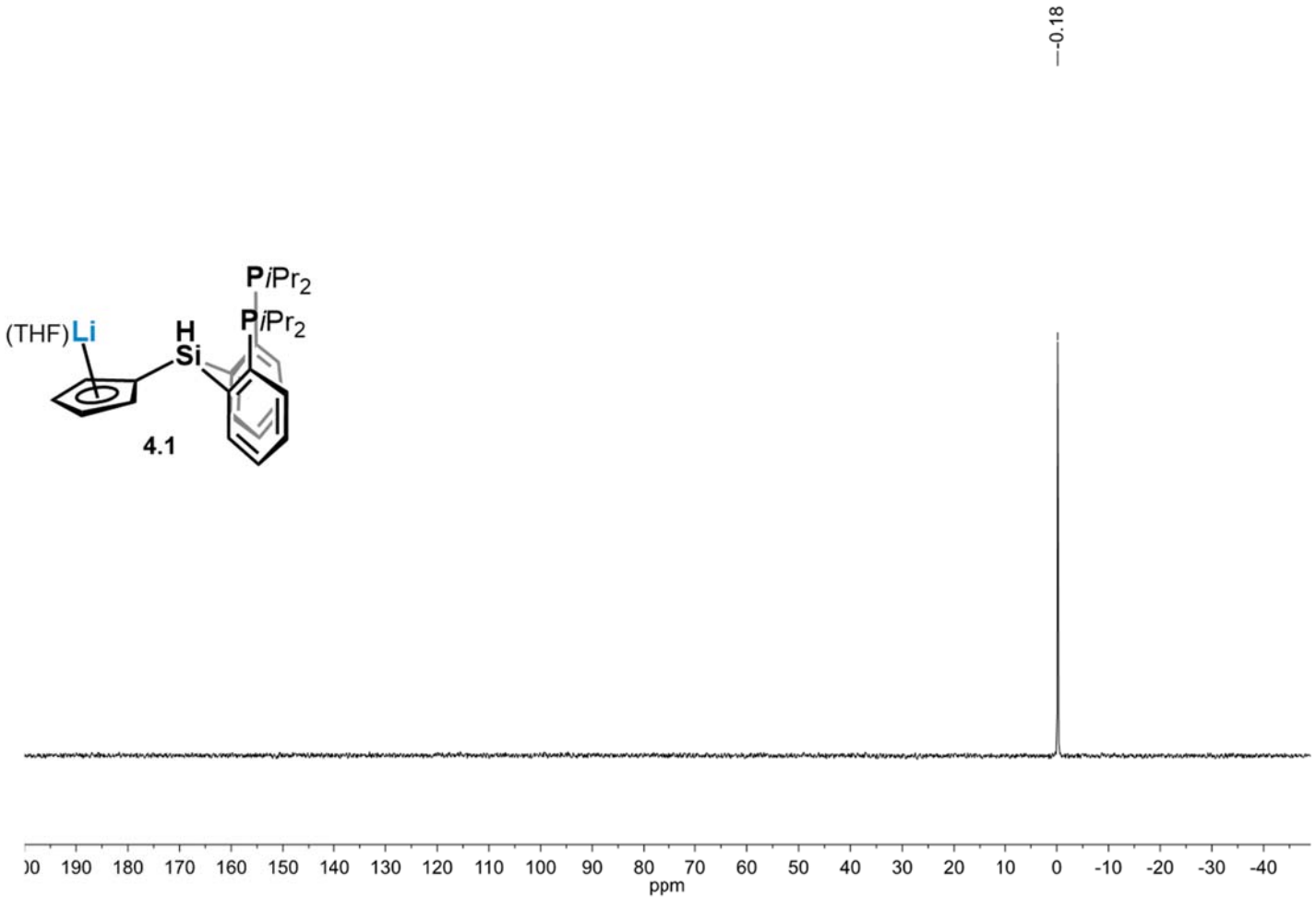

Figure A4.3. ^{31}P NMR Spectrum (5:1 C_6D_6:THF-d_8, 162 MHz) of LiCp' **(4.1)**.

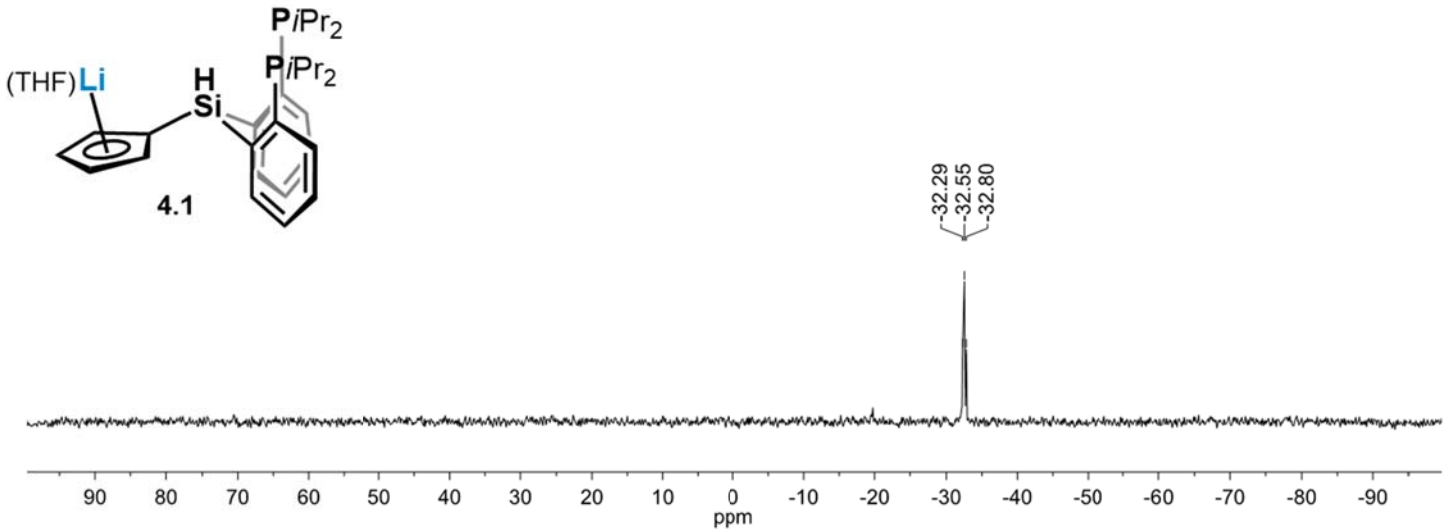

Figure A4.4. ^{29}Si NMR Spectrum (5:1 C_6D_6:THF-d_8, 79 MHz) of LiCp' **(4.1)**.

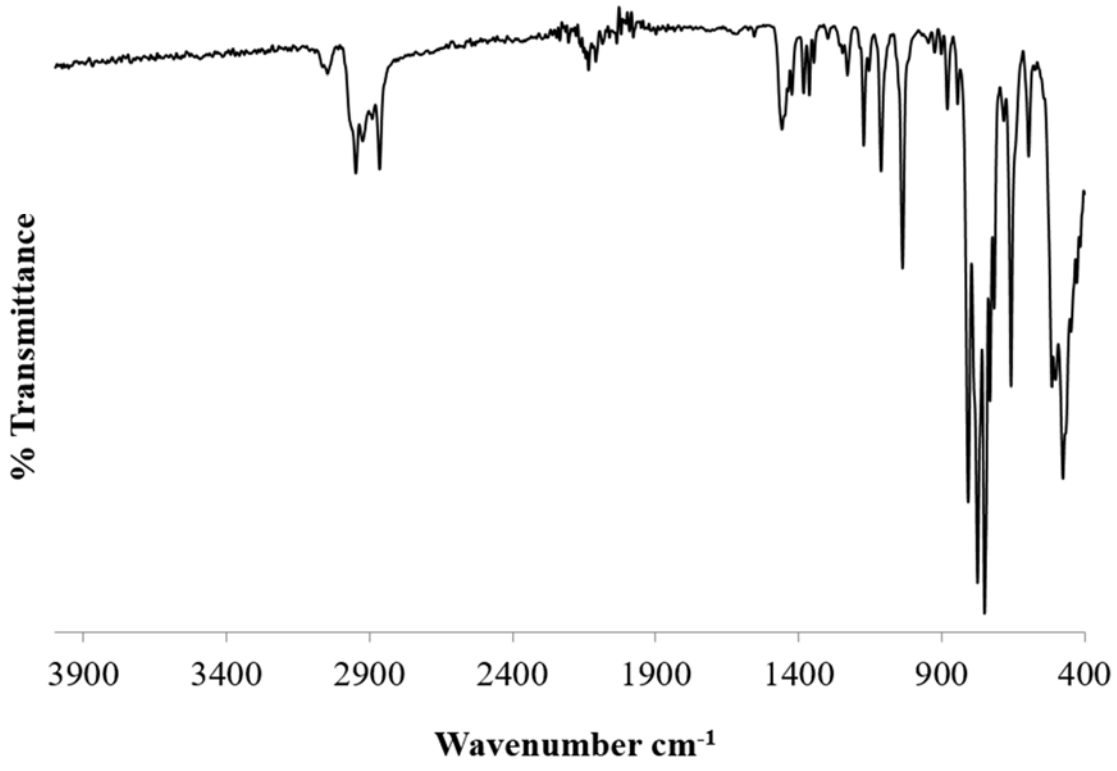

Figure A4.5. Solid-state IR spectrum (KBr) of **4.1**.

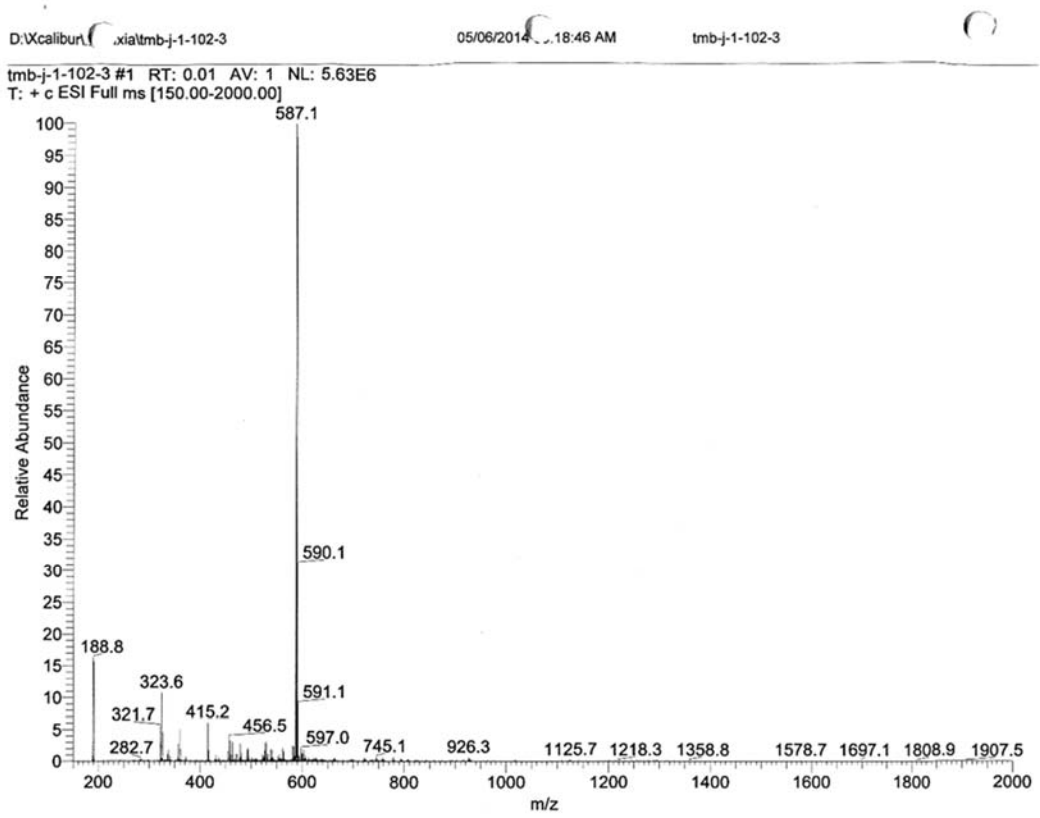

Figure A4.6. ESI-MS spectrum of **4.1**.

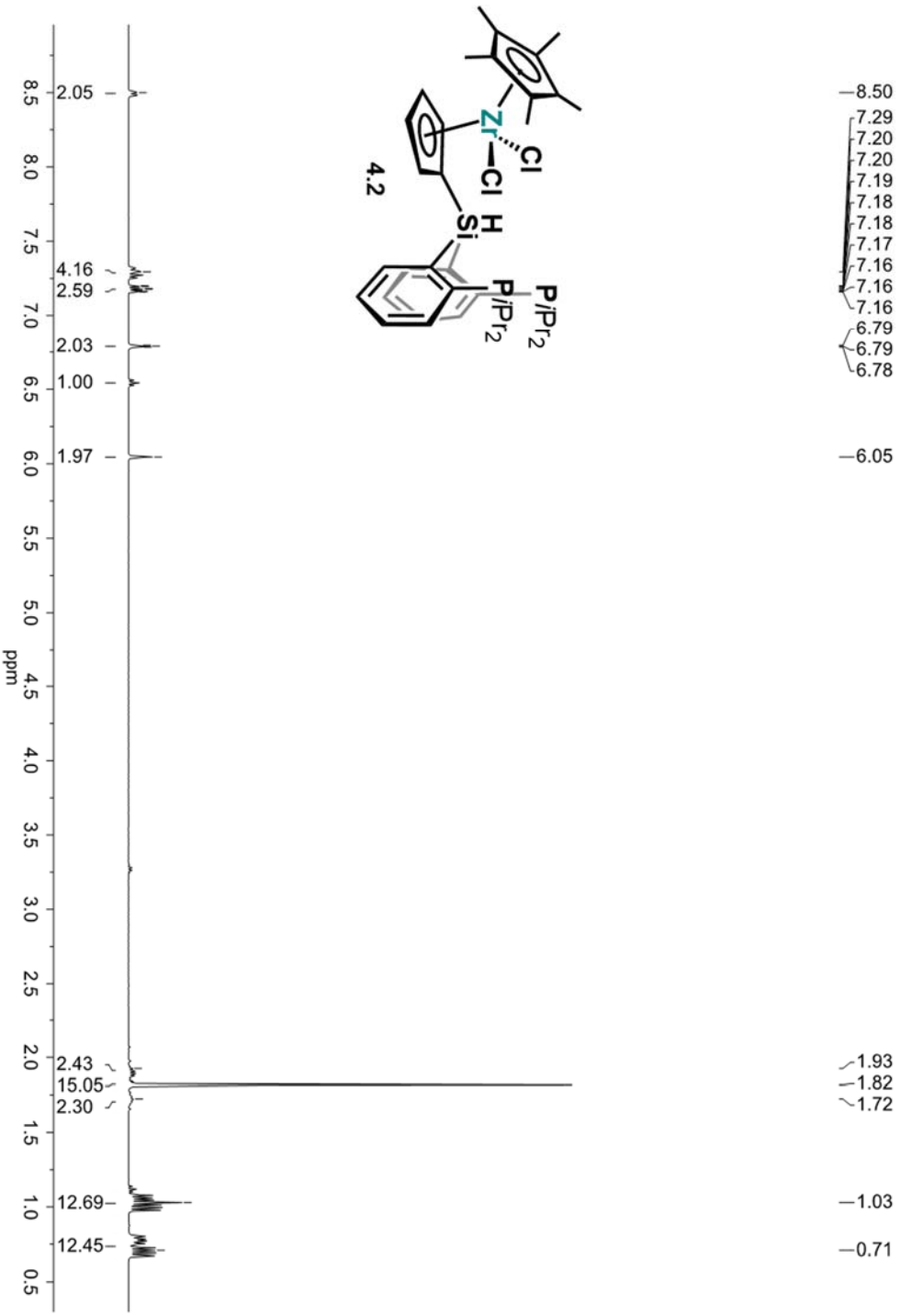

Figure A4.7. ^{1}H NMR Spectrum (C_6D_6, 400 MHz) of Cp*Cp'$ZrCl_2$ **(4.2)**.

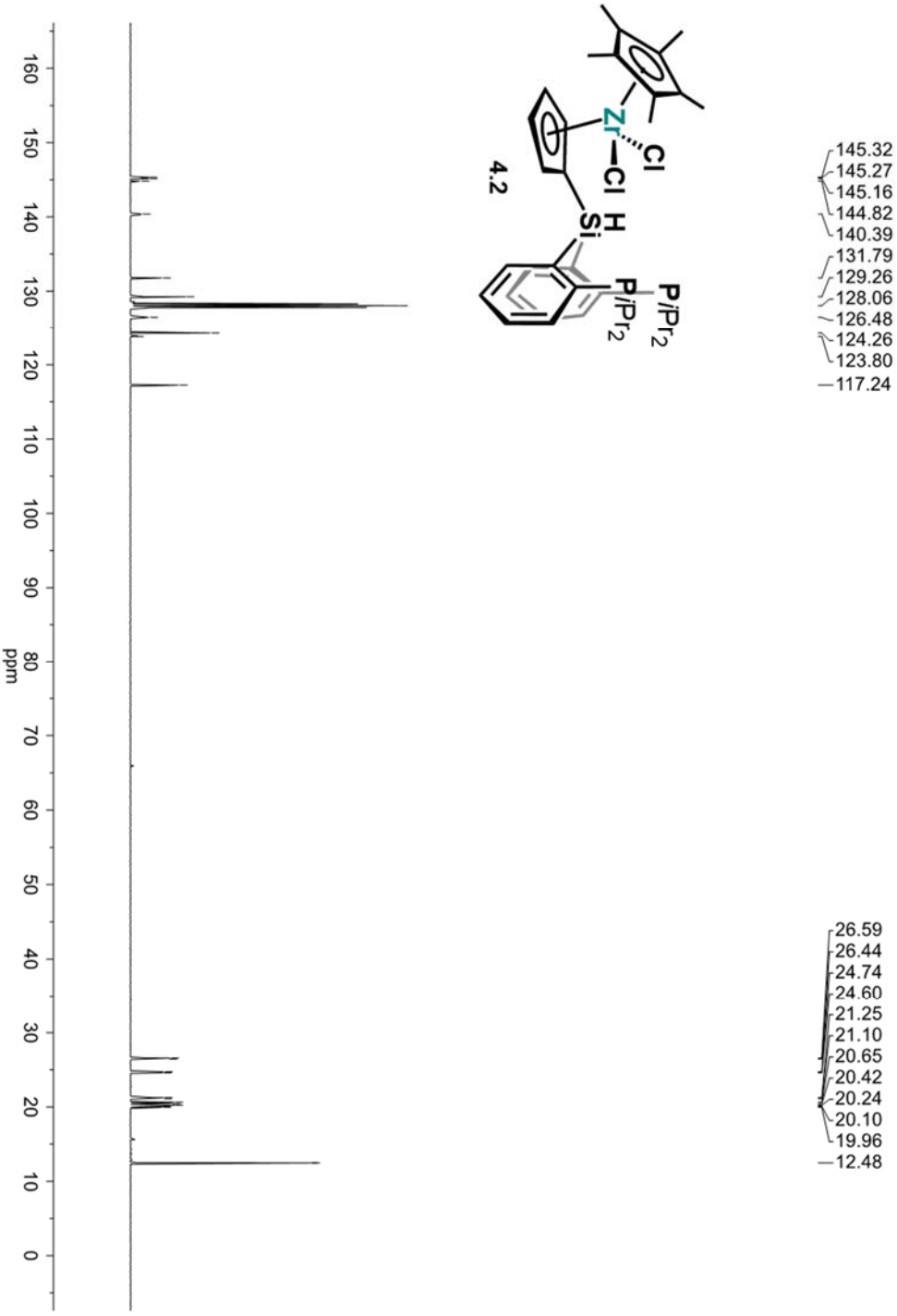

Figure A4.8. ^{13}C NMR Spectrum (C_6D_6, 101 MHz) of Cp*Cp'$ZrCl_2$ **(4.2)**.

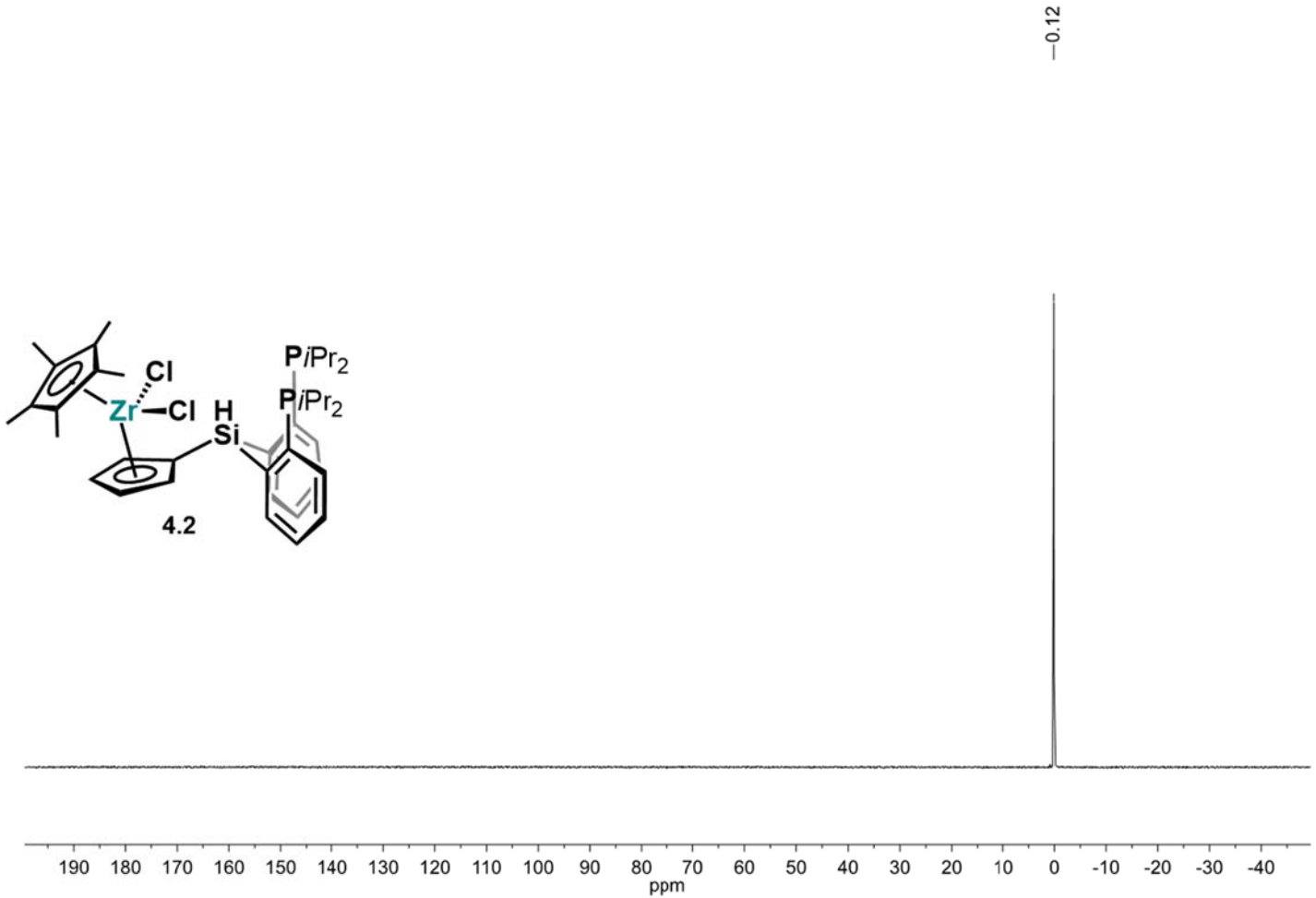

Figure A4.9. ^{31}P NMR Spectrum (C_6D_6, 162 MHz) of Cp*Cp'$ZrCl_2$ **(4.2)**.

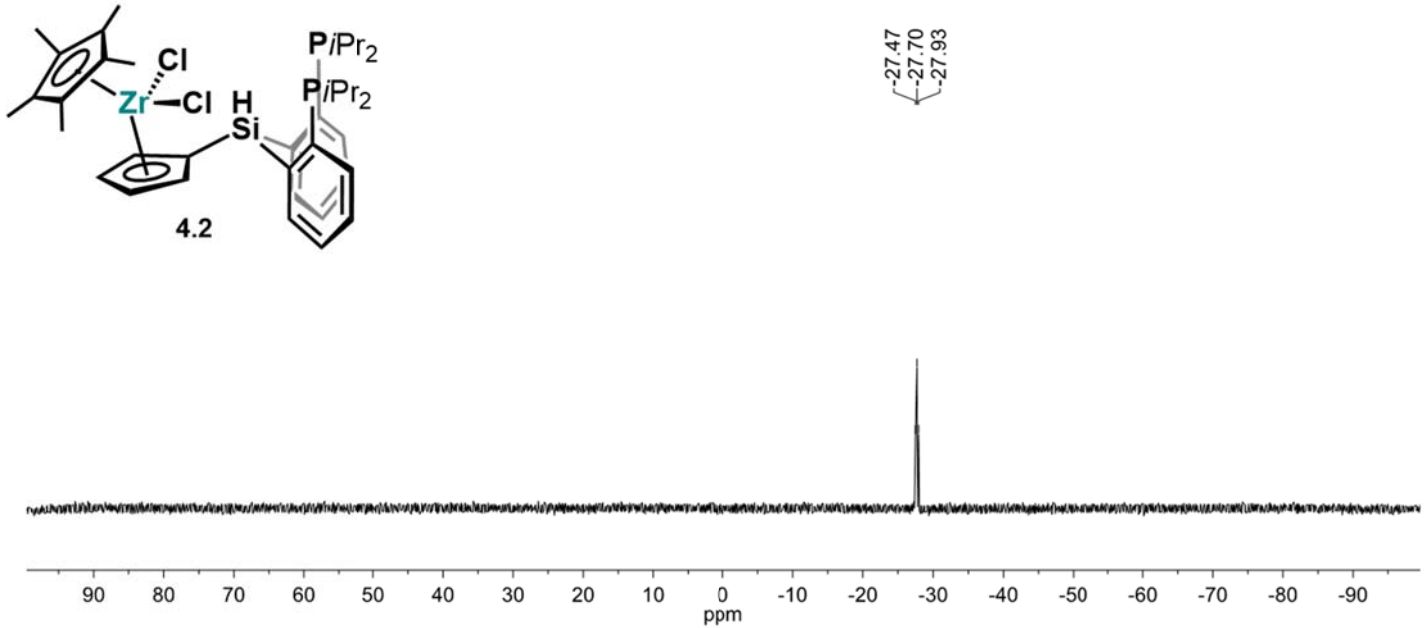

Figure A4.10. ^{29}Si NMR Spectrum (C_6D_6, 79 MHz) of Cp*Cp'$ZrCl_2$ **(4.2)**.

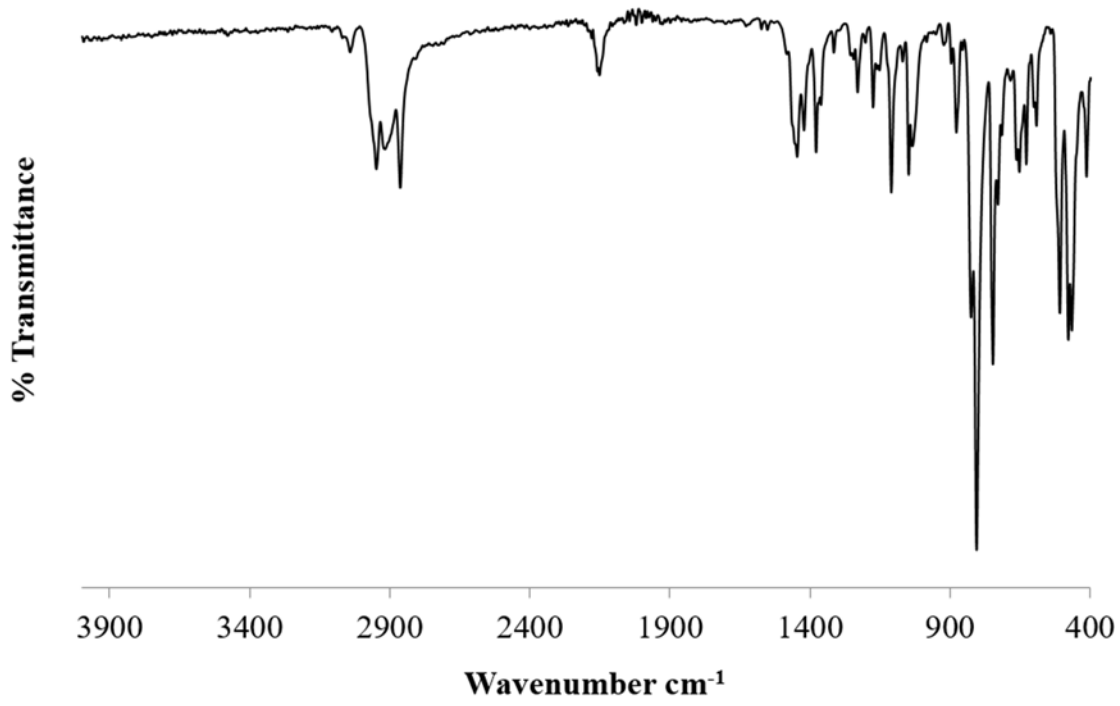

Figure A4.11. Solid-state IR spectrum (KBr) of **4.2**.

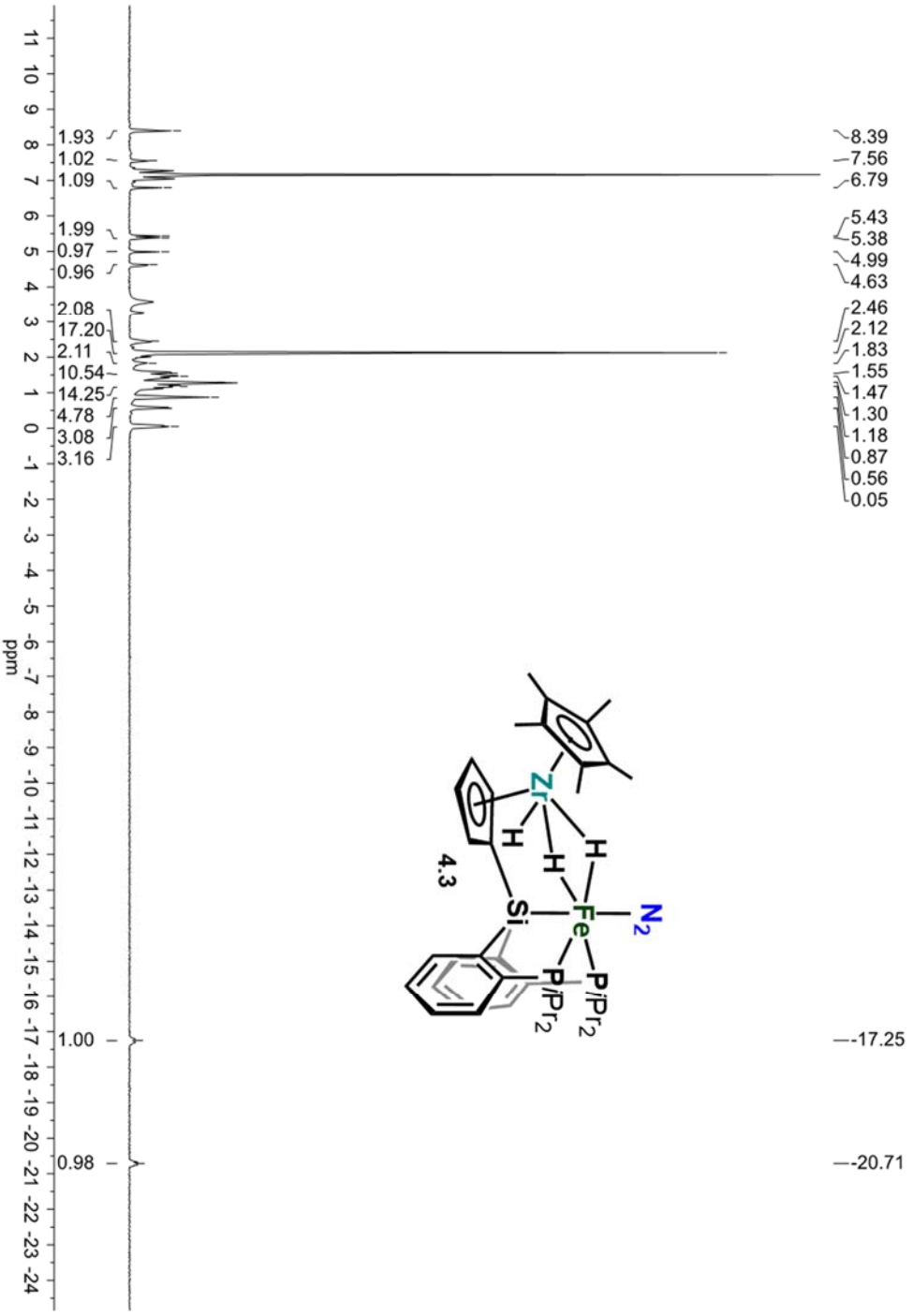

Figure A4.12. ^{1}H NMR Spectrum (C_6D_6, 400 MHz) of $[Fe(\mu\text{-}H)_2Zr(H)]$ **(4.3)**.

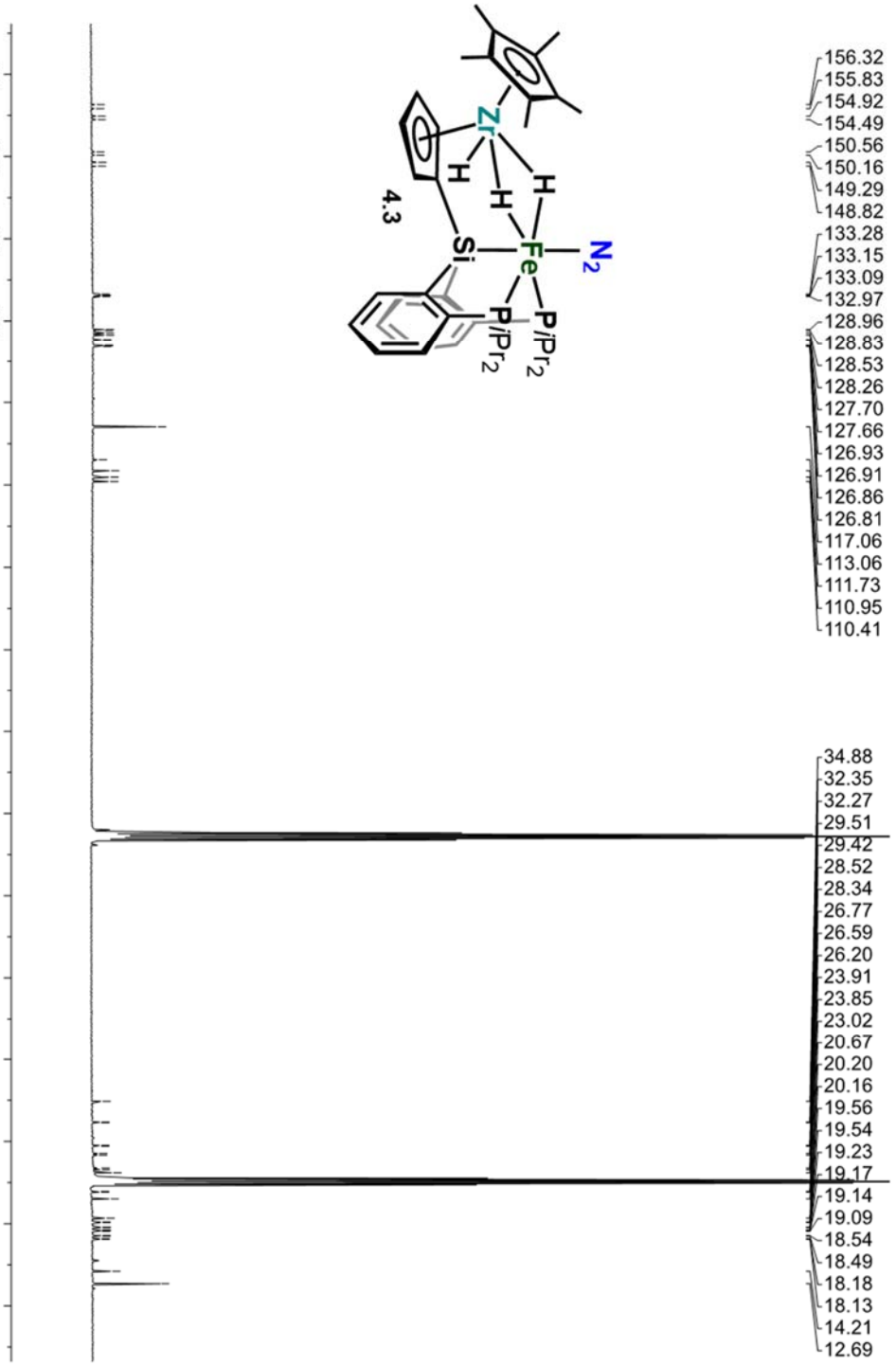

Figure A4.13. ^{13}C NMR Spectrum (C_6D_6, 101 MHz) of $[Fe(\mu\text{-}H)_2Zr(H)]$ **(4.3)**.

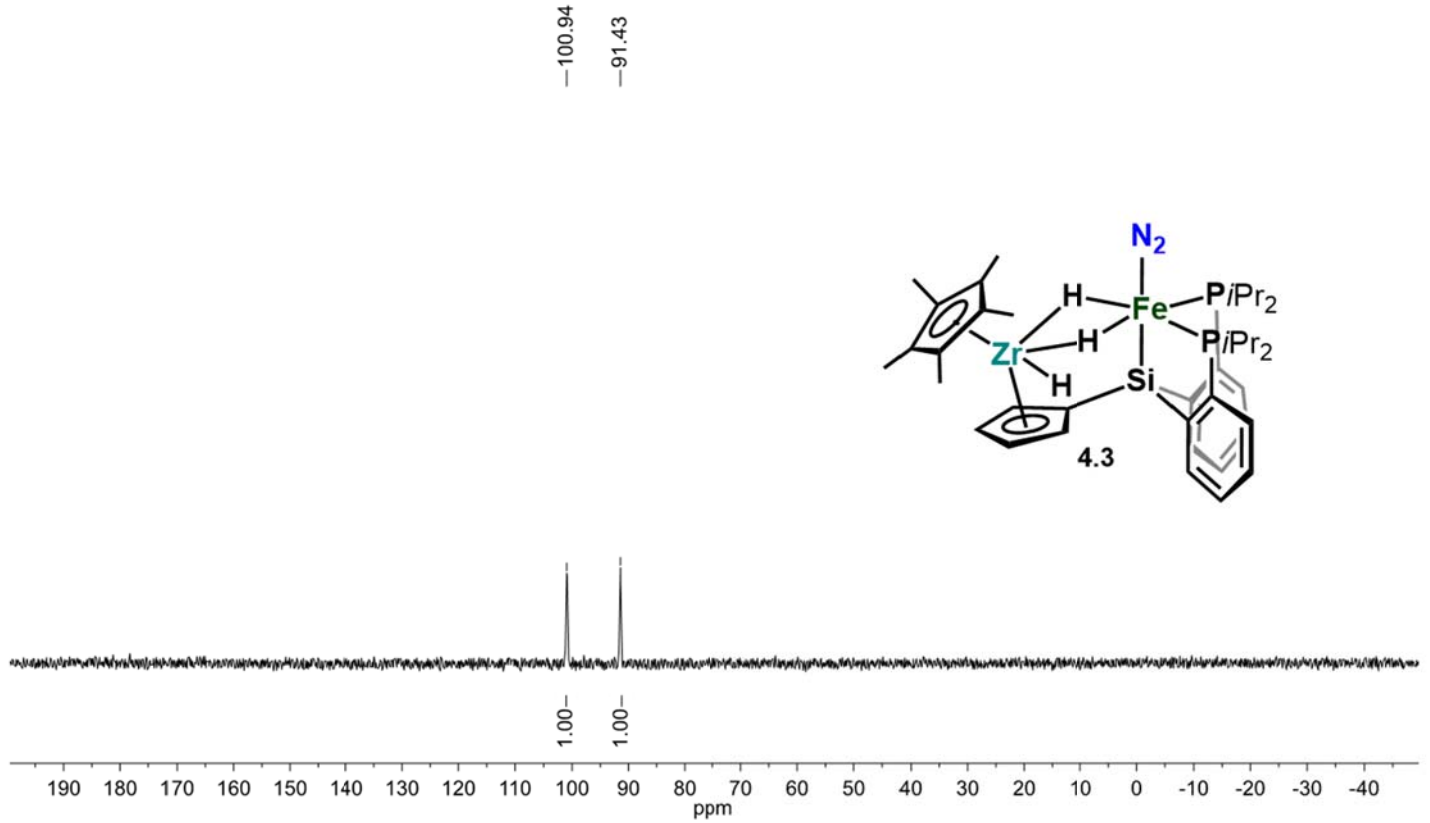

Figure A4.14. ^{31}P NMR Spectrum (C_6D_6, 162 MHz) of [Fe(μ-H)$_2$Zr(H)] **(4.3)**.

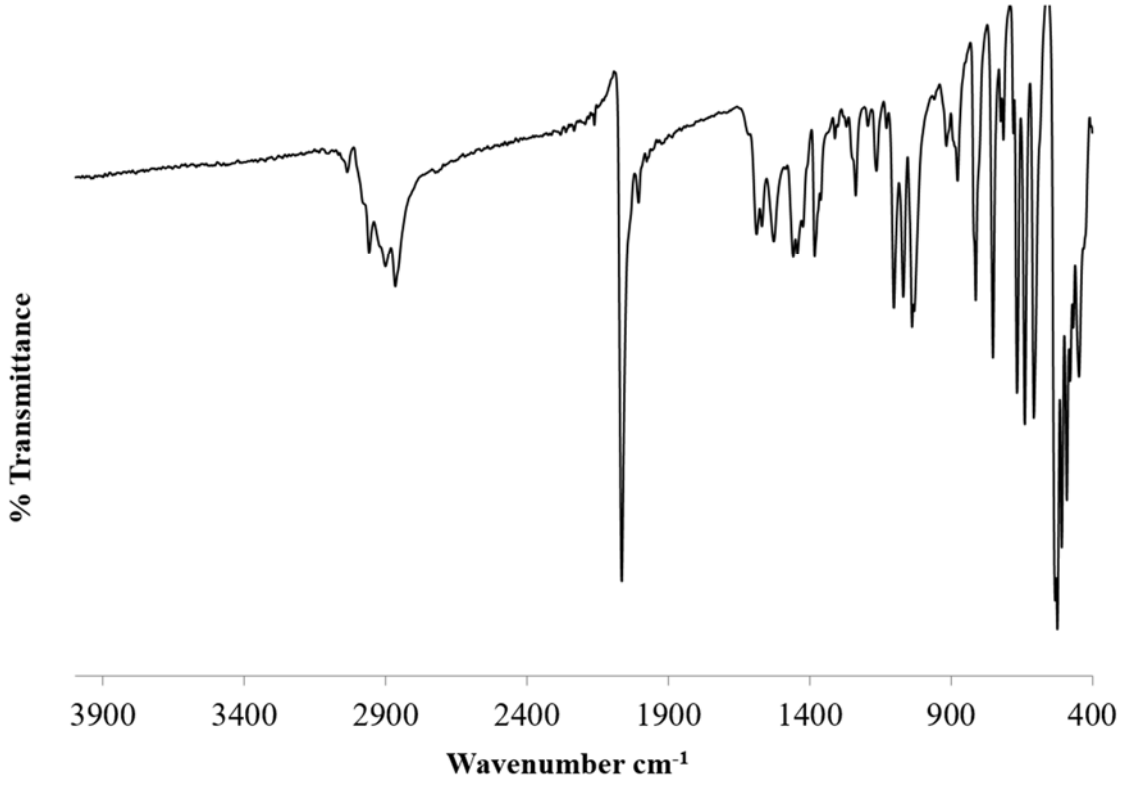

Figure A4.15. Solid-state IR spectrum (KBr) of **4.3**.

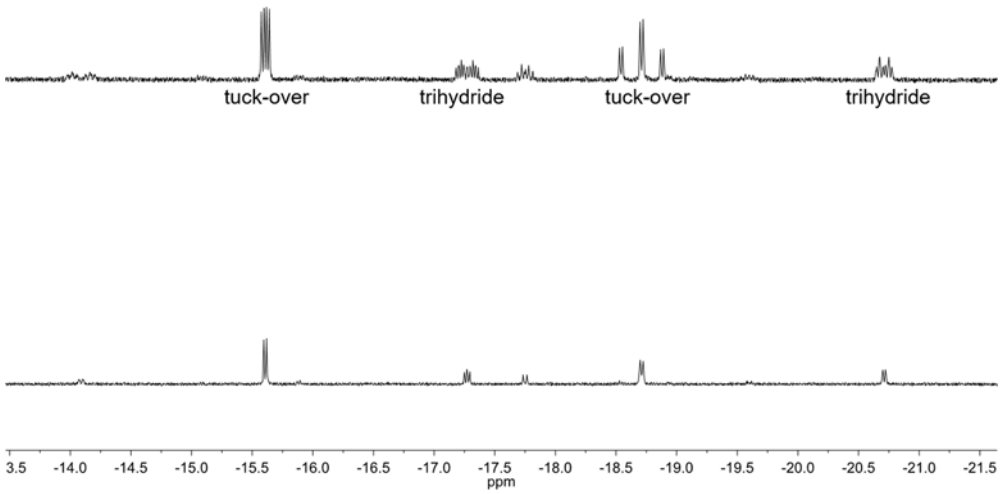

Figure A4.16. ^{1}H (top) and ^{1}H (^{31}P decoupled, bottom) NMR spectra of a mixture of **4.3** and **4.4**.

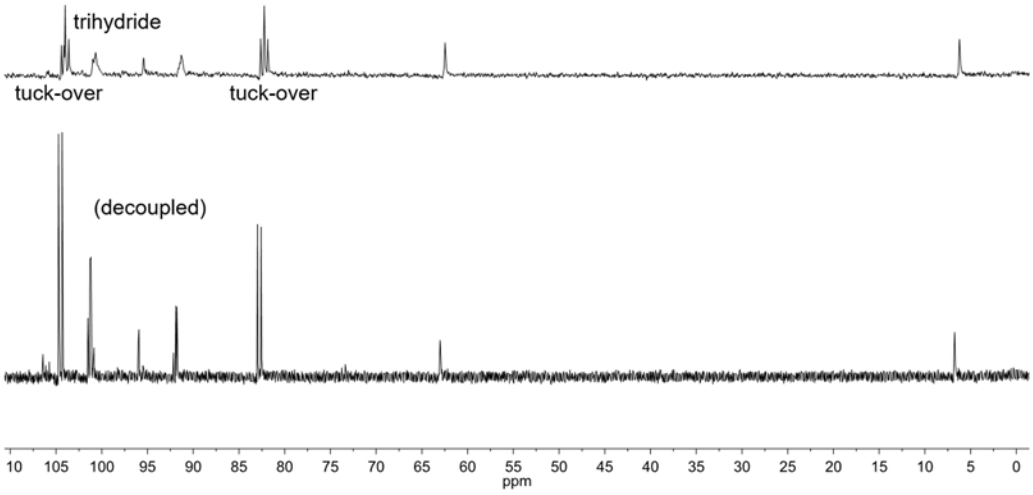

Figure A4.17. ^{31}P (top) and ^{31}P (^{1}H decoupled, bottom) NMR spectra of a mixture of **4.3** and **4.4**.

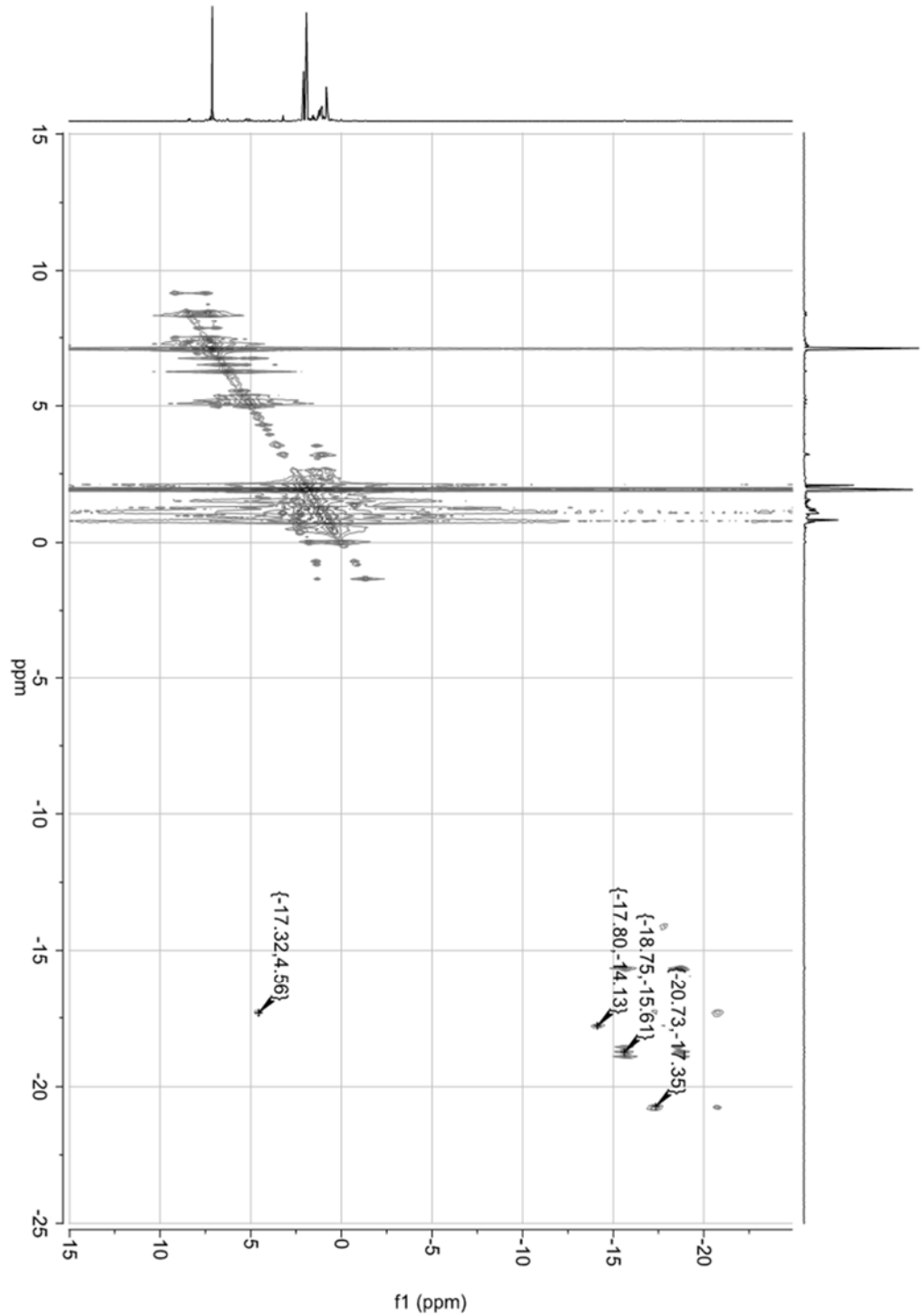

Figure A4.18. COSY NMR spectrum of a mixture of **4.3** and **4.4**.

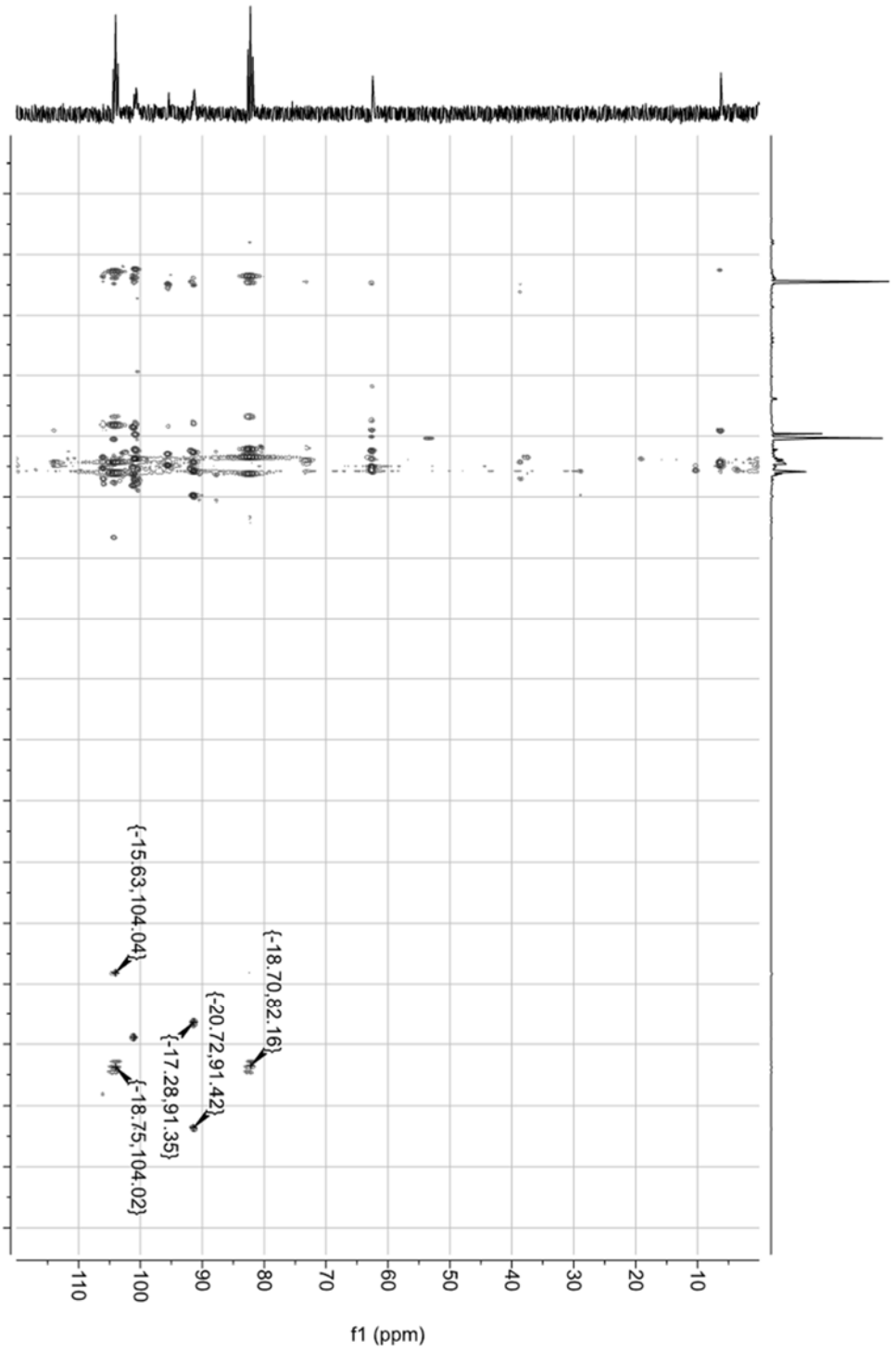

Figure A4.19. $^{1}H–^{31}P$ HMBC NMR spectra of a mixture of **4.3** and **4.4**.

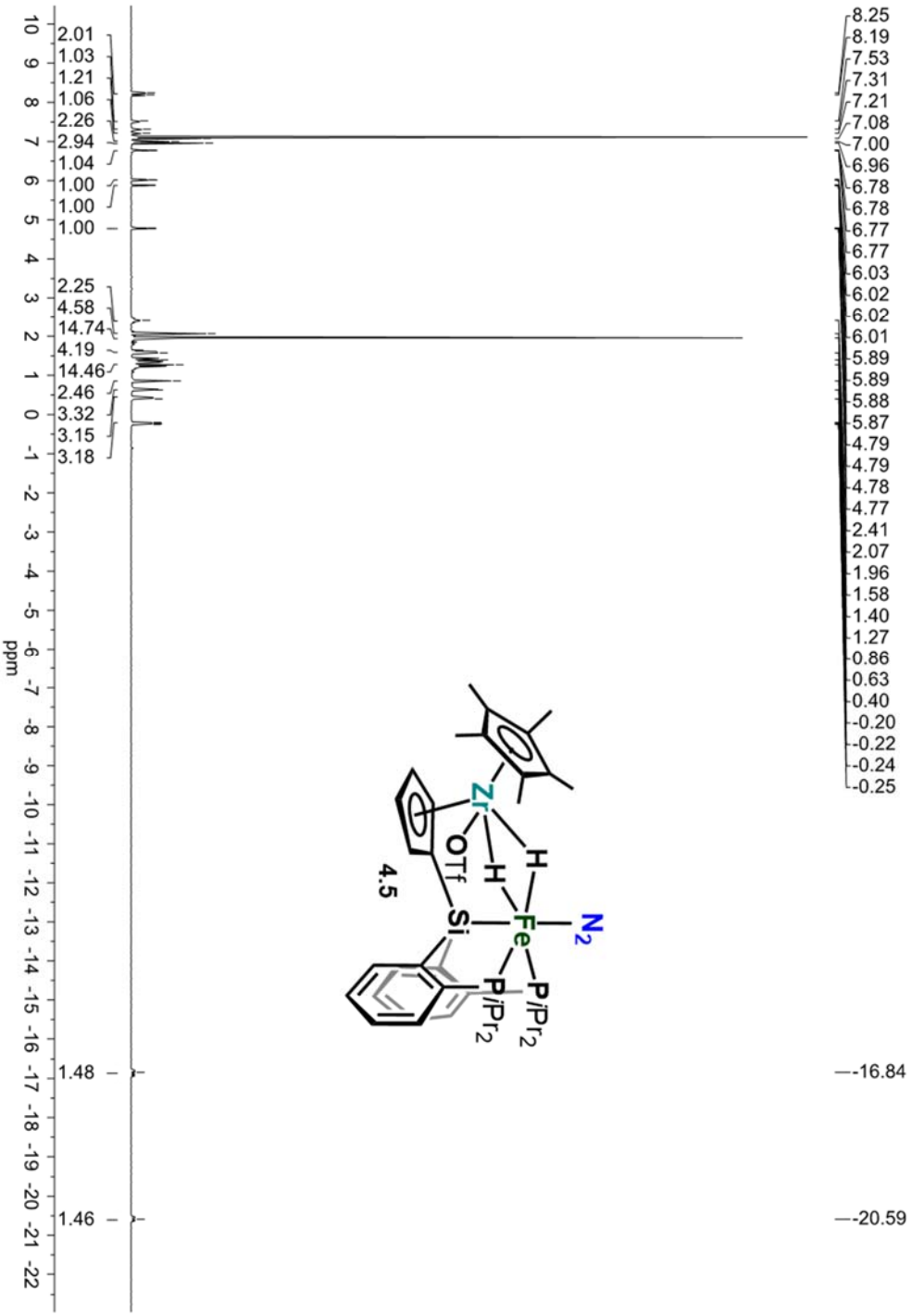

Figure A4.20. ^{1}H NMR Spectrum (toluene-d_8, 400 MHz) of [Fe(μ-H)$_2$Zr(OTf)] **(4.5)**.

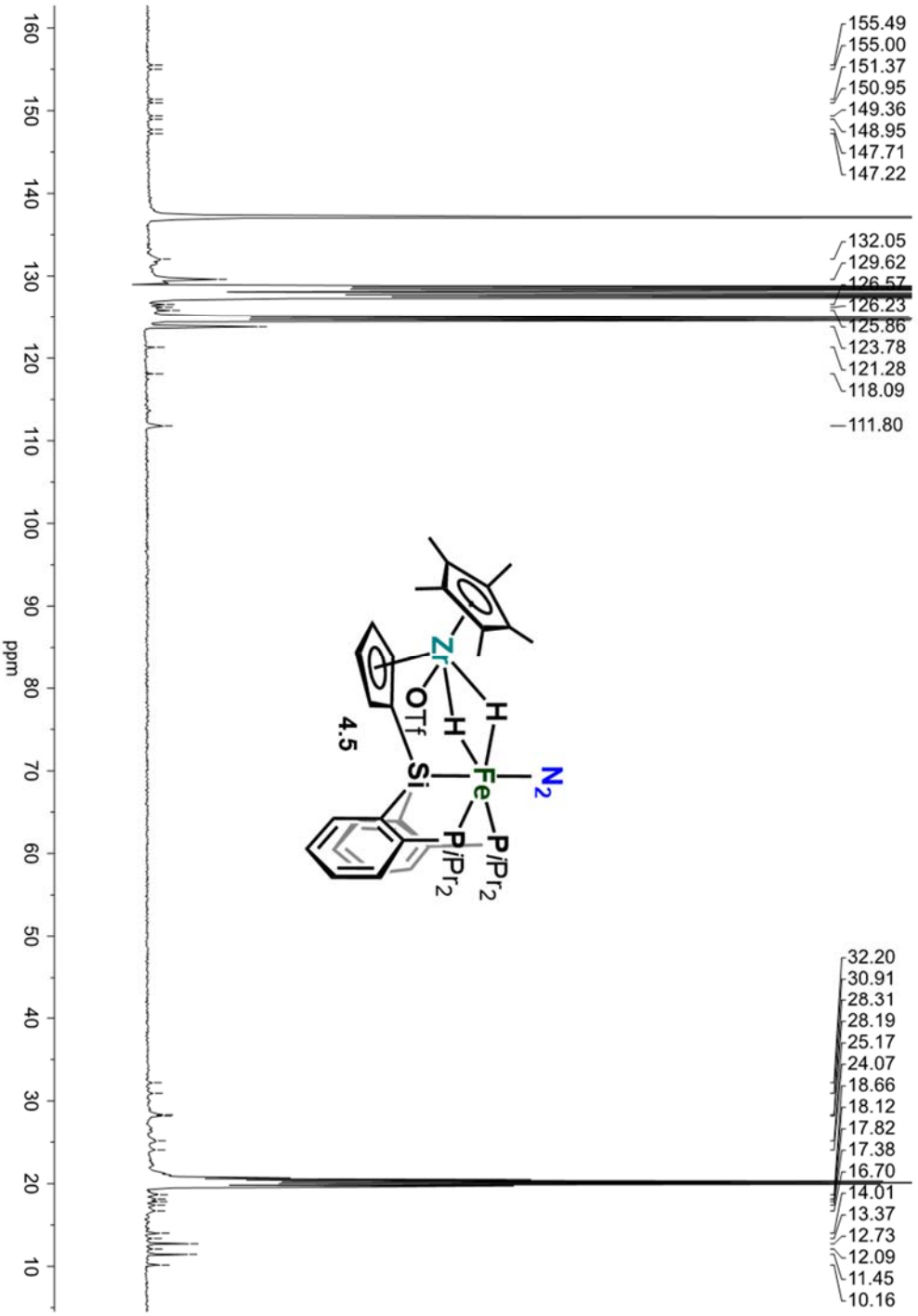

Figure A4.21. ^{13}C NMR Spectrum (toluene-d_8, 101 MHz) of [Fe(μ-H)$_2$Zr(OTf)] **(4.5)**.

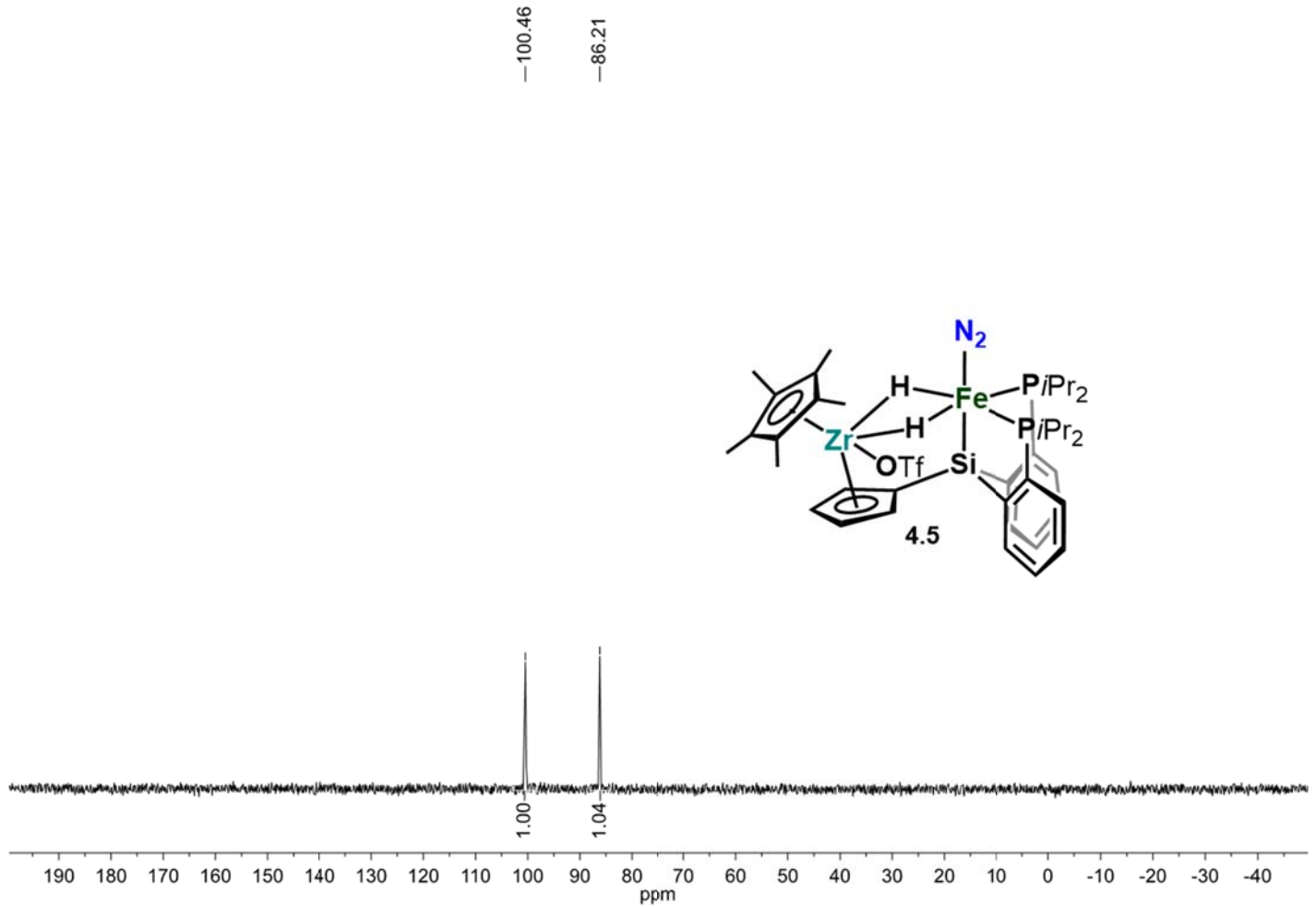

Figure A4.22. ^{31}P NMR Spectrum (toluene-d_8, 162 MHz) of [Fe(μ-H)$_2$Zr(OTf)] **(4.5)**.

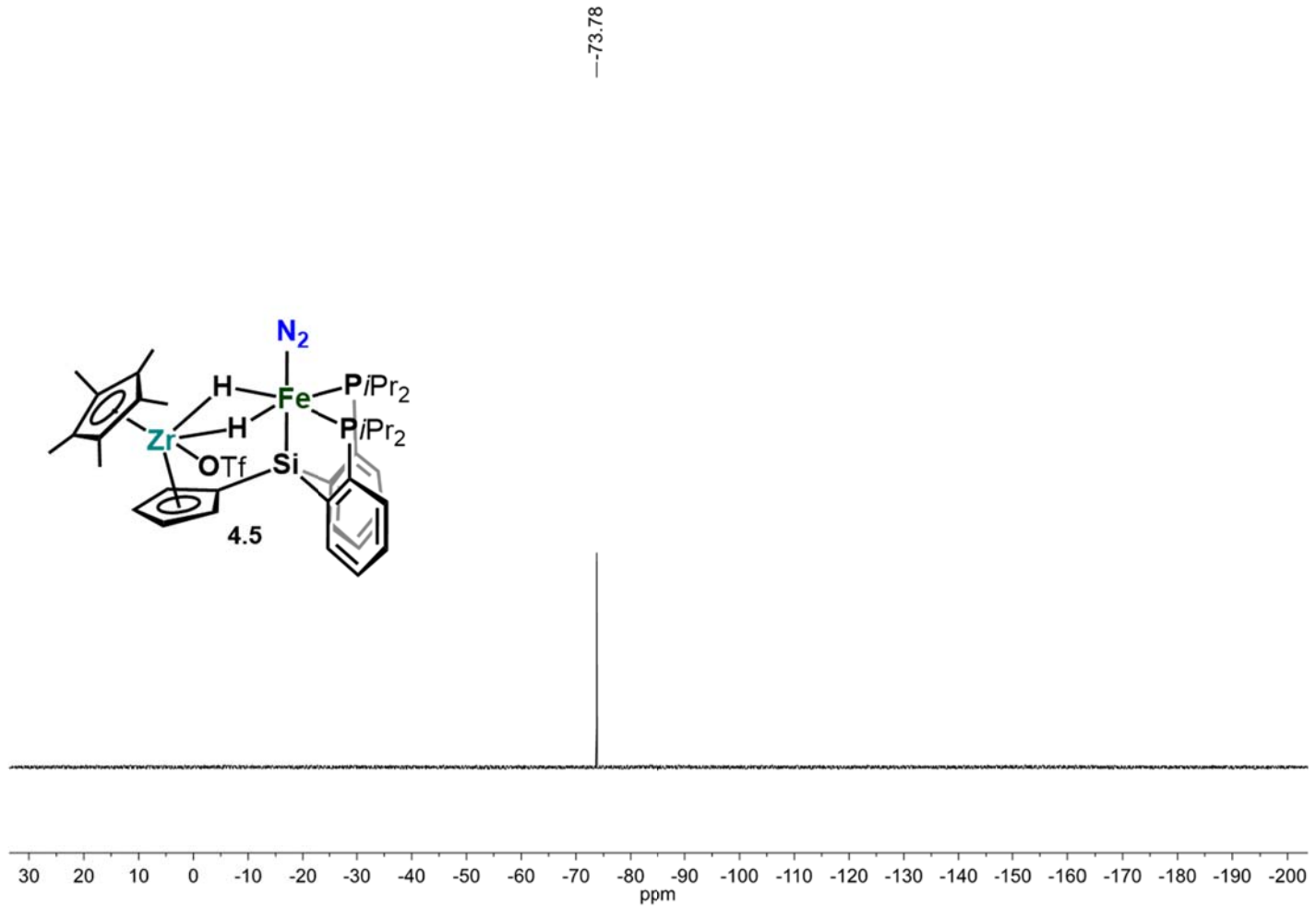

Figure A4.23. ^{19}F NMR Spectrum (toluene-d_8, 376 MHz) of [Fe(μ-H)$_2$Zr(OTf)] **(4.5)**.

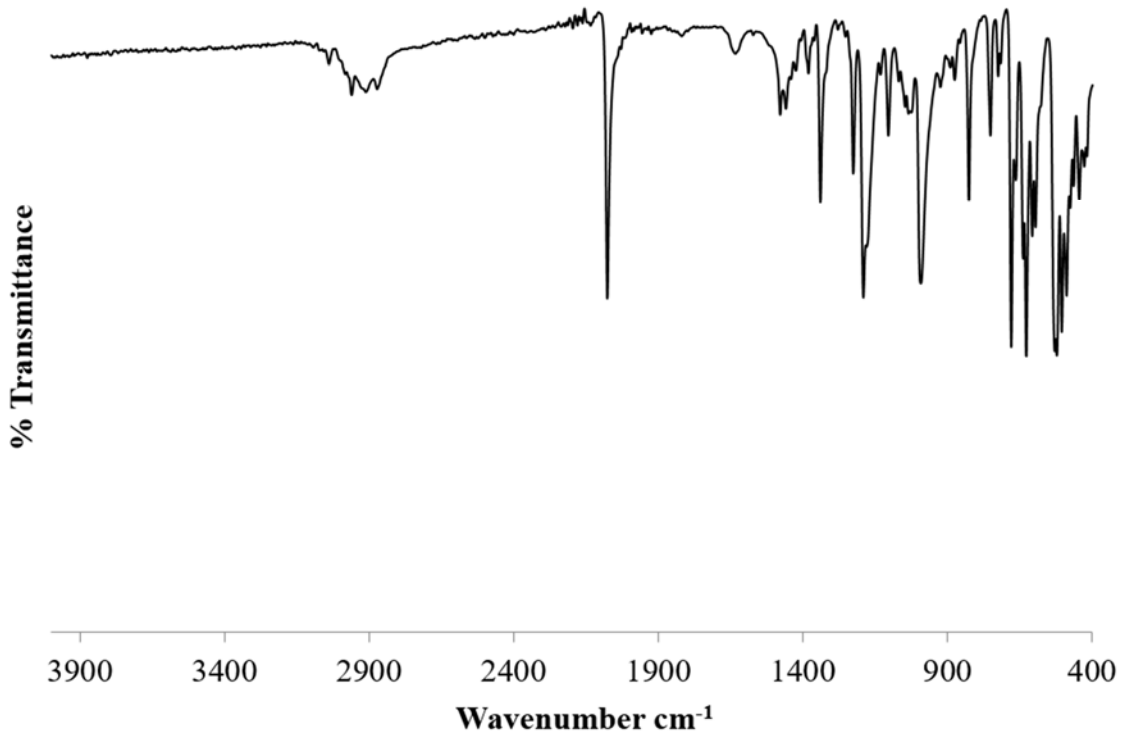

Figure A4.24. Solid-state (KBr) IR spectrum of **4.5**.

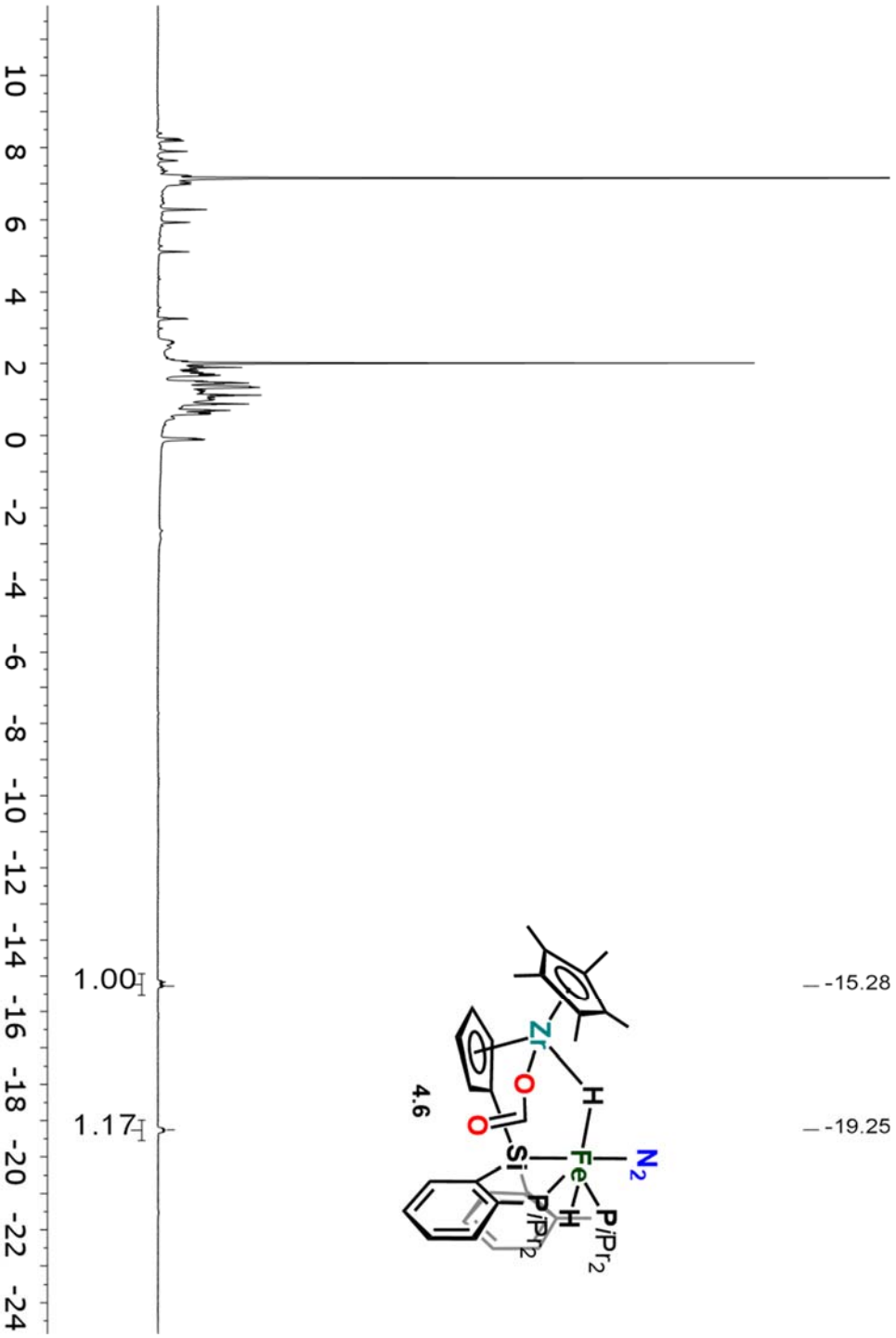

Figure A4.25. ^{1}H NMR Spectrum (C_6D_6, 400 MHz) of [Fe(μ-H)$_2$Zr(OCHO)] **(4.6)**.

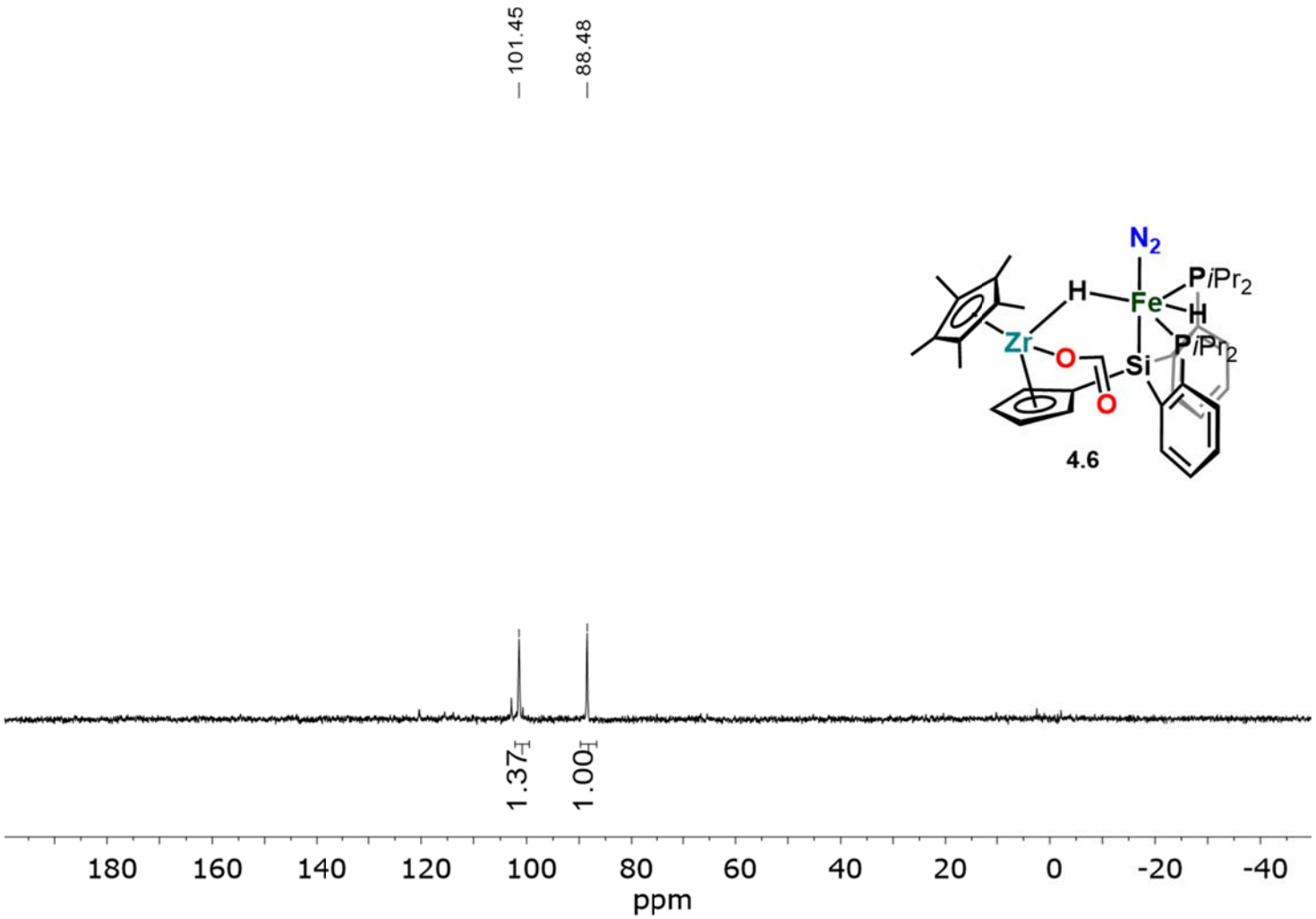

Figure A4.26. ^{31}P NMR Spectrum (C_6D_6, 162 MHz) of [Fe(μ-H)$_2$Zr(OCHO)] **(4.6)**.

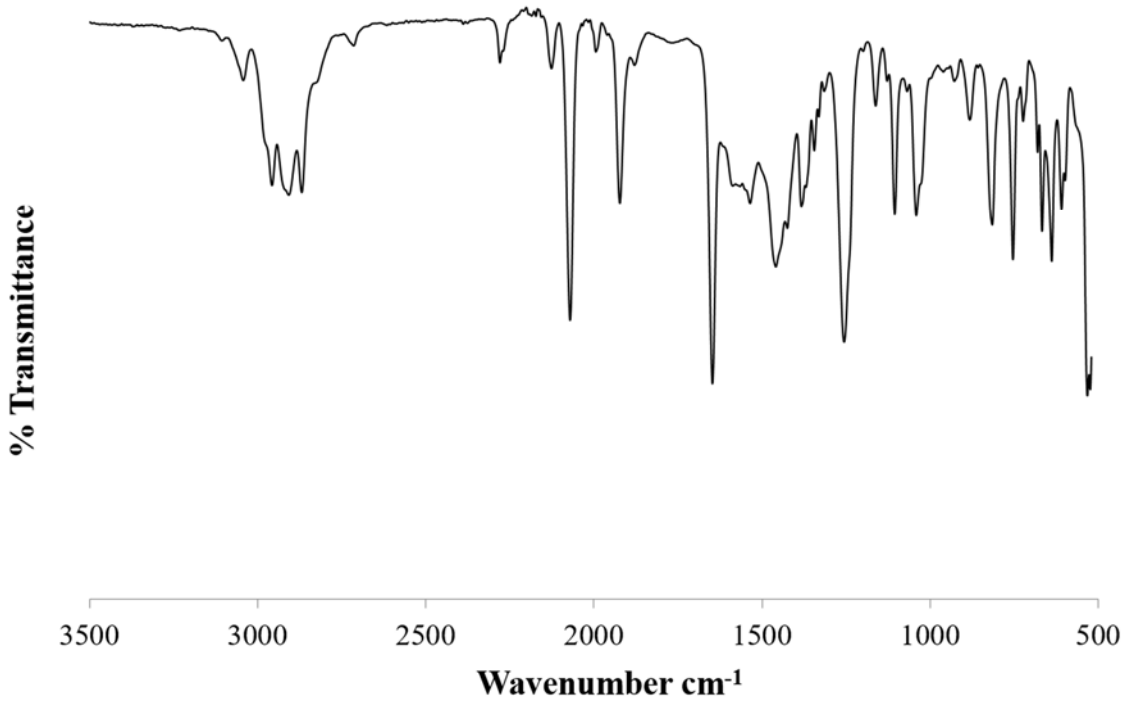

Figure A4.27. IR (thin-film) Spectrum of **4.6**.

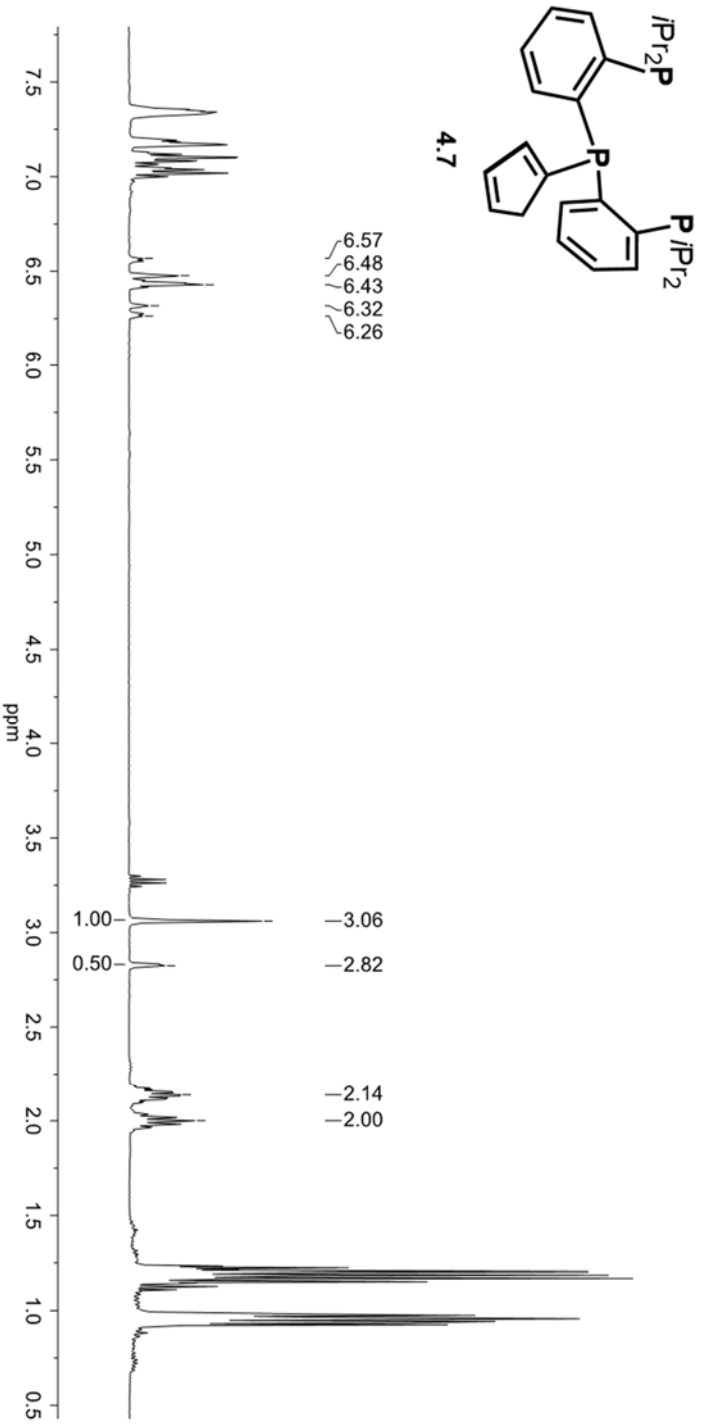

Figure A4.28. ^{1}H NMR Spectrum (C_6D_6, 400 MHz) of P_2^{PCp} **(4.7)**.

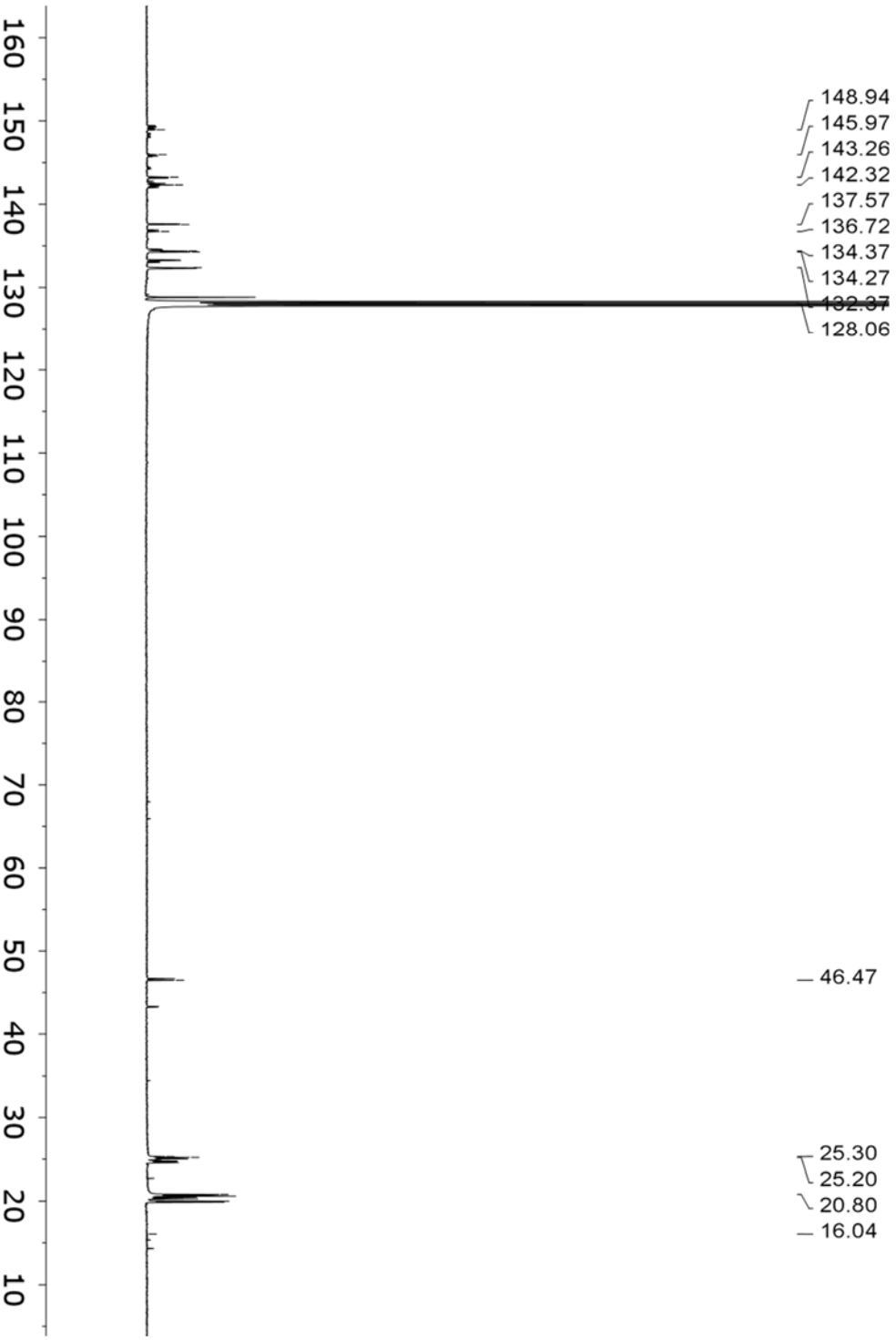

Figure A4.29. ^{13}C NMR Spectrum (C_6D_6, 101 MHz) of P_2^{PCp} **(4.7)**.

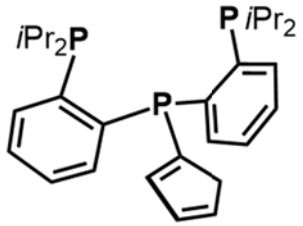

4.7

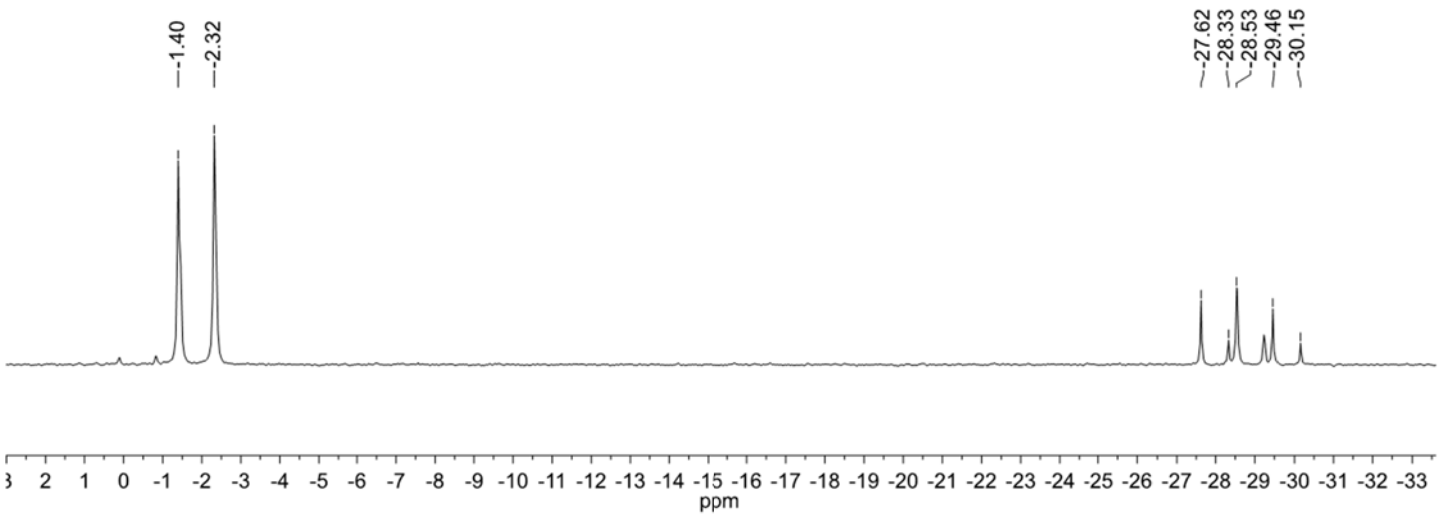

Figure A4.30. ^{31}P NMR Spectrum (C_6D_6, 162 MHz) of P_2^{PCp} **(4.7)**.

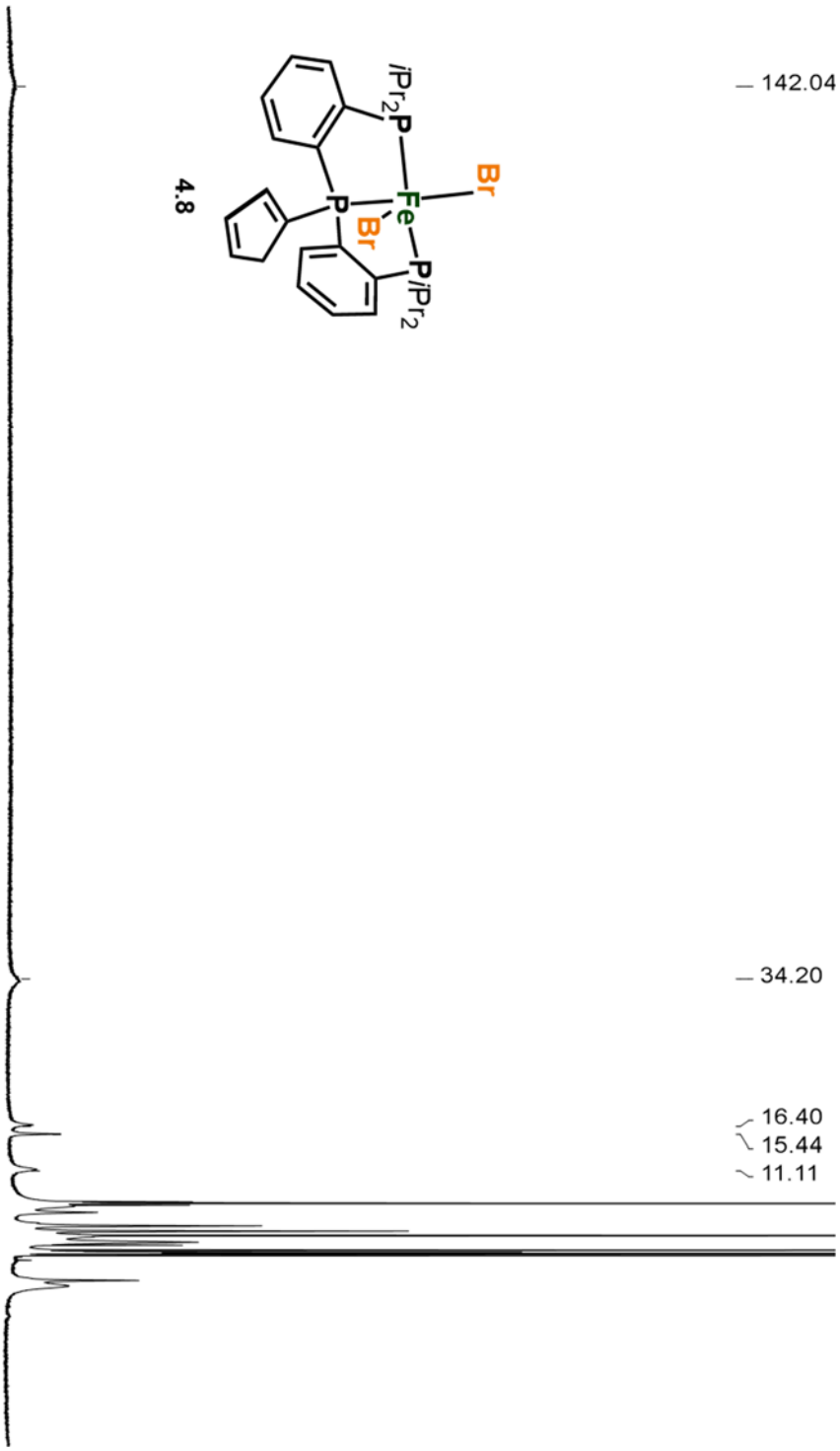

Figure A4.31. ^{1}H NMR Spectrum (C_6D_6, 400 MHz) of $P_2^{PCpF}FeBr_2$ **(4.8-FeBr$_2$)**.

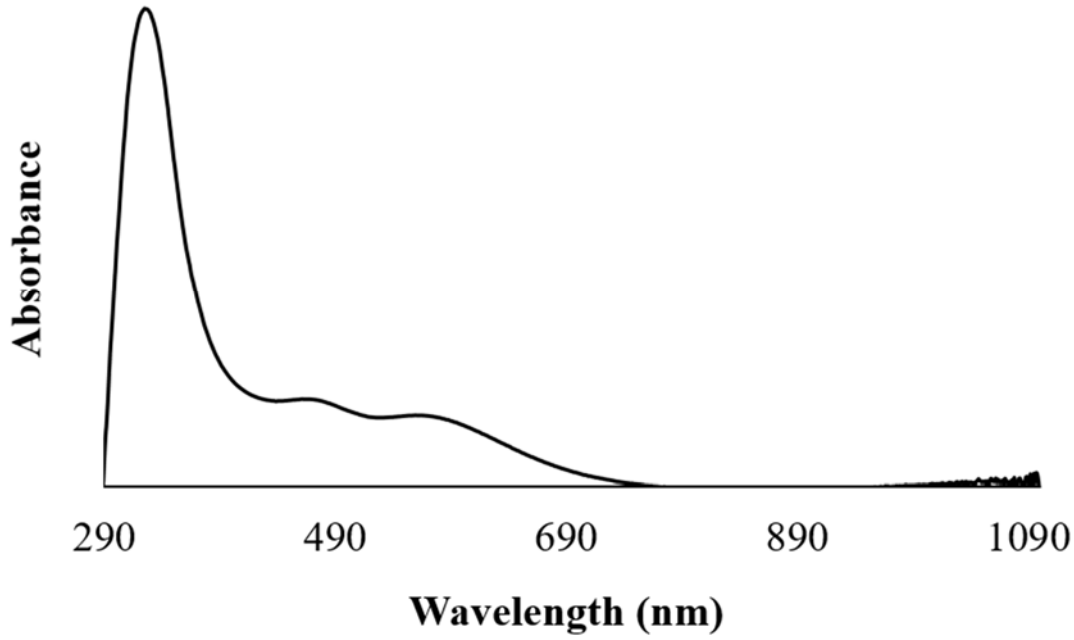

Figure A4.32. UV-Vis spectrum of a THF solution of **4.8-FeBr$_2$**.

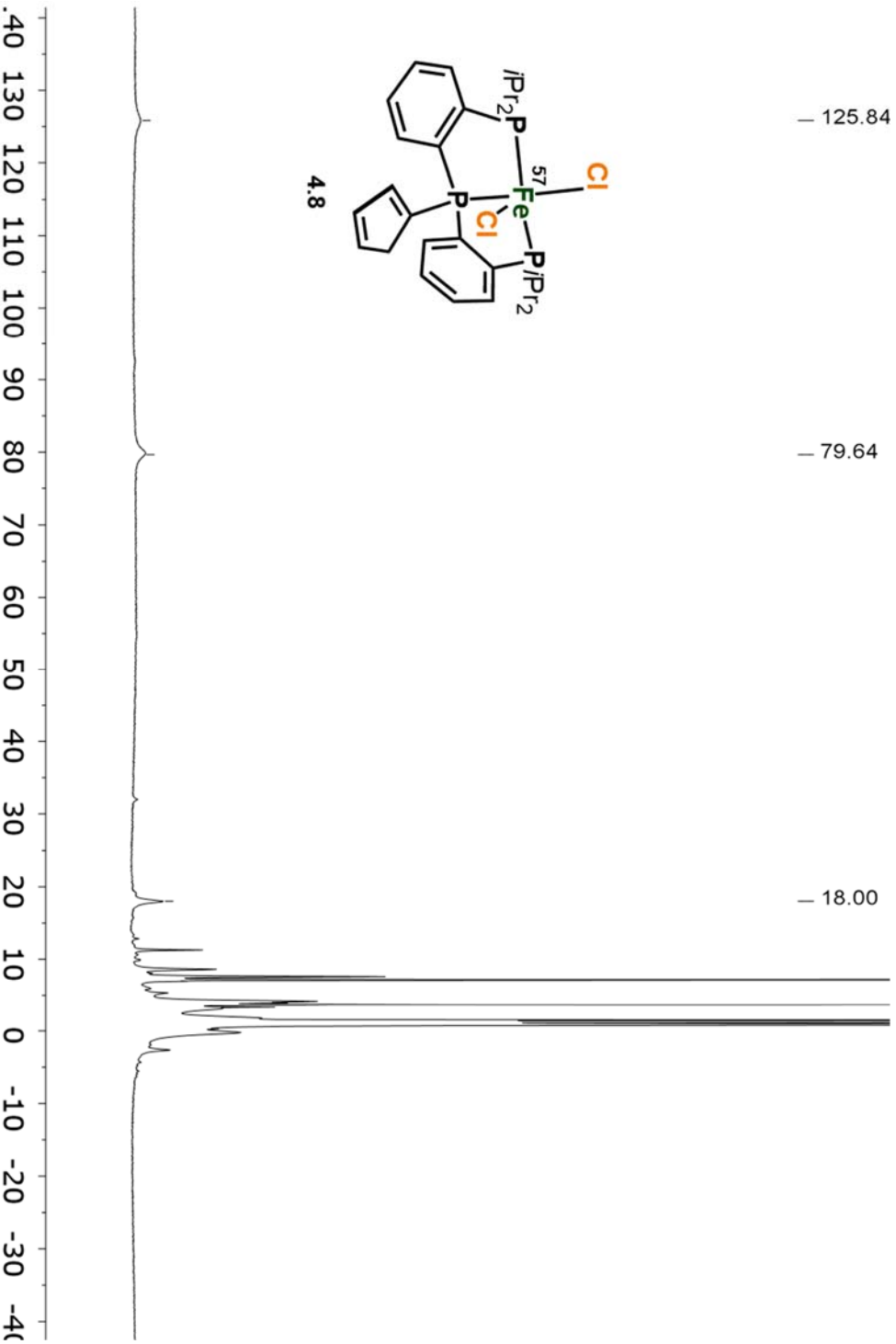

Figure A4.33. ^{1}H NMR Spectrum (C_6D_6, 400 MHz) of $(P_2^{PCp})^{57}FeCl_2$ **(4.8-^{57}FeCl$_2$)**.

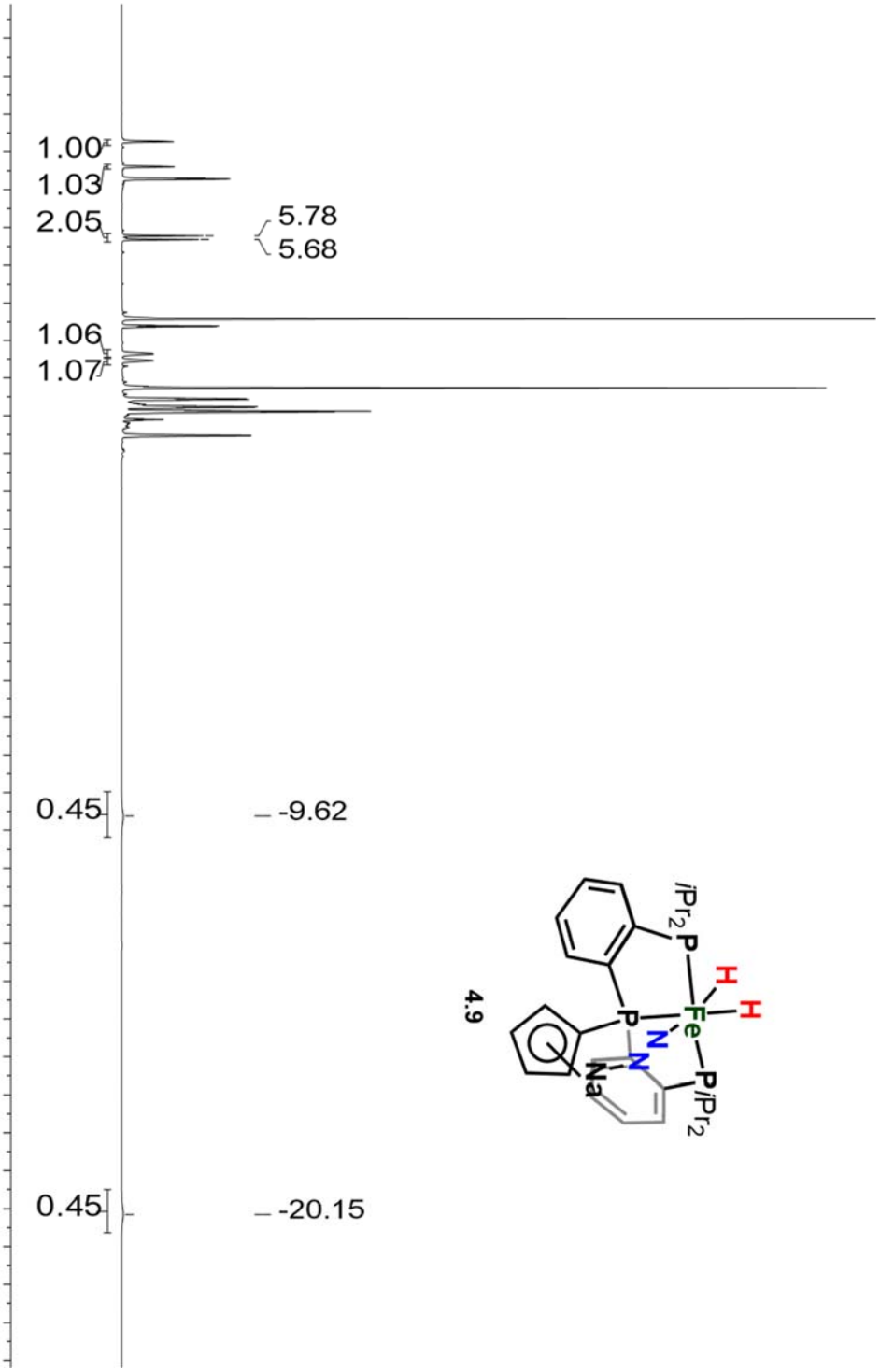

Figure A4.34. ^{1}H NMR Spectrum (THF-d_8, 400 MHz) of [(P_2^{PCp})Fe(N_2)($H)_2$]Na **(4.9)**.

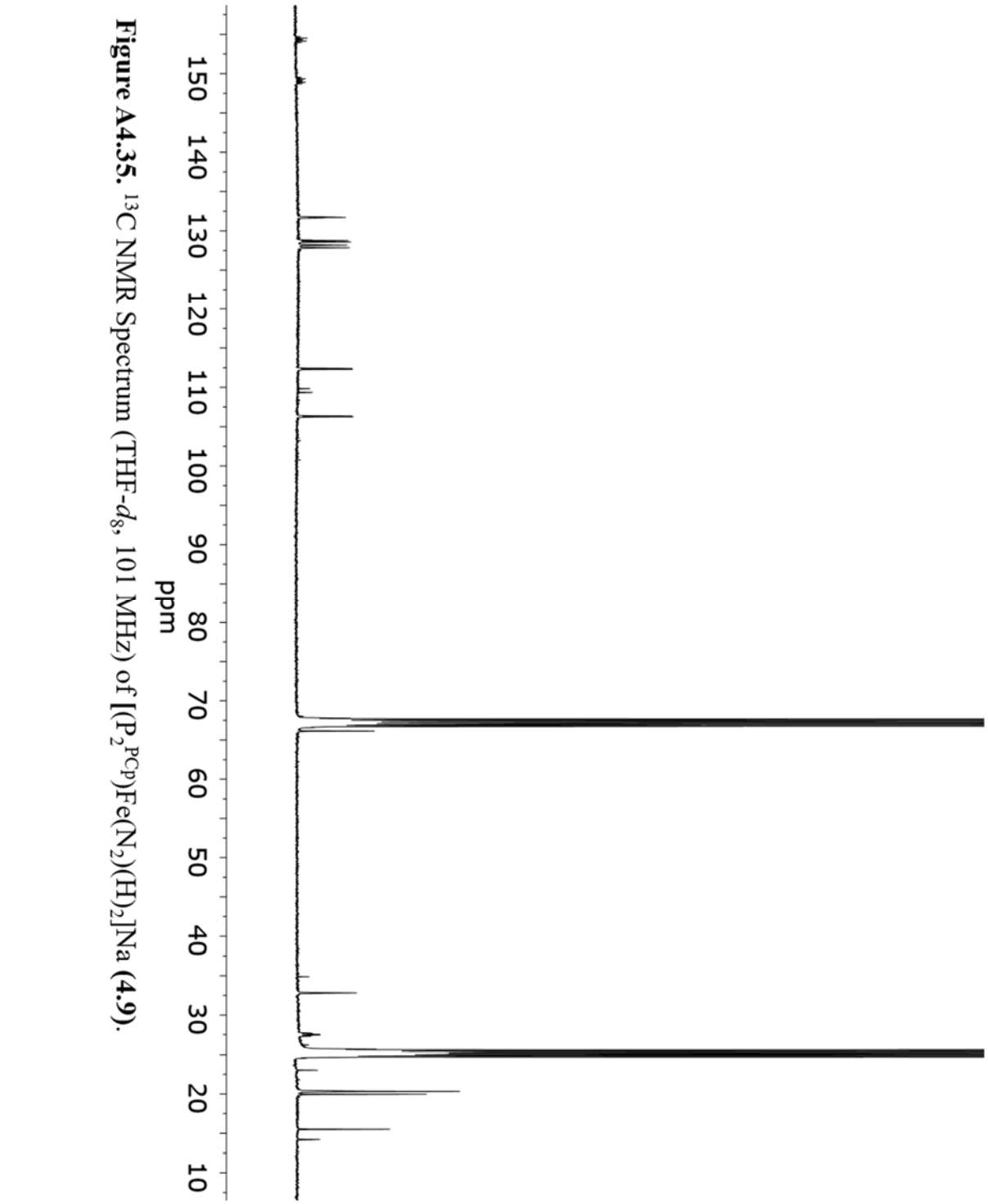

Figure A4.35. ^{13}C NMR Spectrum (THF-d_8, 101 MHz) of **[**(P_2^{PCp})Fe(N_2)($H)_2$]Na **(4.9)**.

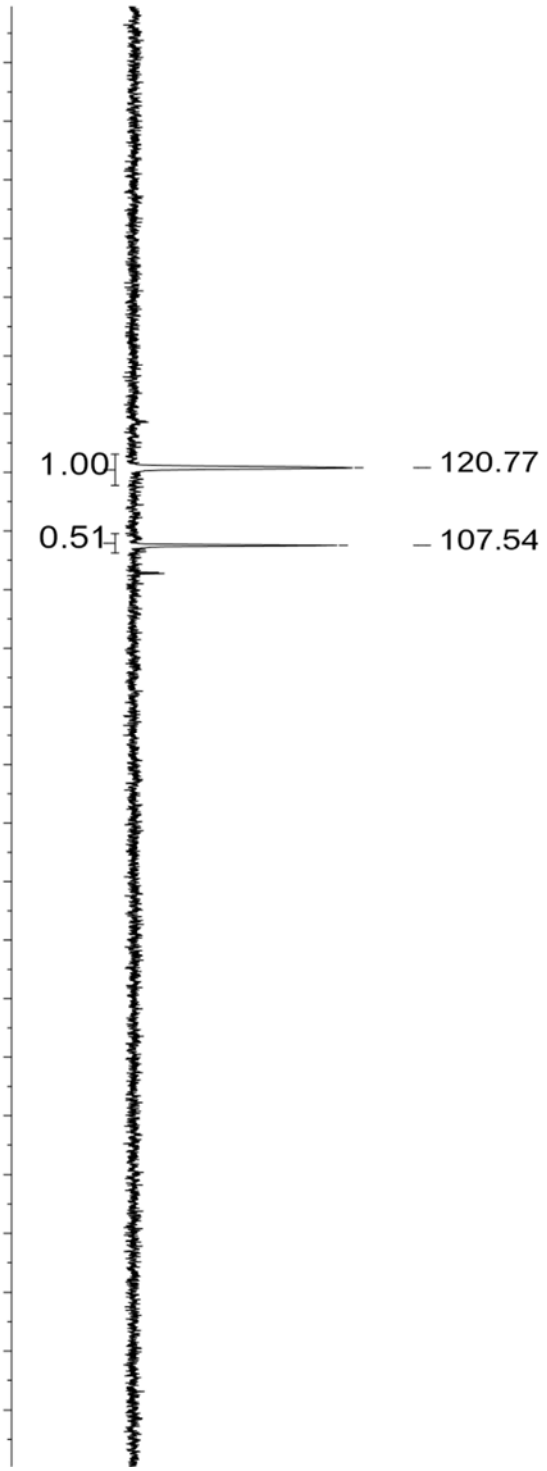

Figure A4.36. ^{31}P NMR Spectrum (THF-d_8, 162 MHz) of **[(P_2^{PCP})Fe(N_2)($H)_2$]Na (4.9)**.

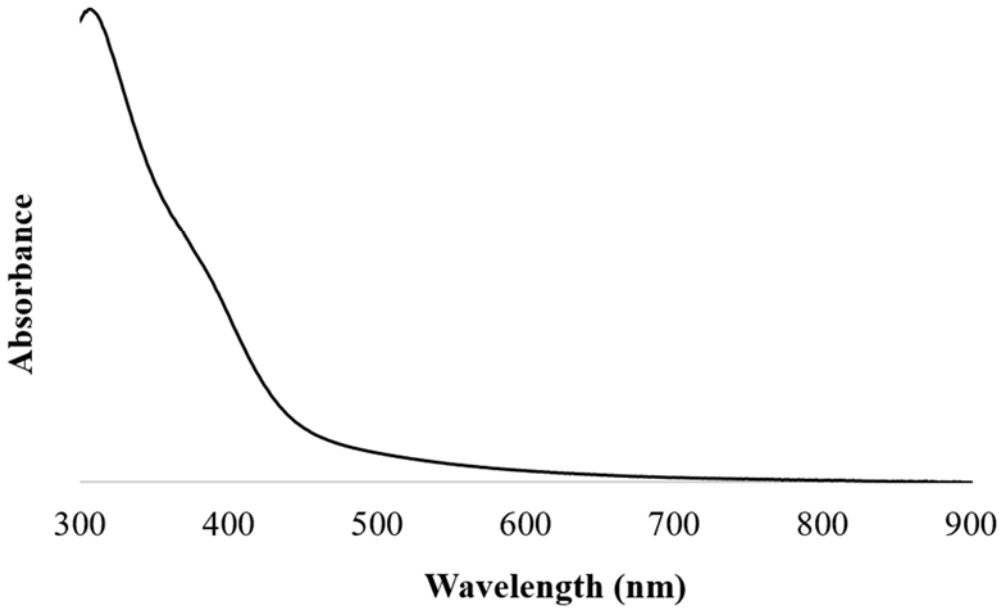

Figure A4.37. UV-Vis spectrum of a THF solution of **4.9**.

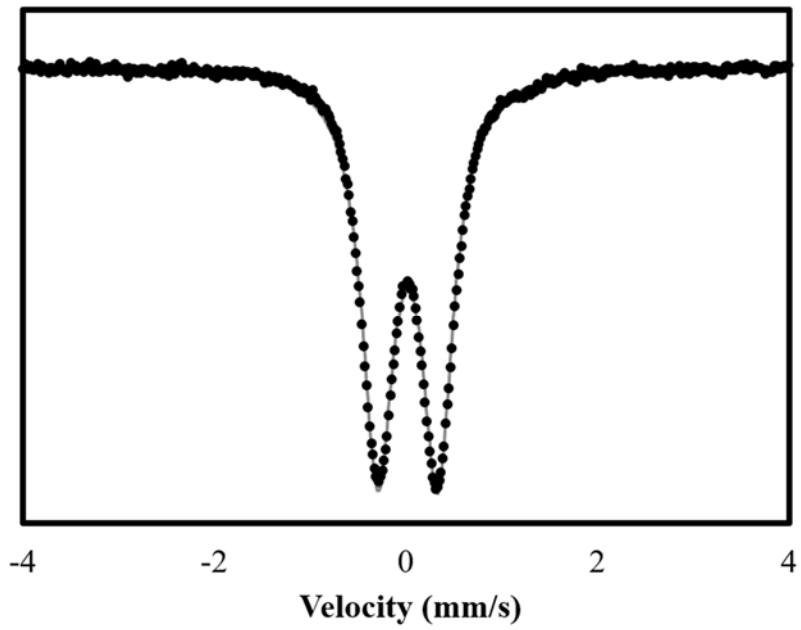

Figure A4.38. Mössbauer spectrum of a THF solution of **4.9**.

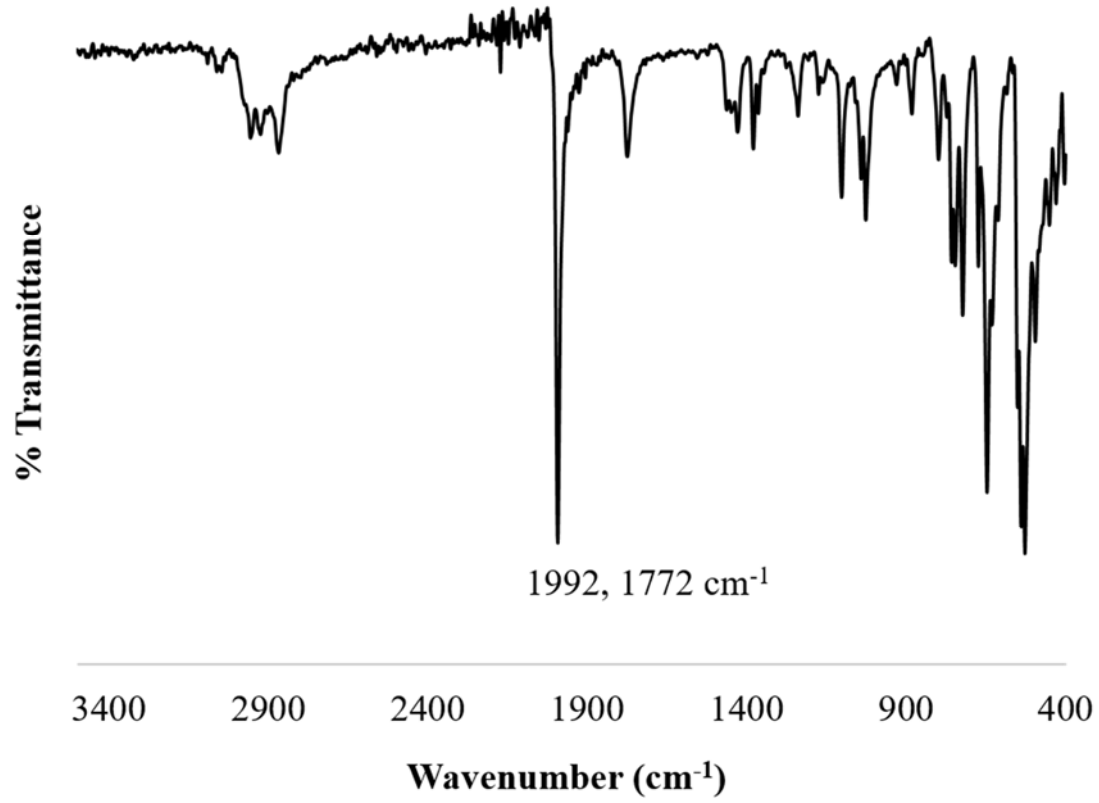

Figure A4.39. Solid-state (KBr) IR spectrum of **4.9**.

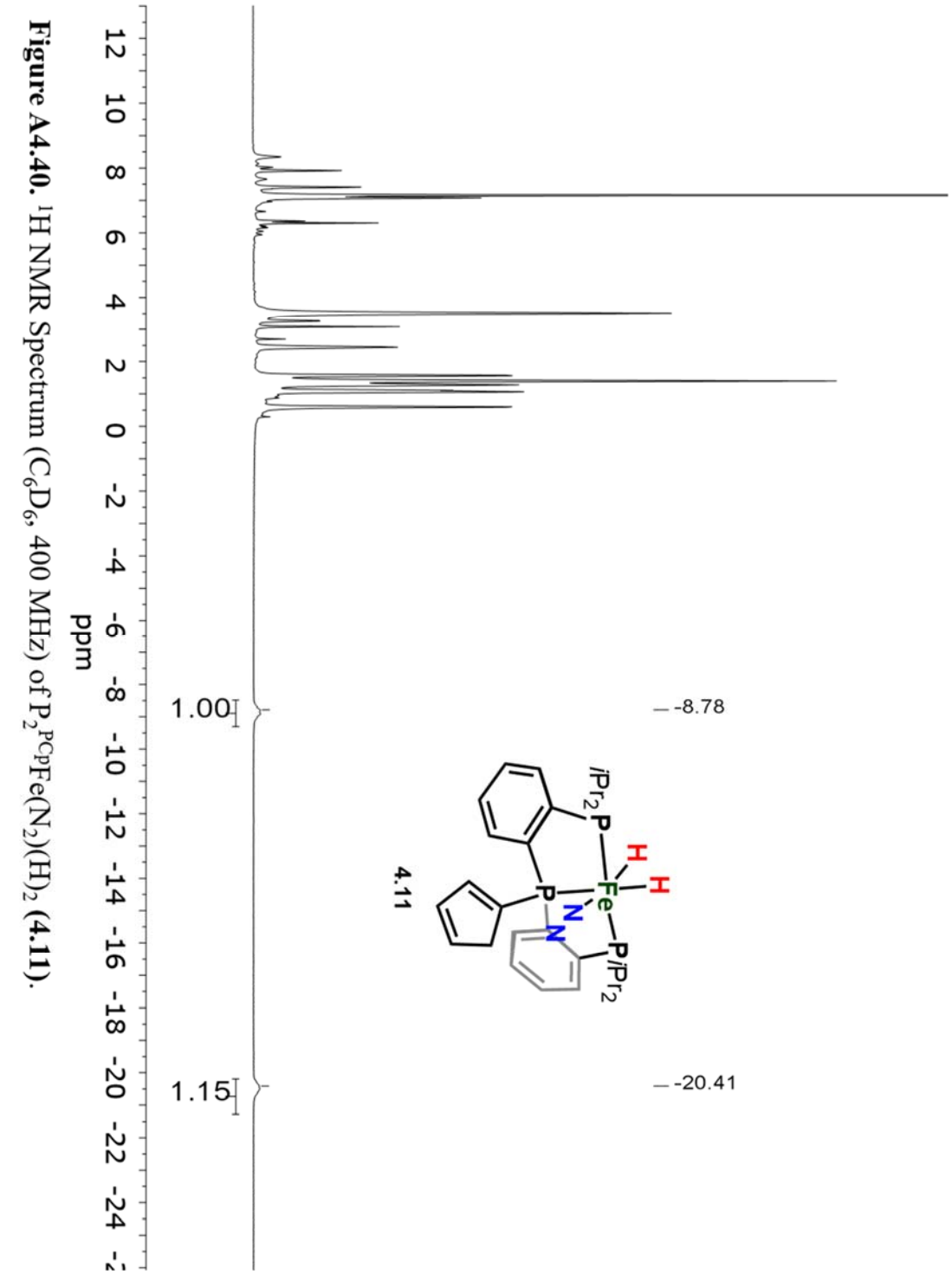

Figure A4.40. ^{1}H NMR Spectrum (C_6D_6, 400 MHz) of $P_2^{PCPr}Fe(N_2)(H)_2$ **(4.11)**.

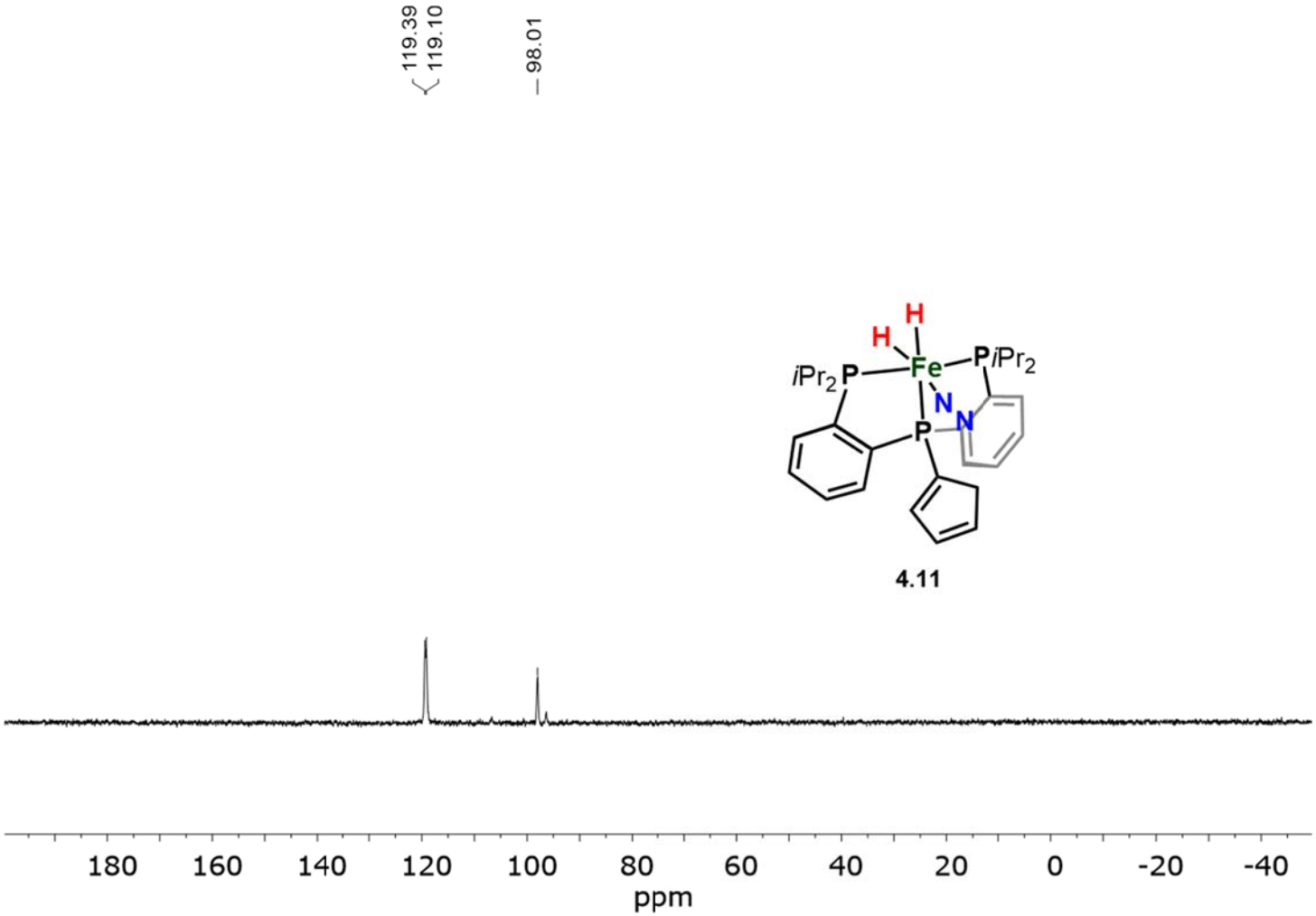

Figure A4.41. ^{31}P NMR Spectrum (C_6D_6, 162 MHz) of $P_2^{PCp}Fe(N_2)(H)_2$ **(4.11)**.

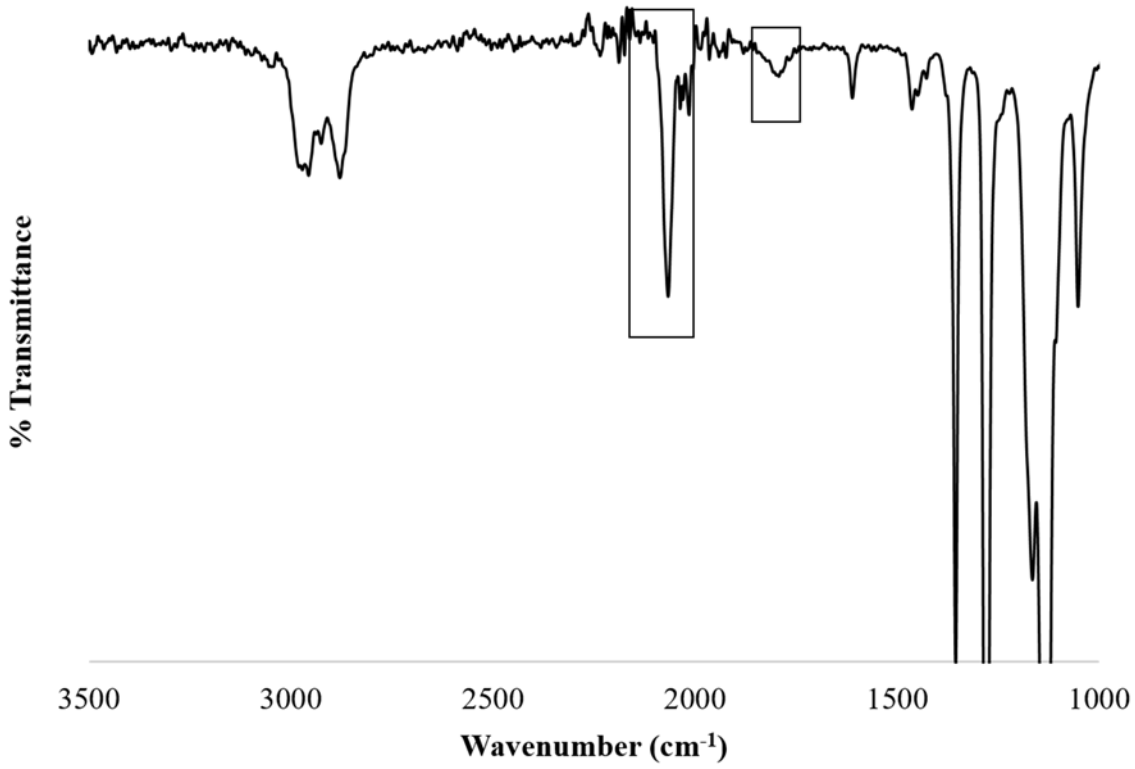

Figure A4.42. IR (thin-film) Spectrum of **4.11**.

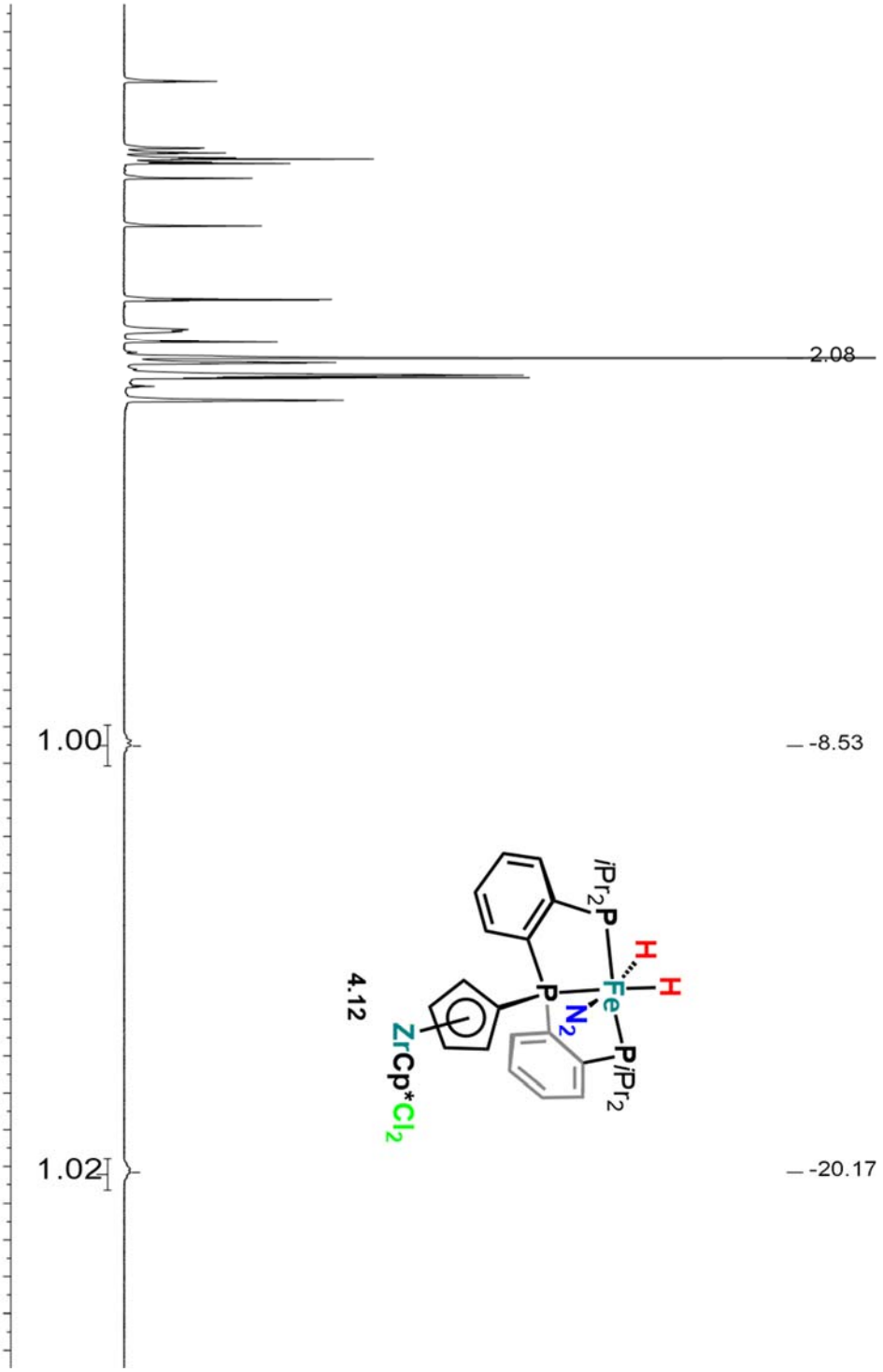

Figure A4.43. ^{1}H NMR Spectrum (toluene-d_8, 400 MHz) of P_2^{PCpP}FeZr **(4.12)**.

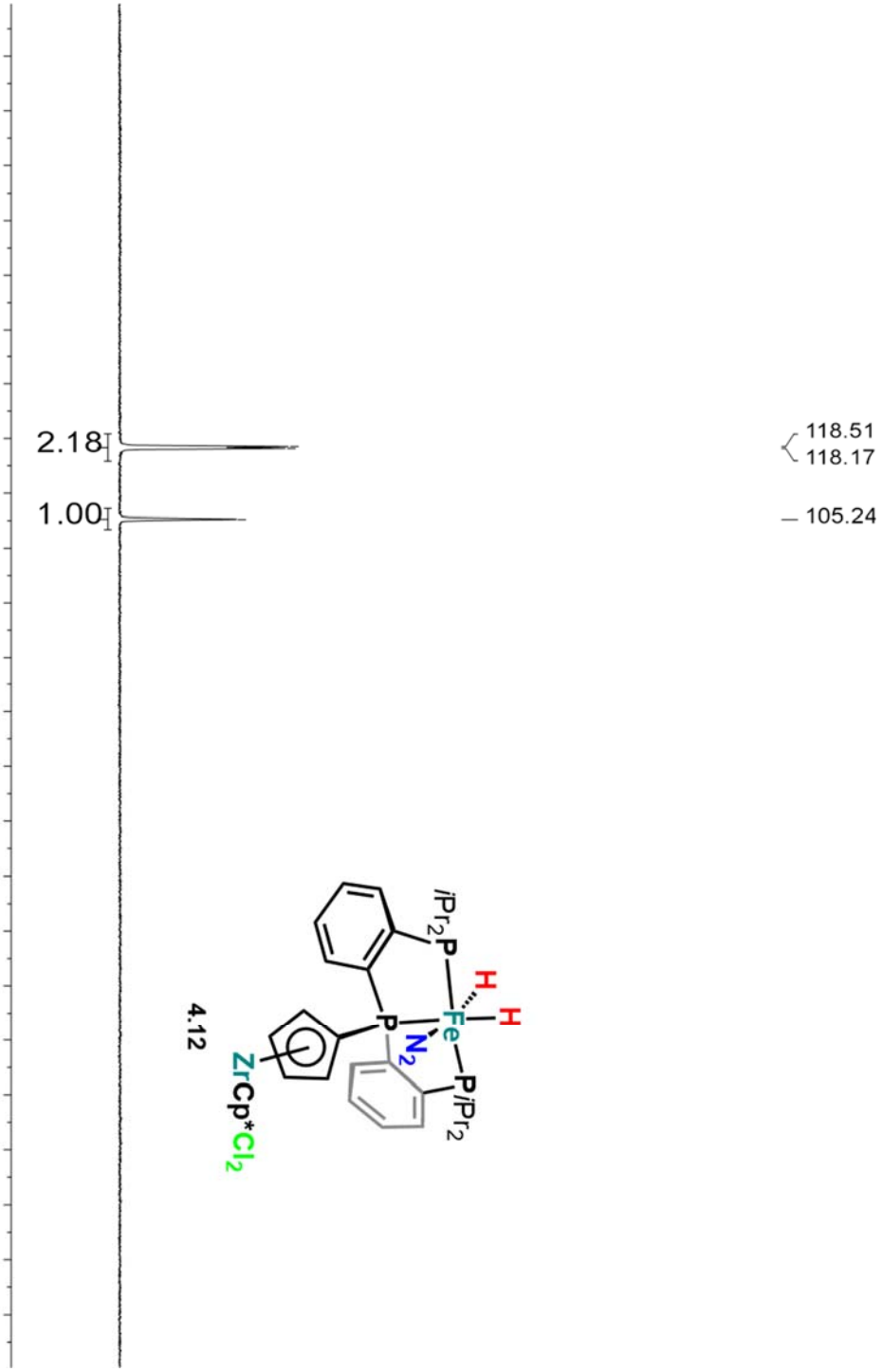

Figure A4.44. ^{31}P NMR Spectrum (toluene-d_8, 162 MHz) of P_2^{PCp}FeZr **(4.12)**.

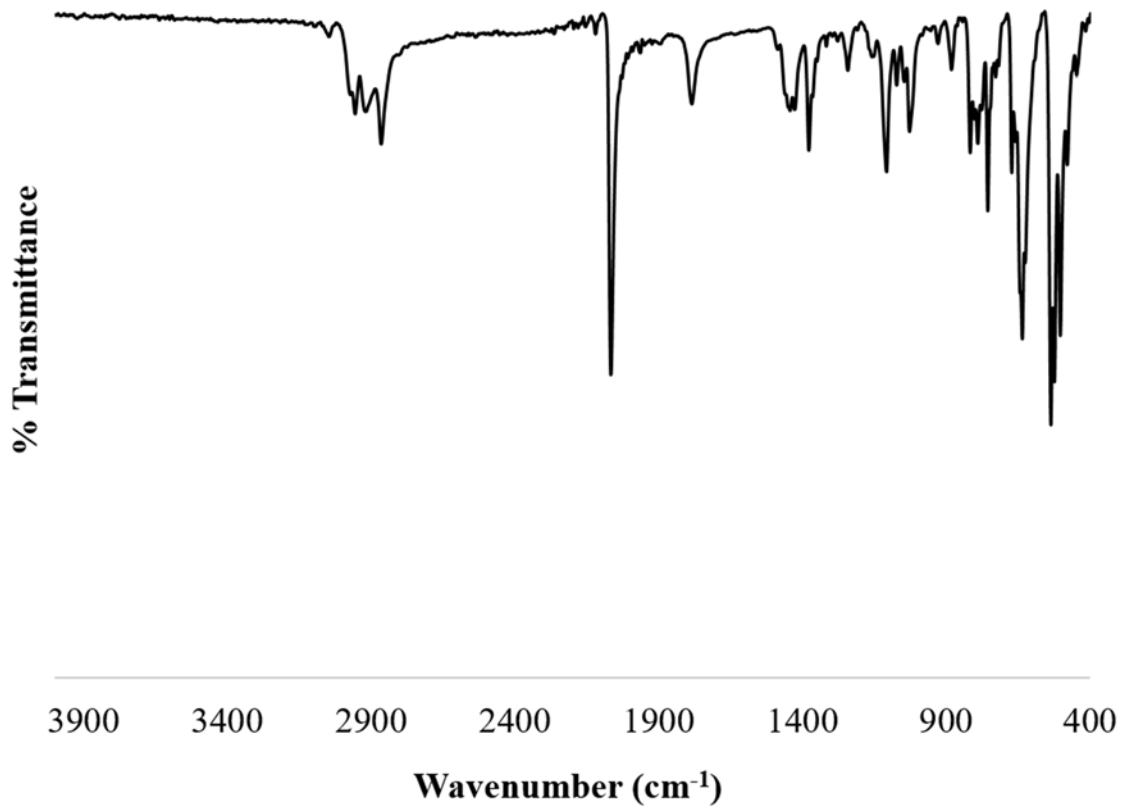

Figure A4.45. Solid-state (KBr) IR spectrum of **4.12**.

A4.3 Miscellaneous Experiments

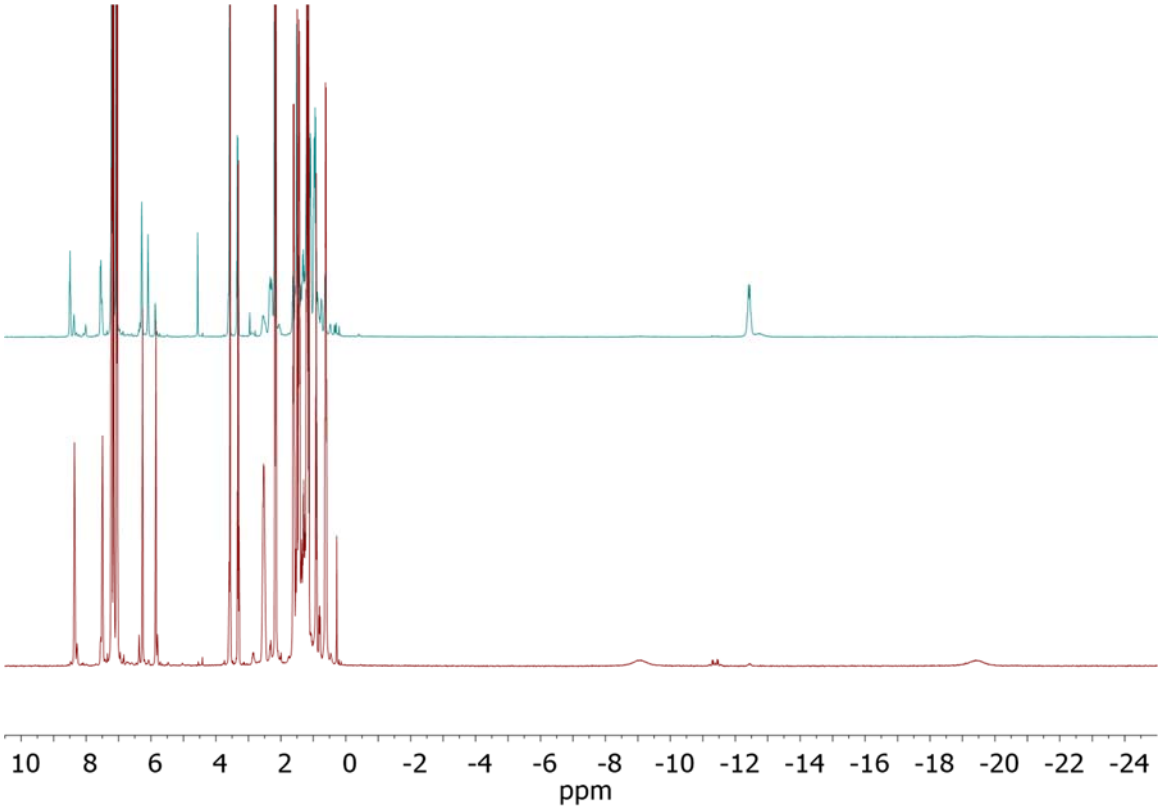

Figure A4.46. ^{1}H NMR Spectra (400 MHz, 10: 1 toluene-d_8 :THF-d_8) of **4.9** before the addition of H_2 (bottom) and after 22 hours total of mixing (top).

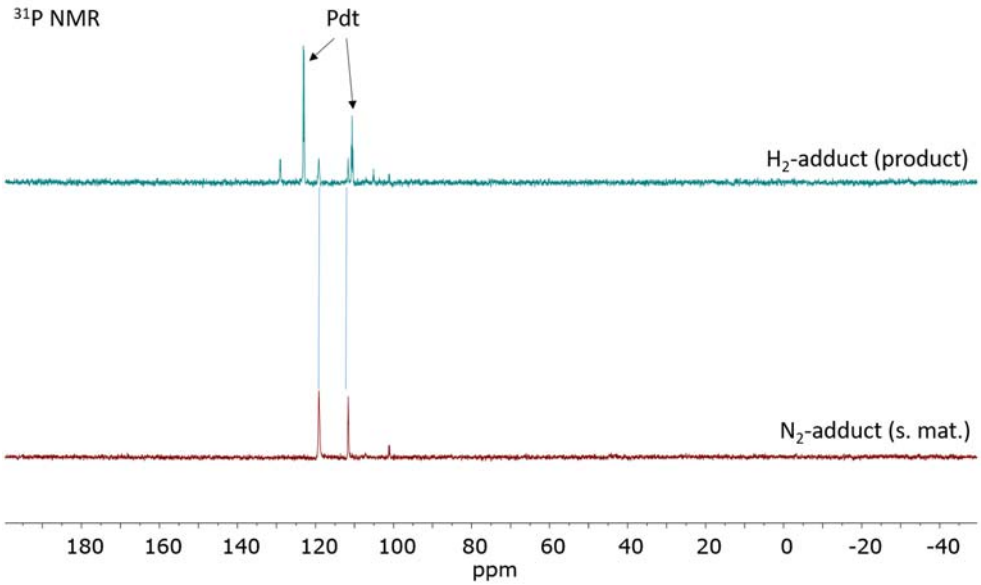

Figure A4.47. ^{31}P NMR Spectra (400 MHz, 10: 1 toluene-d_8 :THF-d_8) of **4.9** before the addition of H_2 (bottom) and after 22 hours total of mixing (top).

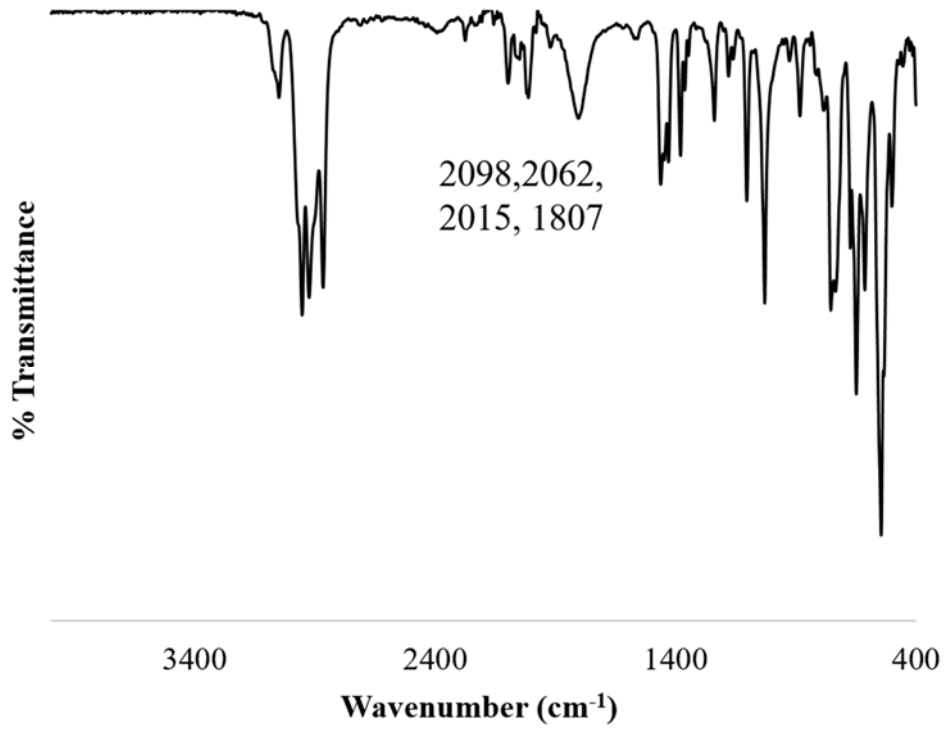

Figure A4.48. Thin firm IR spectrum of **4.9** after the addition of H_2 and 22 hours total of mixing.

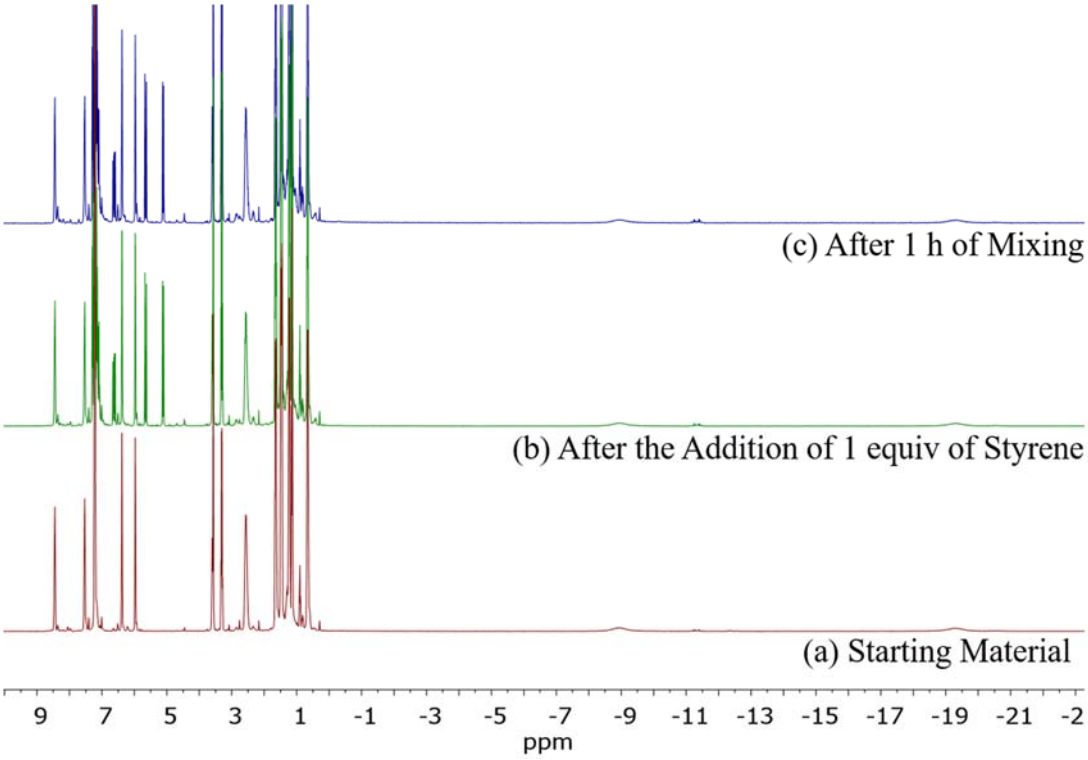

Figure A4.49. ^{1}H NMR spectra (400 MHz, 7:1 C_6D_6:THF-d_8) of (a) **4.9**, (b) **4.9** with 1.0 equiv of styrene and (c) after 1 h of mixing.

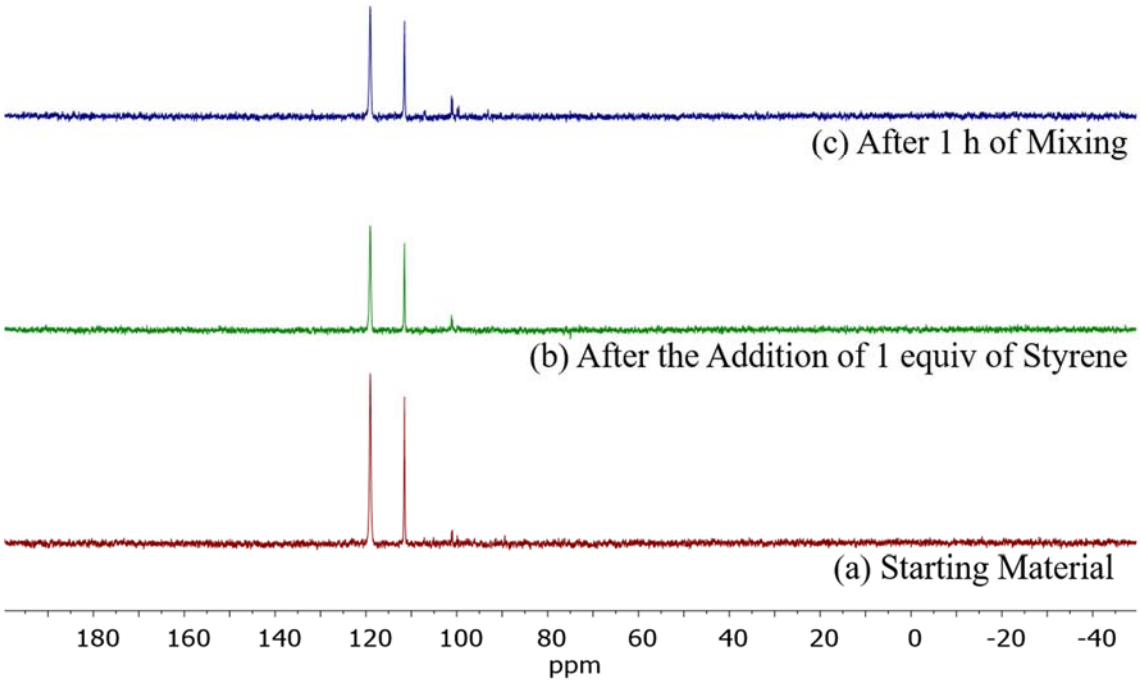

Figure A4.50. ^{31}P NMR spectra (400 MHz, 7:1 C_6D_6:THF-d_8) of (a) **4.9**, (b) **4.9** with 1.0 equiv of styrene and (c) after 1 h of mixing.

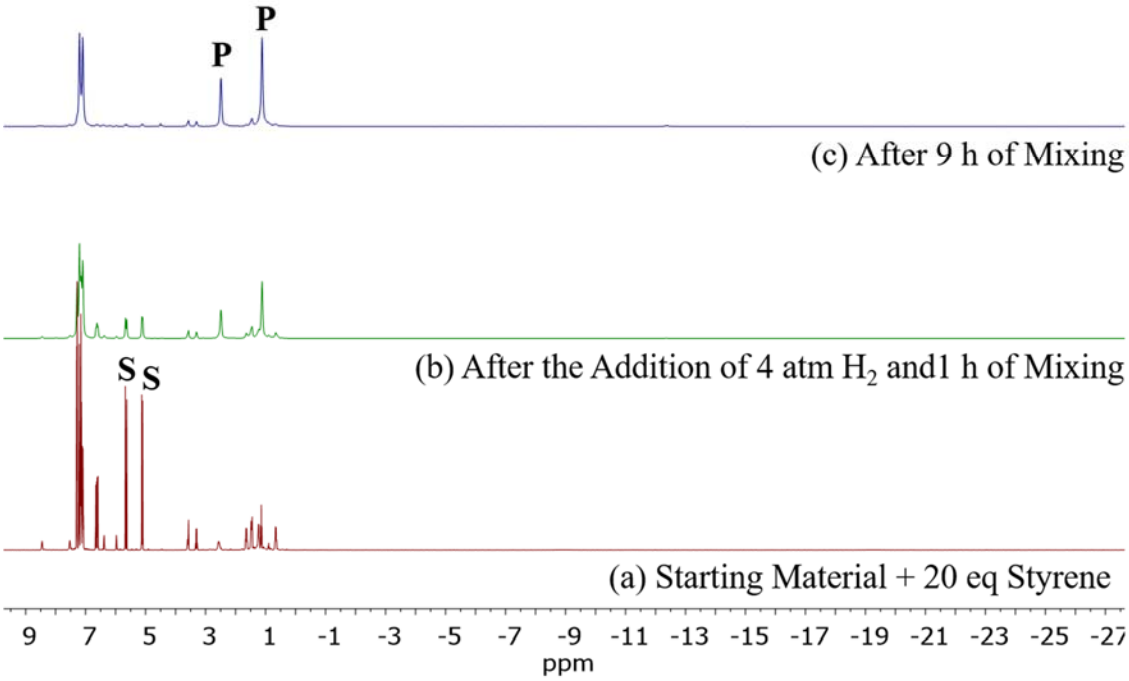

Figure A4.51. ^{1}H NMR spectra (400 MHz, 7:1 C_6D_6:THF-d_8) of a catalytic hydrogenation of styrene: (a) 5 mol% **4.9** and 20 equiv of styrene, (b) after the addition of 4 atm of H_2 and 1 h of mixing; and, (c) after 9 h of mixing. "S" stands for starting material (styrene) and "P" stands for product (ethylbenzene).

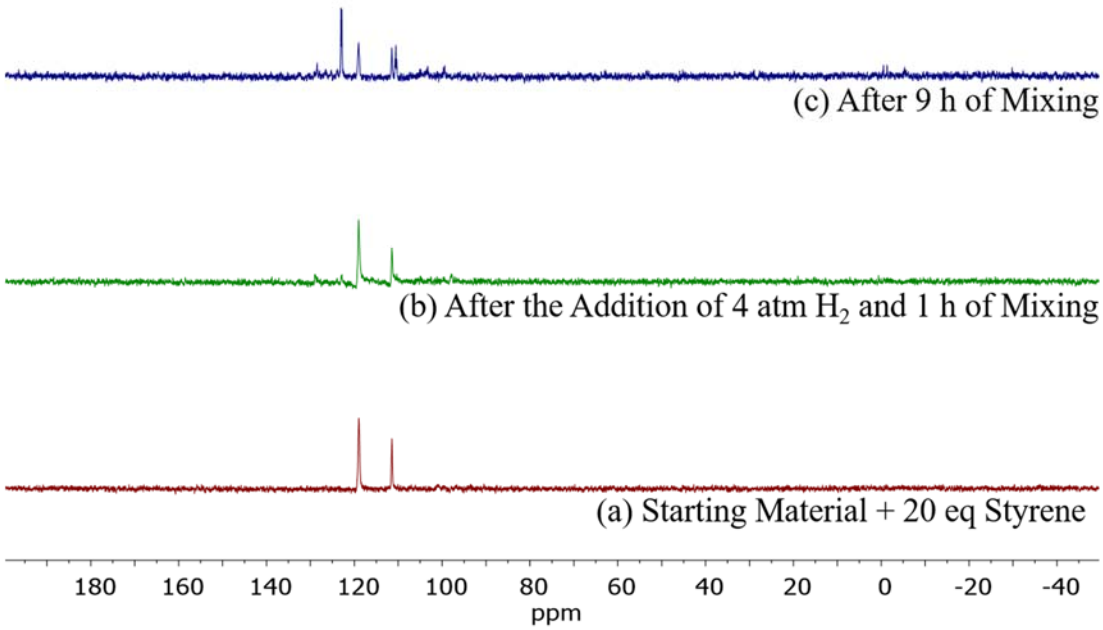

Figure A4.52. ^{31}P NMR spectra (400 MHz, 7:1 C_6D_6:THF-d_8) of a catalytic hydrogenation of styrene: (a) 5 mol% **4.9** and 20 equiv of styrene, (b) after the addition of 4 atm of H_2 and 1 h of mixing; and, (c) after 9 h of mixing.

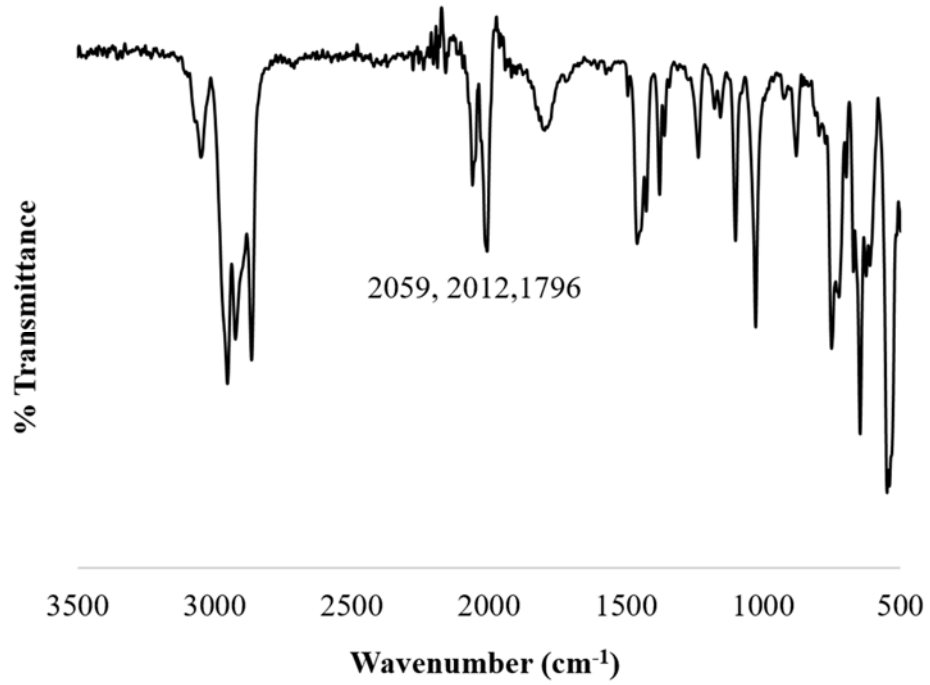

Figure A4.53. Thin firm IR spectrum of **4.9** post-catalytic reaction.

A4.4 X-Ray Diffraction Data

Table A4.8. Crystal structure and refinement data for **4.2**.

Structure	**4.2**
Empirical formula	$C_{39}H_{56}Cl_2P_2SiZr$
Formula weight	776.98
Temperature/K	0.0
Crystal system	orthorhombic
Space group	$P2_12_12_1$
a/Å	13.3888(5)
b/Å	16.4451(5)
c/Å	18.0318(6)
α/°	90
β/°	90
γ/°	90
Volume/Å^3	3970.2(2)
Z	4
ρ_{calc}g/cm^3	1.300
μ/mm^{-1}	0.548
F(000)	1632.0
Crystal size/mm^3	0.192 × 0.145 × 0.119
Radiation	MoKα (λ = 0.71073)
2Θ range for data collection/°	4.954 to 72.118
Index ranges	$-21 \leq h \leq 21$, $-26 \leq k \leq 25$, $-27 \leq l \leq 27$
Reflections collected	131799
Independent reflections	17248 [R_{int} = 0.1026, R_{sigma} = 0.1127]
Data/restraints/parameters	17248/0/419
Goodness-of-fit on F^2	1.027
Final R indexes [I>=2σ (I)]	R_1 = 0.0502, wR_2 = 0.0662
Final R indexes [all data]	R_1 = 0.1052, wR_2 = 0.0747
Largest diff. peak/hole / e Å^{-3}	0.50/-0.54
Flack parameter	-0.005(11)

Table A4.9. Crystal structure and refinement data for **4.3**.

Structure	**4.3**
Empirical formula	$C_{41}H_{63}FeN_2O_{0.5}P_2SiZr$
Formula weight	829.03
Temperature/K	100.02
Crystal system	monoclinic
Space group	$P2_1/c$
a/Å	21.5506(11)
b/Å	21.2217(11)
c/Å	18.0486(9)
α/°	90
β/°	99.070(2)
γ/°	90
Volume/Å^3	8151.1(7)
Z	8
ρ_{calc}g/cm^3	1.351
μ/mm^{-1}	0.751
F(000)	3496.0
Crystal size/mm^3	0.094 × 0.250 × 0.529
Radiation	MoKα (λ = 0.71073)
2Θ range for data collection/°	2.984 to 64.78
Index ranges	$-32 \leq h \leq 31$, $-31 \leq k \leq 31$, $-26 \leq l \leq 26$
Reflections collected	178598
Independent reflections	27812 [R_{int} = 0.0587, R_{sigma} = 0.0476]
Data/restraints/parameters	27812/0/920
Goodness-of-fit on F^2	1.018
Final R indexes [I>=2σ (I)]	R_1 = 0.0429, wR_2 = 0.0899
Final R indexes [all data]	R_1 = 0.0685, wR_2 = 0.0993
Largest diff. peak/hole / e Å^{-3}	2.28/-1.38
Flack parameter	n/a

Table A4.10. Crystal structure and refinement data for **4.4**.

Structure	**4.4**
Empirical formula	$C_{39}H_{55}FeN_2P_2SiZr$
Formula weight	788.95
Temperature/K	99.92
Crystal system	monoclinic
Space group	$P2_1/c$
a/Å	10.6350(7)
b/Å	37.082(2)
c/Å	10.5774(6)
α/°	90
β/°	115.7240(18)
γ/°	90
Volume/Å^3	3758.0(4)
Z	4
ρ_{calc}g/cm^3	1.394
μ/mm^{-1}	0.810
F(000)	1652.0
Crystal size/mm^3	0.118 × 0.207 × 0.224
Radiation	MoKα (λ = 0.71073)
2Θ range for data collection/°	4.39 to 69.784
Index ranges	$-17 \leq h \leq 16$, $-57 \leq k \leq 58$, $-17 \leq l \leq 16$
Reflections collected	80599
Independent reflections	15546 [R_{int} = 0.1113, R_{sigma} = 0.0732]
Data/restraints/parameters	15546/0/431
Goodness-of-fit on F^2	1.107
Final R indexes [I>=2σ (I)]	R_1 = 0.0698, wR_2 = 0.1436
Final R indexes [all data]	R_1 = 0.1063, wR_2 = 0.1566
Largest diff. peak/hole / e Å^{-3}	2.38/-1.29
Flack parameter	n/a

Table A4.11. Crystal structure and refinement data for **4.5**.

Structure	**4.5**
Empirical formula	$C_{52}H_{69}F_3FeN_2O_3P_2SSiZr$
Formula weight	1096.25
Temperature/K	100.0
Crystal system	monoclinic
Space group	$P2_1/n$
a/Å	11.9252(13)
b/Å	29.803(3)
c/Å	14.8702(14)
α/°	90
β/°	104.257(3)
γ/°	90
Volume/Å^3	5122.2(9)
Z	4
ρ_{calc}g/cm^3	1.422
μ/mm^{-1}	0.668
F(000)	2288.0
Crystal size/mm^3	0.2 × 0.1 × 0.05
Radiation	MoKα (λ = 0.71073)
2Θ range for data collection/°	4.794 to 69.962
Index ranges	$-19 \leq h \leq 19$, $-48 \leq k \leq 48$, $-23 \leq l \leq 23$
Reflections collected	127543
Independent reflections	22497 [R_{int} = 0.1548, R_{sigma} = 0.1441]
Data/restraints/parameters	22497/0/614
Goodness-of-fit on F^2	1.004
Final R indexes [I>=2σ (I)]	R_1 = 0.0604, wR_2 = 0.0823
Final R indexes [all data]	R_1 = 0.1406, wR_2 = 0.0980
Largest diff. peak/hole / e Å^{-3}	0.61/-0.69
Flack parameter	n/a

Table A4.12. Crystal structure and refinement data for **4.8**.

Structure	**4.8**	
Empirical formula	$C_{29}H_{41}Br_2FeP_3$	
Formula weight	695.32	
Temperature	220(2) K	
Wavelength	0.71073 Å	
Crystal system	Monoclinic	
Space group	$P2_1/n$	
Unit cell dimensions	a = 10.7898(3) Å	α= 90°
	b = 17.1975(5) Å	β= 94.9717(11)°
	c = 16.7737(5) Å	γ = 90°
Volume	3100.78(16) $Å^3$	
Z	4	
Density (calculated)	1.489 Mg/m^3	
Absorption coefficient	3.222 mm^{-1}	
F(000)	1420	
Crystal size	0.08 x 0.08 x 0.14 mm^3	
Theta range for data collection	2.162 to 27.495°.	
Index ranges	$-14 \le h \le 13$, $-22 \le k \le 22$, $-21 \le l \le 21$	
Reflections collected	90995	
Independent reflections	7096 [R(int) = 0.0488]	
Completeness to theta = 25.242°	99.9 %	
Refinement method	Full-matrix least-squares on F^2	
Data / restraints / parameters	7096 / 0 / 354	
Goodness-of-fit on F^2	1.024	
Final R indices [I>2sigma(I)]	R1 = 0.0441, wR2 = 0.0917	
R indices (all data)	R1 = 0.0647, wR2 = 0.1019	
Extinction coefficient	n/a	
Largest diff. peak and hole	1.236 and -1.310 $e.Å^{-3}$	

Table A4.13. Crystal structure and refinement data for **4.9**.

Structure	**4.9**	
Empirical formula	$C_{29}H_{42}FeN_2NaP_3$	
Formula weight	166.85	
Temperature	99.98 K	
Wavelength	0.71073 Å	
Crystal system	Trigonal	
Space group	R -3:r	
Unit cell dimensions	a = 21.2383(3) Å	α = 116.34°
	b = 21.2383(3) Å	β = 116.34°
	c = 21.2383(3) Å	γ = 116.34°
Volume	4638.11(16) $Å^3$	
Z	31	
Density (calculated)	1.852 Mg/m^3	
Absorption coefficient	2.740 mm^{-1}	
F(000)	2511	
Crystal size	? x ? x ? mm^3	
Theta range for data collection	2.257 to 30.507°.	
Index ranges	$-30 \le h \le 30$, $-29 \le k \le 30$, $-29 \le l \le 28$	
Reflections collected	80684	
Independent reflections	9346 [R(int) = 0.5262]	
Completeness to theta = 26.000°	99.9 %	
Refinement method	Full-matrix least-squares on F^2	
Data / restraints / parameters	9346 / 0 / 341	
Goodness-of-fit on F^2	0.862	
Final R indices [I>2sigma(I)]	R1 = 0.0755, wR2 = 0.1807	
R indices (all data)	R1 = 0.1826, wR2 = 0.2233	
Extinction coefficient	n/a	
Largest diff. peak and hole	0.653 and -0.718 e $Å^{-3}$	

Table A4.14. Crystal structure and refinement data for **4.12**.

Structure	**4.12**	
Empirical formula	$C_{29}H_{43}Cl_2FeN_2P_3Zr$	
Formula weight	222.14	
Temperature	100.0 K	
Wavelength	0.71073 Å	
Crystal system	Monoclinic	
Space group	P 1 21/n 1	
Unit cell dimensions	a = 14.6427(8) Å	α= 90°
	b = 11.9454(6) Å	β= 103.233(3)°
	c = 27.1841(14) Å	γ = 90°
Volume	4628.6(4) $Å^3$	
Z	33	
Density (calculated)	2.630 Mg/m^3	
Absorption coefficient	4.602 mm^{-1}	
F(000)	3416	
Crystal size	0.16 x 0.33 x 0.35 mm^3	
Theta range for data collection	6.761 to 43.721°.	
Index ranges	$-10 \le h \le 22$, $-11 \le k \le 14$, $-52 \le l \le -4$	
Reflections collected	12311	
Independent reflections	8860 [R(int) = 0.0352]	
Completeness to theta = 26.000°	34.5 %	
Absorption correction	None	
Refinement method	Full-matrix least-squares on F^2	
Data / restraints / parameters	8860 / 0 / 493	
Goodness-of-fit on F^2	0.832	
Final R indices [I>2sigma(I)]	R_1 = 0.0338, wR_2 = 0.0664	
R indices (all data)	R_1 = 0.0607, wR_2 = 0.0729	
Extinction coefficient	n/a	
Largest diff. peak and hole	0.455 and -0.353 e $Å^{-3}$	